Universitat
de les Illes Balears

DOCTORAL THESIS
2022

INFLUENCE OF THERMAL TREATMENTS ON Ni-Ti-Zr AND Ni-Mn-Ga-X HIGH TEMPERATURE SHAPE MEMORY ALLOYS

SHOUKAI XU

Universitat
de les Illes Balears

DOCTORAL THESIS
2022

Doctoral Programme in Physics

INFLUENCE OF THERMAL TREATMENTS ON Ni-Ti-Zr AND Ni-Mn-Ga-X HIGH TEMPERATURE SHAPE MEMORY ALLOYS

SHOUKAI XU

Thesis Supervisor: Jaume Pons Morro

Thesis Supervisor: Rubén Santamarta Martínez

Thesis tutor: Eduard Cesari Aliberch

Doctor by the Universitat de les Illes Balears

RESUM

Els aliatges amb memòria de forma (SMA) són coneguts per les seves propietats especials, que s'han utilitzat àmpliament en moltes indústries. Una manera de classificar els SMA és mitjançant les seves temperatures de transformació, i aquest treball es centra en aquelles que treballen a altes temperatures, inclosos els sistemes d'aliatges Ni-Ti-X i Ni-Mn-Ga-X.

Els aliatges binaris Ni-Ti són el SMA amb més èxit des del punt de vista de les aplicacions, però només poden operar per sota de 370 K. Per tant, sovint s'han suggerit i proposat aliatges ternaris Ni-Ti-X que tenen altes temperatures de transformació. Entre totes les possibilitats desenvolupades, els aliatges Ni-Ti-Hf/Zr rics en Ni han cridat molt l'atenció, per una banda, per augmentar les temperatures de transformació del Ni-Ti, i per altra, per mostrar propietats de memòria de forma prometedores com a resultat dels precipitats nanomètrics de fase H. Per tant, en el present treball s'investiga, per primera vegada, l'efecte del tractament tèrmic sobre les propietats funcionals i la corresponent microestructura d'aliatges policristal·lins $Ni_{50.3}Ti_{24.7}Zr_{25}$. L'aliatge $Ni_{50.3}Ti_{24.7}Zr_{25}$ té una transformació B2-B19' d'un sol pas a altes temperatures, i propietats termomecàniques relativament bones després d'un tractament tèrmic adequat (envelliment de 820 K durant 3 h), a causa de la precipitació de la fase H. No obstant això, en aquest aliatge es poden detectar petites deformacions irrecuperables en cicles termomecànics, el que contrasta amb les publicacions d'aliatges Zr15/20 o Hf20 que pràcticament no mostren cap deformació irrecuperable, el que es podria atribuir a una quantitat excessiva de precipitats en fase H a l'aliatge Zr25.

En alguns aliatges amb transició martensítica ferroelàstica suprimida durant el refredament, s'ha trobat un nou estat conegut com a *strain glass* (SG), consistent en deformacions de la xarxa cristal·logràfica desordenades localment. En aquest treball, s'ha descobert que els aliatges $Ni_{50.3}Ti_{29.7}Zr_{20}$, $Ni_{50.3}Ti_{24.7}Zr_{25}$ i $Ni_{50.9}Ti_{24.1}Zr_{25}$ presenten una transformació martensítica suprimida després de diferents tractaments tèrmics. Per tant, s'han realitzat diversos experiments per verificar si es troben en l'estat SG o no. Es considera que la formació primerenca del precursor dels precipitats de fase H, acompanyada de la redistribució d'àtoms de Ti i Zr, altera l'ordenació a llarg abast de la matriu i de la transformació martensítica convencional després dels tractaments tèrmics. En aquesta situació, durant el refredament només es poden formar dominis nanomètrics semblants a la martensita, mentre que la matriu roman, en terme mitjà, en l'estructura de la fase cúbica. Els aliatges $Ni_{50.3}Ti_{29.7}Zr_{20}$ i $Ni_{50.9}Ti_{24.1}Zr_{25}$ mostren un mòdul *E* dependent de la freqüència i es confirma que desenvolupen l'estat SG, mentre que els resultats de $Ni_{50.3}Ti_{24.7}Zr_{25}$ suggereixen l'existència d'un estat "d'incubació" previ a l'estat SG totalment desenvolupat. A més, s'han trobat cicles tensió-deformació atípicament suaus a mostres $Ni_{50.3}Ti_{29.7}Zr_{20}$ envellides durant

temps prolongats i amb poca dependència amb la temperatura, per al que s'ha proposat un model qualitatiu que expliqui aquest fenomen. També s'ha trobat l'efecte *elinvar* abans de la transició SG de l'aliatge $Ni_{50.9}Ti_{24.1}Zr_{25}$ durant el refredament en el DMA, confirmat també mitjançant una tècnica de ressonància ultrasònica d'alta precisió. L'efecte s'atribueix a la formació de dominis finits de martensita amb una distribució àmplia de temperatures M_s molt localitzades.

Alternativament, els aliatges Ni-Mn-Ga tenen un potencial intrínsec com a aliatges amb memòria de forma d'alta temperatura (HTSMA), amb M_s superiors als 400 K, i una alta estabilitat al ciclat tèrmic en aliatges monocristal·lins. Per això la comunitat científica ha centrat els seus esforços en aliatges policristal·lins, ja que són més fàcils de produir. No obstant, els aliatges policristal·lins mostren un alt nivell de fragilitat als límits del gra. Per això, fins ara, s'han estudiat una varietat d'elements quaternaris (Cr, Cu, elements de terres rares...) per afegir a l'aliatge ternari Ni-Mn-Ga i induir precipitats que haurien de millorar la ductilitat de la matriu. Aquest treball es centra en HTSMA quaternaris de la forma Ni-Mn-Ga-X (X = Cu, Sn, Hf i Zr), amb una baixa quantitat de dopants, que encara no s'han investigat. Els aliatges Ni-Mn-Ga-Cu rics en Ni i amb un 1% atòmic en Cu presenten una alta estabilitat tèrmica després de tractaments d'envelliment prolongats, tot i que no es poden induir precipitats. L'inconvenient principal és que els aliatges Ni-Mn-Ga-Cu policristal·lins i monofàsics mostren una baixa resistència de la matriu, i les deformacions irreversibles augmenten bruscament quan s'apliquen esforços per damunt dels 100 MPa en experiments de ciclat termomecànic. El dopat d'aliatges policristal·lins de Ni-Mn-Ga amb Sn provoca la reducció de les temperatures de transformació i de la histèresi per quantitats de Sn superiors al 2% atòmic a causa de la relativa bona compatibilitat entre la fase matriu i la martensita. Malgrat això, l'addició del 4 at.% de Sn provoca una fragilitat extrema del material a causa de l'aparició de petits forats a la matriu després de la fusió per inducció. En comparació, els aliatges policristal·lins Ni-Mn-Ga-Hf/Zr, estudiats per primera vegada aquí, sí que presenten un alt potencial com a HTSMA. Les temperatures de transformació es redueixen amb l'augment de Hf/Zr, però encara hi ha composicions que entren dins de la categoria de HTSMA. Precipitats d'una segona fase dúctil ja comencen a aparèixer quan la quantitat de Hf/Zr és de l'1% atòmic, i augmenten en nombre i mida amb quantitats de Hf/Zr més elevades, tot i que la fracció volúmica de la matriu transformable es redueix inevitablement. La histèresi disminueix sorprenentment fins a uns 8 K per als aliatges Hf4/Zr4, cosa que s'atribueix a la bona compatibilitat entre les xarxes cristal·logràfiques d'austenita i martensita. La martensita b.c.t. es forma en tots els aliatges Ni-Mn-Ga-Hf/Zr, i una petita fracció de martensita 14M modulada també coexisteix amb la primera en aliatges Hf4/Zr4. S'ha investigat i identificat l'estructura dels precipitats, la qual posseeix un paràmetre de xarxa el doble de gran que la dels precipitats convencionals de fase γ (f.c.c.) que es formen en altres aliatges Ni-Mn-Ga-X. S'han construït models estructurals utilitzant una cel·la unitat basada en la f.c.c. convencional però amb un paràmetre de xarxa el doble de gran (constituïda per 32 àtoms), i una cel·la unitat tetragonal centrada en les cares, A6, més petita i

corresponent al grup espacial I4/mmm. La xarxa de precipitats als aliatges amb més del 2% atòmic de Hf/Zr pot millorar la resistència dels aliatges i reduir la deformació plàstica en ciclats termomecànics, però a costa d'una caiguda important de la deformació per transformació i d'obstaculitzar l'efecte de superelasticitat.

Paraules clau: Aliatges de memòria de forma d'alta temperatura (HTSMA), Ni-Ti-Zr ric en Ni, precipitats de fase H, *Strain Glass*, Ni-Mn-Ga-X (X = Cu, Sn, Hf i Zr).

RESUMEN

Las aleaciones con memoria de forma (SMA) son conocidas por sus propiedades especiales, que se han utilizado ampliamente en muchas industrias. Una manera de clasificar los SMA es mediante sus temperaturas de transformación, y este trabajo se centra en aquellas que trabajan a altas temperaturas, incluidos los sistemas de aleaciones Ni-Ti-X y Ni-Mn-Ga-X.

Las aleaciones binarias Ni-Ti son la SMA con más éxito desde el punto de vista de las aplicaciones, pero solo pueden operar por debajo de 370 K. Por tanto, a menudo se han sugerido y propuesto aleaciones ternarias Ni-Ti-X que tienen altas temperaturas de transformación. Entre todas las posibilidades desarrolladas, las aleaciones Ni-Ti-Hf/Zr ricas en Ni han llamado mucho la atención, por un lado, para aumentar las temperaturas de transformación del Ni-Ti, y por otro, para mostrar propiedades de memoria de forma prometedoras como resultado de los precipitados nanométricos de fase H. Por tanto, en el presente trabajo se investiga, por primera vez, el efecto del tratamiento térmico sobre las propiedades funcionales y la correspondiente microestructura de aleaciones policristalinas $Ni_{50.3}Ti_{24.7}Zr_{25}$. La aleación $Ni_{50.3}Ti_{24.7}Zr_{25}$ tiene una transformación B2-B19' de un solo paso a altas temperaturas, y propiedades termomecánicas relativamente buenas después de un tratamiento térmico adecuado (envejecimiento a 820 K durante 3 h), debido a la precipitación de la fase H. Sin embargo, en esta aleación se pueden detectar pequeñas deformaciones irrecuperables en ciclos termomecánicos, lo que contrasta con las publicaciones de aleaciones Zr15/20 o Hf20 que prácticamente no muestran ninguna deformación irrecuperable, lo que se podría atribuirse a una cantidad excesiva de precipitados de fase H en la aleación Zr25.

En algunas aleaciones con transición martensítica ferroelástica suprimida durante el enfriamiento, se ha encontrado un nuevo estado conocido como *strain glass* (SG), consistente en deformaciones de la red cristalográfica desordenadas localmente. En este trabajo, se ha descubierto que las aleaciones $Ni_{50.3}Ti_{29.7}Zr_{20}$, $Ni_{50.3}Ti_{24.7}Zr_{25}$ y $Ni_{50.9}Ti_{24.1}Zr_{25}$ presentan una transformación martensítica suprimida después de diferentes tratamientos térmicos. Por tanto, se han realizado varios experimentos para verificar si se encuentran en el estado SG o no. Se considera que la formación temprana del precursor de los precipitados de fase H, acompañada de la redistribución de átomos de Ti y Zr, altera la ordenación a largo alcance de la matriz y de la transformación martensítica convencional después de los tratamientos térmicos. En esta situación, durante el enfriamiento solo se pueden formar dominios nanométricos similares a la martensita, mientras que la matriz permanece, en promedio, en la estructura de la fase cúbica. Las aleaciones $Ni_{50.3}Ti_{29.7}Zr_{20}$ y $Ni_{50.9}Ti_{24.1}Zr_{25}$ muestran un módulo *E* dependiente de la frecuencia y se confirma que desarrollan el estado SG, mientras que los resultados de $Ni_{50.3}Ti_{24.7}Zr_{25}$ sugieren la existencia de un estado "de incubación" previo al estado SG totalmente desarrollado.

Además, se han encontrado ciclos tensión-deformación atípicamente suaves y con poca dependencia con la temperatura en muestras $Ni_{50.3}Ti_{29.7}Zr_{20}$ envejecidas durante tiempos prolongados, para lo que se ha propuesto un modelo cualitativo que explique este fenómeno. También se ha encontrado el efecto *elinvar* antes de la transición SG de la aleación $Ni_{50.9}Ti_{24.1}Zr_{25}$ durante el enfriamiento en el DMA, confirmado también mediante una técnica de resonancia ultrasónica de alta precisión. El efecto se atribuye a la formación de dominios finitos de martensita con una distribución amplia de temperaturas M_s muy localizadas.

Alternativamente, las aleaciones Ni-Mn-Ga tienen un potencial intrínseco como aleaciones con memoria de forma de alta temperatura (HTSMA), con M_s superiores a los 400 K, y una alta estabilidad en el ciclado térmico en aleaciones monocristalinas. Por eso la comunidad científica ha centrado sus esfuerzos en aleaciones policristalinas, ya que son más fáciles de producir. Sin embargo, las aleaciones policristalinas muestran un alto nivel de fragilidad en los límites del grano. Por eso, hasta ahora, se han estudiado una variedad de elementos cuaternarios (Cr, Cu, elementos de tierras raras...) para añadir a la aleación ternaria Ni-Mn-Ga e inducir precipitados que deberían mejorar la ductilidad de la matriz. Este trabajo se centra en HTSMA cuaternarias de la forma Ni-Mn-Ga-X (X = Cu, Sn, Hf y Zr), con una baja cantidad de dopantes, las cuales todavía no se habían investigado. Las aleaciones Ni-Mn-Ga-Cu ricas en Ni y con un 1% atómico en Cu presentan una alta estabilidad térmica después de tratamientos de envejecimiento prolongados, aunque no pueden inducirse precipitados. El inconveniente principal es que las aleaciones Ni-Mn-Ga-Cu policristalinas y monofásicas muestran una baja resistencia de la matriz, y las deformaciones irreversibles aumentan bruscamente cuando se aplican esfuerzos por encima de los 100 MPa en experimentos de ciclado termomecánico. El dopado de aleaciones policristalinas de Ni-Mn-Ga con Sn provoca la reducción de las temperaturas de transformación y de la histéresis para cantidades de Sn superiores al 2% atómico debido a la relativa buena compatibilidad entre la fase matriz y la martensita. Sin embargo, la adición del 4 at.% de Sn provoca una fragilidad extrema del material debido a la aparición de pequeños agujeros en la matriz después de la fusión por inducción. En comparación, las aleaciones policristalinas Ni-Mn-Ga-Hf/Zr, estudiadas por primera vez aquí, sí presentan un alto potencial como HTSMA. Las temperaturas de transformación se reducen con el aumento de Hf/Zr, pero todavía existen composiciones que entran dentro de la categoría de HTSMA. Precipitados de una segunda fase dúctil ya comienzan a aparecer cuando la cantidad de Hf/Zr es del 1% atómico, aumentando en número y tamaño con cantidades de Hf/Zr más elevadas, aunque la fracción volúmica de la matriz transformable se reduce inevitablemente. La histéresis disminuye sorprendentemente hasta unos 8 K para las aleaciones Hf4/Zr4, lo que se atribuye a la buena compatibilidad entre las redes cristalográficas de austenita y martensita. La martensita b.c.t. se forma en todas las aleaciones Ni-Mn-Ga-Hf/Zr, y una pequeña fracción de martensita 14M modulada también coexiste con la primera en aleaciones Hf4/Zr4. Se ha investigado e identificado la estructura de los precipitados, la cual posee un parámetro de red el

doble de grande que la de los precipitados convencionales de fase γ (f.c.c.) que se forman en otras aleaciones Ni-Mn-Ga-X. Se han construido modelos estructurales utilizando una celda unidad basada en la f.c.c. convencional pero con un parámetro de red el doble de grande (constituida por 32 átomos), y una celda unidad tetragonal centrada en las caras, A6, más pequeña y correspondiente al grupo espacial I4/mmm. La red de precipitados en las aleaciones con más del 2% atómico de Hf/Zr puede mejorar la resistencia de las aleaciones y reducir la deformación plástica en ciclados termomecánicos, pero a costa de una caída importante de la deformación por transformación y de obstaculizar el efecto de superelasticidad.

Palabras clave: Aleaciones con memoria de forma de alta temperatura (HTSMA), Ni-Ti-Zr rico en Ni, precipitados de fase H, *Strain Glass*, Ni-Mn-Ga-X (X = Cu, Sn, Hf i Zr).

ABSTRACT

Shape memory alloys (SMA) are well-known for their unique properties, which have been widely used in many industries. A variety of different alloy systems are briefly categorized by their transformation temperatures, and those ones working at high temperatures are focused in the present work, including Ni-Ti-X and Ni-Mn-Ga-X alloy systems.

The binary Ni-Ti alloys are the most successful material for applications, but can only serve below 370 K. Hence, the Ni-Ti-X ternary alloys have often been suggested and explored with tuned high transformation temperatures. Among all the developed possibilities, Ni-rich Ni-Ti-Hf/Zr alloys have drawn a lot of attention for not only increasing transformation temperature, but also demonstrating promising shape memory properties as the result of nanosized H-phase precipitates. Therefore, in the present work we investigate the thermal treatment effect on shape memory properties and the corresponding microstructure of $Ni_{50.3}Ti_{24.7}Zr_{25}$ polycrystalline alloys which had not been investigated yet. The $Ni_{50.3}Ti_{24.7}Zr_{25}$ alloy demonstrates single step B2-B19' transformation with high transformation temperature and relatively good thermomechanical properties after proper thermal treatment (ageing 820 K 3 h), due to precipitation of H phase. However, small irrecoverable strains can still be observed in thermomechanical cycles of Zr25 alloy in comparison with reported Zr15/20 or Hf20 alloys with basically no irrecoverable strain, which could be ascribed to an excessive amount of H-phase precipitates.

A novel state consisting of locally disordered lattice strains, denoted as strain glass (SG), was found in some alloys with suppressed ferroelastic martensitic transition during cooling. For the present work, $Ni_{50.3}Ti_{29.7}Zr_{20}$, $Ni_{50.3}Ti_{24.7}Zr_{25}$ and $Ni_{50.9}Ti_{24.1}Zr_{25}$ alloys have also been found to present suppressed martensitic transformation after different thermal treatments. Hence, several experimental methods have been performed to verify if they are at SG state or not. It is considered that the early stage formation of precursor H-phase precipitates, accompanied by Ti, Zr atoms redistribution, disrupt the long-range ordering of matrix and normal martensitic transformation after thermal treatments. Only nanometric martensitc-like domains can be formed upon cooling, while the overall matrix remains, in average, in the cubic parent phase structure. $Ni_{50.3}Ti_{29.7}Zr_{20}$ and $Ni_{50.9}Ti_{24.1}Zr_{25}$ alloys show frequency dependent *E* modulus and they are confirmed to develop the SG state, while the results of $Ni_{50.3}Ti_{24.7}Zr_{25}$ suggest an "incubation" state previous to the fully developed SG state. Moreover, special stress-strain smooth loops have been found on $Ni_{50.3}Ti_{29.7}Zr_{20}$ prolonged aged specimen with little temperature dependence, and a qualitative model has been suggested to explain this property. Furthermore, the "elinvar" effect has been found on the $Ni_{50.9}Ti_{24.1}Zr_{25}$ SHT alloy before the SG transition during cooling by DMA measurement, and confirmed through a high

accuracy resonant ultrasonic technique. The effect is ascribed to the formation of finite martensite domains with distributed wide temperature range of local M_s.

Alternatively, the Ni-Mn-Ga alloys were found to intrinsically possess some potential as HTSMAs, with M_s over 400 K and high thermal cycling stability in single crystalline alloys. Then researchers have turned their focus on the polycrystalline alloys since they are easier to produce. However, polycrystalline alloys show a high level of brittleness at grain boundaries. Hence, a variety of quaternary elements (Cr, Cu, rare earth elements ...) have been alloyed into ternary Ni-Mn-Ga to induce precipitates, which should improve the ductility of the matrix. In the present study, we are focusing on the quaternary Ni-Mn-Ga-X (X = Cu, Sn, Hf and Zr) HTSMAs with low amount of additions, which have not been thoroughly investigated yet. Ni-rich Ni-Mn-Ga-Cu (1 at.% of Cu) alloys exhibit high thermal stability after prolonged ageing treatments, although no precipitates can be induced. The single phase Ni-Mn-Ga-Cu polycrystalline alloys show relatively low matrix strength, and the irrecoverable strains increase sharply with over 100 MPa applied stress under thermomechanical cycling. Alloying Sn into Ni-Mn-Ga polycrystalline alloys leads to the reduction of the transformation temperatures, and a narrow hysteresis is observed with over 2 at.% addition due to relatively good compatibility between parent phase and martensite. However, 4 at.% addition of Sn causes an extremely brittleness of material due to the appearance of small holes in the matrix after induction melting. In comparison, Ni-Mn-Ga-Hf/Zr polycrystalline alloys exhibit high potential of shape memory properties. Although the transformation temperatures are decreased with the increase of Hf/Zr addition, they still fit for HTSMA. The ductile second phase precipitates start to appear at 1 at.% addition of Hf/Zr and increase in amount and size with more addition, although the transformable matrix volume fraction is inevitably reduced. The hysteresis surprisingly decreases to about 8 K for Hf4/Zr4 alloys, which is attributed to the good compatibility between the austenite and martensite lattices. The b.c.t. martensite is formed in all the Ni-Mn-Ga-Hf/Zr alloys, and a small fraction of modulated 14M martensite also coexists in Hf4/Zr4 alloys additionally. The precipitates structure has been investigated and identified to possess double lattice parameter than the normal f.c.c. γ phase that forms in other Ni-Mn-Ga-X alloys. Equivalent structural models have been built up, using a double lattice parameter f.c.c. based unit cell (consisted of 32 atoms) or a smaller A6 face-centered tetragonal unit cell corresponding to the I4/mmm space group. The network of precipitates (in the alloys with over 2 at.% Hf/Zr addition) can enhance the strength of the specimens and reduce the plastic deformation under thermomechanical cycling but at the expense of a dramatic drop of the transformation strain, which also inevitably impedes the superelasticity effect.

Key words: High Temperature Shape Memory Alloys (HTSMAs), Ni-rich Ni-Ti-Zr, H-phase precipitates, Strain Glass, Ni-Mn-Ga-X (X = Cu, Sn, Hf and Zr).

DEDICATION

To my family: my mother Sheng Yuehui, my father Xu Hongyi and my other relatives for their never ending support and trust.

ACKNOWLEDGEMENT

It has been four yeas since I started my Ph.D. program in Universitat de les Illes Balears (UIB). During this time I have always been insisting on my career objectives and devote my vigor in the field of material science. Despite all the hardships and mistakes I have met or made, these four years study have been illuminating not only on scientific researches but also on the life path of myself. All the achievement and endeavors would not be successful without all the best people I have ever met.

Prof. Eduard Cesari Aliberch, I am very grateful for this opportunity you gave to me, so I could cross oceans to UIB and enjoy the beautiful life, places and culture of Spain. I am very thankful for your advise and help on my academic life and daily life care. I want to thank you for helping me on the encapsulation experiment which is a high risk for you, and teach me an important experience on using DSC.

Prof. Jaime Pons Morro and Prof. Rubén Santamarta Martínez, I am really lucky and honored to have you as my director and supervisor. I am very grateful that you bring me into this scientific field, and always be patient and willingly to teach and guide me to pursue the knowledge and truth. I also want to thank you for your trust and unconditional selfless support on my Ph.D. studies and my life in this wonderful country. I really cherish every meeting we have, and speaking with you gives me so much confidence, relief and consolation so that I could back on track when I am lost. I do really respect you for sacrifice your precious time on aiding my researches and thesis. And I am really impressed of your experience on microscopy and your perspective on the atomic cell structure which has really opened my horizons.

Prof. Joan Torrens Serra, I am very appreciated that you teach me how to use the equipment in our lab, *e.g.*, induction and arc melting machine, since they are vital for my investigations. And thank you for the encapsulation of my specimens with Prof. Eduard, I am really grateful that you use your time to help me on my studies.

Prof. Sergey Kustov Dolgov, I want to thank you for your help on resonant ultrasonic techniques. I am very impressed on your innovative equipment and you scientific and rigorous attitude on investigations.

I am also grateful for the help from the other member from our group, Dr. Catalina Picornell, Prof. Concepció Seguí, Dr. Francesc Masdeu, Mrs. Aquilina Pérez. I would like to express my gratitude to you for helping and advises on my researches.

I also want to express my thanks to Mr. José Luis Puerto and the other members of the technique center for keeping our lab functioning well. I really enjoy the talking with you about painting art, local foods and your culture. I would like to express my gratitude to Dr. Fernando Hierro for helping me on the SEM and EDX, and your

patience and professionalism really help me accomplish some good results. Dr. Joan Cifre, I am really grateful that you sacrifice a lot of time helping me on testing XRD, DSC, DMA, and helping me change the equipment for mechanical tests, I cannot obtain all of these experiments results without your help.

Finally, I want to give my gratitude to my friends. Andreu, I want to thank you for keeping me company in the daily life, I really enjoy the time we spent together on shopping, traveling, movies, foods and games. You are like a big brother to me and always kind and helpful to me. I will always remember our fascinating trip to Bernabéu to watch football match of Real Madrid. And also I am glad to meet my friends Belen and Sergio, we have good time together with board games and movies, and we share a lot of opinions on our culture with differences and similarity, you really make me feel at home here. Moreover, I want to thank the other friends Moner, Miguel, Diego, David, Lloerçe, Yao Kai. For the four years you have helped me in different ways, I could not reach so far without your generous help.

Partial financial support from Ministerio de Ciencia, Innovación y Universidades - Agencia Estatal de Investigación (MCIU-AEI), SPAIN and Fondo Europeo de Desarrollo Regional (FEDER), EU: project RTI 2018-094683-B-C51 is acknowledged.

NOMENCLATURE

SMA	Shape memory alloy
SME	Shape memory effect
SE	Superelasticity effect
HTSMA	High temperature shape memory alloy
SHT	Solution heat treated
WQ	Water quenched
FC	Furnace cooled
M_s	Martensite start temperature
M_p	Martensite peak temperature
M_f	Martensite finish temperature
A_s	Austenite start temperature
A_p	Austenite peak temperature
A_f	Austenite finish temperature
DSC	Differential scanning calorimetry
XRD	X-ray diffraction
SEM	Scanning electron microscopy
EDX	Energy Dispersive X-Ray
TEM	Transmission electron microscopy
OM	Optical microscopy
SADP	Selected area electron diffraction pattern
BF	Bright field
ε_{Total}	Total strain
ε_{Rec}	Recoverable strain
ε_{Irr}	Irrecoverable strain
σ_{SIM}	Critical stress to induce martensite
e/a	Valence electron concentration per atom
c/a	Tetragonality
DMA	Dynamic thermomechanical analysis
IF	Internal friction
E modulus	Elastic modulus
SG	Strain glass
DFT	Density functional theory

LIST OF PUBLICATIONS

Xu S, Pons J, Santamarta R, *et al*. Strain glass state in Ni-rich Ni-Ti-Zr shape memory alloys. Acta Mater 2021;218:117232.

TABLE OF CONTENTS

Motivation and Objectives

The present work has been planned from the previous results obtained in the research group of the UIB affecting to different families of HTSMAs: Ni-Ti-Zr/Hf and Ni-Mn-Ga-X alloys. According to the knowledge acquired, several goals were initially established for this thesis:

1. It is well known that adding Hf or Zr to the binary Ni-Ti system have drawn attention not only for increasing the transformation temperatures over 370 K, but also for being serious alternatives to the expensive Pd, Pt, and Au elements. Moreover, the Ni-rich Ni-Ti-Hf/Zr high temperature shape memory alloys (HTSMAs) have already demonstrated promising shape memory properties, *i.e.*, high thermomechanical stability at high temperatures and applied stresses with basically little or no irrecoverable strain when nanosized H-phase precipitates are induced by proper thermal treatments. Extensive investigations have been conducted by UIB and other authors on Ni-Ti-Hf/Zr alloys with different Hf/Zr content, but alloys containing 25 at.% of Zr have not been studied yet. Therefore, one of the goals of this study is focused on the investigation of the shape memory properties and microstructure of the $Ni_{50.3}Ti_{24.7}Zr_{25}$ polycrystalline alloy to ascertain if that composition has the same potential as other compositions of the Ni-Ti-Hf/Zr systems.

2. Previous work of UIB research group showed that $Ni_{50.3}Ti_{29.7}Zr_{20}$ undergoes short range atomic reordering processes in the B2 phase producing diffuse streaks in the diffraction patterns after prolonged ageing at 520 K, with a concomitant suppression of the thermal martensitic transformation. In addition, other alloys in the Ni-Ti-Zr system ($Ni_{50.3}Ti_{24.7}Zr_{25}$ and $Ni_{50.9}Ti_{24.1}Zr_{25}$) have also been found to present a suppressed martensitic transformation after different thermal treatments. It is well known that a novel state consisting of locally disordered lattice strains, denoted as strain glass (SG), was found in alloys with suppressed ferroelastic martensitic transition when cooling. It has been proposed that point defects, dislocations and/or nanosized precipitates are responsible for disrupting the long-range ordering of a "normal" martensitic transformation, and the phenomenon has been already observed in several SMA systems as Ni-Ti, Ni-Ti-Fe/Co, Ni-Mn-Ga-Co and more. Therefore, another objective of the present thesis is to experimentally verify by different techniques whether there is a SG state or not in the Ni-Ti-Zr alloys with suppressed martensitic transformation, as well as to investigate the mechanical properties of this unique state.

3. The Ni-Mn-Ga system was found to possess some potential as HTSMA, with M_s over 400 K and high thermal cycling stability in single crystalline alloys. However, the polycrystalline alloys show a high level of brittleness at the grain boundaries. Different fourth elements (V, Cr, Cu, rare earth elements, ...) have been used to alloy

ternary Ni-Mn-Ga in order to induce precipitation of a ductile second phase, which should improve the ductility of polycrystalline alloys. Among all the explored possibilities, several authors have reported that Ti not only can improve the mechanical properties due to the formation of Ni_3Ti precipitates, but also can increase the martensitic transformation temperatures. In the same column of the periodic table, Zr substituting Cu in Ni-Mn-Ga-Cu alloy has also been investigated. However, neither the shape memory response nor the mechanical properties of the Ni-Mn-Ga-Zr system has been studied yet. In addition to that, to the authors' knowledge, no studies have been reported on the addition of Hf either, despite this element is in the same column as Ti and Zr. Therefore, one of the main goals of the present work is to systematically characterize the shape memory properties and microstructure of Ni-Mn-Ga-Zr/Hf alloys.

4. Finally, the shape memory properties and precipitation process of Ni-Mn-Ga-Cu alloys with relatively high amount of Cu addition have been already reported. The γ and γ’ precipitates that form in these alloys have a rather large size, which is not the best morphology and distribution to optimize the mechanical properties. Therefore, low amount of Cu addition has been investigated in this thesis. On the one hand, the first objective is trying to induce nanometric precipitates of the second phase by proper thermal treatments and, on the other hand, a second objective is to investigate the thermomechancial properties of this quaternary system with low Cu content, which has not been studied yet. Furthermore, alloying with Sn has also been initially explored as a potential candidate of Ni-Mn-Ga-X HTSMA.

Summarizing the set of objectives, two common elements can be appreciated: all the envisaged materials are high temperature shape memory alloys (they contain compositions transforming over 370 K) and they require suitable thermal treatments to optimize the functional properties. Therefore, these are the unifying points throughout this thesis, which is aimed to bring in a deeper insight in many properties of these materials as well as to explore new promising alloys that could be attractive to the industry for potential applications.

Chapter Ⅰ INTRODUCTION

1.1 Shape Memory Alloys

1.1.1 Martensitic Transformation

The phase known as martensite was firstly found in high carbon steel, where the steel at high temperature (in austenite) can turn into a harder phase after fast quenching. This new phase received the name honoring Adolf Martens (1850 - 1914), who made important contributions to materials engineering and metallography. After thoroughly studying the characteristics of the martensite on steels, more metals and alloys were found to exhibit a similar solid-state phase transformation and nowadays the term martensite has been widely extended even to other type of materials as ceramics and polymers.

The martensitic transformation (MT) is defined as a diffusionless, displacive first-order transformation from the stable phase at high temperatures, austenite or parent phase, to the one stable at lower temperatures, martensite [1, 2]. Diffusionless normally indicates that there is no time for diffusion of atoms in a short or long range, but there are rather cooperative and homogeneous atomic displacements within the interatomic distances, *i.e.*, displacive, instead. As a result, the overall crystal structure can change as well as the cell volume, but the atomic order and the composition will be inherited from the austenite after the transformation. As a first order transformation, it exhibits an enthalpy change, being the transformation from austenite to martensite (direct or forward martensitic transformation) exothermic, and the one from martensite to austenite (reverse martensitic transformation) endothermic. However, contrary to other first order transitions, the martensitic transformation takes place in a finite temperature interval, in which the austenite and martensite coexist.

As shown in Fig. 1.1.1, the direct martensitic transformation takes place on cooling from a fully austenitic material when the temperature reaches the martensite start temperature (M_s). At this point, a small fraction of austenite rapidly transforms into martensite, but the rest of material will only continue transforming with further cooling. The martensitic transformation will be completed at the martensite finish temperature (M_f). The reverse transformation occurs upon heating from a completely martensitic material when the temperature achieves the austenite start temperature (A_s), and it will be completed at the austenite finish temperature (A_f). These transformation temperatures (M_s, M_f, A_s, and A_f) are independent of the heating or cooling rate and the differences between them results a thermal hysteresis. The hysteresis (ΔT) is an important parameter for shape memory alloys

and, as a result, it can be calculated as the difference between the austenite finish temperature and the martensite start temperature (A_f-M_s). The hysteresis reflects the energy loss during the phase transformation, and it is partially associated to the fact that the austenite/martensite and martensite/martensite mobile boundaries are meeting the different defects existing in the materials during their frictional movement. When the hysteresis is small, the energy dissipation is low, and the transition is normally called thermoelastic martensitic transformation. Thermoelastic transformations also exhibit small volume change, with the order of 0.5% or lower, which can be mostly accommodated with elastic strains, and require a low driving force to undergo the transformation. As a result, it possesses a high reversibility upon heating or cooling. On the contrary, the non-thermoelastic, or burst transformation, show less reversibility, accompanied by a large hysteresis and significant volume change. Moreover, the interfaces show limited mobility, and they can stop once the martensite has reached the critical size. The strain generated during shear is accommodated by plastic deformation, leading to the low reversibility. Indeed, the reverse transformation can occur by austenite nucleation upon high temperature. Despite a high hysteresis is usually considered as a negative feature, it can be useful for some damping and actuator applications. However, in this thesis, only alloys exhibiting a thermoelastic martensitic transformation will be investigated.

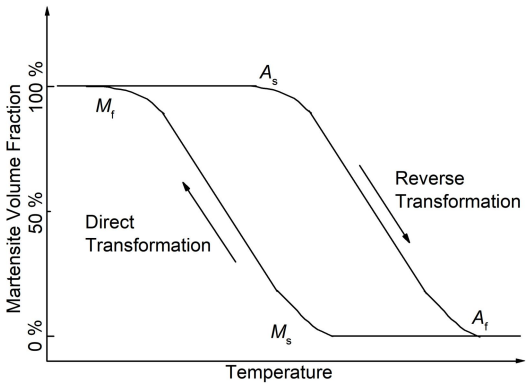

Fig. 1.1.1. Schematic diagram of the martensite volume fraction as a function of temperature during the direct and reverse martensitic transformation .

The thermoelastic martensitic transformation starts from a heterogeneous nucleation, preferentially in crystalline defects, grain boundaries, free surfaces, ... Then, the difference of the Gibbs free energy between the two phases acts as the main driving force to produce and maintain the shear and lattice distortion during transformation. An important feature of this transformation is the existence of an invariant habit plane, which forms the interface between the austenite and the martensite. The progress of the transformation is based on the movement of this habit plane. However, the experimental observations of the interface were crystallographically inconsistent with the habit plane (Fig. 1.1.2 (a)). The discrepancy was solved by two equivalent phenomenological theories, which were independently created by Wechsler-Lieberman-Read (WLR) [3, 4] and Bowles-Mackenzie (BM) [5, 6]

in order to quantitatively predict all the crystallographic parameters of the martensitic transformation, as the invariant habit planes and the orientations between the parent and martensite phases. The key step to solve the inconsistency is using a *lattice invariant shear* (LIS), which can be introduced by two different mechanisms: slip (Fig. 1.1.2 (b)) and twins (Fig. 1.1.2 (c)). Both mechanisms minimize the large strains associated with the martensitic transformation without changing the structure of the crystalline phases, and its creation depends on the alloy system and composition. However, twinning is much more frequently observed in thermoelastic shape memory alloys than slip [7].

Another important feature of the martensitic transformation is that a single crystallographic orientation in the parent phase can transform into multiple different orientations of the martensite (variant), due to the higher symmetry of the austenitic crystallographic structure. These variants are generally twin related between them and help to further accommodate the strain by using favorable habit plane variants (h.p.v.) and creating the so-called *self-accommodated* structures. The process is spontaneously induced upon cooling without any external stress by creating adjacent twins variants that produce strains in opposite directions, resulting in a strain compensation and a low macroscopic shape change. These favorable twinned variants can be easily detwinned and/or reoriented under an external stress due to the high mobility of their interfaces. Under the presence of an external stress, the most favorable variants (those straining the material in the direction closest to the applied stress) will grow at the expense of other variants, resulting in a macroscopic strain in the martensitic state [7].

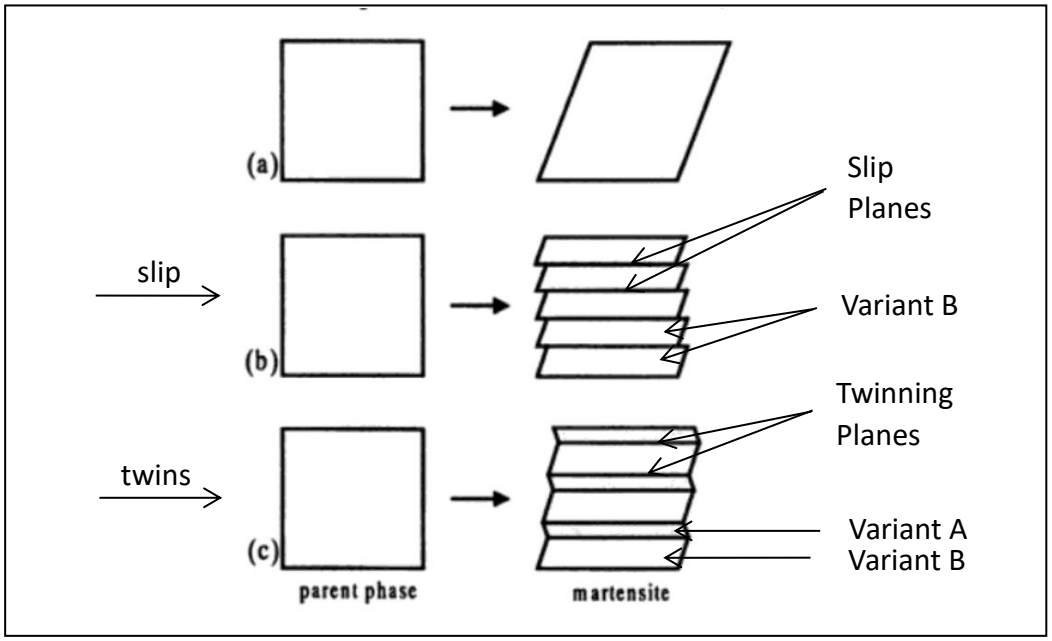

Fig. 1.1.2. Schematically representation of the two mechanisms of the lattice invariant shear (LIS) in the martensitic transformation [7].

As mentioned before, thermoelastic martensitic transformations are solid to solid phase transformations without compositional change. Therefore, the Gibbs free energy of the martensite and parent phases (G^m and G^P, respectively) can be defined, and the difference between both Gibbs free energies will act as the driving force of the direct or reverse martensitic transformation ($\Delta G^{P\text{-}M}$ or $\Delta G^{M\text{-}P}$, respectively). These terms only represents the so-called chemical energy term and they are temperature-dependent, having the same value at the thermodynamic equilibrium temperature T_0. Ideally, the direct or reverse martensitic transformation should occur at T_0 upon cooling or heating, respectively (see dash line path in Fig. 1.1.3 (a)). However, that is not the real situation because, besides the chemical term, other non-chemical terms participate in the process, which introduce the necessity of a higher driving force (overheating or undercooling in a thermal induced transformation) to continue the transformation. The elastic strain energy is the essential term of the non-chemical part in the thermodynamic balance of the martensitic transformation. The elastic energy arises from the lattice elastic deformation needed to accommodate a different structure in the matrix, and it is "stored" during the forward martensitic transformation and "released" during the reverse transformation. Once the transformation has started (M_s), the elastic energy term makes necessary a higher driving force (undercooling) to progress and complete the martensitic transformation (M_f), as described by the inclined solid line path in Fig. 1.1.3 (a). However, another non-chemical term should be introduced to account for the hysteresis of the transformation: the dissipation term. The dissipation of energy during the transformation has multiple sources, being the interaction of the mobile interfaces with the existing crystallographic defects among the most important ones. Another part of the dissipation term comes from the relaxation of elastic strain energy to form lattice defects like dislocations, mostly when the moving interfaces are disturbed by other defects like precipitates, grain boundaries, etc ... This frictional work is not stored in the matrix, like the elastic strain term, and the dissipation energy term is one source of irreversibility. Considering only the chemical term and the frictional work, a hysteresis between the forward and reverse transformation would be generated, moving the transformation temperatures away from T_0 by undercooling or overheating, respectively (shown in Fig. 1.1.3 (b) as dash line paths). Therefore, if the two most significant non-chemical terms (elastic energy term and dissipation term) are simultaneously considered, the resulting loop will be the one represented in Fig. 1.1.3 (b) as a solid line path, which is rather close to the experimental ones. Therefore, on the one hand, in transformations with a high stored elastic energy, a large undercooling temperature range would be needed (more inclined slope in the loop), without much influence in the hysteresis. On the other hand, in transformations with a high amount of dissipated energy in the form of frictional work, the transformation temperatures would be shifted away from the thermodynamic equilibrium temperature T_0, increasing the hysteresis.

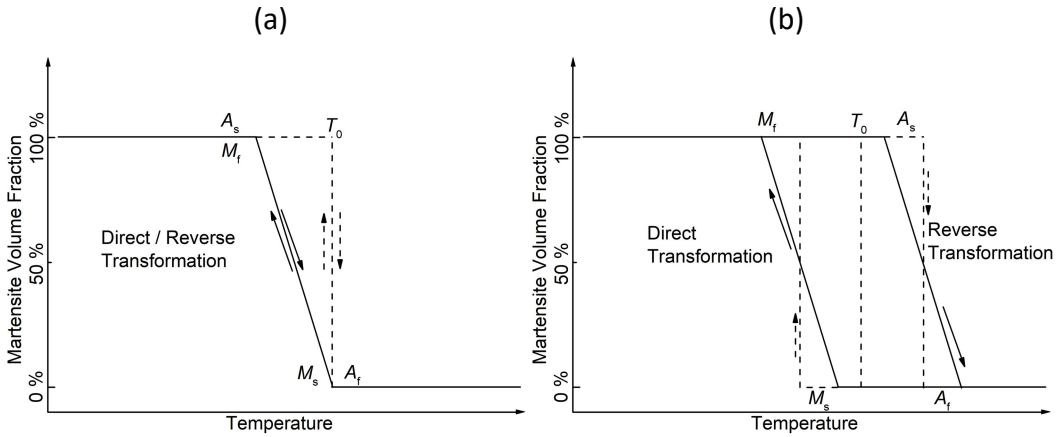

Fig. 1.1.3. Schematic diagrams of the martensite volume fraction as a function of temperature for a thermoelastic martensitic transformation, considering different energy terms: (a) chemical energy only (dashed line); chemical and elastic energies (full line). (b) chemical and frictional energies (dashed line); chemical, frictional and elastic energies (full line). Adapted from [8].

Based on the kinetics, thermoelastic martensitic transformations have been traditionally classified as time-independent athermal or time-dependent isothermal transformations. It is considered that most of them are athermal (in other words, not thermally activated), which means that the martensitic transformation at a constant temperature will not continue unless the equilibrium condition is broken by a temperature gradient, an external applied stress, a magnetic field, etc. Nevertheless, few alloys undergo an isothermal martensitic transformation (at constant temperature and time-dependent), being similar to diffusional transformation from the perspective of the kinetics [9]. On these cases, the time dependence of the transformation has been correlated to the migration of atoms/point defects, as the quenched-in defects could impede the motion of interfaces during transformation. Thus, in these alloys, the martensitic transformation can be suppressed by rapid quenching. However, besides the traditional classification mentioned above, there are some alloys with martensitic transformation that can be thermally activated during continuous cooling (induced by temperature and time). Hence, some authors claim for a different classification in which the term “thermal activated transformation” should be the main feature to classify martensitic transformations [10].

As it will be shown with detail in the next section, the thermoelastic martensitic transformation can also be activated by an external stress at a constant temperature. In addition to that, in cases where either the austenite or the martensite is ferromagnetic, the forward or reverse martensitic transformations can be triggered by an external magnetic field. However, the alloys studied in the present work are not magnetic around the transformation temperatures, and therefore, do not exhibit martensitic transformation induced by magnetic fields. Therefore, no further information on these mechanisms or on ferromagnetic shape memory alloys will be provided in this section.

1.1.2 Shape Memory Properties

Thermoelastic martensitic transformations give rise to unique properties, combining temperature changes and applied stress. Some of these features are essential for applications, and they are described below.

Shape Memory Effect (SME)

The direct and reverse martensitic transformation can exhibit different features, or phenomena, depending on the temperature, stress, and their initial state. One of the most famous phenomena is the so-called *shape memory effect* (SME), which give the name to shape memory alloys (SMA). Fig. 1.1.4 presents a 3D graph where the SME is shown for a typical Ni-Ti SMA as a function of strain, stress, and temperature. At the starting point (A in the figure), the alloy should be completely in austenite, *i.e.*, at a temperature above A_f. Then, the material is cooled down until a temperature below M_f, in which all the alloy transforms into martensite (B point, at the origin of the Cartesian axes). As no external stress is applied, the martensite is formed mainly in a self-accommodated twinned microstructure; as a result, basically no obviously macroscopic shape change is obtained during the process. When gradually applying an external stress to the alloy, the specimen undergoes, first, an elastic deformation until the critical stress σ_s is reached. At that stress, the detwinning (or reorientation) of the self-accommodated martensite starts, in which the growth of favorable oriented variants will take place at the expense of the not so well oriented variants. This detwinning process will finish at σ_f. This zone is distinguished by a small increase in stress but a significant growth in strain (translated into a macroscopic shape change), producing an obvious plateau in the strain-stress curve. Further increase of the applied stress will yield to an elastic deformation of the detwinned martensite (point C). Upon removing the external stress, the elastic part of the total strain is recovered, while the strain derived from the detwinning process is preserved (D point), thus keeping most of the significant macroscopic shape change obtained during loading. Finally, when heating the deformed alloy over the A_f temperature, the detwinned martensite transforms back to austenite state (A point). It has to be noted that all the martensitic variants formed at the same austenitic grain will come back to the same orientation of the austenite, and therefore, the original macroscopic shape in austenite will also be recovered. If the process starts a second time by cooling the specimen down to M_f (from A to B point in Fig. 1.1.4), the original self-accommodated martensitic structure is obtained again, alongside the original shape before applying any external stress.

Fig. 1.1.4 shows some schematic diagrams of the atomic arrangement at points A, B, C and D, which are enlarged and coloured in Fig. 1.1.5 (a). It turns out that the self-accommodated twins possess similar macroscopic volume and shape compared

with austenite state (represented by the dashed frame) due to the randomly distributed orientation of the shear corresponding to all the variants, while the detwinned martensitic structure shows a considerable shape change and macroscopic strain in respect to the initial dash frame.

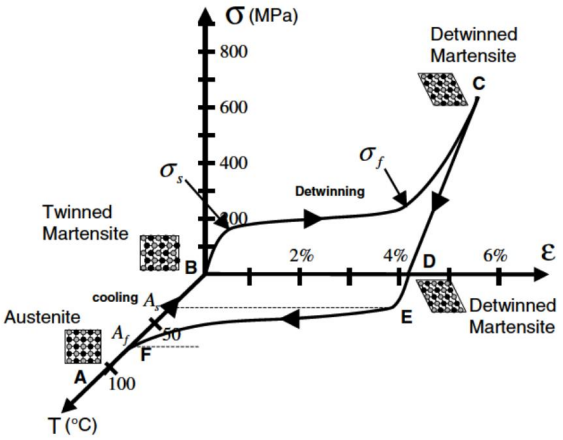

Fig. 1.1.4. Schematic diagram of the shape memory effect (SME) for a typical Ni-Ti shape memory alloys [11].

The aforementioned process is sometimes called One-way shape memory effect (OWSME) to highlight the difference with another effect called Two-way shape memory effect (TWSME). The latter effect is obtained when the material can recover ("remember") spontaneously the macroscopic shape of both the martensitic and the austenitic states upon cooling or heating, respectively, without any external applied stress (*i.e.*, going from A to B, and from B to A, respectively, in Fig. 1.1.4). Fig. 1.1.5 (b) shows the path difference between the OWSME (blue arrows) and the TWSME (red arrows) to go from the austenite and detwinned martensite or vice versa. It must be noted that, to obtain the TWSME, some previous thermomechanical procedures are required, being the most common the shape memory training, the superelastic training and the thermal cycling under biased constant stress. During training, an anisotropic distribution of dislocation arrays is introduced in the matrix, promoting the subsequent nucleation of the "appropriate" variants, helping to obtain the shape that was induced previously in the low-temperature phase (TWSME) [12]. Despite the obvious benefits of this effect, there are some drawbacks that inhibit its extensive use into applications. On the one hand, to obtain this effect, some previous training with thermomechanical treatments is needed to obtain the effect. On the other hand, both the levels of free recoverable strain and stress, when an opposite force is applied, are lower than those from the OWSME. Lastly, TWSME is not suitable for SMAs working at high temperature, as the higher diffusion rates results in a partial or total recovery of the trained microstructure.

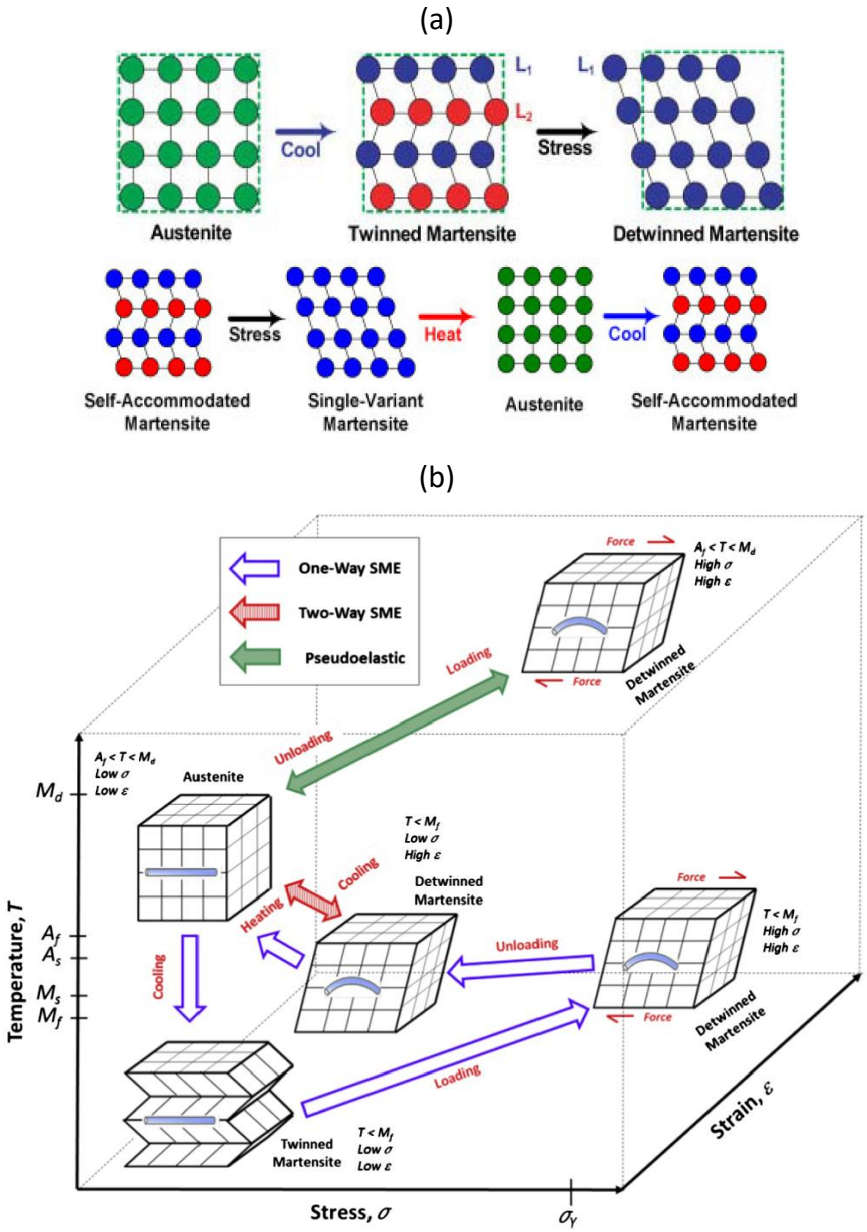

Fig. 1.1.5. Schematic diagrams of (a) atomic arrangements during the martensitic transformation induced by temperature and/or stress [13], (b) transformation paths for the OWSME and TWSME and superelasticity effect (pseudoelastic in the legend of the figure) [14].

Superelastic Effect (SE)

The superelasticity effect (SE) is another relevant characteristic of SMAs commonly used for real applications. Similarly to the elastic deformation, the strain induced under loading can be fully recovered after unloading. However, the mechanism of SE effect is completely different, as it involves the reversible stress-induced martensitic transformation. In absolute values, the recoverable strain induced by superelasticity is much higher (one order of magnitude for some alloys) than the one from the elastic deformation. Thus, the additional prefix “super” is used.

A superelastic cycle starts with the material completely in austenite, so at temperatures over A_f, as indicated in the strain-stress curves from Fig. 1.1.6 (a). When applying the external stress keeping the temperature constant, the material is deformed elastically until it reaches the value σ^{Ms}. At this moment, the stress provides enough energy for the transformation to take place, and the stress-induced transformation begins, promoting the nucleation and subsequent growth of variants with strains close to the external stress. If the stress increases, the martensitic transformation will continue until σ^{Mf}, where a detwinned martensite will be obtained (Fig. 1.1.6 (a)). Further stress will elastically deform the martensite. Then, when the applied stress is released, first the elastic strain of the martensite is recovered and, between σ^{As} and σ^{Af}, the reverse martensitic transformation occurs, showing a mechanical hysteresis in the stress-strain curve (Fig. 1.1.6 (a)). At lower stress, the elastic deformation of the austenite is also recovered.

Despite the transformation is mechanically induced, the temperature plays a significant role. Fig 1.1.6 (b) shows the stress at which the direct and reverse martensitic transformation start (or finish) as a function of temperature, clearly showing that the transformation stresses continuously increase with temperature. As an example, three constant temperatures has been indicated in Fig 1.1.6 (b) ($T_3 > T_2 > T_1 > A_f$) representing the temperatures at which three different SE cycles are obtained (vertical lines). When increasing the stress at a constant temperature, the corresponding vertical line crosses $M_s(\sigma)$ and $M_f(\sigma)$ lines, which means that the austenite fully transforms into detwinned martensite. Releasing the stress, the vertical line goes down throughout $A_s(\sigma)$ and $A_f(\sigma)$ lines, indicating that the reverse martensitic transformation occurs. The stress-strain curve of the entire process would be similar to the one shown in Fig 1.1.6 (a). It needs to be noted that irreversible deformation will be induced to the material whenever the applied stress overcomes the critical stress to induce plastic deformation (σ_{PD}), which breaks the perfect SE effect and leaves some level of irrecoverable strain after unloading. In Fig. 1.1.6 (b) σ_1, σ_2 and σ_3 are the critical stresses to induce plastic deformation at T_1, T_2 and T_3, respectively, and therefore they represent the maximum stress for the SE cycles at those temperatures. Usually, the yield point (σ_{PD}) of any metallic material decreases with increasing temperature, which is represented with the decreasing red dashed line in Fig. 1.1.6 (b). Indeed, the same negative temperature tendency is observed for the yield stress σ_s to form detwinned and/or reoriented martensite (purple line in Fig. 1.1.6 (b), introducing a temperature dependence of the SME. Following the examples drawn in this figure, loading the material at T_1 (close to A_f) allows to completely finish the stress-induced martensitic transformation before inducing plastic deformation because $\sigma(M_f)$ is lower than σ_1. In addition, $\sigma(A_f) > 0$ and, then, perfect superelastic behaviour is obtained at this temperature. However, both critical stresses coincide at T_2 ($\sigma(M_s) = \sigma_2$), *i.e.*, martensite and plastic deformation are induced together when loading at stress levels above σ_2, thus, irrecoverable strain will remain after unloading. Finally, at T_3 the plastic deformation takes place at σ_3, well below the start of the martensitic transformation, so the material can

accumulate a large plastic deformation, or even fracture, before any martensite is induced. The alloys with high transformation temperatures may present a softened state in the austenite phase, due to the elevated temperature, which restricts the temperature range for a perfect superelasticity effect. This temperature range is usually denoted as *superelastic window*. Therefore, the high temperature shape memory alloys usually need a strengthening treatment to enlarge the superelastic window well above the A_f temperature.

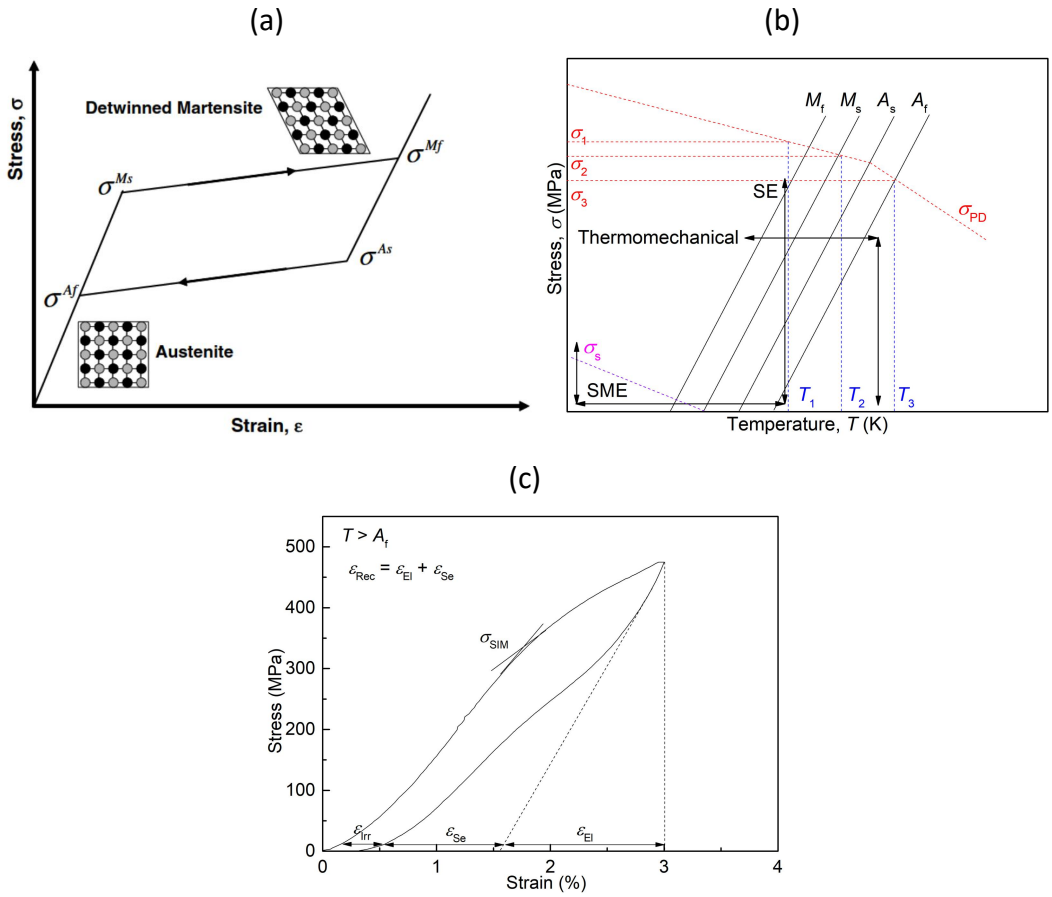

Fig. 1.1.6. Schematic diagrams for the superelasticity effect. (a) Stress-strain curve showing perfect superelastic effect [11]; and (b) plot of the stress and temperature of the martensitic transformation together with the SE, SME and thermomechanical paths; (c) experimental superelastic cycle showing the criteria used in the present work to determine the main characteristics of experimental SE stress-strain curves.

Fig. 1.1.6 (c) presents an experimental stress-strain curve performed at a particular constant temperature above A_f, showing the superelasticity effect (imperfect) in one of the samples of this thesis. Since the specimens studied in this thesis are polycrystalline alloys with many defects, the curve is not exactly as the ideal one shown in Fig. 1.1.6 (a), and the plateau in that figure is substituted by a more subtle change of the slope in the experimental curve. Upon loading, one of the key parameters to focus on is the critical stress to induce the martensitic transformation (σ_{SIM}), which is obtained by the tangent method, as indicated in Fig. 1.1.6 (c). Among

other characteristics, the recoverable and irrecoverable strains are also very valuable data. As it can be seen in Fig. 1.1.6 (c), the recoverable strain includes the elastic strain (ε_{El}) and the strain derived from the reverse stress-induced martensitic transformation (ε_{Se}). This particular sample also presents some irrecoverable strain (ε_{Irr}).

Isobaric thermal cycles (thermomechanical cycles)

Isobaric thermal cycling, also typically known as thermomechanical cycling, is an excellent characterization technique to fully represent the transformation characteristics induced by both temperature and external stress in conditions close to the real use of the SMA in many applications. During cooling, the constant applied stress in the thermomechanical tests can help to induce the martensitic transformation and to directly form detwinned, reoriented martensite plates with the orientation close to the direction of the uniaxial external stress. Despite the transformation is induced thermally, the distribution of the martensitic variants is not random anymore in these experiments, but the fraction of properly oriented variants and, consequently, the amount of macroscopic recoverable strain, raises with the increasing external stress.

Fig. 1.1.7 shows a complete thermal cycle performed under constant compressive stress. The cycle can be divided into two parts: the branch corresponding to cooling from a temperature over A_f (austenite), which shows the forward martensitic transformation, and the part corresponding to heating from a temperature below M_f (martensite), which shows the reverse martensitic transformation. In the cooling branch, decreasing the temperature, three regions can be easily identified: the thermal contraction of the austenite, the direct martensitic transformation and the thermal contraction of the martensite, respectively. On its turn, in the heating branch, the thermal expansion of the martensite, followed by the reverse martensitic transformation and, finally, by the thermal expansion of the austenite can be observed. Fig. 1.1.7 illustrates the criteria followed in this thesis to determine the main characteristics of SMAs when performing thermomechanical cycles. Thus, the transformation temperatures at that particular compressive stress (M_s, M_f, A_s, A_f) are obtained by the tangent method (cross points of the slope lines in Fig. 1.1.7), while the thermal hysteresis (ΔT) is calculated as the width from the middle points of the heating and cooling lines corresponding to the martensitic transformation. The deformation associated to the whole phase transformation is characterized as the total strain (ε_{Total}), and it corresponds to the difference between the strain at the M_f value and the slope line of the austenite thermal expansion, as shown in Fig. 1.1.7. The total strain includes the recoverable strain (ε_{Rec}) and the irrecoverable strain (ε_{Irr}). The latter one is measured by the strain difference between the start and the finish points of the cycle, whereas the recoverable stain is determined by the difference between the total and the irrecoverable strains ($\varepsilon_{Rec} = \varepsilon_{Total} - \varepsilon_{Irr}$). However, it has to

be noted that this relationship is not completely accurate, as there is also a contribution introduced by the differences in the thermal expansion behaviors that has been neglected in this work.

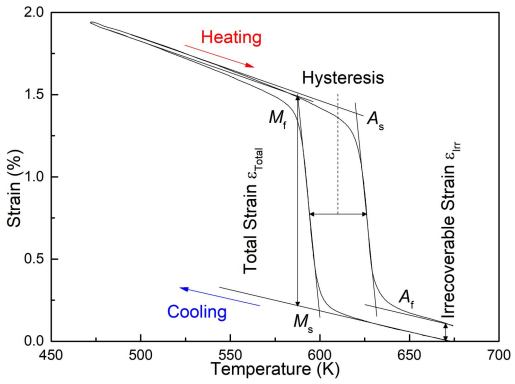

Fig. 1.1.7. Experimental isobaric thermal cycle (thermomechanical cycle) under a constant compressive applied stress, indicating the criteria used in this thesis to calculate the transformation temperatures and the total, irrecoverable and recoverable strains.

As it has been already introduced, the forward and reverse martensitic transformations occur within a range of temperature and/or stress. The effect of this feature on both SE and isobaric thermal cycles can be easily understood from the schematic temperature-stress diagram in Fig. 1.1.6 (b). The thermally induced transformation temperatures during the forward and the reverse transformations (M_s, M_f and A_s, A_f, respectively) depend on the stress following a Clausius-Clapeyron-type relationship:

$$\frac{\Delta\sigma}{\Delta T} = -\frac{\Delta H}{T_0 \varepsilon_{Rec}} \quad \text{(Eq. 1.1.1)}$$

Where $\Delta\sigma$ is the applied stress difference; ΔT the transformation temperature difference; ΔH the transformation enthalpy change; ε_{Rec} the recoverable strain; and T_0 the equilibrium temperature. This relationship mathematically shows that the higher the applies stress is, the higher the transformation temperatures should be. Normally, in a wide range of temperatures and stresses, this relationship shows a linear tendency (*i.e.*, the applied stress divided by temperature, $\Delta\sigma / \Delta T$ is constant and positive). In the experimental sections of this thesis, the link between this relationship and the activation energy change during the phase transition will be discussed.

As a summary and review of the present section, it is worthy to outline that the shape memory effect, the superelasticity effect, and the plastic deformation can show up in the same sample at different temperatures. This is clearly illustrated in Fig. 1.1.8, where all three phenomena are plotted as a function of stress, strain, and temperature. Fig. 1.1.8 shows that an applied stress below M_f generate a SME loop, which needs heating over A_f to complete the cycle and recover the original shape of

the material. As already mentioned, the stress to induce the martensitic transformation grows with temperature, while the stress to induce the plastic deformation decreases with temperature. Therefore, if we increase the temperature up to the range of A_f - M_d, a closed SE loop can be obtained, using higher stresses than the ones used for the SME, without inducing plastic deformation. In some alloys with a low σ_{PD}, it may be impossible to induce the complete SE loop without any macroscopic plastic deformation. Finally, at very high temperatures (over M_d), plastic deformation can easily occur before or simultaneously with the martensitic transformation, deteriorating, or even suppressing, the superelastic effect. Therefore, the selection of the temperature is vital for both experiments and applications to get the desired response of the material under an applied external stress..

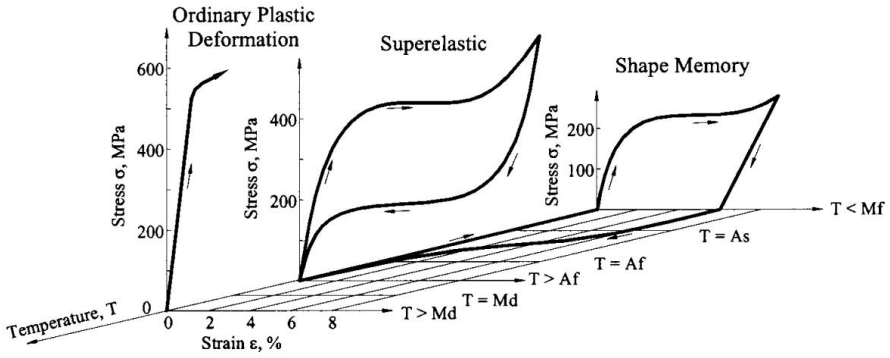

Fig. 1.1.8. Stress-strain-temperature diagram illustrating the dependence of the stress-strain behavior (SME, SE, plastic deformation) with temperature in a Ni-Ti shape memory alloy [15].

1.1.3 Strain Glass

As it has been introduced before, the diffusionless martensitic transformation consists in the structural transition from a high symmetry austenitic phase into a lower symmetry martenitic phase induced by cooling and/or applied external stress. The different crystal structures generate an intrinsic strain between the austenite and martensite lattices. In the process, diverse variants of martensite with different orientations of their intrinsic strain are formed. In the thermal transformation, the variants form self-accommodated groups with twinning relationships to compensate their intrinsic strains. Under an external stress, the variants with intrinsic strain in the direction of the applied stress grow at the expense of the disoriented variants, producing a macroscopic strain in the material. This behavior is denoted as *ferroelasticity*, in analogy with ferromagnetism or ferroelectricity. In the latter systems, the ferroic property is the magnetization or electric polarization, which can be tuned by an external field through movement of magnetic or electric domain walls. For ferroelastic shape memory alloys, the lattice strain between austenite and martensite constitutes the ferroic degree of freedom. In the “normal” martensitic transformation (or ferroelastic transition), the martensitic domains keep a uniform intrinsic strain within all their volume, which can be considered as a long-range

ordering of lattice strains. However, such a uniform long-range ordering of lattice strains appears to be frustrated and disrupted into locally disordered lattice strains in some alloys with suppressed martensitic transformation on cooling (giving no sign in the typical experimental techniques used to characterize the transition, like DSC). This situation is a novel state denoted as "*strain glass*", in analogy with typical glasses (structural glass, spin glass, relaxor ferroelectrics), which present a frozen state at low temperature with the lack of long-range order and consisting of only short-range ordered arrangements (distances of few lattice constants).

The strain glass (SG) state has been found in systems that contain nanometric sized spatial heterogeneities that frustrate the long-range ordering of lattice strains typical for the ferroelastic transition. SG was first reported in the Ni-rich Ni-Ti SMA system (Ni content above 51 at.%), in which randomly distributed nano-clusters of R-like phase were formed under cooling induced by point defects (excess Ni atoms), yielding to an absence of the martensitic transformation [16]. Later, phase diagrams and the Landau free energy theory were used to reveal the evolution of this phenomenon as a function of the excess of Ni atoms [17-19]. Similarly, substituting Ni by Co, Cr or Mn atoms in the binary Ni-Ti introduces point defects that destabilize the martensitic transition, first changing the normal transition path from B2->B19' to B2->R->B19' and finally to B2->R. At last, the martensitic transformation is completely suppressed (*i.e.*, the SG state is achieved) when the amount of the third element exceeds a critical value [20]. Fe addition above 6 at.% in $Ti_{50}Ni_{50-X}Fe_X$ leads to the SG as well, accompanied by R-like nanometric domains [21]. In this ternary alloy, the transition boundary from SMA to SG was determined in detail by changing Ni in steps of 1 at.% and it was attributed to the induced change in the local lattice structure by Fe point defects [22].

Since the discovery of the SG state in alloys with suppressed ferroelastic transition, four different sources of spatial heterogeneities have been found to give rise to this phenomenon:

(1) Point defects can induce SG state instead of the MT in Ni-Ti alloys and several Ni-Ti-X families, as described in the previous paragraph. Adding Cr (above 9 at.%) instead of Pb in Ti-Pb alloys also induces the SG state upon cooling and exhibits SME and SE with the applied external stress around the ideal SG freezing temperature T_0 [23]. The SG state has also been found in other SMA like Fe-based alloys [24, 25], ferromagnetic systems like Co doped Ni-Mn-Ga, Ni-Fe-Ga and Ni-Mn-Sn alloys [26-29], and Ti-Nb-based alloys with doped oxygen atoms, which show unique properties like the Invar effect [30, 31].

(2) A big amount of dislocations introduced by cold deformation also leads to the SG state in the $Ti_{50}Ni_{45}Fe_5$ alloy and in the Ni-rich Ni-Ti system. Moreover, the latter system exhibits a quasi-linear superelasticity with a large recoverable strain (about 4%) [32, 33].

(3) Three dimensional defects (*i.e.*, precipitates) can also successfully induce the SG state. Nanosized, randomly distributed Ti_3Ni_4-like precipitates formed by ageing treatment in the binary Ni-Ti have been reported to suppress the thermoelastic martensitic transformation [34], while the B2 to R transition gradually appeared again by further ageing associated with the size increase of the precipitates [35]. Additionally, Chien *et al*. reported that the strain glass transition temperature can be tuned with ageing [36].

(4) The atomic configurational order/disorder in a Ni-Co-Mn-In alloy, with nano-sized ordered domains and antiphase boundaries that break the long-range order, can also induce the SG state [37].

There are some typical properties and features of the SG state that can be experimentally observed. Low frequency dynamical mechanical analysis (DMA) exhibits a minimum in the storage/elastic modulus (*E*) and a maximum in the internal friction (*IF*) signals of lower magnitude than alloys with a normal martensitic transformation. In addition, both *E* and *IF* anomalies show a frequency dependence, the former following a Vogel-Fulcher relationship that determines the experimental freezing temperature [16]. This is the main signature that is normally ascribed to the SG state. Nevertheless, in a study using low and high (ultrasonic) frequencies and alloys with different Ni contents, the *IF* and *E* anomalies were interpreted as relaxational premartensitic anelasticity, instead of attributing them to the freezing of "martensitic-like" disordered nanodomains into a glassy state with no long-range correlation [38]. However, SG transition is strongly supported by the direct observation of an average austenite crystal structure in electron diffraction patterns obtained below the frozen temperature, together with diffuse spots at positions close to the corresponding martensite phase, as well as mottled patterns in conventional TEM and randomly distributed nanodomains in HRTEM images [16, 39-41]. The so-called zero-field-cooling (ZFC) and field-cooling (FC) measurements of static strain also reveal a direct evidence of the broken ergodicity in a frozen strain glass state when they differ well below the peak associated to the glass transition temperature [42]. This behavior is clearly different than other phenomena as the premartensitic tweed, which shows ergodicity (similar ZFC and FC curves) and less stickiness than the SG state due to a lower defect concentration [43].

Alloys in the SG state can undergo a stress-induced martensitic transformation and exhibit the related shape memory and superelastic effects. Wang *et al*. [44] reported that the shape memory and superelasticity effect appear in SG specimens under external stress, and verified the stress induced martensitic transformation by *in-situ* X-ray diffraction. Changing the applied stress can lead to different transforming routes from parent phase to strain glass state and/or martensite, resulting in changes to the damping effect and the entropy change [45, 46]. The form of the stress-strain curves also changes from a sharp and wide loop to a round and slim one and the apparent yield stress rises with increasing interstitial oxygen atoms in the Ti-Nb

system (*i.e.*, going from a well-defined transformation to the SG state) [30]. The long-range ordered martensite (R phase) can also appear spontaneously from the SG state by further cooling, as it has been reported in Ti-Ni-Fe alloys [39] and Ni-Co-Mn-Ga alloys [28], indicating that not only kinetics but also thermodynamics play an important role in this transition process. Finally, the Invar effect (no thermal expansion as a function of temperature) and Elinvar effect (extremely small variation of elastic modulus as a function of temperature) have been observed in SG state specimens after cold rolling, and have been associated to a strong texture of the nano-domains developed after cold rolling [31].

1.1.4 Crystallographic information

The unique properties of SMAs derive from the crystallographic structures of the austenitic and martensitic phases, as mentioned above, and hence, it is necessary to further describe them as well as the peculiarities of specific alloys. In addition, the presence of second phases in the form of precipitates also affects the properties of SMAs. Therefore, this section will present a detailed crystallographic description of the phases existing in the studied alloy compositions, including matrix and precipitates, together with basic information of other common phases related to these alloy systems.

Ni-Ti-based alloys

Basically, the high temperature phase (austenite) of all Ni-Ti and Ni-Ti-X alloys possesses a high symmetry ordered cubic structure denoted as "*B2*", with space group 211 (Pm-3m) and lattice parameter a_0 around 3 Å [47]. In the stoichiometric binary alloy, Ni and Ti atoms occupy first neighbor positions, as it is shown in Fig. 1.1.9 (a), where Ni is plotted at the center position (1/2 1/2 1/2) and Ti atoms at the corners (0 0 0). Center and corner positions define two interpenetrated sublattices of the B2 structure. For ternary Ni-Ti-X alloys, one sublattice tends to be fully occupied by one of the elements, while the other site will be randomly occupied by the other two elements according to the alloy composition.

Concerning the low temperature phase (martensite), several crystalline structures have been reported for both binary and ternary Ni-Ti-based alloys. The most common martensitic structure, present both in binary alloys and in the Ni-Ti-X alloys studied in the present work, is the B19' martensite. The B19' phase shows a monoclinic structure with space group 11 ($P2_1/m$), illustrated in Fig. 1.1.9 (b). The lattice parameters of this structure dependent on composition. For Ti-49.2 at.% binary alloy, these are a = 2.898 Å, b = 4.108 Å, c = 4.646 Å and β = 97.78° [48], whereas for Ni-Ti-Zr/Hf alloys the β angle can increase up to 103° [49]. The B19' phase is considered to be a three-dimensional close-packed structure instead of just a two-dimensional close-packed stacking structure of the martensitic phases in other

SMAs families.

Besides the B2 to B19' single step transition, there are other popular transition sequences involving additional martensitic phases that can be found in Ni-Ti alloys, as the B2-B19 or the B2-R single step transitions, or the B2-R-B19' and the B2-B19-B19' two-step transitions. The B19 martensite is commonly found in Ni-Ti-Cu ternary alloys, and its structure is an orthorhombic unit cell with space group 51 (Pmma), hence having self-accommodated structures with three different variants (pyramid shape like) to favorably compensate strains [50]. In addition, the structure relationship of B2-B19-B19' is clearly explained by basal plane shear and shuffle [51]. On its turn, R-phase has a trigonal unit cell (rhombohedral distortion from cubic), although conventionally is described as a hexagonal structure with the space group 143 (P3) [7]. The R-phase can be induced or stabilized before the B19' martensite in Ni-Ti alloys by introducing dislocations arrays, precipitates or by third element doping [52]. This phase was first considered as a pre-martensitic phenomenon, or precursor state, to the subsequent B19' martensite with certain periodic atom displacements. However, nowadays is well established that the B2-R is also a martensitic transformation and not a precursor effect for the normal B2-B19' transition, showing its own TEM diffraction patterns and shape memory properties [53].

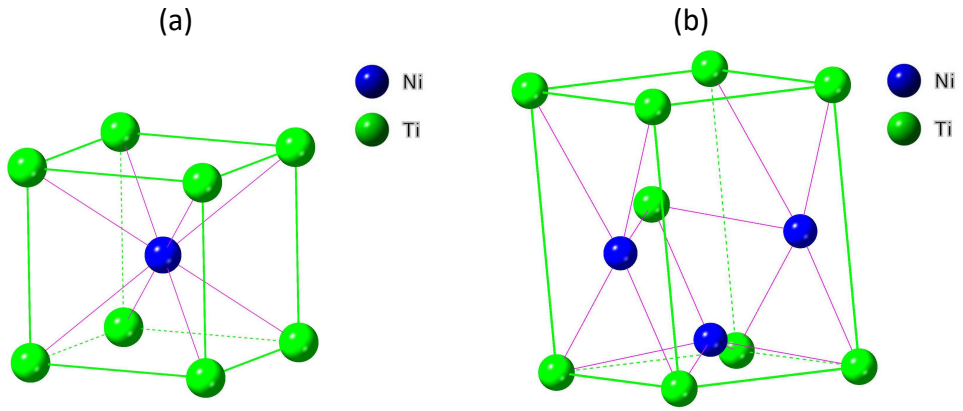

Fig. 1.1.9. Unit cell of (a) B2 austenite, (b) B19' martensite. The Ni, Ti atoms are presented in blue and green colors, respectively.

Apart from the phases involved in the martensitic transformation, there exist precipitated phases that can heavily influence the transformation and the functional properties of Ni-Ti-based alloys. These precipitates are strongly dependent on the alloy composition. For binary Ni-Ti alloys, normally the single NiTi phase is only appearing in the region of 50.0 at.% - 50.5 at.% (below 923 K), while $TiNi_3$ and Ti_2Ni stable phases appear in Ni-rich and Ni-poor Ni-Ti alloys, respectively [7]. Moreover, additional metastable phases can also be induced by different thermal treatments, being the Ni_4Ti_3 the most common for Ni-rich alloys. Ni_4Ti_3 precipitates are formed by low temperature ageing, and they are rather coherent with the matrix, resulting in a useful hardening effect. The Ni_4Ti_3 phase exhibits a rhombohedral structure with space group 146 (R3), unit cell containing 14 atoms and lattice parameters a = 6.70 Å,

α = 113.8° for an alloy with 51 at.% of Ni [54]. For Ni-poor Ni-Ti alloys, Ti_2Ni are the common precipitates, although they are usually misinterpreted with Ti_4Ni_2O due to their similar structure [7].

The H phase has been observed in Ni-rich Ni-Ti-Hf/Zr alloys and intensively studied due to its significant strengthening effect. Han *et al*. [55] first found these precipitates in a $Ni_{36.5}Ti_{48.5}Hf_{15}$ alloy through proper ageing. The electron diffraction patterns contain fundamental reflections equivalent to the B2 structure and additional satellites corresponding to threefold periodicity along the $<110>_{B2}$ directions and fourfold periodicity along $<210>_{B2}$ directions. The authors reported a face-centered orthorhombic structure (F 2/d 2/d 2/d) with lattice parameters a = 1.287 nm, b = 0.874 nm, c = 2.622 nm, though the atomic positions within the cell were not determined. Yang *et al*. [56] proposed a complete structural model for the H-phase precipitates in $Ni_{50.3}Ti_{29.7}Hf_{20}$, consisting of 192 atoms in the orthorhombic unit cell. Furthermore, R. Santamarta *et al*. [57] reported a similar structural model (only differing in the lower amount of atomic shuffling, in relation to the Yang's model) which was confirmed to be valid for both, Ni-rich Ni-Ti-Hf and Ni-Ti-Zr alloys. The lattice correspondence between the austenite and the H phase, deduced from the electron diffraction patterns, is $a_H = 4a_0$, $b_H = 2\sqrt{2}\,a_0$, $c_H = 6\sqrt{2}\,a_0$. The unit cell for Ni-Ti-Zr alloys after relaxation of the atomic positions to minimize the energy (according to density functional theory (DFT) calculations) is shown in Fig. 1.1.10. It is worth to note that the positions of Ni atoms coincide with one sublattice of the B2 structure, while the Ti and Hf/Zr atoms occupy the second sublattice and develop an ordered superlattice in the H phase (they occupy random positions in the B2 austenite phase). Therefore, the H phase can be interpreted as an ordered superstructure of the B2 structure obtained after a recombination of the Ti and Hf/Zr atoms in their sublattice. The fixed lattice correspondence and similar interatomic distances of the B2 and H structures results in a high level of coherency between both phases, as it has also been confirmed by HRTEM observations and DFT calculations [57].

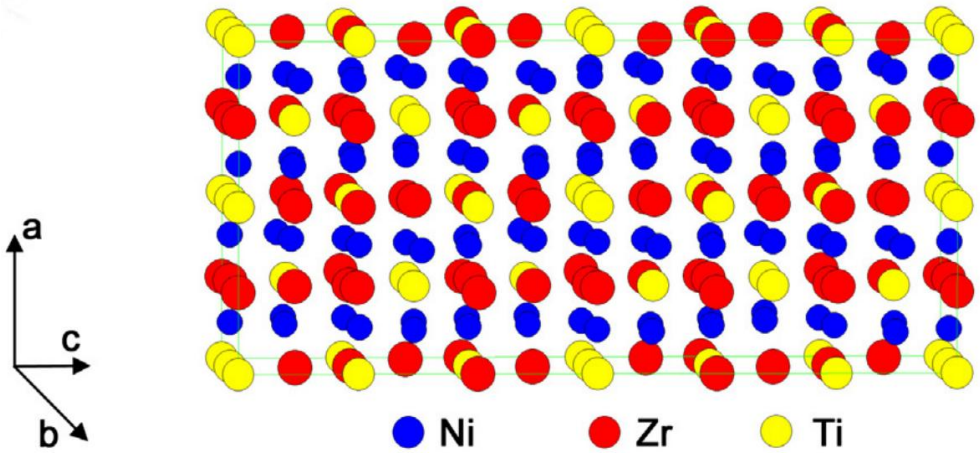

Fig. 1.1.10. Unit cell of the H phase in Ni-Ti-Zr alloys proposed in reference [57].

Ni-Mn-Ga-based alloys

The parent phase of the stoichiometric Ni_2MnGa shows a $L2_1$ structure (also known as Heusler structure), which describes an ordered body center cubic (b.c.c.) atomic arrangement for ternary alloys. The $L2_1$ unit cell can be viewed as 8 b.c.c. cells with either Ni atoms at the corners (Fig. 1.1.11 (a)) or alternating Ga and Mn atoms at the corners (Fig. 1.1.11 (b)). The lattice parameter of this structure in Ni-Mn-Ga-based alloys is normally around a_{L21} = 5.8 Å.

As for the martensitic phases of Ni-Mn-Ga-based alloys, there is a large variety of structures, depending on the composition and the valence electron concentration, although normally they are roughly divided into non-modulated martensite and modulated martensites. The non-modulated tetragonal martensite can be described by two different types of unit cells [58]. One is the $L1_0$ structure shown in Fig. 1.1.11 (c), a face centered tetragonal structure with space group 139 (I4/mmm), which uses two axes that have been rotated ±45° from one of the axes of the $L2_1$ austenite. Therefore, the epitaxial relationship between the cubic austenite and the tetragonal martensite can be described as $[100]_{L10}||[1\text{-}10]_{L21}$, $[010]_{L10}||[110]_{L21}$, $[001]_{L10}||[001]_{L21}$. The second equivalent description is a body centered tetragonal with F4/mmm space group (also number 139) which is usually denoted as "*b.c.t.*" to distinguish it from the $L1_0$ description. The b.c.t. structure, represented in Fig. 1.1.11 (d), has all three axes parallel to the ones of the austenite, reason why sometimes the term "cubic axes" is used, but with an obvious shrink of the "*a*" and "*b*" lattice parameters and an elongated "*c*" lattice parameter. This description of the non-modulated martensite will be normally used along this work, as it is more intuitive and convenient than the $L1_0$ description. Fig. 1.1.11 (e) has been included to further clarify the relationship between the $L1_0$ and b.c.t. descriptions. This figure shows 8 b.c.t. unit cells with the $L1_0$ unit cell drawn inside, showing that the $L1_0$ and b.c.t. describe the same atomic configuration but with different selection of axes. Fig. 1.1.11 (e) also helps to visualize that the lattice parameters between the two descriptions exhibit this relationship: $a_{b.c.t.} = \sqrt{2}\, a_{L10}$, and $c_{b.c.t.} = c_{L10}$, which introduces large differences on the reported lattice parameters depending on the selection of crystallographic cell. Using the $L1_0$ unit cell, the typical lattice parameters are around a_{L10} = 3.8 Å and c_{L10} = 6.5 Å, being the tetragonality $c/a > 1$ [59, 60]. It should also be noted that sometimes a_{L10} is considered as doubled (a'_{L10} = 7.6 Å), resulting in $c/a' < 1$ [61–63]. As for the b.c.t. description, the equivalent lattice parameters are about $a_{b.c.t.}$ = 5.4 Å and $c_{b.c.t.}$ = 6.5 Å.

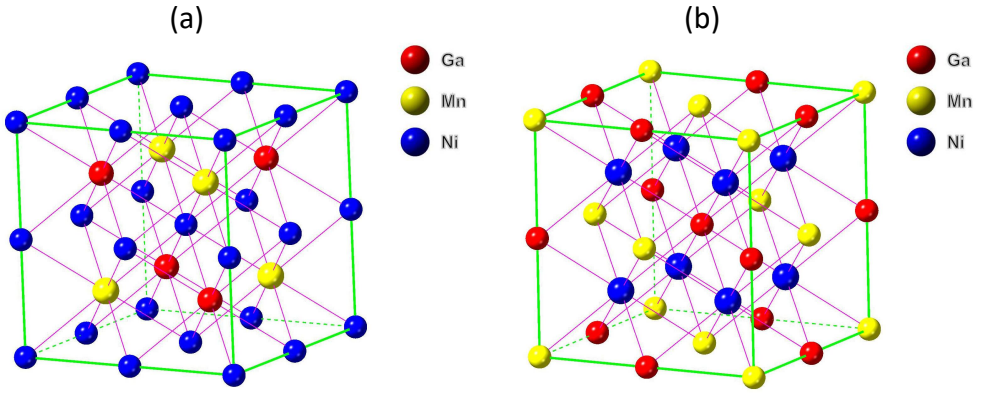

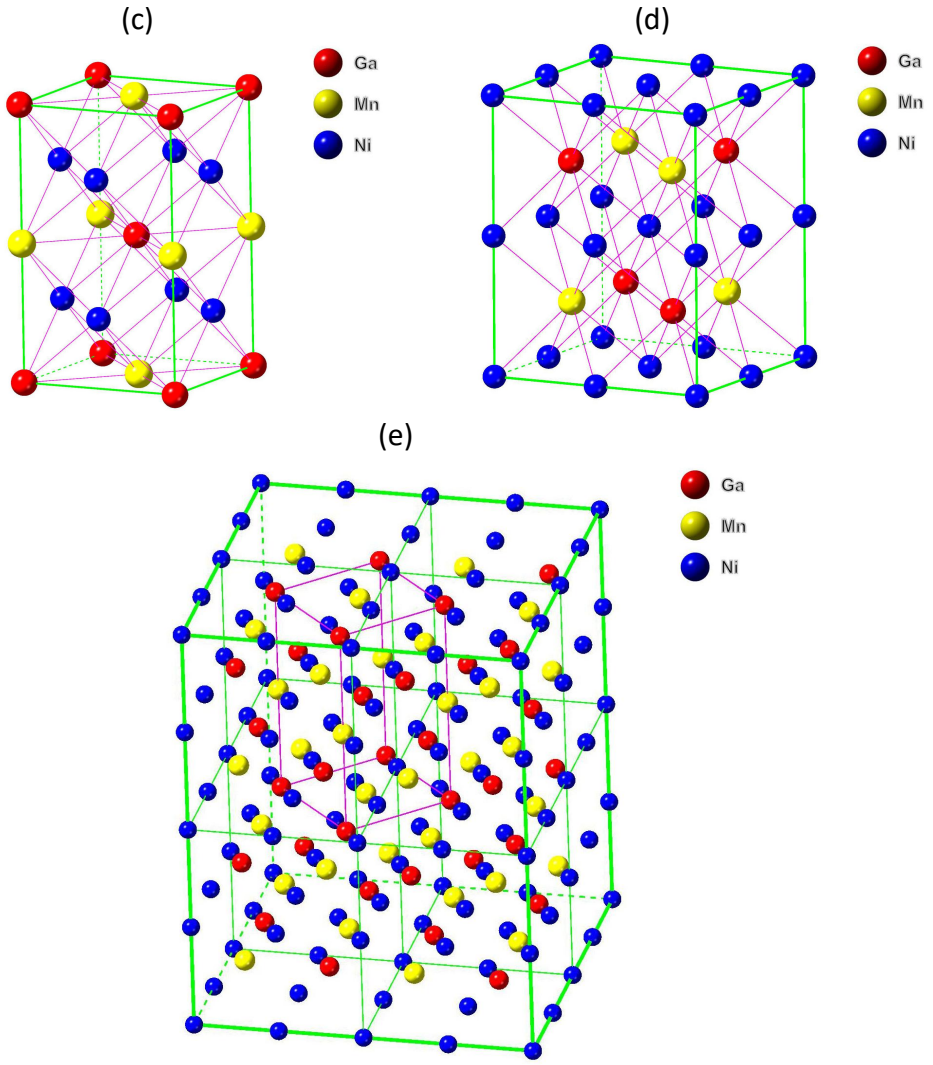

Fig. 1.1.11. Unit cells of (a) $L2_1$ parent phase with Ni at the corners of the b.c.c. units, (b) $L2_1$ parent phase with alternating Ga and Mn at the corners of the b.c.c. units, (c) $L1_0$ face centered tetragonal martensite, (d) body centered tetragonal (b.c.t.) martensite. (e) Relation between the $L1_0$ and b.c.t. descriptions of the non-modulated martensite. In all the cells, the Ni, Mn and Ga atoms are represented in blue, yellow and red colors, respectively, using arbitrary atomic radii as for observation convenience.

Among all the modulated martensites that can be found in the literature, below will be described in detail the 14M, also known as seven-layered martensite, which is very often observed. It can be easily distinguished by the presence of 6 satellite reflections in the diffraction patterns at 1/7 of the distance between the fundamental reflections along a direction derived from $<110>_{L21}$, corresponding to the direction of modulation. Therefore, the unit cell is constructed with the crystallographic axes along the [1-10], [001] and [110] directions of the $L2_1$ austenite [64]. Figs. 1.1.12 (a) and (b) present two different projections of the $L2_1$ austenitic structure, which is the Heusler cell that has already been introduced above, to show the orientation of the axes. The structural model for the 14M martensite is a periodic stacking of nearly close-packed planes, derived from the $\{110\}_{L21}$ planes, similar to the 9R or 18R structures in Cu-based alloys [65]. The positions of two consecutive

basal planes are shifted by ±(1/3 + δ) along the **a** axis and +1/2 along the **b** axis, where δ is a deviation parameter from the perfect close-packed stacking that can be quantified from the experimental lattice parameters (a, c and β), using the equation $\delta = (a + c\cos\beta)/(6a)$ [66]. The 14M unit cell is depicted in Fig. 1.1.12 (c) and corresponds to the $(5\text{-}2)_2$ stacking sequence in Zdanov notation, which means that 5 consecutive basal planes are shifted along the positive direction of the **a** axis and the next 2 planes in the negative direction, being necessary to repeat the sequence two times to end the unit cell with a plane containing the same atomic species as in the first atomic layer. It should be noted that the **c** axis of the monoclinic 14M unit cell is not exactly parallel to $[110]_{L21}$ direction. There is another structural model based on a modulation function. In this model, the displacement (Δj) of each plane (j) from its regular position is considered to follow a sine compound function: $\Delta j = A\sin(2\pi j/L) + B\sin(4\pi j/L) + C\sin(6\pi j/L)$, where L is the modulation period and the constants A, B and C can be adjusted based on the experimental results, *i.e.*, the intensity of TEM diffraction pattern [67]. It should be noted that both models generate almost the same diffraction intensities of the satellite spots [64]. However, the HRTEM images and simulations performed by Pons *et al.* [68] confirm the first structural model based on $(5\text{-}2)_2$ stacking of basal planes. The lattice parameters reported in the latter work are a = 4.23 Å, b = 5.51 Å, c = 29.4 Å and β = 93.5°.

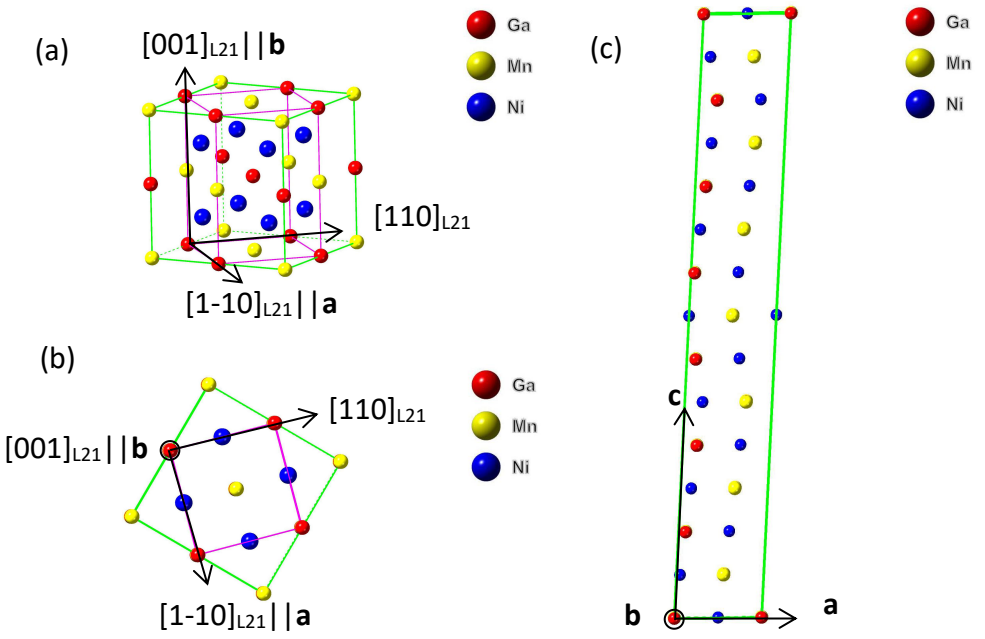

Fig. 1.1.12. Relationship between the austenite $L2_1$ unit cell and the axes of the 14M martensite unit cell, (a) austenite viewed along an arbitrary direction, and (b) along the [001] direction; (c) 14M martensite unit cell viewed along the **b** direction.

Besides the 14M modulated martensite, other modulated structures in Ni-Mn-Ga-based alloys have been reported, as the five-layered martensite (10M) and the less frequently reported ten-layered martensite. The five-layered martensite shows a $(3\text{-}2)_2$ stacking sequence, with lattice parameters around a = 4.2 Å, b = 5.5 Å, c = 21.0 Å and a small monoclinicity angle (β) about 90° - 91° [64]. The ten-layered

martensite exhibits a (5-5) stacking sequence and orthorhombic structure, with lattice parameters are around a = 4.3 Å, b = 5.4 Å, c = 21.0 Å, β = 90° [64].

Precipitates can be introduced into Ni-Mn-Ga-based alloys commonly by compositional design and thermal treatments, and they can have a key role in the shape memory properties of the alloys. The relevant precipitates for the present work are the so-called γ phase and γ' phase, which are represented in Figs. 1.1.13 (a) and (b), respectively. The γ phase exhibits a disordered face centered cubic structure with space group 225 (Fm-3m), and all the sites (corners and face centers) are randomly occupied by any of the Ni, Mn and Ga atoms (represented in orange color in Fig. 1.1.13 (a)). The specific occupation ratio depends on the composition of the precipitates. It was reported that the γ phase exhibits almost constant lattice parameter (a = 3.635 Å) in a series of Ni-Mn-Ga ternary alloys [69]. On its turn, the γ'-phase unit cell is an ordered face centered cubic that can be described by Mn atoms at the corner sites and Ni and Ga atoms at the face center sites for a Ni_2MnGa nominal composition (Fig. 1.1.13 (b)). The unit cell of the γ' phase has a similar lattice parameter than the γ phase, and it was reported that the γ phase can be transformed into ordered γ' phase by proper thermal treatments for certain compositions [70]. R. Santamarta *et al.* [71] reported the effect of these precipitates on the thermal stability of several ternary Ni-Mn-Ga alloys and linked it with the alloy composition in the equilibrium phase diagram. This previous work has been used as a guide to select the compositions of the Ni-Mn-Ga-X alloys of the present thesis. Finally, alloying the ternary alloy with Fe, Cu, Cr ... is a usual route to induce the γ phase or the γ' phase and modify the shape memory properties, as it will be further discussed in the corresponding chapter. It should be noted that the lattice parameter of γ phase can be slightly modified by quaternary additions. For instance, a lattice parameter of a = 3.614 Å was reported for Ni-Mn-Ga-Cr alloys [62], and a = 3.620 Å for Ni-Mn-Ga-Fe alloys [72].

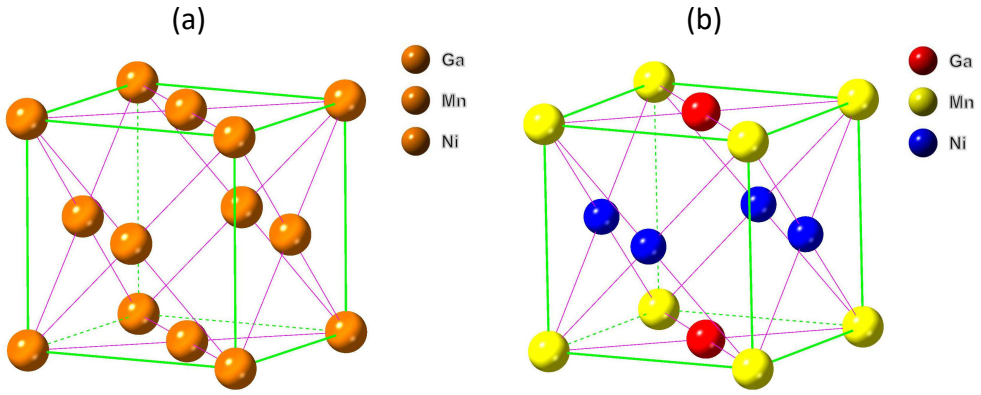

Fig. 1.1.13. Unit cell of (a) disordered γ phase, and (b) ordered γ' phase. The orange color in (a) means that the sites can be randomly occupied by Ni, Mn and Ga. The blue, yellow and red colors in (b) are representing Ni, Mn and Ga atoms, respectively.

1.1.5 Applications

Due to the special properties described in 1.1.2, several practical designs and commercial applications using SMAs have been introduced into biomedical, automotive, aerospace, robotics, and energy industries among others. The number of SMA applications is huge, and this section only aims to show a small selection of applications from different areas.

Probably the field with higher number of applications is actuation, in which the direct reaction of the SMA to the environmental stimuli (temperature or stress) is used. SMAs present various advantages in this field in comparison to other alternatives, being the most important ones those described below, according to references [14, 73]. Firstly, SMAs can replace some conventional actuators, like electrical and hydraulic ones, simplifying the complexity and size of the actuator, providing large working stresses and large strains. For example, Table 1.1 presents a comparison of energy density, frequency, and efficiency among different actuators. It is obvious that NiTi SMA exhibits the highest energy density, though the frequency and efficiency are more limited than other options. Secondly, the stress-strain performance of SMAs can provide significant recoverable deformation, and the presence of hysteresis can dissipate energy leading to damping and vibration isolation during the superelastic response. Thirdly, the actuation response can occur in three dimensions, leading to a variety of approaches like bend, stretch, twist, and their combination. Hence, SMAs can be fabricated and designed into any geometric configurations and shapes needed by the clients (springs, tubes, strings, ...) in order to solve a wide range of engineering problems or substitute actual complex applications.

Table 1.1. Micro-actuators comparison of energy density, frequency, and efficiency [14].

Micro-actuators	Maximum energy density (J/m^3)	Maximum frequency (Hz)	Efficiency (%)
NiTi thin film	2.5×10^7	<100	1
Electrostatic	1.8×10^5	<10,000	50
Electromagnetic	4.0×10^5	<1000	<1
Piezoelectric	1.2×10^5	<5000	30
Bimetallic	4.0×10^5	<100	0.01
Thermo-pneumatic	5.0×10^5	<100	10
Conductive polymer	3.4×10^6	<1000	60

As a result of the advantages mentioned above, a lot of applications have been developed to be used in different fields, being NiTi-based alloys the most spread and well-known SMA system. The NiTi family, also known as Nitinol, is the most used SMA on the current market due to its high biocompatibility, stability during thermal

cycles, corrosion resistance, elevated work output capability and ductility. An example of its applications is the nitinol SMA wires actuators designed to track helicopter rotor blades while in-flight, so the vibrator loads from different sources could be reduced by the actuator, therefore, the lifetime of the blades could be increased [74]. However, the artificial vessels or stents, formed by NiTi SMA wires covered with a silicon rubber tube, are probably among the most impressive applications of NiTi SMA. The SMA in these devices undergo an R to austenite phase transition at 307 K, resulting in a slight reduction of the length and a diameter expansion [75]. Hence, a small volume of the contracted stent (smaller than the blood vessel) in the R phase at room temperature is implanted into the blood vessel. Finally, the NiTi stent expands inside the vessel due to the R to austenite reverse martensitic transformation activated by the body temperature, acting as a support to prevent tightening of the blood vessel.

In the field of aeronautics, a $Ni_{60}Ti_{40}$ (wt.%) SMA structure with morphing capability called the variable geometry chevron (VGC) was developed and installed on the nozzle exit system of the Boeing 777-300 ER commercial aircraft to diminish the engine noise. The SMA plates, when heated, deflect the composite panel towards the jet flow during takeoff / landing to decrease the noise produced by the engine. During the flight, the panel returns to the original straight position without interaction with the flow, so the engine can achieve the full power (showed in Fig. 1.1.14) [14, 76].

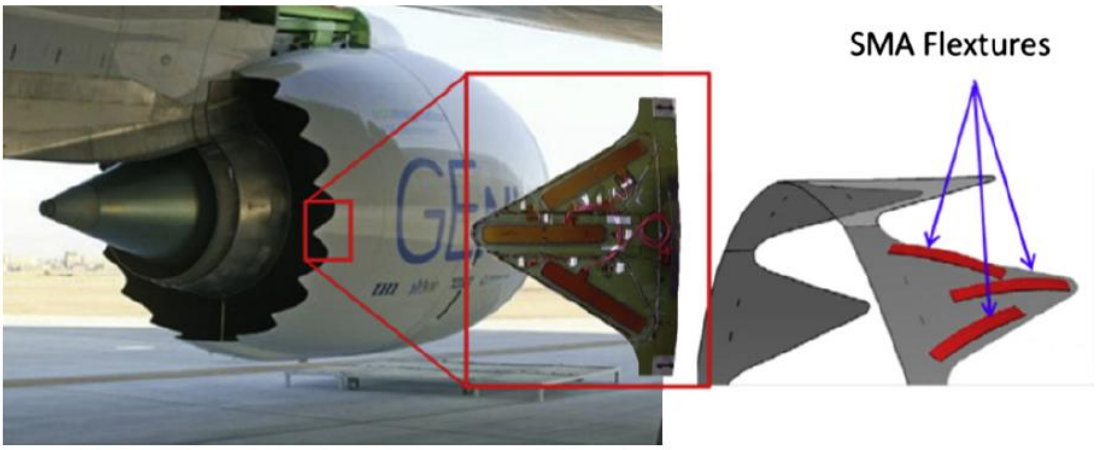

Fig. 1.1.14. A SMA application design named as variable geometry chevron (VGC) from the Boeing 777-300 ER commercial aircraft [14, 76].

Another design in the aerospace industry is the so-called shape memory rock splitter (SMARS), which was presented by O. Benafan *et al*. [77]. This device, whose components and working method are shown in Fig. 1.1.15, is aimed to collect specimens in the outer space without carrying explosives. To crack the hard rock, the hole must be drilled first, and later, the device is put inside the hole. Then, the SMA bar is heated to undergo the reverse transformation to austenite, producing an elongation of the bar that pushes the tip, generating a high stress to crack the hard

rock. In this design, to obtain the dimension stability and maximize the stress generation, a NiTiZr20 based HTSMA is selected after ageing at 820 K for 3 h followed by furnace cooling and some training. The alloy shows over 1.5 GPa stress and a strain of ~2 - 3% under an activation temperature slightly above 373 K.

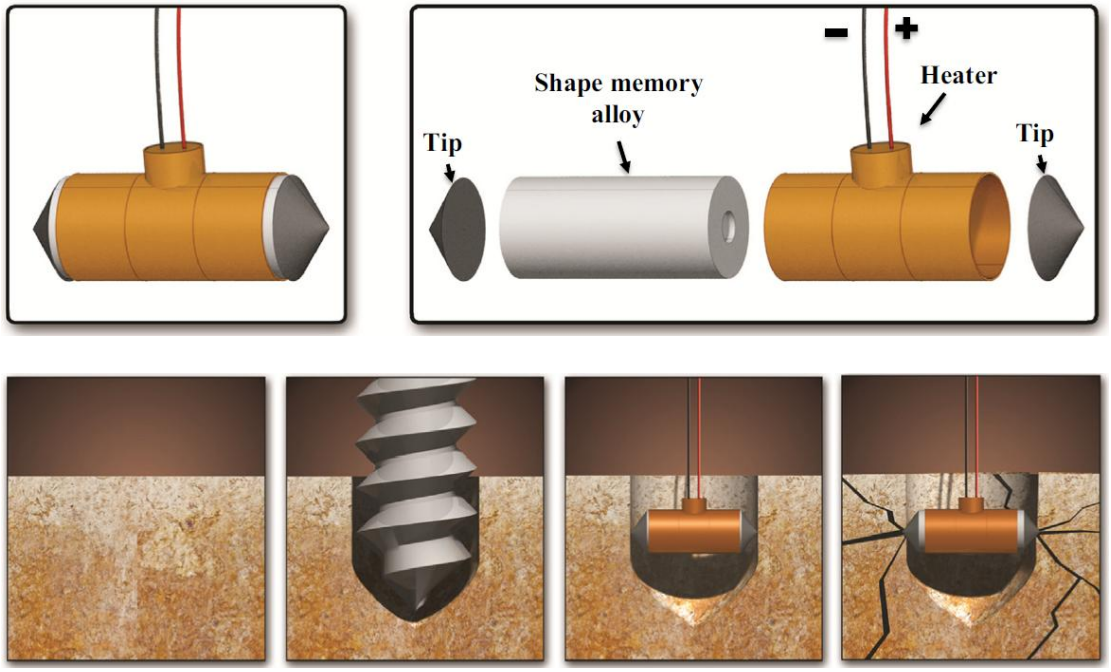

Fig. 1.1.15. A design for planetary exploration named as shape memory alloy rock splitter (SMARS) [77].

Finally, based on the high-energy density elastocaloric property of some SMA, a lot of solid-state heating-cooling devices are being designed to be environmental-friendly alternatives to replace actual conventional cooling devices. As an example, a continuous operating elastocaloric fluid cooling system based on SMA was reported by Kirsch SM *et al*. [78] (Fig. 1.1.16). In this design, NiTiCo strings are successively subjected to loading-unloading tensile cycles with a strain of about 3%. During loading, the strings transform into martensite and release the latent heat into the surrounding media (hot side), which is taken away by the gas flow. Upon unloading, the SMA strings transform back to austenite, returning to its original length and absorbing heat from the surrounding media (cold side). However, the mechanical deformation to induce the elastocaloric effect could limit the frequency and efficiency of the heat transfer, and other materials with caloric properties are being studied. In this sense, the magneto-caloric effect (MCE) has been found in ferromagnetic shape memory alloys like Ni-Mn-Sn-Ga [79].

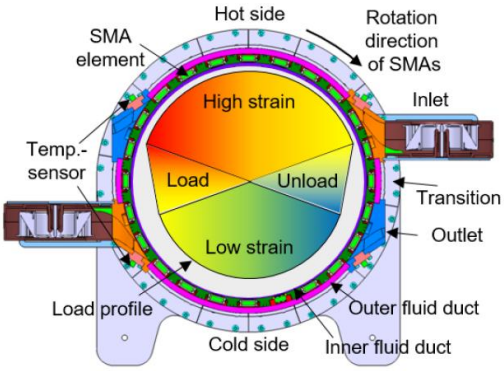

Fig. 1.1.16. Cross-section of the elastocaloric heating and cooling device reported in [78].

Despite all the advantages and developed applications mentioned above, there are still several challenges to overcome to widely spread the use of SMA actuators. An important restriction for SMA is related with their typical high heat capacity and energy density metallic alloys, which lead to low-heat transfer (in or out) to the ambient intermediate medium (normally gas or liquid). Therefore, a limitation in the response frequency and working efficiency is inherent to SMA actuators. Another problem is derived from the evolution of the SME with multiple transformation cycles (*i.e.*, fatigue) [80]. Although there are some investigations on NiTi or NiTiCu that shows SMA wires bearing up to 10^5 cycles with about 3.5% strain [81], and reports on NiTiHf20 alloys that exhibits over 10^4 fatigue life after certain thermal treatment, still many SMAs suffer from mechanical instabilities, especially when a high number of cycles is applied. Furthermore, one or more further limitations and challenges are generally present in any known SMAs: relatively small usable recoverable strain, low available critical working stress, low controllability, inappropriate transformation temperatures, brittleness, hardness, etc.

Therefore, newer enhancements and SMA systems are needed to fulfill the practical requirements. While intensive works and studies are carried on to expand the current alloy families, function performance, increasing fatigue lifetime and stability for future applications, multiple methods are improving SME properties like composition design, fabrication processes, microstructure optimization by mechanical training and phase enhancement, etc. Countless investigations are currently focusing on NiTi-, Cu-, NiMnGa-, TiTa-systems and their corresponding derivatives. Among others, some of the most widely used methods to enhance the properties of SMAs are composition design (element combination and/or proportional variation), thermal treatments and thermomechanical training. Therefore, these orientations will become the major guidelines for the investigations of this thesis.

1.2 High Temperature Shape Memory Alloys

As it has been shown above most of the current practical designs are working below 370 K as they are using commercial NiTi binary alloys, which show high reliability in working lifetime and stability under cycling. However, there are applications that need to work beyond the range of transformation temperatures of the binary NiTi. Therefore, a large variety of SMAs are being developed with different ranges of transformation temperatures. Normally, those SMAs that possess martensitic transformation temperatures above 370 K, are defined as high temperature shape memory alloys (HTSMAs). J.Ma *et al*. [13] classified HTSMAs into three groups as a function of their martensitic transformation temperatures for potential applications: group one corresponds to alloys exhibiting martensitic transformation temperature in the range of 370 K - 670 K, group two for alloys in the temperature range of 670 K - 970 K, and group three for those transforming above 970 K.

It is expected for HTSMAs to possess the similar features to those transforming at ambient temperatures as NiTi, that is, good shape memory response with relatively large recoverable strain, little or no irrecoverable strain, thermomechanical stability, etc. However, there are new challenges that need to be faced when dealing with high temperatures, such as avoiding softening, plastic deformation and creep overcoming surface oxidation and other gas/liquid corrosion [13]. Besides, there are more specific difficulties to solve, as it is detailed below:

(1) HTSMAs are intended to show sustainable long time high temperature thermomechanical cycling, and meanwhile provide comparable good SME and/or SE responses and work output. These requirements are particularly necessary for applications as thermally driven actuators, but they can be tough to be fulfilled due to the martensitic transformation mechanisms and metal softening at high temperature. On the one hand, as it has been already shown in Fig. 1.1.6, increasing the temperature inevitably decreases the critical stress for plastic deformation (σ_{PD}) as a consequence of the larger atomic thermal excitation. Therefore, plastic deformation can take place before the expected SE response and produce undesirable irrecoverable strain. Conventional cold work hardening as well as training can improve the strength of the matrix, but for most of the HTSMAs the brittleness and the low ductility makes quite inefficient the procedure to strengthen the matrix through repeatable deformation, and usually, it is not stable at high temperatures. On the other hand, the critical stress to induce martensitic transformation (σ_{SIM}) from parent phase increases with temperature according to the Clausius-Clapyron relationship, which is inevitable for all the HTSMAs. Therefore, at high temperatures over A_f the difference between σ_{PD} and σ_{SIM} is gradually reduced, and consequently, plastic deformation easily appears when stress is applied [13].

(2) Cold work hardening and training usually enhance the shape memory behavior by

introducing favorable defects into the matrix, but HTSMAs operating at high temperature can accelerate the recovery effect by diffusion and/or rearrangement of defects, leading to the deterioration of the strengthening effect. In addition, water quenching after thermal treatment could affect to the martensitic transformation by introducing some disordering at the crystal structure and retaining a high number of heterogeneous vacancies. These defects can reach an equilibrium distribution in any of the two phases (austenite or martensite) by short range diffusion rearrangement, stabilizing that phase in detriment of the other [82]. Long stay at high temperatures can accelerate the diffusion process and produce martensite or austenite stabilization, depending on the ageing temperature and time, which is a common situation for HTSMAs.

(3) Operating at high temperatures can also cause compositional or structural instability, resulting in second phases, or precipitates, to reach (or approach) the equilibrium state and composition. As a result, the designed properties of HTSMAs will be no longer the same, especially in features like the transformation temperatures, which normally are extremely sensitive to the matrix composition. Additionally, high temperatures stimulate the growth of existing precipitates. This situation is especially critical for nano-sized precipitates that can over grow up and loose coherency with the matrix, decreasing the matrix hardening effect. Finally, oxidation can also be a factor influencing the composition of the material, leading to deterioration of shape memory responses, especially at higher operating temperatures as the ones in groups two and three from the classification in reference [13]. Regarding nickel based alloys, it has been found that multiple oxide layers are formed, efficiently avoiding the further oxygen penetration depending on temperature and time. However, beneath the more external titanium oxide layer, the Ni-rich layer exhibits different MTT than the NiTi specimens without oxidation [83, 84].

(4) Single crystal SMAs can generate huge strains along orientations close to the external stress by induced lattice shear during the phase transformation and/or detwinning. In comparison, polycrystalline counterparts have easier and lower-cost fabrication procedures, although the recoverable strain becomes significantly decreased because the randomly distributed grains can only generate an average strain of the individual crystals with different orientation. Suitable texture introduced into polycrystalline alloys is an effective way to increase recoverable strain and approach the single crystal performance. Traditional cold working, equal channel angular extrusion (ECAE) and training can be used to generate this texture, but they are difficult to precisely control and, in HTSMA, their effects are limited by the issues explained in (3). Furthermore, grain boundaries can show other problems during the phase transformation. For example, the grains in textured polycrystalline alloys and alloys with cubic to tetragonal transformation (with lower number of variants compared to monoclinic martensite) actually have lower freedom to deform cooperatively [85], which helps to reach fracture. Moreover, the repeatable

deformation strains during the phase transition cycling, especially stress induced, may also cause inter-granular fracture. In addition, high temperatures can lead to diffusion processes as recrystallization and grain growth, which could diminish the expected effect of texture and grain refinement resulting in poor shape memory properties [13].

Hence, a carefully compositional design for developing new HTSMAs systems along with controlling the fabrication process and using other optimization techniques are needed to deal with these above-mentioned challenges. A large number of works are focusing on the improvement and development of new alloy systems of HTSMAs based on systems that already possess excellent performance at low temperatures. In this regard, adding extra elements into the already known SMAs systems is the most common method to explore new compositions, as the resulting alloys are expected to inherit part of the supreme shape memory properties and/or other outstanding characteristics of the original materials. That is the case, for instance, with Ni-Ti-X alloys (with X = Pt, Pd and others) and Ni-Mn-Ga-X alloys (with X = Cu, Fe, Al, Cr, rare earth elements, etc.), which will be further discussed in the next subsections.

1.2.1 Ni-Ti-X Ternary Alloy System

Ni-Ti is the most well-known shape memory alloy system, and it has been already successfully used in practical applications due to its excellent shape memory features and performances, as it has been already discussed previously. Nevertheless, the NiTi binary alloy system is limited because of its low transformation temperatures (< 370 K). This restriction has promoted a large number of studies using addition of Pd, Pt, Au, Hf and Zr as ternary elements into the binary Ni-Ti alloy system to increase the transformation temperatures above 370 K.

Ni-Ti-Pd alloys is a potential HTSMA system in the temperature range of 470 K - 570 K [13], and a lot of research has been focused on the Ti-rich or Ti-poor Ti-Ni-Pd HTSMAs, as it is presented hereafter.

When Pd is added into nearly equal atomic Ni-Ti and Ti is kept constant at 50 at.% (*i.e.*, Pd substitutes Ni), the M_s shows a parabolic relationship as a function of the Pd content that goes from about 270 K to 770 K [13]. If Pd is fixed at 30 at.% in the ternary $Ti_XNi_{70-X}Pd_{30}$ (X = 48.5 - 51.0 at.%) system, M_s decreases when Ti content is less than 50 at.%. Additionally, it has been found that the shape memory properties can be improved in aged $Ti_{50.6}Pd_{30}Ni_{19.4}$ alloy, as the result of the hardening effect of Ti_2Ni precipitates [86].

B. Kockar *et al*. [87] presented good ductility, mechanical stability and less irrecoverable strain for a $Ti_{50.3}Ni_{33.7}Pd_{16}$ alloy as the consequence of refined grain size obtained by equal channel angular extrusion (ECAE), although the transformation

temperature is quite low (around 370 K). $Ti_{50.5}Ni_{24.5}Pd_{25}$ shows M_s over 430 K, and training can provide a relatively stable high strain of TWSME with higher work output (0.12 J/g) as compared to Ni-Ti or Cu-based SMAs. However, strains and work output of the TWSME can be deteriorated by the severe plastic deformation introduced by ECAE [88]. Additionally, high stress-free thermal stability with a narrow hysteresis (8.5 K) and M_f about 454 K had been found in $Ti_{50.3}Ni_{24.7}Pd_{25}$ alloy [89]. Furthermore, (Ni,Pd)-rich Ti-Ni-Pd alloys exhibit an increase in the transformation temperature (up to 407 K for A_f) after proper ageing treatment at 673 K (up to 100 h) due to the formation of precipitates [90]. Also, (Ni, Pd)-rich $Ti_{49.7}Ni_{24.3}Pd_{26}$ aged alloys with fine nano-sized precipitates provide 3% transformation strain in biased thermomechanical cycling under 300 MPa and 2% strain of TWSME, although the irrecoverable strain still exists due to the defects and retained martensite during cycling [91].

However, there are still some challenges for the Ti-Ni-Pd alloy system as well as some solutions to overcome them. The most common problem is the low critical stress for the dislocations slip, which can cause low stability and irrecoverable strain during the high temperature thermomechanical transformation. To reduce the effect of this issue, some methods have been applied to harden the matrix, such as inducing Ti_2Ni precipitates by ageing in off-stoichiometric compositions [86], and strengthening by thermomechanical training [88]. Adding 5 at.% of Ta to $Ti_{50.5}Ni_{24.5}Pd_{25}$ can improve the dimensional stability, but at the expense of lowering the transformation temperatures and the martensite volume fraction due to the precipitation process [92]. However, alloying Ti-rich alloys with Sc can reduce the transformation temperatures with only 1 at.% of the quaternary element, further reducing the hysteresis (7 K) due to a low amount of precipitates, high alloy purity and twinless / small twin ratio [93, 94]. As for most of the HTSMAs, creep is inevitable during the thermal mechanical cycling at high temperature. Kumar *et al*. [95] shows that low cycling frequencies (low cooling/heating rates) in $Ti_{50.5}Pd_{30}Ni_{19.5}$, high upper cycling temperature (over 770 K) and high constant stress (over 300 MPa) can accelerate the creep combined with phase transformation due to the time-dependent mechanism of creep.

Substitution of Ni by Pt in the equiatomic binary Ni-Ti system also tends to elevate the transformation temperatures, and M_s presents a parabolic relationship as a function of the Pt content [96]. Indeed, M_s can be increased up to over 1270 K with 50 at.% Pt content [96]. Similar to the Ti-Ni-Pd system, Pt addition presents a lot of advantages for HTSMAs, and numerous investigations have been carried out on near stoichiometric composition of Ti-(Ni, Pt) alloy system. Brian Lin *et al*. [97] reported that Ti-poor $Ti_{49.8}Ni_{42.7}Pt_{7.5}$ demonstrates as good mechanical properties as Ni-rich Ni-Ti binary alloys, with large total recoverable strain (6%) and low hysteresis serving below 420 K. F. Yang *et al*. [98] reported that very stable precipitates $Ti_2(Ni, Pt)_3$ can be formed in Ti-poor $Ti_{49.5}Ni_{29.5}Pt_{21}$ alloy induced by ageing above 870 K or be transformed from the P_L phase by ageing at 870 K for 200 h, where the P_L phase is

another precipitated phase formed by ageing at 770 K for 1000 h. Moreover, after proper annealing procedure, $Ti_{50.5}Ni_{29.5}Pt_{20}$ demonstrates promising characteristics for actuators with good dimensional stability serving up to 570 K. In addition, they show low hysteresis (11 K), and a transformation strain of 2% at 172 MPa, with a work output 4 J/cm^3 [99]. Finally, the annealing treatment can change the hardness of the Ni-rich $Ni_{50}Ti_{42.5}Pt_{7.5}$ alloy by forming different precipitates, but lowering it in respect to the as-cast specimen [100].

There is still some space for optimizing Ti-Ni-Pt materials for actuators, since they have good ductility to endure cold working and training. However, despite the good SME properties obtained with above mentioned precise and complex methods, the high cost of Pt still cannot be ignored.

Casalena L *et al*. [101] reported that the Ti-(NiAu) alloy exhibits transformation temperatures over 670 K with Au 40 at.%, and it demonstrates good SME response with full recoverable strain under 100 MPa. However, with further applied stress, the irrecoverable strain increases sharply. Similarly to the Ti-Ni-Pt/Pd systems, it should be noted that the cost of high amount of Au additions avoids these alloys to be widely used for practical designs.

In summary, despite the excellent properties of Ti-Ni-(Pd, Pt, and Au) systems for HTSMAs, the cost is an inevitable problem facing their commercial usage, and cheaper alternatives need to be developed. In comparison, Ni-Ti-(Hf and Zr) involve lower manufacture cost, and hence, it has led to intensively investigations.

The earliest researches show that in the Ni-poor (or Ti-rich) Ni-Ti-(Hf, Zr) alloy system, the martensitic transformation temperatures can be increased with the addition of the ternary element (Hf, Zr) when substituting Ti (over 3 or 5 at.%, respectively), as it is shown in Fig. 1.2.1 [13]. On the contrary, Ni-rich (over 50 at.%) Ni-Ti-(Hf, Zr) treated alloys can lead to a decrease in transformation temperature similar to the binary Ni-Ti alloys, which is not desired for HTSMAs. However, it has been reported that the Ti-rich Ni-Ti-(Hf, Zr) system suffers from thermal instability, shows a large hysteresis during the phase transformation due to the low strength of the matrix, and plastic deformation can be easily induced [102], with the subsequent large irrecoverable strain (up to 10%) [103]. In addition, $Ni_{49}Ti_{36}Hf_{15}$ samples exhibited a decrease in transformation temperatures upon ageing at 973 K for 20 h as a consequence of the precipitation of $(Ti, Hf)_2Ni$, accompanied by an increase in the yield strength [104].

Therefore, unconventional and traditional methods have been used to improve the shape memory properties of Ni-poor Ni-Ti-(Hf, Zr) alloys. A special thin film deposit fabrication method was investigated on Ni-poor Ni-Ti-Zr alloys, increasing the critical slip stress by forming the Ni-Zr second phase after crystallization heat treatment. This improvement is obtained at the expense of some recoverable strain, and the

optimum Zr content is about 20 - 23 at.% with transformation temperatures over 300 K - 400 K, respectively [105]. A network structure of precipitates was produced by spark plasma sintering method (SPS), with big particles located at grain boundaries and fine precipitates inside the matrix [106]. The brittle and hard $(Ti, Hf)_2Ni$ precipitates can improve the SME properties by strengthening effect, but the martensitic transformation temperature and the enthalpy change are also decreased [106]. Texture was introduced into a $Ni_{49.4}Ti_{38.6}Hf_{12}$ matrix by hot rolling, which reduced the hysteresis as the result of the B2 to R phase transformation assisted by $(Ti, Hf)_2Ni$ precipitates [107]. However, the strengthening effect is reduced due to the loss of partial coherency of the precipitates, and high temperatures can cause a dynamic recovery or even a partial re-crystallization, decreasing the texture produced during hot rolling [107]. Moreover, the SME properties can be improved with sintered TiB_2 [108], quaternary element addition like Pb, Ta, rare earth element Y [109-111]. However, on the other hand, Cu addition deteriorates the SME [112].

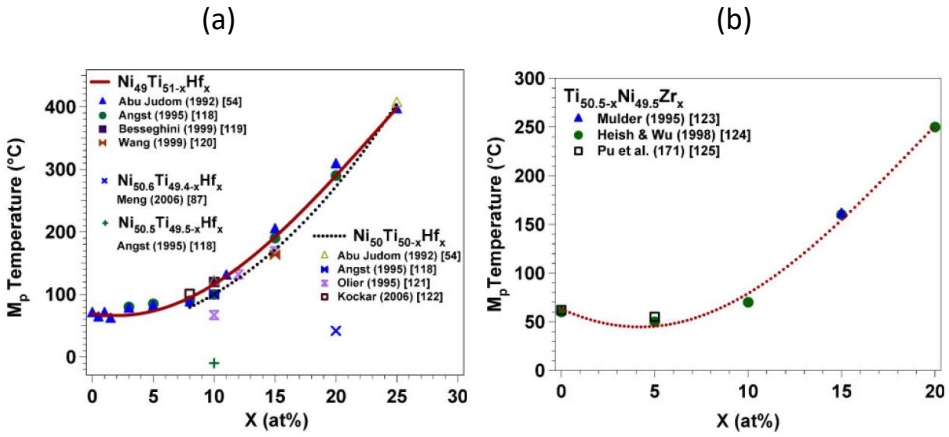

Fig. 1.2.1. Composition dependence of martensitic transformation peak temperature in Ni-poor Ni-Ti-X alloy system, (a) as a function of Hf, (b) as a function of Zr, substituting Ti [13].

Recently, many researchers have turned their interest into the Ni-rich Ni-Ti-(Hf, Zr) alloy system due to possibility to prevent the decrease of the transformation temperatures by proper thermal treatments. It is well known that, in binary Ni-rich Ni-Ti system, precipitates like Ni_4Ti_3, Ni_3Ti_2, Ni_3Ti can be formed in the matrix as a function of ageing time and temperature, which can also be tailored to strengthen the matrix, improve the SME properties and controlling the transformation temperature [53]. A pioneer research on $Ni_{53}Ti_{41}Zr_6$, with low concentration of Zr, shows that ageing can affect the microstructure, the mechanical behavior, and the martensitic transformation temperatures as the result of formation and evolution of precipitates. The precipitation process can be divided into three steps depending on the ageing time: short range ordering, fine coherent precipitates, and incoherent precipitates coarsening for increasing ageing times, respectively [113, 114]. Meng *et al*. [115] investigated three Ni-rich Ni-Ti-Hf alloys with 20 at.% Hf, reporting that $(Ti+Hf)_3Ni_4$ precipitates can be formed upon ageing at 823 K, similar to the Ni_4Ti_3 precipitates formed in the Ni-rich Ni-Ti system. The transformation temperatures can

be increased notably in the first aging hour and decreased slowly when aging over 2 h. In addition, the formation of precipitates can improve the thermal stability, and produces a strengthening effect on the matrix with proper thermal treatments, accompanied by an improved recoverable strain [116]. A three-stage transformation (B2-R-B19' and B2-B19') was reported in a $Ni_{50.3}Ti_{34.7}Hf_{15}$ alloy due to the formation of heterogeneous precipitation of $(Ti, Hf)_3Ni_4$ particles as a function of the ageing treatment, which can improve the hardness [117].

More recent investigations still confirm that the precipitates are responsible for the strengthening effect and improvement of the dimensional stability, but they report a more complicated structure than the $(Ti, Hf)_3Ni_4$ [118]. This new structure shows extra n/3 $(101)_{B2}$ type reflections along the $[111]_{B2}$ zone axis and $[010]_{B2}$ zone axis by electron diffraction patterns and FFT from high resolution STEM images [119]. This finding is similar to the selected area electron diffraction patterns from one of the variants of the precipitates described early by Han *et al*. in a $Ni_{36.5}Ti_{48.5}Hf_{15}$ alloy [55]. Later, Yang *et al*. [56] proposed a complete structural atomic model for this unique type of precipitates with similar unit cell as suggested by Han *et al*., and denoted it as "*H phase*". Yang's model contains 192 atoms in an orthorhombic unit cell introducing shuffle and displacements of Hf atoms. Furthermore, Santamarta *et al*. [57] reported that these precipitates also form in Ni-rich Ni-Ti-Zr alloys and they can be interpreted as a superstructure of the B2 phase with a threefold periodicity along a $<110>_{B2}$ direction and a fourfold periodicity along $<210>_{B2}$ directions, in the B2 sublattice occupied by Hf/Zr and Ti atoms. As a result, the precipitates exhibit good coherency with the austenite, confirmed by HRTEM observations and DFT calculations. More detail of this H-phase structure has been carefully introduced in the former section 1.1.4.

It has also been confirmed that increasing the Ni content or the Hf/Zr content (for a fixed Ni content) of the alloys can lead to a faster growth of the H-phase precipitates [57]. Concerning the size of the precipitates, ageing induced nano-sized precipitates provide a good thermomechanical stability with high transformation strain (3.5% at 400 MPa) and high work output (14 J/cm^3) [120]. However, precipitates of hundreds of nanometers in size expand the hysteresis by interacting with martensite variants [121]. Therefore, thoroughly investigations focused on the shape memory properties of the Ni-rich, but relatively close to 50 at.% and high Hf/Zr content (15 - 25 at.%) alloy systems, as it will be shown hereafter.

In the $Ni_{50.3}Ti_{34.7}Hf_{15}$ alloy, the ageing effect on transformation temperatures and shape memory properties as a function of time and temperature were attributed to the evolution of the inter-particle spacing and composition variation with the growth of the precipitates [122]. This alloy exhibits an excellent dimensional stability, especially after ageing at 720 K for 10 h, with a fully 3.3% recoverable strain in tension at 300 MPa but showing a rather low transformation temperature (M_s ~250 K) [123], due to the limited Hf addition.

Regarding the compositions containing 20 at.% Hf, ageing at 820 K for 3 h provides the most stable SME response with nano-sized (~20 nm) coherent precipitates, demonstrating 3% recoverable strain at 500 MPa along with 16.45 J/cm^3 work output [124]. It also exhibits a 3% recoverable strain in superelasticity experiments and a perfect stability upon mechanical cycling up to 200 MPa confirmed through *in-situ* synchrotron X-ray diffraction [125], as well as an improvement of the hardness [126]. Hayrettin *et al*. [127] revealed that the TWSME can be obtained after 600 thermomechanical cycles under 200 MPa, with a recoverable strain as high as 2.95%, which is an 85% of the maximum actuation strain under the same stress level. In addition, Saghaian *et al*. [128] showed that the same composition and thermal treatment (820 K for 3 h) leads to a high dimensional stability in the mechanical tests up to 1500 MPa along the [001] direction, while over 4% superelasticity recoverable strain can be achieved along [011] and [111] directions, and hence, a large work output of 25 - 30 J/cm^3 was obtained. Concerning the fatigue life, a crucial parameter, O. Karakoc *et al*. [129] reported that polycrystalline alloys hardened by nano-sized precipitation can withstand over 10000 cycles under 300 MPa and 570 K upper cycling temperature, providing 2 - 3% actuation strain. However, under 400 MPa and 620 K as upper cycling temperature the same alloy only provided 1530 cycles with 4% strain, along with large irrecoverable strain compared to the former fatigue treatment. Moreover, fatigue experiments showed that ageing at 820 K for 3 h with ~20 nm size of precipitates demonstrated a promising actuation life with stable shape memory response as compared to furnace cooled sample with larger precipitates [130]. Nonetheless, it should be emphasized that over ageing can cause poor shape memory properties with large irrecoverable strain during thermal mechanical cycles as the result of the coarsening and loss of coherency of the precipitates, which has been attributed to Hf diffusion [57, 124, 131]. To end with, adding Al to the ternary alloy can lead to a decrease in the transformation temperatures and cycling stability [132].

Ni-rich Ni-Ti-Hf alloys with 25 at.% Hf have been investigated much less than compositions with lower Hf. Patriarca *et al*. [133] reported over 4% local strain by Digital Image Correlation experiments under 535 K at over 800 MPa applied stress together with 29 K of hysteresis in polycrystalline specimen aged at 770 K for 4 h. Moreover, $Ni_{50.3}Ti_{25}Hf_{24.7}$ single crystal shows excellent thermomechanical stability both along the [011] direction (5.4% transformation strain) in compression and along the [111] direction in tension (8.1% transformation strain), together with a remarkable resistance to cyclic degradation and transformation temperatures over 670 K [134].

As it has been briefly mentioned before, not only the Hf/Zr content but also the Ni content plays an important role in the precipitation of the H phase. Therefore, a series of investigations have focused their attention on higher Ni contents due to its influence on the short range ordering (seen as precursor of H phase) [135] and the precipitates coarsening [57]. Saghaian *et al*. [136] reported that the strength of the

matrix can be raised by increasing Ni content at the expense of the recoverable strain and a larger volume fraction of precipitates (generated through furnace cooling treatments). For instance, stable thermomechanical cycles with < 1% recoverable strain can be obtained in a Ni-rich (52 at.%) alloy over 1500 MPa, while the plastic deformation appears under 1000 MPa with < 2% recoverable strain for an alloy with 50.7 at.% of Ni. In addition, in comparison to 50.3 at.% Ni, an alloy with 51 at.% Ni showed more strength of matrix with shorter ageing time, but also lower martensitic transformation temperature (M_p) accompanied by a reduced critical stress to induce plastic deformation [137]. A $Ni_{51.2}Ti_{28.8}Hf_{20}$ alloy aged at 820 K presented full recoverable shape memory response and good superelasticity effect (4% strain) along with near 30 J/cm^3 high work output [138]. However, that alloy exhibited no MT above 170 K after a solution heat treatment, although it recovered the transformation, with M_p over 320 K, by ageing at 920 K for 3 h due to the growth of precipitates up to 40 - 70 nm [138]. Finally, a Ni 51 at.% alloy (aged at 820 K for 3 h) showed the highest hardness in martensite state (about 500 HV) in respect to the other alloys with less Ni (50 - 51 at.%) and/or other thermal treatment [139].

Ni-rich Ni-Ti-Zr alloys have not drawn as much attention as the Hf counterparts. A Ni-rich Ni-Ti-Zr alloy with only 6 at.% Zr showed low transformation temperatures (less than 350 K), even after applying ageing treatments that produced precipitates, as it was first reported by A.M. Sandu *et al* [113, 114]. Hence, more Zr has been normally added to increase the transformation temperatures. Evirgen *et al*. [121] reported that a $Ni_{50.3}Ti_{29.7}Zr_{20}$ alloy presented M_s over 370 K after ageing at 770 K and above, and exhibited a good thermomechanical stability up to 300 MPa with the assistance of small size precipitates. One the other hand, bigger precipitates resulted in larger hysteresis due to the restriction on the growth of variants in between the precipitates [121]. Compared to alloys containing Hf, a high amount of Zr (20 at.%) results in a faster formation of the H phase [57]. This composition can provide also 3% recoverable strain in stable superelasticity cycles under 520 K after the same thermal treatment as the Ni-rich Ni-Ti-Hf alloys (820 K for 3 h), and hence similar size of the H-phase precipitates as well [140]. For alloys containing 15 at.% Zr, the martensitic transformation temperatures are lower than alloys containing 20 at.% Zr (M_s < 350 K), even with long time ageing under 870 K, and the hysteresis is larger (~55 K compared to ~30 K) under a similar thermal treatment [141]. Moreover, $Ni_{50.3}Ti_{34.7}Zr_{15}$ alloys exhibited good thermomechanical stability in tension with little irrecoverable strain up to 300 MPa when ageing at 820 K and 770 K for up to 100 h, while ageing at 870 K produced irrecoverable strain at 200 MPa since it contained bigger size of the H-phase precipitates [141].

1.2.2 Ni-Mn-Ga-X Quaternary Alloy System

The Ni-Mn-Ga family (especially off-stoichiometric Ni_2MnGa Heusler alloys) has drawn an enormous attention as a promising material for fast actuators due to the large strain induced by magnetic field [142-145]. But also, several Ni-rich Ni-Mn-Ga

compositions were found to possess some potential as high temperature shape memory alloys (HTSMA), showing M_s over 400 K [146], good shape memory properties [147], high thermal cycling stability (over 1000 cycles) together with large recoverable strain (over 6%) [148] in single crystalline specimens. Indeed, a $Ni_{53}Mn_{25}Ga_{22}$ alloy demonstrated a super-strain as high as 15%, but the relatively high cost of time and difficulty to fabricate single crystals limit its usage [149]. It has to be mentioned that all Ni-Mn-Ga-based HTSMAs present the martensitic transformation in the paramagnetic state, well above the Curie point. Therefore, no coupling between magnetic and structural properties take place in this case, at difference with the alloys with transformation temperatures below 370 K.

Recently, the interest has focused on polycrystalline Ni-Mn-Ga alloys, which are easier and cheaper to produce. The polycrystalline alloys can also exhibit good functional properties and stability (*e.g.*, an exceptional thermal stability under ageing at 770 K for some compositions [70, 71]. However, they normally show a high level of brittleness at the grain boundaries, which hinder practical applications. Some common strategies to face this problem are to introduce a fourth element to the Ni-Mn-Ga alloys, or to increase the amount of Ni at expenses of Mn and/or Ga, with the purpose of inducing the precipitation of a ductile phase, especially at the grain boundaries. During this process, not only the martensitic transformation temperatures (MTT) are inevitably shifted as a result of the composition modification of the matrix, but also other shape memory properties can be changed. In case of increasing Ni up to 57 at.% in a ternary alloy, M_p can be raised up to ~717 K, but also a dual phase consisting of martensite and an f.c.c. phase (γ phase) appear, together with a significant reduction of the shape memory strain [150]. The γ phase is distributed mainly along the grain boundaries, but also inside the matrix, and it can substantially enhance the strength and plasticity of the specimen, although it deteriorates the shape memory properties as well [69]. In addition, the dual phase can exhibit a high thermal stability with no significant changes in the shape memory properties after 500 thermal cycles up to 923 K accompanied by 2.6% strain [151].

In comparison, the addition of a fourth element to the Ni-Mn-Ga system has been much more investigated than ternary alloys with a large amount of Ni. Table 1.2 shows the elements used to alloy Ni-Mn-Ga found in the literature by the author and listed according to the families (columns) of the periodic table.

Table 1.2. The known candidates as the four elements added into Ni-Mn-Ga alloy system.

Family Element	**IIIB**	**IVB**	**VB**	**VIB**	**VIII**	**IB**	**IIB**	**IIIA**	**IVA**	**VA**
1	Y	Ti	V	Cr	Fe	Cu	Zn	B	C	Sb
2	Nd, Sm Gd, Tb (La ~ Lu)	Zr	Nb		Co			Al	Si	
3					Pt			In	Sn	

In the ⅢB column, Y additions to $Ni_{50}Mn_{28}Ga_{22-X}Y_X$ (X = 0, 0.2, 1, 3) promotes grain refinement, increases the MTT (over 370 K when X = 3 at.%), and helps to the formation of a Y-rich second phase at the grain boundaries, improving the compressive strength and ductility of the alloy [152]. Alloying with Gd, a rare earth element, also shifts the MTT to higher temperatures due to the increase in the valence electron concentration (*e*/*a*) value; the strength, and the ductility are also improved as the result of the grain refinement and the formation of a network of a Gd-rich second phase [153]. Moreover, low Gd additions to Ni-Mn-Ga have been reported to show already grain refinement and a high recoverable strain of 7.5%, related to multiple steps of the transformation under external stress [154, 155]. Additionally, 0.2 at.% Gd in thin films has exhibited thermal stability over 100 cycles, and fully recoverable strain under 300 MPa thermomechanical cycles [156]. Nd, Sm, Tb rare earth elements exhibit low solubility in the Ni-Mn-Ga matrix and promote precipitation process located at grain boundaries, together with changes on the MTT according to the modifications on the *e*/*a* value [157]. Finally, Ni-Mn-Ga melt-spun ribbons doped with Tb expands the MT temperature range as the heterogeneous local stress fields resulting from coherent nano-sized precipitates [158].

Concerning doping Ni-Mn-Ga with elements from the ⅤB column of the periodic table, use of V results in a shift of MTT to higher values only for low amounts of V (< 1 at.%), which do not promote the precipitation of γ phase. However, with further addition of the fourth element, the MTT decreases sharply along with the development of the γ phase [61]. On the other hand, alloying with Nb causes a decrease of the MTT first, and then an increase when adding more than 6 at.% of Nb due to the combined effect of the increment of the *e*/*a* and the unit cell volume. However, the material does not show an obvious improvement of the mechanical properties because of the formation of a low ductility hexagonal Nb-rich second phase that cannot accommodate the transformation strain [159].

Cr additions to the ternary alloy (2 - 6 at.%) presents an evolution of the MTT similar to Ni-Mn-Ga-V alloys. Increasing the Cr content, promotes a continuous decrease of the MTT, mainly attributed to the drop of the valence electron concentration and to an increase in the unit cell volume. The γ phase precipitation appears even with 2 at.% of Cr, and it has been associated to an improvement of the ductility of the alloy [62].

Following with the Ⅷ column in the periodic table, introducing Fe into Ni-Mn-Ga by substituting Mn can reduce the MTT from over 970 K to about 620 K with 16 at.% of Fe, and the plasticity can be improved with the assistance of the f.c.c. γ phase [160]. The γ phase can interrupt the propagation of possible cracks in the material, but also hinders the progress of the martensitic transformation and the martensite growth and/or detwinning [161]. Moreover, Fe additions over 4 at.% show good thermomechanical stability and higher recovery strains (up to 4.5%) in comparison to alloys doped with Co, Cu and Ni-rich ternary alloys, despite they also exhibit a decline

of the recoverable strain when increasing Fe content [162]. The nice stability exhibited by Ni-Mn-Ga-Fe alloys, with Fe over 4 at.%, has been attributed to the absence of γ' (an ordered γ phase) precipitates, which are present when using Cu, Co or 4 at.% of Fe as dopants or in Ni-rich ternary alloys [162]. Using melt-spinning aids to refine grains, and promote precipitation of the second phase preferentially at the grain boundaries after further thermal treatments, which results in an improvement of the shape memory properties [163]. With Co substituting Mn, M_p decreases from about 670 K, with 4 at.%, to over 620 K, with 8 at.%, while the recoverable strain also decreases from 2.1% to 0% due to the high volume fraction of γ phase [164]. However, low amount of Co additions (less than 4 at.%) lead to alloys with low thermal stability, especially on the enthalpy change [165]. Adding Ta to Ni-Mn-Ga-Co results in the formation of unfavorable ordered γ' precipitates, which decreases ductility [166]. To the author's knowledge, Pt (5 at.%) has been reported to substitute Ni in a $Ni_{50}Mn_{25}Ga_{25}$ Heusler alloy [167], but it focuses only in the large magnetic field induced strain (MFIS), thus the potential for HTSMA is still unclear.

In the IB column of the periodic table, Cu is, a priori, a good candidate to reduce the brittleness of Ni-Mn-Ga HTSMA polycrystals due to its intrinsic ductility and the low cost of the material. The transition temperature can be tailored as a function of Cu, which is related to the change of valence electron concentration [168]. For instance, a $Ni_{50}Mn_{18}Ga_{25}Cu_7$ alloy presents MTT over 870 K together with a face centered tetragonal structure, and can bear 70% compression strains without cracks [169]. Santamarta *et al*. [58] systematically investigated the thermal stability and microstructure of several Ni-Mn-Ga-Cu alloys with the Cu substituting Mn and/or Ga, reporting that the MTT and the initial hysteresis are proportional to the *e*/*a* ratio. Among the compositions studied, the alloy with the lowest amount of Cu (5 at.%) showed the best stability, whereas the alloys with higher amount of the fourth element show lower thermal stability due to their tendency to form the ordered f.c.c. γ' phase [58]. As a note, this system is promising in the magnetic refrigeration field as it can show a high magnetic entropy change by tuning the ferromagnetic Curie temperature and MTT [59].

Zn atoms (IIB column) prefer to take Ga positions in the stoichiometric $Ni_{50}Mn_{25}Ga_{25}$, which leads to a MTT increment due to the competition between the cell volume effect and the valence electron concentration (*e*/*a*), as it was shown by first-principles calculations [170].

Regarding the elements from the IIIA, IVA and VA columns of the periodic table, adding B decreases the MTT rather linearly but it refines the grain and enhances the critical stress for dislocation slip, and hence the SME is greatly improved with up to 6.8% recoverable strain using 1 at.% of B [171]. Al is considered to elevate the MTT as a consequence of the increase in the *c*/*a* ratio, but the reports found by the authors are mainly focusing on magnetic properties, *e.g.*, the magnetic field induced strain (MFIS), while the shape memory properties have not been fully studied [60,

[172, 173]. In and Si reduce the MTT [174], and C can slightly increase the MTT as well as it promotes the non-modulated martensite [63], while Sn additions decrease the MTT but exhibit promising magneto-caloric effect [79, 175]. Finally, adding Sb to $Ni_{50}Mn_{38}Ga_{12-X}Sb_X$ (X = 0 - 6 at.%) alloys caused a drop of the MTT from over 600 K to over 400 K with increasing Sb amount, but only the magnetic properties of magnetic Heusler alloys, *e.g.*, spin glass, were studied [176].

To conclude this subsection, and concerning the elements of the IVB column of the periodic table, several authors have reported that Ti not only can enhance the shape memory effect, which has been attributed to the presence of Ni_3Ti [177, 178], but also brings about an increase of the MTT caused by an structure instability of the austenite due to the energy difference when Ga sites are occupied by Ti [179]. The amount and size of Ni_3Ti precipitates can be altered by thermal ageing, which promotes a decrease of the MTT but enhances the strength of the matrix [180, 181]. In the same column of the periodic table, there are investigations about using Zr (4, 8 at.%) to replace the Cu in Ni-Mn-Ga-Cu alloys, reporting the formation of the γ phase with a lattice parameter of a = 0.6902 nm [182]. The hysteresis is reduced by introducing the γ phase [183], but further precipitation induced by additional ageing alters the matrix composition and hence the martensitic transformation temperature [184]. However, the shape memory response of the Ni-Mn-Ga-Zr system has not been studied yet, nor the mechanical properties. To authors' knowledge, no studies have been reported on the addition of Hf either, despite this element is in the same column as Ti and Zr. Therefore, an important part of this work will deal with the effect of Hf and Zr additions to Ni-Mn-Ga polycrystalline alloys.

Chapter Ⅱ EXPERIMENTAL METHODS

2.1 Materials Manufacture and Preparation

$Ni_{50.3}Ti_{29.7}Zr_{20}$, $Ni_{50.3}Ti_{24.7}Zr_{25}$ and $Ni_{50.9}Ti_{24.1}Zr_{25}$ alloys (compositions in at.%) were induction melted under argon atmosphere using high purity elemental materials (Ni 99.98 wt.%, Ti 99.95 wt.%, Hf 99.9 wt.%, Zr 99.9 wt.%) in a graphite crucible, and cast into a copper mold. The ingots were homogenized at 1320 K for 72 h, and then sealed in mild steel cans followed by hot extrusion at 1170 K with an area reduction ratio of 7:1. These alloys were initially manufactured in the *Materials and Structures Division* from the NASA Glenn Research Center, in Cleveland (Ohio, USA), and the resulting ingots are denoted as "*as-extruded*" in the present work. Subsequently, the ingots were cut in smaller pieces using a low-speed diamond saw and/or a spark erosion machine. These pieces were encapsulated in quartz tubes under partial Ar atmosphere for further thermal treatments in the facilities of the Materials Physics group at UIB.

Several Ni-Mn-Ga and Ni-Mn-Ga-Cu (with only 1 at.% Cu) high temperature shape memory alloys were induction melted under Ar atmosphere using high purity elements at Adaptamat Ltd, in Finland. The ingots were homogenized at 1295 K for 96 h, and slow cooled to the ambient temperature inside the furnace to produce very homogeneous "as-treated" specimens. Then, the ingots were cut into smaller specimens using a low-speed diamond saw, and subsequently encapsulated in quartz tubes under partial Ar atmosphere for further thermal treatments in the facilities of the Materials Physics group at UIB. The details of the latter thermal treatments will be provided in Chapter 4.

Other ternary Ni-Mn-Ga and quaternary Ni-Mn-Ga-X (X = Sn, Hf, Zr) high temperature shape memory alloys were prepared at the UIB facilities using high purity elemental materials (Ni 99.99+ wt.%, Mn 99.99 wt.%, Ga 99.9999 wt.%, Sn 99.99 wt.%, Hf 99.7 wt.%, Zr 99.95 wt.%). Ternary Ni-Mn-Ga alloys were cast by induction melting under argon atmosphere by placing Ni at the bottom, Ga at the middle, and Mn at the top of the graphite crucible, which is previously sprayed with boron nitride (high temperature dry lubricant and release agent). From an empirical point of view, pure Ni bars, as the majority component of the alloy, are the induction heat source, and then Ga is firstly melted to cover the Ni forming the compact Ni-Ga pool in the bottom. Finally, the small Mn pieces covering the surface of the hot liquid are gradually melting into it. Mn pieces can also react with the remaining oxygen, leaving oxides on the surface instead of inside the liquid. On its turn, Ni-Mn-Ga-Sn alloys were prepared by induction melting using a pre-alloyed $Ni_{51.2}Mn_{31.1}Ga_{17.7}$ ingot fabricated at Adaptamat Ltd. with additional pure Ni, and Sn pieces to get the desired

compositions. Finally, Ni-Mn-Ga-Hf/Zr alloys were initially produced from raw materials by induction melting using high purity elemental materials. After several trials, it was proved that the induction furnace from the UIB cannot produce a proper ingot, since Hf and Zr react easily with oxygen and form oxides layers, which block the wetting, melting, and flowing process. Hence, two separated melting steps were finally used to fabricate homogeneous ingots: first the Ni-Mn-Ga ternary alloy was produced by induction melting; then, pure Hf/Zr pieces were added to the Ni-Mn-Ga ingot and subsequently arc melted with the ternary alloy five times, manually removing the surface oxides layer each time. The final button-shaped ingots were cut into long bars using a low-speed diamond saw and/or a wire EDM machine (ARTA 123 PRO). To end with, the pieces were encapsulated in quartz tubes under partial Ar atmosphere for further thermal treatments. Additional information on these thermal treatments will be provided in Chapters 5 and 6.

Different experimental techniques were used along this thesis to investigate all the alloys, so further information about them is presented in the following subsections.

2.2 Differential Scanning Calorimetry

The transformation temperatures are key parameters for the SMAs characterization, especially when they need to be used on practical applications. Usually, the differential scanning calorimetry (DSC) technique is the primary choice for determining the stress-free transformation temperatures. Fig. 2.2.1 (a) shows the heat flow registered by the calorimeter as a function of temperature, indicating the start, peak, and finish temperatures of the forward transformation (M_s, M_p, M_f, respectively) and the start, peak and finish temperatures of the reverse transformation (A_s, A_p, A_f, respectively). Among the possible options to determine the transformation temperatures, the tangent method was used along this Ph.D. thesis to determine M_s, M_f, A_s, and A_f. The tangent method consists in finding the temperature at which two tangents intersect, one from the baseline near the peak (normally rather horizontal), and the other from the maximum tangent from the peak (often located near half-height of the peak), as shown in Fig. 2.2.1 (a). On its turn, M_p and A_p are calculated simply as the maximum of the peaks. It has to be noted that some slight differences in the transformation temperatures can be obtained when changing the temperature range to draw the slopes from the baseline, so the transformation start and finish temperatures reported here are assumed to contain an error bar around ±2 K.

As it has been explained in Chapter 1, the forward martensitic transformation is an exothermic process, while the reverse martensitic transformation is endothermic. DSC thermograms allow to calculate the heat exchange (enthalpy change) of the martensitic transformation by integrating the peak over the baseline. Analogously to the transformation temperatures determination, this calculation can be slightly influenced by the temperature range chosen for the integration. The heat absorbed,

or released, during any first order phase transformation can be calculated simply by integrating the transformation peaks measured by DSC with respect to time, as written in Eq. 2.2.1. In this equation, $\left(\frac{dQ}{dT}\cdot\frac{dT}{dt}\right)$ is the heat flow signal (the **Y**-axis in the thermogram), and $\frac{dT}{dt}$ is the cooling heating rate of the experiment in the DSC (normally a constant), Moreover, the stress-free phase transformation occurs at constant pressure, so the work is $W = P\,\Delta V$ and the heat released/absorbed in the process is equal to the enthalpy change of the transformation, as shown in Eq 2.2.2.

$$Q = \int\left(\frac{dQ}{dT}\cdot\frac{dT}{dt}\right)dt \quad \text{(Eq. 2.2.1)}$$

$$Q = \Delta U - W = (U_2 + PV_2) - (U_1 + PV_1) = H_2 - H_1 = \Delta H \quad \text{(Eq. 2.2.2)}$$

Most of the DSC experiments were conducted on a DSC823e from Mettler-Toledo (Fig. 2.2.1 (b)), using a constant heating/cooling rate of 10 K/min for all the experiments in this thesis. The cycles started at high temperature, far from A_f, to ensure that a full transformation could be registered. Normally, each specimen was thermally cycled twice to check the stability of the alloy, which was calculated as the difference of the peak temperatures (ΔM_p) between cycles. More thermal cycles were applied when the specimens exhibited low thermal stability. In addition, stress-free thermal cycling experiments (up to 20 cycles) were conducted on a DSC3+ from Metter-Toledo (Fig. 2.2.1 (c)) located at the *Serveis Cientificotècnics* (SCT) center of UIB at constant heating/cooling rate of 10 K/min. The hysteresis is normally determined as the difference between A_f and M_s in the first cycle (A_f-M_s), but A_f and M_s can heavily change if the transformation becomes diffused or separated due to the existence of defects or other factors. Therefore, in the present work, the hysteresis from DSC was calculated as the differences between the peak temperatures (A_p-M_p), which is also coherent with the criteria used to track the thermal stability when cycling.

The samples for DSC analysis, were cut into ~2 mm thickness pieces from the cast bars after the corresponding thermal treatment. Then, they were mechanically polished using grinding SiC paper up to P4000 (particles of around 5 microns), purged and cooled with water, and then cleaned with acetone. The shape and weight were adjusted for the DSC technique, *i.e.*, small enough to fit the standard Al-crucibles and around 60 - 160 mg in weight to get a significant signal in the DSC. The tested sample and reference were put into the measurement cell for thermal tests (Fig. 2.2.1 (d)).

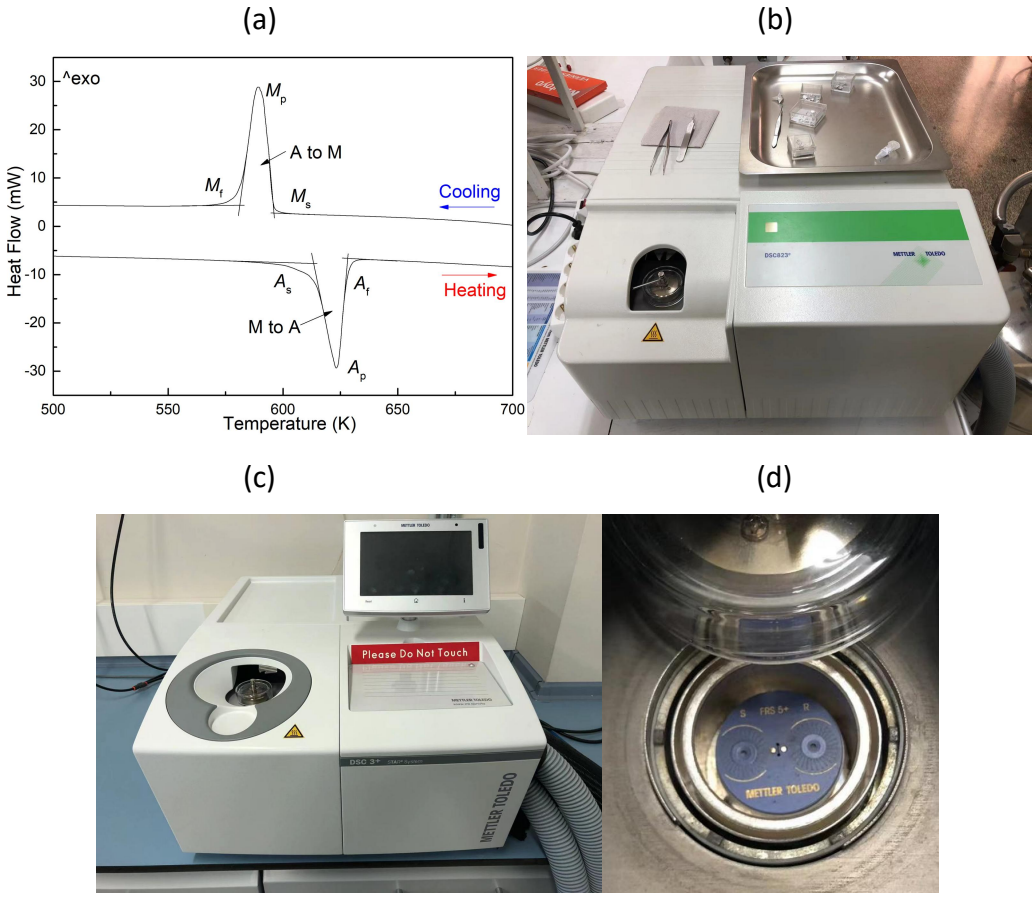

Fig. 2.2.1. (a) Schematic plot of the heat flow versus temperature measured by DSC during a forward and reverse martensitic transformation, indicating the method to determine the transformation temperatures, (b) DSC823e equipment used in this thesis, (c) DSC3+ equipment used for thermal cycling, and (d) measurement cell for sample and reference of DSC823e equipment.

2.3 Microstructure Characterization

2.3.1 X-ray Diffraction Phase Structure Analysis

The specimens for X-Ray Diffraction (XRD) were mechanically grinded with P4000 abrasive SiC paper. A Bruker-AXS D8 X-ray diffractometer in a θ-θ configuration (Fig. 2.3.1) operated with Cu-Kα radiation (λ = 1.5406 Å) was used for the structural identification of the crystalline phases. An additional heating-cooling chamber (nominal temperature 73 K - 724 K), not shown in Fig. 2.3.1, was used for *in-situ* XRD analysis under N_2 atmosphere in order to track the phase transformation as a function of temperature. As the holder is made of stainless steel, it can generate extra peaks in the diffractograms. Therefore, to avoid the influence of these peaks in the diffractograms, two approaches were used depending on the positions of the sample peaks: *i)* manually delete the peaks from the holder when there is no coincidence with sample peaks; *ii)* cover the holder with SiO_2 amorphous particles, to

prevent diffraction from the holder.

The lattice parameters of the crystalline structures studied in this work by XRD were calculated using multiple steps, including manual calculation, the JADE software for Rietveld refinement, and the "CrystalMaker" simulation software. More details about this procedure are presented by means of a practical example used in this Ph.D. thesis to calculate the lattice parameters of several Ni-Mn-Ga-X alloys with non modulated b.c.t martensite. Once the diffractograms are obtained, the most intense peaks are identified and indexed as the $(202)_{b.c.t.}$ and $(220)_{b.c.t.}$ planes. A first estimation of d_{202} and d_{220} interplanar distances is then calculated using JADE software with the Cu-Kα wavelength and the Bragg's Law (Eq. 2.3.1). Afterwards, using Eq. 2.3.2 with the Miller indexes and the experimental interplanar distances of those peaks from the b.c.t. martensitic structure, a first approximation of the lattice parameters is manually calculated. Then, these raw lattice parameters are introduced into the JADE software to run a very basic Rietveld refinement using the complete diffractogram and generating the refined lattice parameters. Finally, the final lattice parameters and the corresponding diffracted peaks are double-checked with the "CrystalMaker" software to simulate the XRD pattern and visualize the crystalline structure of the unit cell.

$$2d\sin\theta = n\lambda \quad \text{(Eq. 2.3.1)}$$

$$\frac{1}{d_{hkl}^{\,2}} = \frac{h^2+k^2}{a^2} + \frac{l^2}{c^2} \quad \text{(Eq. 2.3.2)}$$

Fig. 2.3.1. The Bruker-AXS D8 X-ray diffractometer used in the present work.

2.3.2 Optical Microscopy, Scanning Electron Microscopy and EDX Composition Analysis

In order to observe the microstructure of the studied alloys, Optical Microscopy (OM)

and Scanning Electron Microscopy (SEM) were used. The specimens used for these techniques were first cut and well mechanical grinded up to 1 µm, and then etched using a solution of 30 vol.% nitric acid in methanol for several minutes. The etched specimens were observed through the Olympus B061 metallographic optical microscope (Fig. 2.3.2 (a)) to obtain a generic view of the microstructure, especially when the grains and precipitates are large and have some heterogeneous distribution. Normally, after the optical microscope observations, the scanning electron microscope Hitachi S-3400N (Fig. 2.3.2 (b)) was used for observations at larger magnifications and to characterize smaller precipitates or martensitic plates, using either secondary electrons (SE) or back-scattered electrons (BSE) detectors. The latter mode of operation of the SEM is very useful to easily identify the precipitates from the matrix, as it shows a different contrast as a function of the Z number of the elements present in the sample.

A Bruker-AXS XFlash Detector 4010 energy dispersive X-ray spectroscope (EDX) installed in the Hitachi S-3400N was used to analyze the composition of the matrix and the embedded precipitates. An example of the spectra obtained with this technique in a Ni-Mn-Ga-Zr alloy is shown in Fig. 2.3.2 (c). It should be noted that the intensity of the background could inevitably affect the final quantitative results, especially when the content of the element is extremely small (*e.g.*, Zr peak in Fig. 2.3.2 (c)). In those cases, the applied voltage was properly increased to harvest more information. Normally, for each specimen, two areas were chosen for EDX quantitative measurements, and three points of the matrix, three points of the precipitates and a generic spectrum of the whole area were registered in order to get an average composition.

(a) (b)

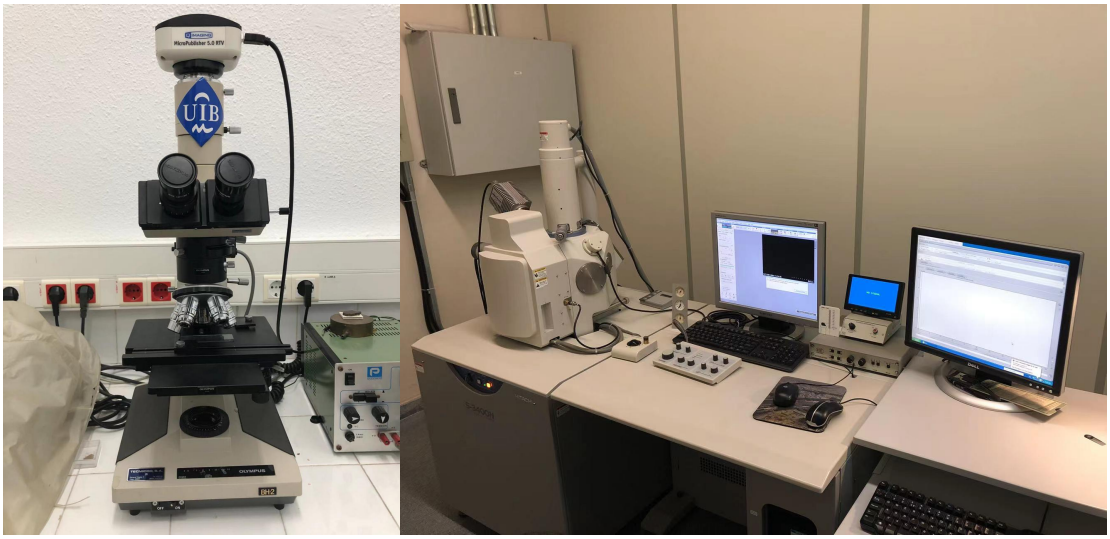

(c)

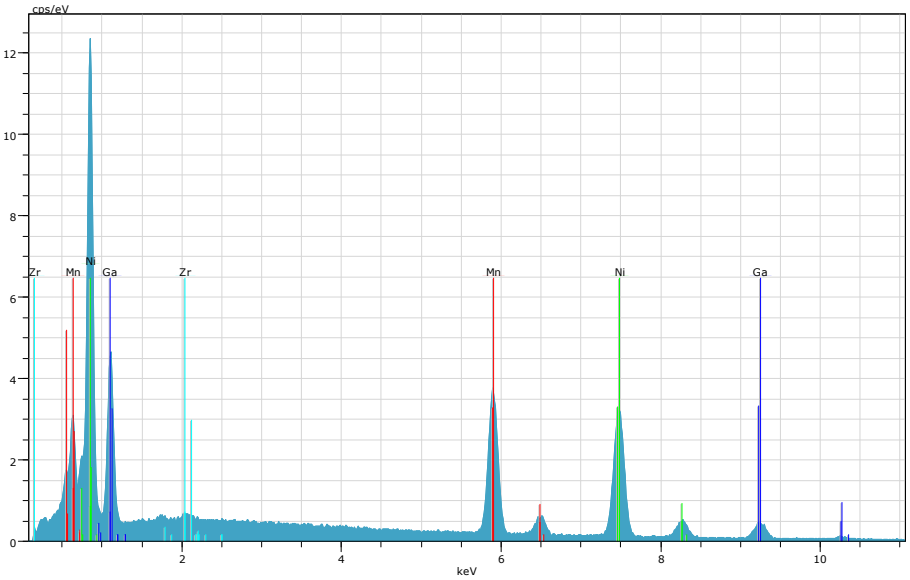

Fig. 2.3.2. (a) Optical and (b) scanning electron microscopes used in this Ph.D. thesis; (c) energy dispersive X-ray (EDX) spectrum from the matrix of a $Ni_{53.0}Mn_{29.6}Ga_{16.9}Zr_{0.5}$ alloy after a solution heat treatment at 1270 K for 48 h.

2.3.3 Transmission Electron Microscopy Observation

Transmission electron microscopy (TEM) observations were conducted on a Hitachi H600 conventional microscope (Fig. 2.3.3) operating at 100 kV, normally using a double-tilt holder. Additionally, an *in-situ* cooling holder with liquid nitrogen was used for some observations on Ni-Ti-Zr specimens. Conventional bright field and dark field images, together with selected area diffraction patterns (SADP) were used to characterize the microstructure of the studied alloys. Two-beam condition for some bright field images were obtained in order to better observe the defects in the matrix such as dislocations, small precipitates or stress fields.

As for the specimens, discs of 3 mm in diameter and thickness below ~100 µm are required to fit the TEM holder. First, the specimens were cut into small plates and polished with P1200 abrasive paper until the thickness is around ~500 µm. Then, the thin plates were mechanically cut into several small discs with 3 mm diameter using a MODEL 360 abrasive slurry disc cutter by South Bay Technology. Thereafter, the discs were mechanically grinded with P1200 and P4000 abrasive paper up to the final thickness (~100 µm). Finally, the discs were double jet electro-polished (Struers Tenupol 5 device) with a solution of 30 vol.% nitric acid in methanol at ~255 K and ~100 mA to generate a perfect hole in the center with edges transparent for the electron beam.

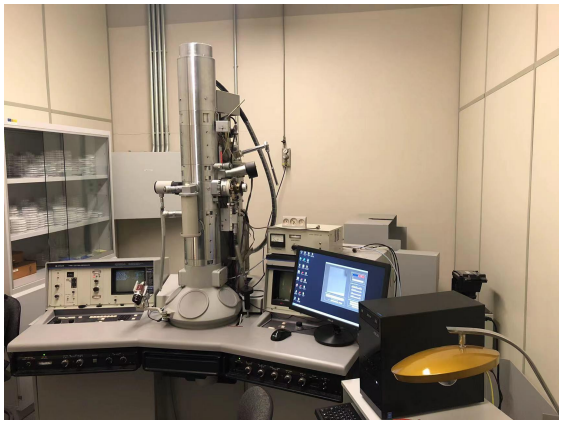

Fig. 2.3.3. Transmission electron microscopy used in this Ph.D. thesis.

2.4 Thermomechanical Shape Memory Properties Characterization

2.4.1 Dynamic mechanical Analysis

Dynamic mechanical analysis (DMA) is a technique in which a time dependent harmonic stress is applied to the sample and the corresponding oscillating strain is measured. In not perfectly elastic materials, a delay (phase shift, δ) between the applied sinusoidal stress and the corresponding strain induced in the samples is obtained due to the viscosity of the specimen. Then, a complex modulus, which represents the response of the material to the applied stress, is normally defined as $G = \sigma / \varepsilon = G' + iG''$. The real component of the modulus, $G' = E = \cos\delta \cdot \sigma / \varepsilon$, is the part that remains in phase (elastic part) and it is generally known as *storage modulus*, while the imaginary part, $G'' = \sin\delta \cdot \sigma / \varepsilon$, is known as *loss modulus* and corresponds to the out-of-phase component (viscous part). One of the key parameters measured with the DMA is the internal friction (*IF*) or damping of the material, defined as the tangent of the phase shift, δ , between the stress and strain sinusoidals, $\tan\delta = G''/G'$. It can also be expressed as $\tan\delta = \Delta W/(2\pi W) = Q^{-1}$, where ΔW is the energy dissipated during the deformation cycle and W is the amplitude value of the elastic energy (stored energy) [185].

In the present work, a DMA Q800 TA instrument (Fig. 2.4.1 (a)) in the single cantilever mode (Fig. 2.4.1 (b)) was used to measure the storage modulus and internal friction of the samples as a function of temperature and frequency to characterize the strain glass state of the alloys in Chapter 3. In the single cantilever mode, one end of the sample is attached with a screw bolt and remains totally fixed, whereas the other end can move up and down upon the external force applied by the device along the vertical direction (Fig. 2.4.1 (b)). All the components are located in a closed chamber that can be heated with an internal furnace and cooled using liquid nitrogen.

The DMA technique is normally designed for materials with low elastic modulus, as polymers, so the measured alloys, with higher stiffness, can be hard to deform by the oscillating force, which is limited to 18 N in our device. Thus, it is important to reduce the thickness of our alloys (below 0.9 mm) to improve the accuracy of the measurements. For that reason, the samples were first mechanically grinded and reduced in thickness to form a long and thin rectangle plate. Then, a fixed strain amplitude was settled to 0.05% of the maximum calculated deformation, a value which is not too high to deform the sample and not too small to be detected by the machine. The frequency of the oscillating stress was set to 0.2, 0.4, 1, 5, 10, 15, and 20 Hz for the different experiments. The temperature range from each experiment was from 373 K to 173 K, with a temperature rate of 2 K/min, although, due to the limited cooling capacity, the lowest temperature sometimes could not be reached at that temperature rate. Finally, it is worthy to note that the storage modulus and internal friction raw data present some oscillations in their temperature dependence, probably due to fluctuations in the controller of instrument, so the plots have been smoothed in temperature ranges of 20 K.

(a)

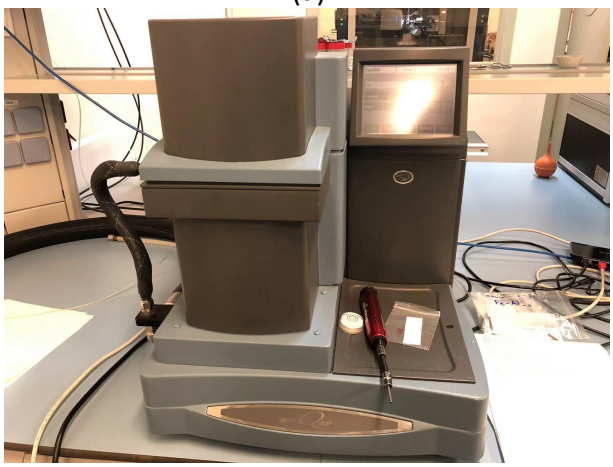

(b)

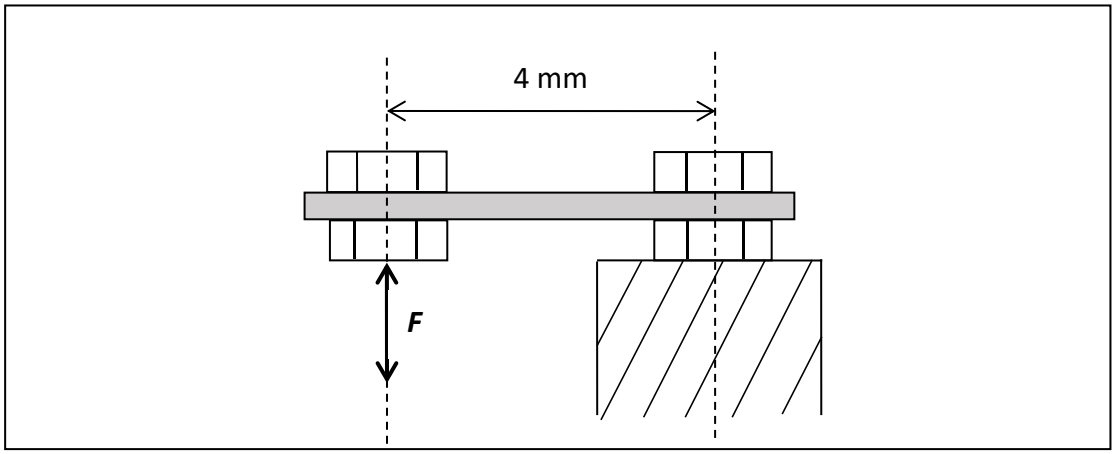

Fig. 2.4.1. (a) Image of the DMA Q800 equipment used in this Ph.D. thesis and (b) schematic diagram of the single cantilever test mode of the DMA.

2.4.2 Load-biased Compression thermomechanical Experiments

Thermomechanical tests in compression, consisting of cooling/heating cycles under a constant load, were conducted on a Zwick Z100 mechanical testing machine (Fig. 2.4.2 (a)). A home-made chamber to modify the temperature was installed in the machine, and a high temperature axial extensometer (MTS 632.53) was attached to the compression heads for a more accurate measurement of the transformation strain (Fig. 2.4.2 (b)). A schematic diagram of the setup is shown in Fig. 2.4.2 (c). The compression heads are made of Inconel superalloy to keep a high strength and hardness at high temperatures. Each compression head is entangled by an electric heater and a copper tube coil for cooling and contains a K-type thermocouple installed close to the compression surface. Nitrogen gas flows into the copper tube coil for normal cooling above room temperature or liquid nitrogen for experiments below room temperature. The temperature of each compression head is controlled independently by a Eurotherm CustPart 3216#56610 temperature controller, running the same program simultaneously in both controllers to ensure a nearly equal temperature in both heads (temperature difference lower than 1 K) and, therefore, in the sample. The whole chamber is covered by calcium-magnesium silicate sheet (fabricated by Superwool 607 HT long fibers) for thermal isolation. The temperature chamber allows for cooling/heating experiments in the range 220 K - 800 K with a maximum controlled rate of ±5 K/min, while the constant external stress on the sample is applied by the Zwick Z100 machine.

All the thermomechanical tests started with the sample in austenite state, above A_f. The specimens were installed in the chamber and kept at least 20 minutes before each test to reach a homogeneous temperature. A minor stress (~5 N) was applied to the sample during this process to monitor thermal expansion. The nominal external stress in compression was applied by the Zwick machine at a strain rate ~5×10^{-4} s^{-1} and kept constant during the whole thermal cycling, cooling below M_f and heating back to the initial temperature at 5 K/min. Each specimen was cycled under different stress levels of 20, 60, 100, 200 and 300 MPa.

The strain and temperature data from the extensometer and thermocouples, respectively, were recorded by a PC computer with a Labview data acquisition program. Fig. 1.1.7 shows a schematic diagram of the results obtained in a cooling-heating load-biased thermomechanical cycle in compression. The distance between the two arms of the extensometer is 12 mm (in the zero strain position). Then, the specimens for these experiments were cut with a length of ~11 mm, in order to attach the extensometer arms on the compression heads at positions very close to the edges. In this way, the effect of thermal dilatation of the heads on the ε vs. T curves is minimized and the initial and final slopes of the curves (above and

below the martensitic transformation) mostly correspond to the thermal expansion of the sample. Furthermore, the top and bottom surfaces of the prismatic sample, in contact with the compression heads, were cut as parallel between them and perpendicular to the long side as possible to obtain the best parallelism with the compression heads and avoid inhomogeneous biased stress on the specimen.

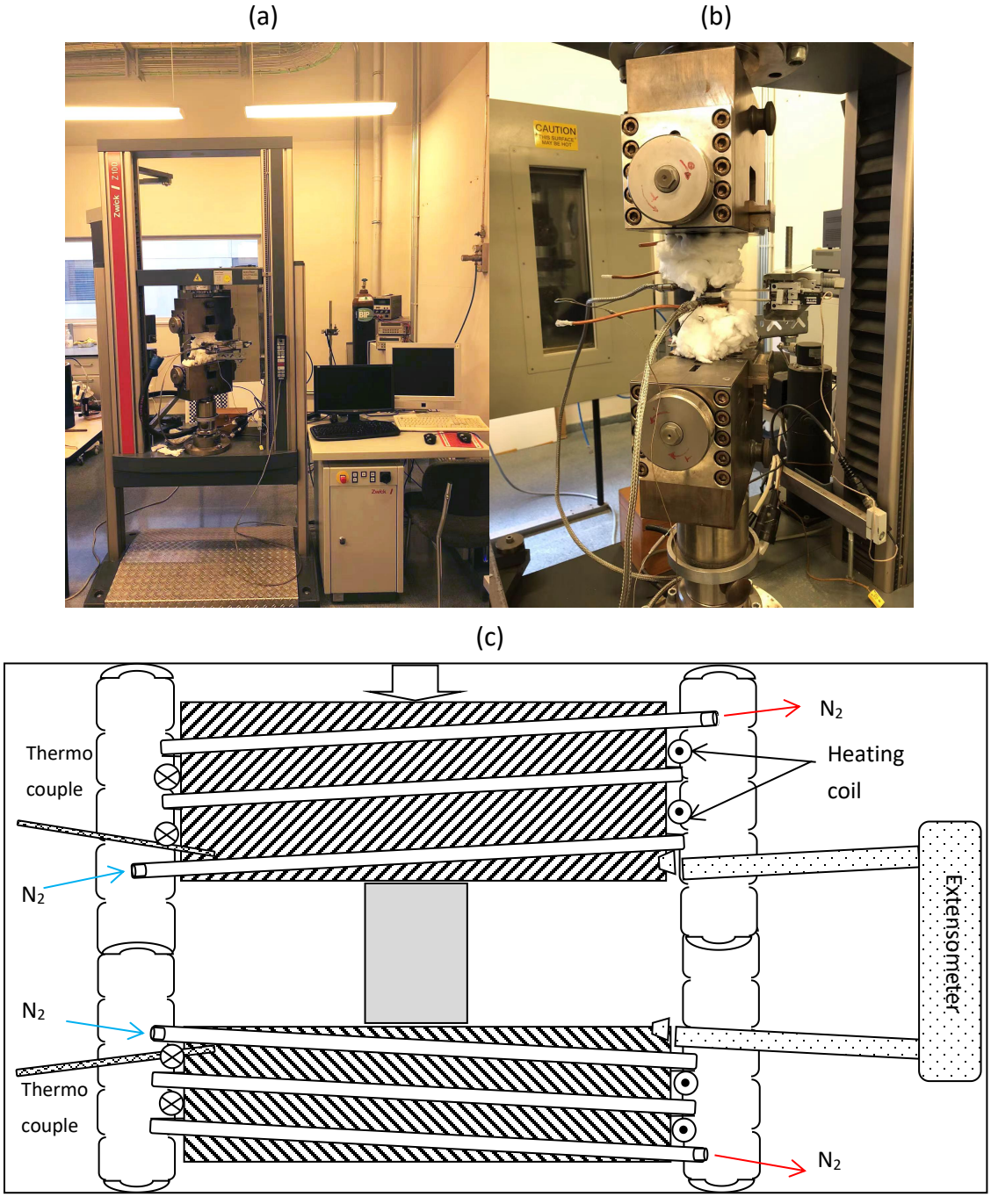

Fig. 2.4.2. (a) Photograph of the main part of the Zwick Z100 testing machine, (b) the hand-made heating/cooling test chamber in the center, and (c) schematic diagram of the heating/cooling chamber used for the thermomechanical and isothermal compression mechanical tests.

2.4.3 Isothermal Compression Mechanical Experiments

Isothermal compression mechanical tests were obtained to characterize the superelasticity effect of the studied alloys with the same testing machine and heating/cooling chamber used for the thermomechanical tests (Fig. 2.4.2). The specimens were first heated up far away from Af followed by slow cooling down to the target temperature (for instance, Af + 10 K, kept constant during the whole experiment) to ensure the austenite state of the sample. Then, the loading/unloading experiment in compression was applied on the specimen under a strain rate of about ~5×10^{-4} s^{-1} until the maximum targeted strain. Before removing the sample, a thermomechanical heating/cooling cycle up to Af + 100 K and down back to the target temperature using a quite low constant stress (3 MPa) was applied to register eventual strain recovery due to residual stabilized martensite. Finally, the specimens were removed and cooled down to room temperature for dimension measurement, and then put back in the heating chamber for the next mechanical test. For each sample, several cycles were tested, gradually increasing the target strain to induce more transformation strain until a large irrecoverable strain was measured. Moreover, the whole procedure was performed at different temperatures for each specimen, such as Af + 10 K, Af + 30 K, Af + 50 K ...

Chapter Ⅲ Ni-RICH Ni-Ti-Zr

It has been widely discussed in the introduction chapter that the Ni-Ti-Zr alloy system has been thoroughly investigated for the good shape memory properties. Especially for the Ni-rich Ni-Ti-Zr/Hf alloy system, the H-phase precipitates can be induced after ageing, and can not only elevate the MTTS but also improve the shape memory properties. A wide range of Hf content alloys has been thoroughly investigated from 15 at.% up to 25 at.%, which demonstrate excellent SME after proper thermal treatment [123, 129, 133]. However, to the author's knowledge, Zr has only been studied with the content up to 20 at.% [57, 121, 140]. Therefore, the Zr 25 at.% alloys are used for this study of shape memory properties and related micro-structure.

3.1 Results of Analysis and Observation of $Ni_{50.3}Ti_{24.7}Zr_{25}$

3.1.1 Calorimetric Analysis

Table 3.1 lists the composition and related thermal treatment of the studied alloy. The original as-extruded specimens were subjected to solution heat treatment followed by ageing treatments for different times and temperatures. It is well know that for Ni-rich Ni-Ti-Zr alloys the ageing treatment can produce H-phase precipitates, and the parameters of ageing have great influence on the SME properties and microstructure. Therefore, three ageing temperatures (720 K, 770 K, 820 K) and different ageing times (1 h, 2 h, 3 h or 6 h, 12 h), together with an extra furnace cooling method are chosen for this study based on the former work [57]. The furnace cooling process is designed to induce equilibrium phases with fully developed H-phase precipitates as a control group. The SHT specimen (encapsulated in quartz) is put inside of the furnace and heated up from room temperature to 970 K within 90 minutes, and then slow cooled from 970 K to 370 K in 48 h, followed by water quenching to room temperature.

Table 3.1. Nominal composition of the studied alloy and the corresponding thermal treatments.

Nominal Composition	Thermal Treatment		
	Step one	Step two	Step three
$Ni_{50.3}Ti_{24.7}Zr_{25}$	Hot extrusion	SHT 1270 K 1 h	Ageing at 720/770/820 K X h or furnace cooling

The DSC results of $Ni_{50.3}Ti_{24.7}Zr_{25}$ for different treatments are presented in Fig. 3.1.1, where every sample was subjected to two consecutive cooling/heating cycles. It is obvious that the ageing treatments tend to elevate the transformation temperatures, except for 1 h at 720 K in Fig. 3.1.1 (a), which is already known that is associated with the precipitation of H phase and corresponding composition variation of matrix [122]. Additionally, the higher the ageing temperature is, the more the MTT grow, as shown in Fig. 3.1.1 (e), *e.g.*, the M_p increases from 371 K for the SHT state to 442 K and 484 K after ageing at 770 K and 820 K for 3 h, respectively. And similarly, the M_p grows with ageing time but only for ageing at 720 K and 770 K, *e.g.*, M_p of specimens aged at 770 K for 1 h, 2 h and 3 h are 423 K, 441 K and 442 K, respectively. As for the samples aged at 820 K, the promotion of temperature by ageing seems to be saturated, as the MTT after ageing for 2 h and 3 h are slightly lower than after 1 h ageing. It should be noted that all the temperatures plotted in Fig. 3.1.1 (e) are extracted from the first DSC cycle except one from 820 K ageing marked by an arrow, which is from the second cycle due to incomplete first DSC cycle.

Moreover, it is clear that the ageing temperature has big influence on the transformation behavior, *i.e.* for ageing at 720 K the reverse transformations show broad and low height peaks, and the peaks become sharper when elevating the ageing temperature. It is known that ageing at lower temperature and less time can induce low degree of unstable precipitation, and conversely high ageing temperature and time can generate well developed and coarsened precipitates. Only the proper size of precipitates can provide strengthening effect to the matrix and further improve the thermal stability of the samples [122]. However, with the ageing at 820 K, the specimen still demonstrates not stable behaviour when transforming at high temperature, above 550 K, as seen from Fig. 3.1.1 (c). Additionally, it should be noted that the first cycle of the specimen aged at 820 K for 1 h shows an incomplete reverse transformation, because the programmed upper temperature of the heating run resulted to be lower than A_f, which led to a low enthalpy change of the subsequent direct transformation.

Furthermore, a wide first direct transformation with double peak appear in the samples aged at 770 K in Fig. 3.1.1 (b), but the effect disappears in the second cycle. Therefore, this cannot be considered as a multi-stage transformation, but to the effect of quenched-in defects combined with the internal stress induced by precipitates that is eliminated after the reverse transformation [117]. Fig. 3.1.1 (d) shows no sign of martensitic transformation for the furnace cooled specimen at the selected temperature range which is ascribed to the coarsening of precipitates, as will be presented in the next section.

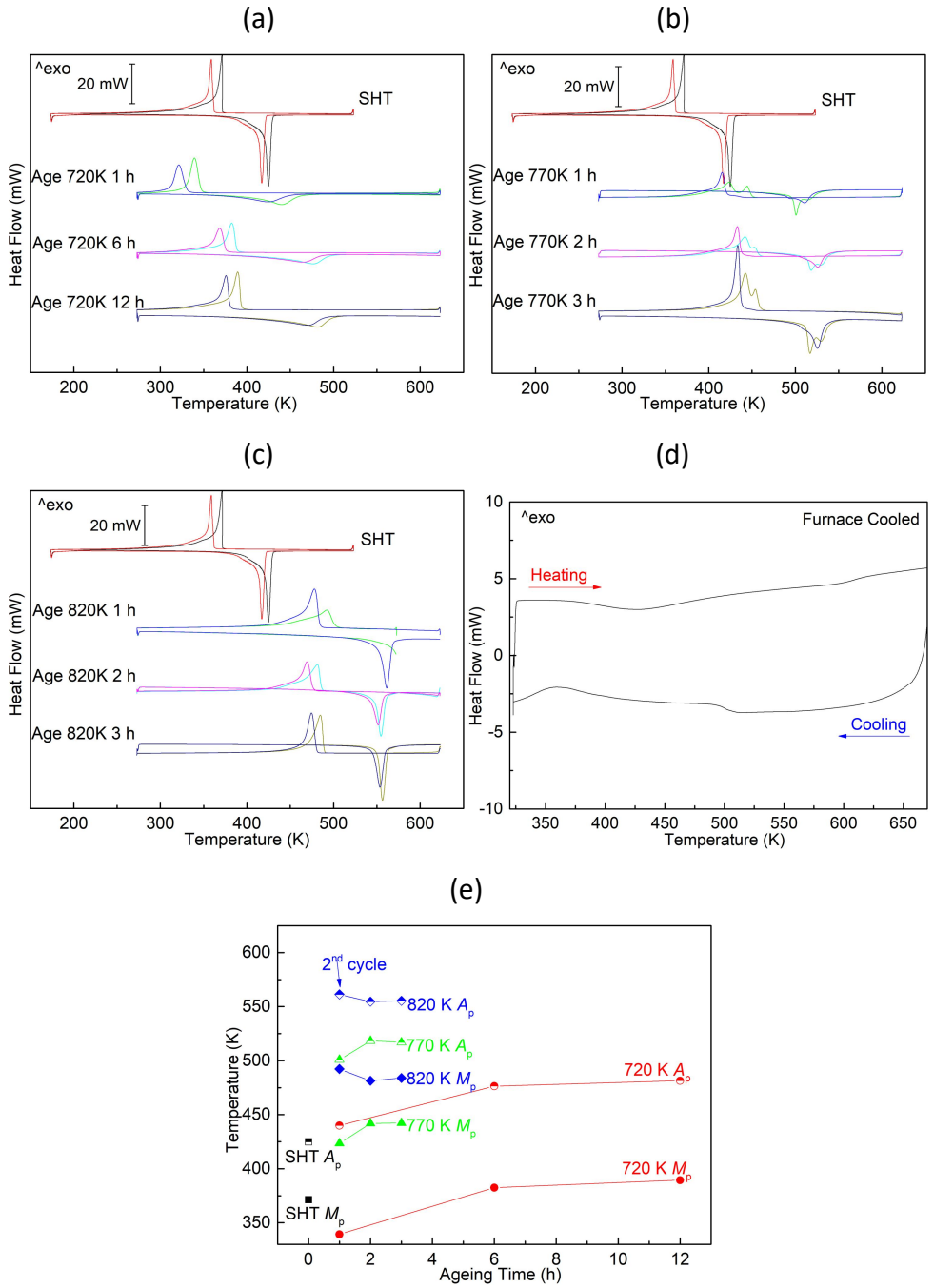

Fig. 3.1.1. DSC analysis of $Ni_{50.3}Ti_{24.7}Zr_{25}$ alloy solution heat treated at 1270 K for 1 h with additional ageing at (a) 720 K, (b) 770 K, (c) 820 K and (d) furnace cooling treatment; (e) plot of the MTTs tendency as a function of ageing time and temperature.

3.1.2 Phases and Microstructure

To further understand the thermal response of the $Ni_{50.3}Ti_{24.7}Zr_{25}$ alloys, the microstructure of the solution heat treated and aged specimens was studied by TEM, XRD at room temperature, at which, according to the DSC results, the specimens are in the martensitic state.

Fig. 3.1.2 presents the TEM results of $Ni_{50.3}Ti_{24.7}Zr_{25}$ in the SHT state, where bright field images of the matrix are shown in Figs. 3.1.2 (a), (c) and the corresponding diffraction patterns in Figs. 3.1.2 (b), (d) with $[11\text{-}1]_{B19'}$ and $[101]_{B19'}$ zone axes, respectively. It confirms that for the solution heat treated $Ni_{50.3}Ti_{24.7}Zr_{25}$ specimen the martensite plates possess the B19' structure at RT. The B19' martensite has a monoclinic structure that belongs to the $P2_1/m$ space group [7]. In addition, the SADPs in Fig. 3.1.2 present diffuse scattering between the fundamental spots of martensite, which is related to the black nano-sized particles embedded in martensite plates, visible in the TEM BF images. The XRD spectrum of Fig. 3.1.2 (e) shows the major peaks from B19' martensite and a small extra peak at $2\theta \approx 40°$ consistent with the 004 reflection of the H phase (practically coincident with the 110_{B2}). Then, the TEM and XRD results indicate that the H-phase precipitation already starts after the solution heat treatment. As the H phase is rich in Zr, the large content of this element in the present alloy enhances the stability of the H phase, compared to the previous studies performed in alloys with 15 at.% and 20 at.% Zr [121, 140, 141].

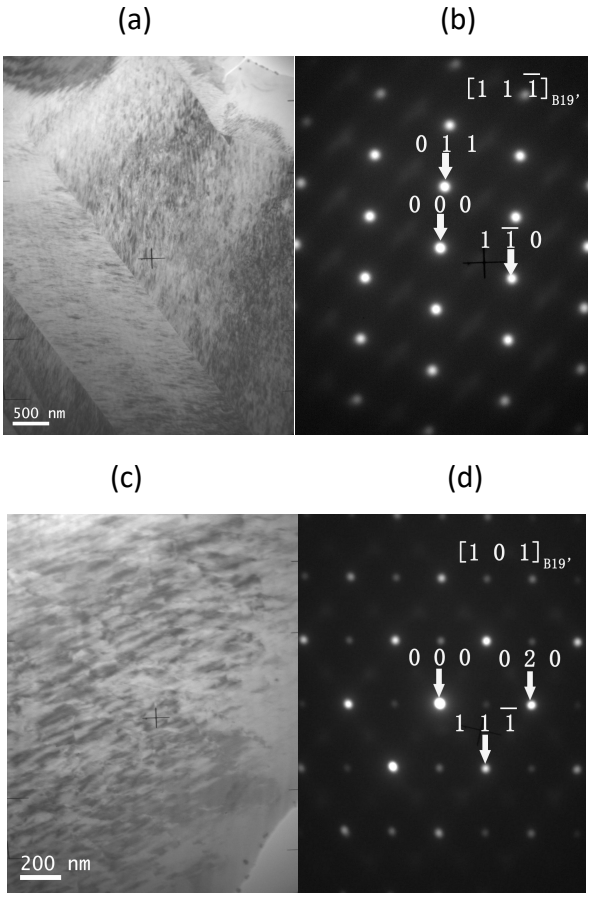

(e)

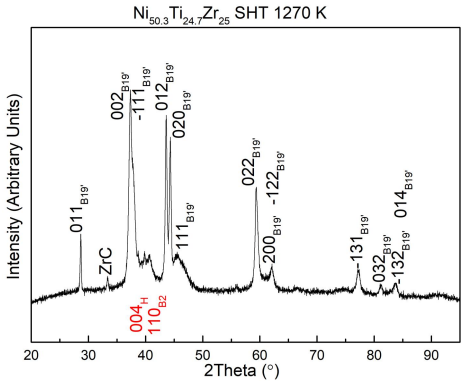

Fig. 3.1.2. TEM and XRD observation of $Ni_{50.3}Ti_{24.7}Zr_{25}$ SHT 1270 K 1 h: (a) bright field image (BF), (b) corresponding selected area diffraction pattern (SADP) of matrix under $[11\text{-}1]_{B19'}$ zone axis; (c) BF image of another area, (d) corresponding SADP of matrix under $[101]_{B19'}$ zone axis; (e) X-ray diffraction pattern (XRD).

Fig. 3.1.3 (a) shows a big particle of ZrC with about 5 µm in length and 2 µm in width, which is a common inclusion for the studied alloys. Those carbides, also observed by A. Evirgen *et al*. [123], were introduced during induction melting, where carbon diffuses from the graphite crucible. Figs. 3.1.3 (b) and (c) show other selected zone of the SHT specimen, with big martensite variants around 100 - 1000 nm in thickness. Some dislocations can be observed in (c) under the two-beam condition, which were generated during the previous DSC thermal cycles.

(a) (b) (c)

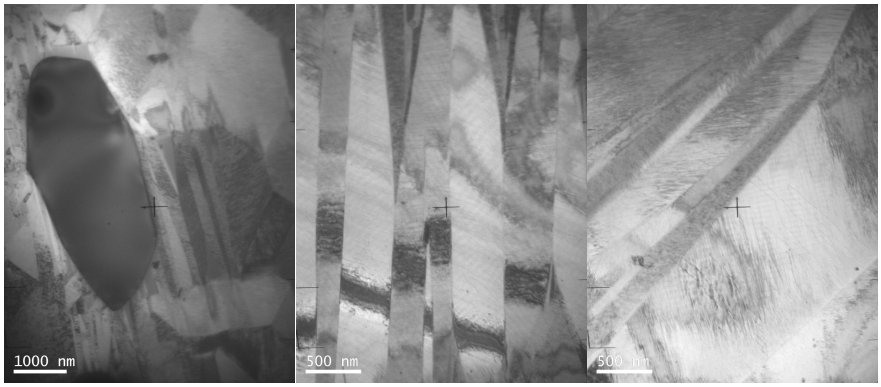

Fig. 3.1.3. TEM observation of $Ni_{50.3}Ti_{24.7}Zr_{25}$ alloy SHT 1270 K 1 h: (a) big particle of ZrC with matrix, (b) martensite plates from other area, (c) two beam condition of martensite plates with dislocations.

As expected, a slightly different microstructure appears at room temperature for the sample additionally aged at 770 K, shown in Fig. 3.1.4. The (a) and (b) panels show the bright field image of the matrix and the corresponding SADP, respectively. The diffraction pattern shows three pairs of martensite variants in the $[110]_{B19'}$ zone axis, marked in white, yellow, and green color. Additional spots, marked in red, reveal a

cubic symmetry and can be indexed as the 110_{B2}-type reflections of the $[111]_{B2}$ zone axis. As it is already known, B2 austenite and H phase can both contribute to these spots in the $[111]_{B2}$ zone axis ($[210]_H$) due to their structural relationship [56]. However, R. Santamarta *et al*. [57] only observed residual austenite in the small gaps between large size H-phase precipitates by HRTEM. Therefore, there is high possibility that such spots that show cubic symmetry are mainly derived from H phase instead of austenite. As a result of the tiny size of precipitates, the weak 1/3<110> satellites typical of the H phase are invisible in the diffraction pattern. In other orientations, the nano-sized precipitates show a better contrast and they are visible in large amounts, embedded in the martensite plates, as shown in Figs. 3.1.4 (c) and (d). Some individual nanoprecipitates are marked by arrows in (d).

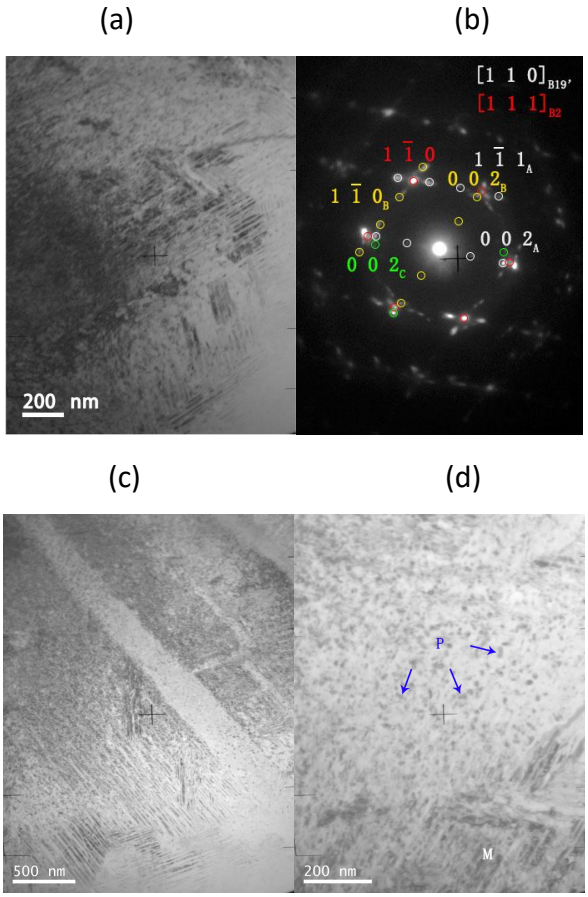

Fig. 3.1.4. TEM results of $Ni_{50.3}Ti_{24.7}Zr_{25}$ alloy SHT 1270 K 1 h with additional ageing at 770 K for 3 h: (a) BF image of the matrix, (b) corresponding SADP of (a); (c) other area with better contrast of nano-sized precipitates embedded in the martensite, (d) enlarged image of (c).

Fig. 3.1.5 shows the TEM observations of $Ni_{50.3}Ti_{24.7}Zr_{25}$ SHT and additional ageing at 820 K for 3 h. The SADP in Fig. 3.1.5 (b) contains diffracted spots from different phases. From one side, spots of two variants of B19' martensite exhibiting (011) Type I twinning in the $[100]_{B19'}$ zone axis, indexed in white color, can be clearly observed. Moreover, additional spots showing a cubic symmetry are presented in the middle of the $001_{M,T}$-type reflections and they are indexed in red color. Again, they are

consistent with the 011_{B2}-type reflections in the $[100]_{B2}$ zone axis and also with the corresponding fundamental spots of the H phase. Like in the previous case (Fig. 3.1.4 for ageing at 770K) and according to the HRTEM observations [57], the size of precipitates are too small to retain significant amount of austenite phase in their interspaces. Therefore, it can be considered that the main contribution to these spots comes from the H-phase nanoprecipitates. Actually, two possible zone axes of H phase can be related to $[100]_{B2}$, which are $[100]_H$ and $[310]_H$ according to F. Yang *et al*. [56]. In order to simplify the indexation of the patterns in Figs. 3.1.4 and 3.1.5, the spots have been marked in red color with the basis of the B2 structure. Figs. 3.1.5 (c) and (d) were taken in two-beam conditions and show a much better contrast of the H-phase nanoprecipitates with ellipsoidal shape. The size of the precipitates is below 50 nm.

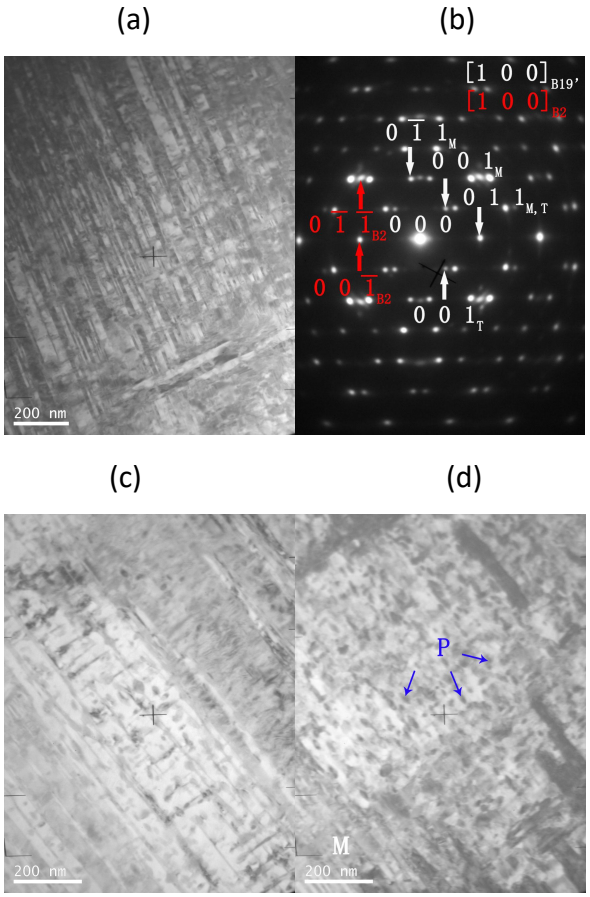

Fig. 3.1.5. TEM results of $Ni_{50.3}Ti_{24.7}Zr_{25}$ SHT 1270 K alloy aged at 820 K for 3 h: (a) BF image of the matrix, and (b) corresponding SADP of (a); (c) and (d) are other areas of matrix with precipitates.

Unlike the ageing treatments at 770 K or 820 K for 3h, the H-phase precipitates are fully developed in the samples submitted to the prolonged furnace cooling process, due to the long time spent at temperatures above A_f. The corresponding microstructure is shown in Figs. 3.1.6 (a), (c), (d), while panel (b) is the diffraction pattern of (a). The pattern is again complex, as it includes two pairs of B19' martensite variants in the $[110]_{B19'}$ zone axis, marked in white and yellow colors,

together with the spots marked in red, revealing cubic symmetry and arising from the fundamental spots of the H phase in the $[210]_H$ zone axis, compatible with the $[111]_{B2}$ zone axis. In this case, such reflections are considered to come not only from the H-phase particles, but also from small regions of retained austenite in between the large particles, as observed previously by HRTEM [57]. As shown in the TEM images, the H-phase particles adopt elongated shapes with hundreds of nm in length and the martensite plates cannot absorb them, forming arrays of tiny plates in the spaces between the H-phase particles. This is the same situation reported in the literature for the alloy with 15 at.% and 20 at.% Zr [121, 140, 141], though a larger number of big particles are revealed by the TEM observations in the present 25 at.% Zr alloy, which restricts the growth of the martensite plates. Therefore, the martensitic transformation becomes extended in a large temperature range, which is the reason of the absence of a clear transformation peak in the DSC thermograms shown in Fig. 3.1.1 (d).

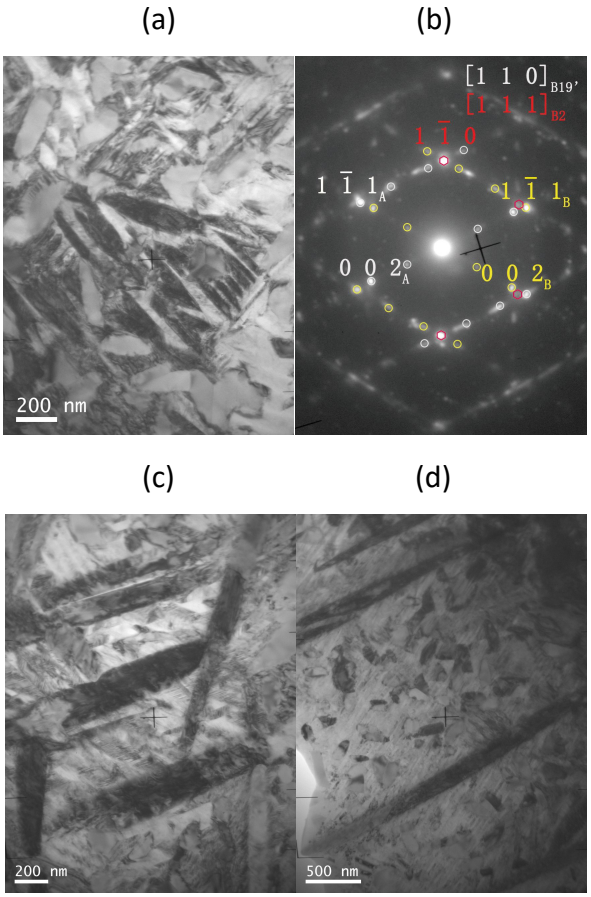

Fig. 3.1.6. TEM results of $Ni_{50.3}Ti_{24.7}Zr_{25}$ SHT 1270 K alloy with additional furnace cooling treatment: (a) BF image of matrix with big precipitates and (b) corresponding SADP of (a); (c) and (d) other zones of matrix with different magnification.

3.1.3 Thermomechanical Experiments

Based on the former analysis, it can be concluded that the nano-sized H-phase

precipitates are introduced by ageing at 770 K and 820 K and lead to high temperature martensitic transformation above 400 K. The shape memory effect of the $Ni_{50.3}Ti_{24.7}Zr_{25}$ aged specimens have been investigated by thermomechanical tests and the results are shown in Fig. 3.1.7. The panel (a) shows the thermal cycles under constant stress from 100 MPa to 600 MPa of $Ni_{50.3}Ti_{24.7}Zr_{25}$ aged at 770 K for 3 h. The corresponding total, recoverable and irrecoverable strains and thermal hysteresis are plotted as a function of the applied stress in Fig. 3.1.7 (b). It is clear that some level of irrecoverable strain occurs for 200 MPa and higher stresses, which means that 200 MPa stress already causes some plastic deformation during the martensitic transformation and/or retention of stabilized martensite. As for the recoverable strain, ε_{Rec}, it continuously grows up to about 0.8% with the increasing compression stress until 400 MPa, but then it saturates and even decreases at higher stress due to increased amount of irrecoverable strain. Additionally, the hysteresis is also growing from 69 K to 74 K with the increase of compression stress.

The response of $Ni_{50.3}Ti_{24.7}Zr_{25}$ alloy aged at 820 K is presented in Figs. 3.1.7 (c) and (d). The general trends are very similar to the sample aged at 770 K, *i.e.*, the maximum recoverable strain is 0.86% and it is also attained under 400 MPa applied stress. The irrecoverable strain values stabilize around 0.24% for applied stress levels between 300 MPa and 500 MPa and raise up to 0.35% under 600 MPa. Such lower values, compared to the sample aged at 770 K, indicates a better strengthening effect of the H-phase precipitates introduced by ageing at 820 K for 3 h. Nevertheless, the hysteresis is raised from 80 K to 91 K with increasing applied stress, that is higher than the specimen aged at 770 K (74 K maximum). Figs. 3.1.7 (e) and (f) show enlarged plots of the thermomechanical cycles performed under 100 MPa and 300 MPa, respectively, illustrating the tangent method used for the quantification of the transformation temperatures and total/irrecoverable strains. Moreover, it can be observed that the cooling and heating curves do not overlap in the temperature range below M_f. Good overlapping is only achieved after an extended overcooling down to ~300 K, which indicates a difficult transformation of the last austenite domains due to the accumulated strain around the grain boundaries and non-transforming precipitates. The effect is slightly intensified with the increase of the applied compressive stress, as seen in Fig. 3.1.7 (f). Therefore, if the cooling run is not extended to sufficiently low temperatures, a low fraction of residual untransformed austenite may remain. In the same way, if the heating run is extended well above the normal A_f temperature, the heating curve gradually approaches to the cooling one and the irrecoverable strain practically vanishes, as seen in Fig. 3.1.7 (a) for the cycle under 100 MPa. This observation also indicates a difficult end of the reverse transformation, which means that a significant part of the irrecoverable strain measured under high stress levels may arise from residual stabilized martensite.

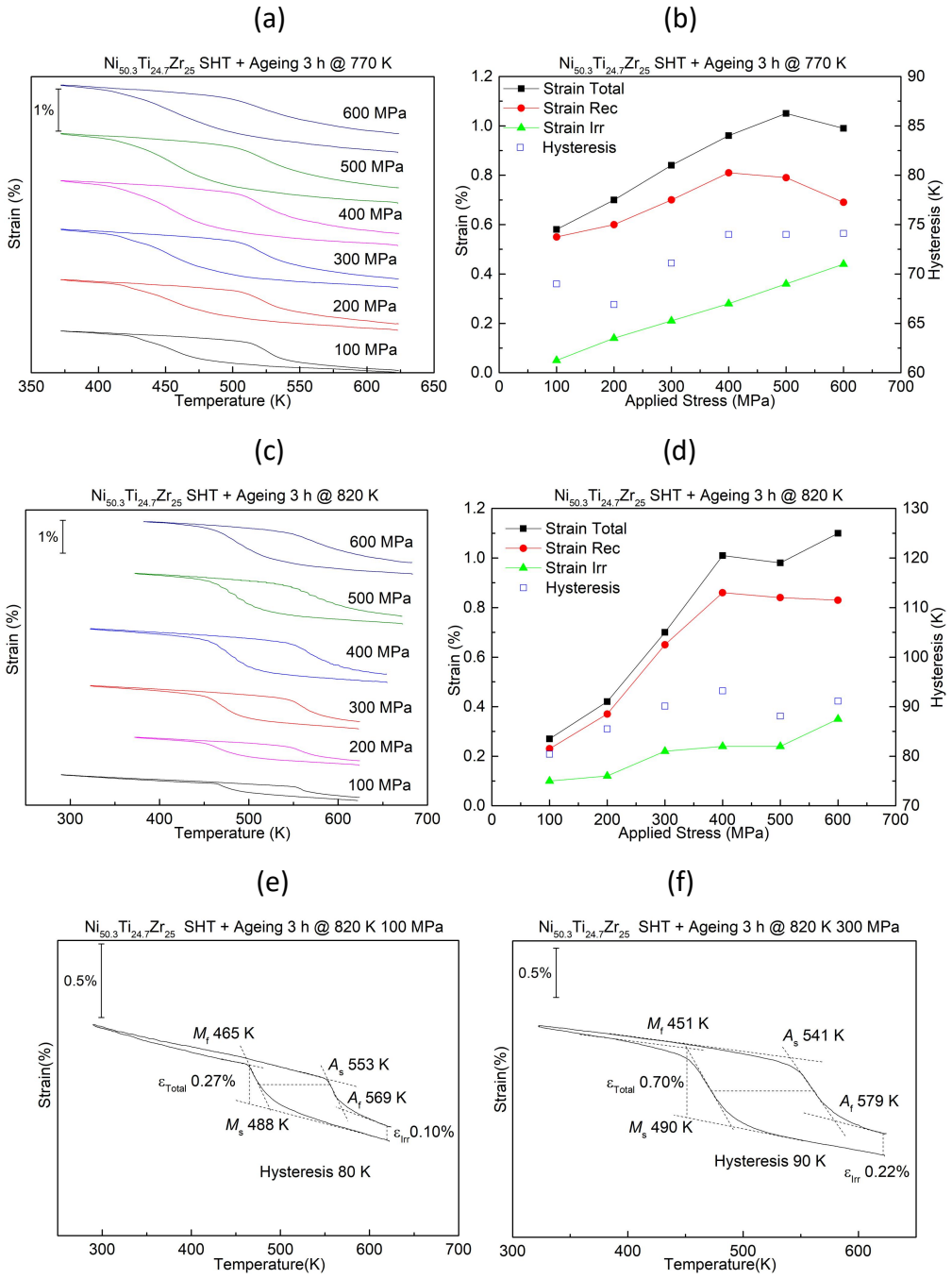

Fig. 3.1.7. Thermomechanical tests under constant stress for $Ni_{50.3}Ti_{24.7}Zr_{25}$ SHT alloy with additional ageing treatment (a) at 770 K 3 h and (c) at 820 K 3 h. The corresponding shape memory properties extracted from the mechanical tests are plotted in (b) and (d). Panels (e) and (f) show the enlarged cycles of the alloy aged at 820 K recorded under 100 MPa and 300 MPa, respectively.

Figs. 3.1.8 (a) and (b) illustrate the relationship between the applied compression stress and the transformation temperatures (A_s, A_f, M_s and M_f), which is based on the Clausius-Clapeyron equation (Eq. 3.1.1). The equation is valid in Equilibrium Thermodynamics and results in a linear dependency between σ and T with positive slope, as the direct transformation is exothermic, then $\Delta H < 0$. Positive slopes are

indeed visible in Figs. 3.1.8 (a), (b) for the M_s and A_f temperatures. The specimen aged at 820 K 3 h specimen shows less absolute value of slope than that aged at 770 K 3 h specimen, *e.g.*, the slopes of M_s are 9.0 MPa/K and 13.7 MPa/K, respectively. It means that the sample aged at 820 K has larger M_s increment under the same stress condition, due to the different microstructure, *i.e.*, higher fraction of H phase and bigger precipitate size.

Nevertheless, M_f and A_s temperatures exhibit negative slopes of the σ-T plot. This is due to the non-equilibrium processes related with the difficult completion of the martensitic transformation discussed above, arising from the internal stresses around the lattice defects (grain boundaries, H-phase nanoprecipitates, dislocations, …) accumulated at the end of the transformation. Such effects increase with the external applied stress and this causes a progressive decrease of the M_f and A_s temperatures, leading to the negative slope.

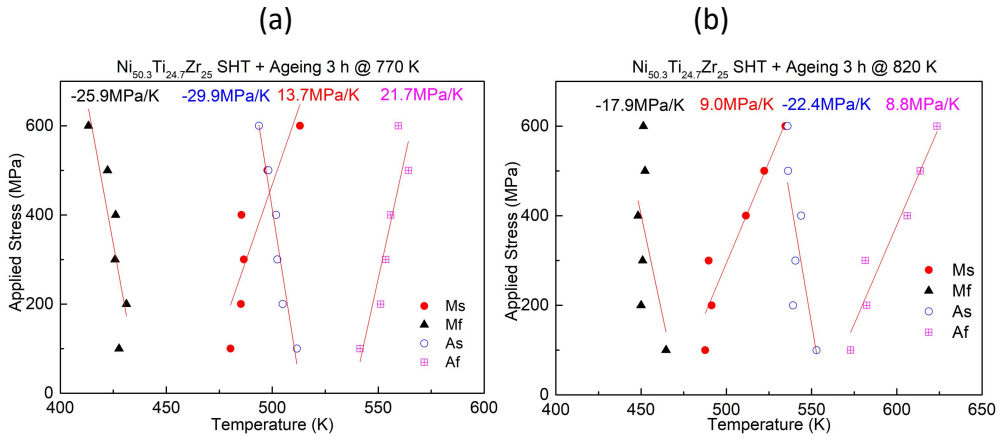

Fig. 3.1.8. The relationship between compression stress and transformation temperatures according to Clausius-Clapeyron relationship of $Ni_{50.3}Ti_{24.7}Zr_{25}$ (a) aged at 770 K for 3 h, (b) aged at 820 K for 3 h.

$$\frac{\Delta\sigma}{\Delta T} = -\frac{\Delta H}{T_0 \varepsilon_{Rec}} \quad \text{(Eq. 3.1.1)}$$

$$T_0 = \frac{M_s + A_f}{2} \quad \text{(Eq. 3.1.2)}$$

$$W = \frac{\sigma A_0 \varepsilon_{Rec} L_0}{V_0} = \sigma \varepsilon_{Rec} \quad \text{(Eq. 3.1.3)}$$

σ - Applied stress; ε_{Rec} - Recoverable strain (%); T_0 - Equilibrium temperature;

A_0 - Cross section of specimen; L_0 - Original length of specimen.

The work output performed by the specimen during the reverse transformation (when sample expands against the applied compressive stress) can be obtained form Eq. 3.1.3 [186]. The values for $Ni_{50.3}Ti_{24.7}Zr_{25}$ alloy aged at 770 K and 820 K are plotted in Figs. 3.1.9 (a) and (b), respectively. For the sample aged at 770 K, the work output is almost saturated about 4 J/cm^3 at 500 MPa applied stress, as the result of turning point of the recoverable strain. For the sample aged at 820 K, the work output increase to 5 J/cm^3 under 600 MPa, and has not yet reached the saturation level, which is another indication of a stronger strengthening effect induced by this particular distribution of H-phase precipitates. However, the studied alloys show less work output compared with $Ni_{50.3}Ti_{29.7}Hf_{20}$ alloys, which demonstrate about 16.5 J/cm^3 under 500 MPa in polycrystalline state [124] and 25 - 30 J/cm^3 in single crystals [128].

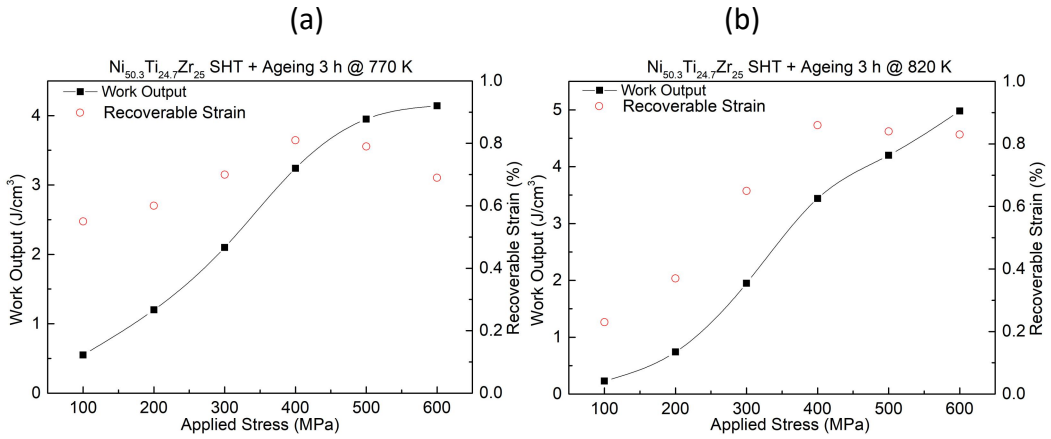

Fig. 3.1.9. Work output as the function of compression stress for $Ni_{50.3}Ti_{24.7}Zr_{25}$ SHT (a) aged at 770 K for 3 h, and (b) aged at 820 K for 3 h.

3.2 Results of Analysis and Observation of Strain Glass

An remarkable phenomenon was found during the research of the $Ni_{50.3}Ti_{29.7}Zr_{20}$ alloy, consisting of the suppression of the thermal martensitic transformation after prolonged ageing in austenite at relatively low temperature, at 520 K, which was accompanied by short range atomic reordering processes in the B2 phase revealed by diffuse streaking in the diffraction patterns, as reported by Perez-Sierra *et al*. [187]. Actually similar diffuse streaks were reported by Sandu *et al*. in $Ni_{52}Ti_{42}Zr_6$ due to short range ordering of the Zr atoms as a previous step to the formation of precipitates by aging at 770 K [113, 114]. Additionally, $Ni_{51.2}Ti_{28.8}Hf_{20}$ also presented the suppression of MT under solution heat treated condition, with diffuse streaks on SADP due to atomic short range ordering as well [138]. Previous research in Ni-Ti-based and other shape memory alloys with suppressed martensitic transformation considered a new state of the material denoted as “strain glass”. Therefore, in this chapter a variety of methods are used to verify this unique

structure in Ni-rich Ni-Ti-Zr alloys with different compositions.

3.2.1 Calorimetric Analysis

Besides the $Ni_{50.3}Ti_{29.7}Zr_{20}$ alloy, other two alloys with increased content of Ni or Zr have been investigated in this work. The nominal composition and the applied thermal treatments are listed in the Table 3.2.

Table 3.2. Nominal composition of the studied alloys and thermal treatments.

Nominal Composition	Thermal Treatment		
	Step one	Step two	Step three
$Ni_{50.3}Ti_{29.7}Zr_{20}$	Hot extrusion	SHT 1170 K 1 h	Ageing 520K X h
$Ni_{50.9}Ti_{24.1}Zr_{25}$	Hot extrusion	SHT 1170 K/1270 K 1 h	Ageing 820K 3 h
$Ni_{50.3}Ti_{24.7}Zr_{25}$	Hot extrusion	SHT 1270 K 1 h	Ageing 520K X h

Fig. 3.2.1 (a) presents the DSC results of $Ni_{50.3}Ti_{29.7}Zr_{20}$ alloy, the exo and endo peaks lying in the top and bottom half of the figure correspond to the direct and reverse thermal transformation, respectively. It is obvious that the $Ni_{50.3}Ti_{29.7}Zr_{20}$ solution heat treated sample presents the normal martensitic transformation, but the peaks gradually diminish in area for increasing ageing time at 520 K. The peak temperature A_p shifts from about 291 K to 257 K after 9 h ageing time, and the DSC signal becomes diffuse and fades into the background. Finally, the martensitic transformation peak is completely suppressed after 12 h ageing at 520 K. The ageing treatment was extended up to 14 days and also showed no transformation peak in the DSC signal. It should be noted that this material has poor reproducibility of the MT when repeating the solution heat treatment, which is associated with the rapidity of the water quenching and ampoule breaking manual process. Therefore, to correctly represent the ageing effect, neighbor specimens or even the same piece were used during these experiments.

Fig. 3.2.1 (b) shows the DSC results of $Ni_{50.9}Ti_{24.1}Zr_{25}$ alloy. The received ingot was just after hot extrusion at 1170 K and, in this condition, it shows normal martensitic peaks above 350 K. However, unlike $Ni_{50.3}Ti_{29.7}Zr_{20}$, the $Ni_{50.9}Ti_{24.1}Zr_{25}$ presents a suppressed transformation in the DSC just after solution heat treatment without additional ageing. Actually, the as-extruded state of $Ni_{50.9}Ti_{24.1}Zr_{25}$ alloy is containing a high amount of H-phase precipitates introduced during hot extrusion, while after SHT the matrix is free of visible precipitates, as will be presented in the section 3.2.3 about microstructure. The transformation peaks appear again after ageing at 820 K for 3 h, the peak temperatures are a little bit higher than as-extruded state. However, this state of specimen shows weak stability, as the peaks disappear after only three DSC cycles.

Fig. 3.2.1 (c) shows the DSC results of $Ni_{50.3}Ti_{24.7}Zr_{25}$ alloy. The received ingots were

under the solution heat treatment at 1270 K for 1 h followed by water quench, and show normal martensitic transformation with MTTs above 350 K. However, the SHT state exhibits poor thermal stability in two consecutive DSC cycles as the result of changing microstructure. Under the additional ageing at 520 K for 3 days, the transformation peak is gradually deteriorating and shifts to 220 K (M_p), and finally no peaks are detected by DSC after ageing for 6 days.

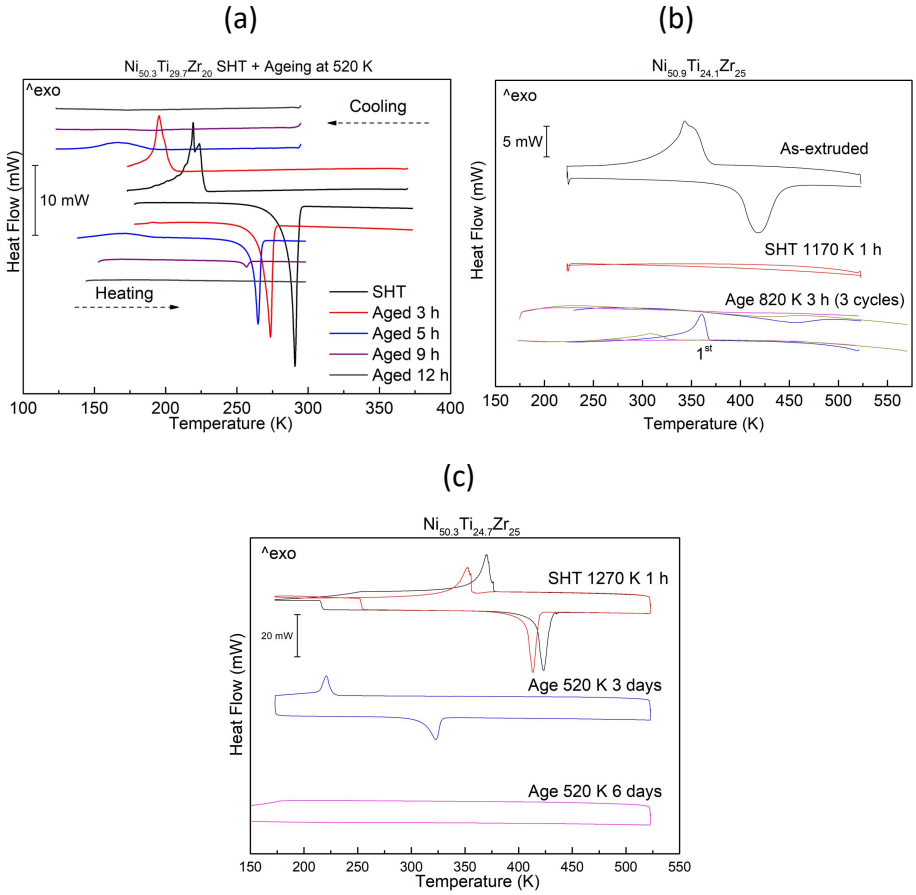

Fig. 3.2.1. DSC measurements of (a) $Ni_{50.3}Ti_{29.7}Zr_{20}$, (b) $Ni_{50.9}Ti_{24.1}Zr_{25}$, and (c) $Ni_{50.3}Ti_{24.7}Zr_{25}$ under different thermal treatments.

3.2.2 DMA

As it is already known that the dynamical mechanical analysis (DMA) is one of the methods to illustrate the unique properties of strain glass, the alloys under investigation were subjected to DMA to identify the SG structure. The measurements were made at a constant strain amplitude of $5 \cdot 10^{-4}$, heating-cooling rate of 2 K/min and a frequency range of the oscillating stress between 0.2 and 20 Hz.

Fig. 3.2.2 presents the DMA analysis of $Ni_{50.3}Ti_{29.7}Zr_{20}$ alloy listed by the sequence of thermal treatment, *i.e.*, start from the solution heat treated state in panel (a) to additional ageing in air at 520 K for different times up to 21 days in panel (f). Each plot contains the results of storage modulus (*E*) and internal friction (*IF*) data

measured by the DMA equipment at different frequencies of the oscillating stress, which have been settled in the top half and bottom half of the figure, respectively. However, it should be noted that the DMA is a more appropriate test method for the soft material like polymer, so it is inevitable to have low accuracy in testing hard material like NiTi SMAs. Actually, a sine-like oscillating wave appears in the row data derived from the DMA equipment that is much obvious at low frequency (0.2 Hz). Therefore, thin specimens were used to reduce the error and the curves were submitted to a smoothing processing, as has been discussed in Chapter 2 about experimental methods. In addition, to confirm or rule out the DMA results, an ultrasonic technique with much higher accuracy for *E* and *IF* measurement was used and will be presented in the last section of this chapter as supplementary experiments.

For the SHT state (Fig. 3.2.2 (a)), the *IF* curves present a clear peak associated with the normal martensitic transformation under cooling, which possess the same peak temperature independently of the frequency. Moreover, as typical for the martensitic transformation, the *IF* peak value actually decreases with the increase of the frequency. As it is well known, the internal friction spectrum during a martensitic transformation consists of three parts, *i.e.*, transitory term, phase transition term and intrinsic term, which can be separated through several methods [188]. The transitory part gives the main contribution to the experimental peak, depending on the heating/cooling rate, and is inversely proportional to the strain amplitude and frequency [38]. In the present experiments, the strain amplitude and cooling rate were kept constant, the frequency was the only variable parameter affecting the transitory term and the whole *IF* peak recorded during the martensitic transformation. On its turn, the storage modulus starts to increase with the nucleation and growth of martensite variants. Unlike other SMAs, the $Ni_{50.3}Ti_{29.7}Zr_{20}$ SHT alloy does not exhibit the typical dip appeared related to the transformation. The dip is a turning point of the storage modulus curve that is formed by decreasing *E* value upon cooling in the austenite state and increasing *E* value during the martensitic transformation. Instead, the *E* value shows nearly temperature independence during the whole austenite state (Fig. 3.2.2 (a)), which could be attributed to the “elinvar effect”. This topic will be further discussed in section 3.2.5.

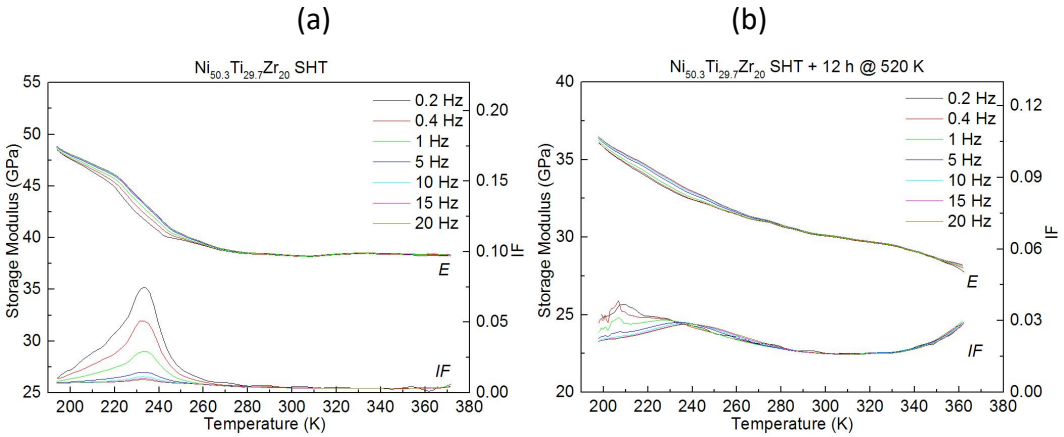

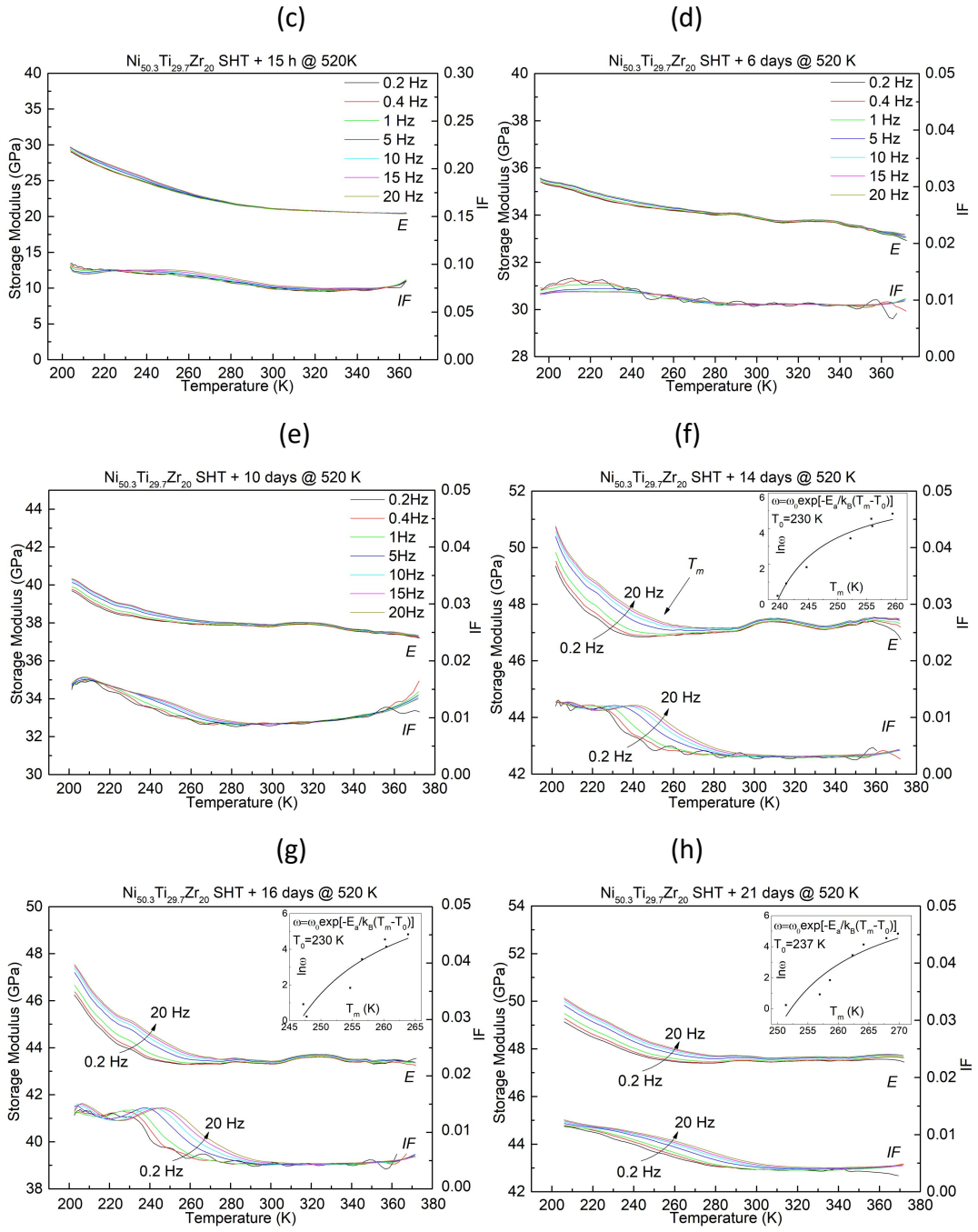

Fig. 3.2.2. DMA results of $Ni_{50.3}Ti_{29.7}Zr_{20}$ alloys: (a) solution heat treated at 1170 K for 1 h sample, and additional ageing at 520 K for (b) 12 h, (c) 15 h, (d) 6 days, (e) 10 days, (f) 14 days, (g) 16 days, (h) 21 days.

After ageing at 520 K for 12 h (treatment that shows MT suppression in the DSC, Fig. 3.2.2 (a)), the *IF* curves present weaker diffused peaks with very little frequency dependence in the low temperature side, but the *E* modulus shows a continuous increasing trend upon cooling, as seen in Fig. 3.2.2 (b). The tendencies of *E* modulus and *IF* continue for increasing ageing times up to 6 days at 520 K, as seen from Figs. 4.2.2 (c) - (d). After 10 days ageing, a small peak appears at the low temperature end of the *IF* curve, concomitant with an incipient frequency dependence of the *E* modulus (Fig. 3.2.2 (e)). Finally, after ageing treatment at 520 K for 14 or 16 days, a

clear frequency dependence appears in the *E* modulus and the corresponding *IF* peak anomalies at about 240 K (Figs. 3.2.2 (f), (g)). The storage modulus data show again a rather flat curve at high temperatures followed by an increase upon cooling. The increasing part of the *E* curves starts at a temperature denoted as T_m (marked by an arrow in Fig. 3.2.2 (f) for the curve at 20 Hz) and is widely dispersed in the sequence of frequencies. This temperature has been extracted from the curves using the "peak max" in TA analysis program. The insets of Figs. 3.2.2 (f), (g) show a reasonable fitting of the experimental T_m values for different frequencies ($f = \omega/2\pi$) to the empirical Vogel-Fulcher relationship given in Eq. 3.2.1 and its equivalent Eq. 3.2.2, where T_0 represents the ideal glass transition temperature. The best fitting gives T_0 = 230 K for both 14 and 16 days ageing times.

Therefore, the DMA results indicate the development of the strain glass state in the $Ni_{50.3}Ti_{29.7}Zr_{20}$ SHT alloy after 14 to 16 days ageing at 520 K. The intermediate ageing time between the disappearance of the transformation peaks in the DSC signal and evidence of SG in DMA data (from 12 h to 14 days) is considered as an "incubation period", which shows no standard thermal martensitic transformation but not yet well-developed strain glass state. Extending the ageing treatment up to 21 days the *IF* peaks and the temperature dependence of the *E* modulus seem to decline, as shown in Fig. 3.2.2 (h), which points to an over-aged condition for the SG state. In this case, the fitting process gives an ideal freezing temperature T_0 = 237 K .

$$\omega = \omega_0 \exp\left[\frac{-E_a}{k_B(T_m - T_0)}\right] \quad \text{(Eq. 3.2.1)}$$

$$\ln\omega = -\frac{E_a}{k_B}\left(\frac{1}{T_m - T_0}\right) + \ln\omega_0 \quad \text{(Eq. 3.2.2)}$$

The height of the *IF* peak corresponding to the martensitic transformation in the SHT state reaches the value 0.08 at 0.2 Hz frequency, whereas the *IF* peak value decreases to ~0.01 in the SG state for all frequencies. Such a significant decrease is consistent with the typical behavior of other Ni-Ti alloys with SG [16, 44]. A similar drop of *IF* is also observed during the incubation period in Fig. 3.2.2. On its turn, the values of *E* modulus change between 40 and 48 GPa for the SHT state and decrease below 40 GPa during the incubation time for SG. However, in the SG state they raise up to ~45 - 50 GPa. However, considering the low accuracy of the DMA measurement, such differences in the absolute values of the *E* modulus are not much reliable.

Fig. 3.2.3 presents the DMA results of $Ni_{50.9}Ti_{Z4.1}Zr_{25}$ alloy with different heat treatments. This alloy contains more Ni and Zr compared with the former $Ni_{50.3}Ti_{29.7}Zr_{20}$ and already presents strain glass in the SHT state without prolonged additional ageing (Figs. 3.2.3 (a), (b)). This is consistent with DSC results of suppressed thermal martensitic transformation in Fig. 3.2.1 (b). Two temperatures for the solution heat treatment were tested (1270 K and 1170 K) and both show frequency-dependent *E* modulus and *IF* peak, with reasonable fitting of the

Vogel-Fulcher relationship, as shown in the insets of Fig. 3.2.3. The solution heat treatment temperature seems to have little impact on the induction of the strain glass state, except for the slightly different values of T_0, equal to 232 K and 220 K for the treatments at 1270 K and 1170 K, respectively. The specimen SHT at 1170 K was then subjected to additional ageing at 520 K for 1 day and 2 days in air. The results show a decrease of T_0 to 211 K and 208 K, respectively (Figs. 3.2.3 (c), (d)). For the 2 days sample, the decrease of T_0 and the limited cooling capacity of the DMA device cause incomplete IF peaks.

Finally, for the $Ni_{50.3}Ti_{24.7}Zr_{25}$ alloy, the DSC results showed the suppression of the martensitic transformation after 6 days ageing at 520 K (Fig. 3.2.1 (c)). The DMA results, shown in Fig. 3.2.3 (e), also demonstrate the development of the strain glass state in this alloy, with T_0 = 222 K. This is an intermediate composition in terms of Ni and Zr content compared to the former two alloys and shows and intermediate response in front of the strain glass, in the sense that the strain glass is not yet formed just after the solution heat treatment (due to the less Ni content than $Ni_{50.9}Ti_{24.1}Zr_{25}$) but needs lower ageing time at 520 K than $Ni_{50.3}Ti_{29.7}Zr_{20}$, due to the larger Zr content. The comparative results demonstrate the important role of the excess Ni and Zr content for the development of the strain glass state, as well as for the H-phase precipitation. As it will be further discussed later, the strain glass state in these alloys is linked to the precursor stages of H-phase precipitation.

It should be noted that the Vogel-Fulcher relationship fitting curves (shown in the insets of Figs. 3.2.2 and 3.2.3) have been plotted as "lnω vs. T_m" diagrams, in analogy with most of the literature about strain glass [16, 32, 34]. Moreover, in these papers, the frequency "ω" corresponds to temporal frequency (in units of "Hz"), but in the present author's thesis, the "ω" is corrected as angular frequency ($\omega = 2\pi f$) with units of "rad/s". Fig. 3.2.3 (e) shows the "ω vs. T_m" curve plotted on a semilogarithmic diagram (equivalent to the insets) to visualize the true values of the angular frequency.

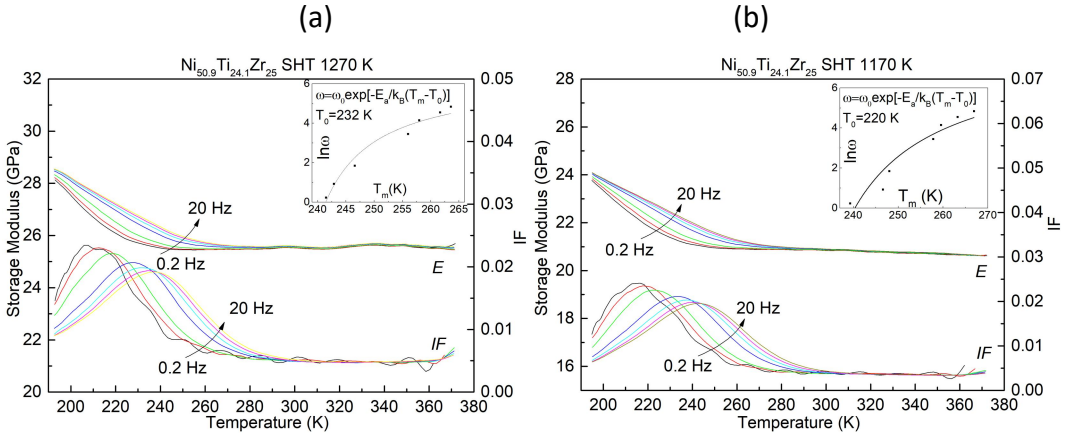

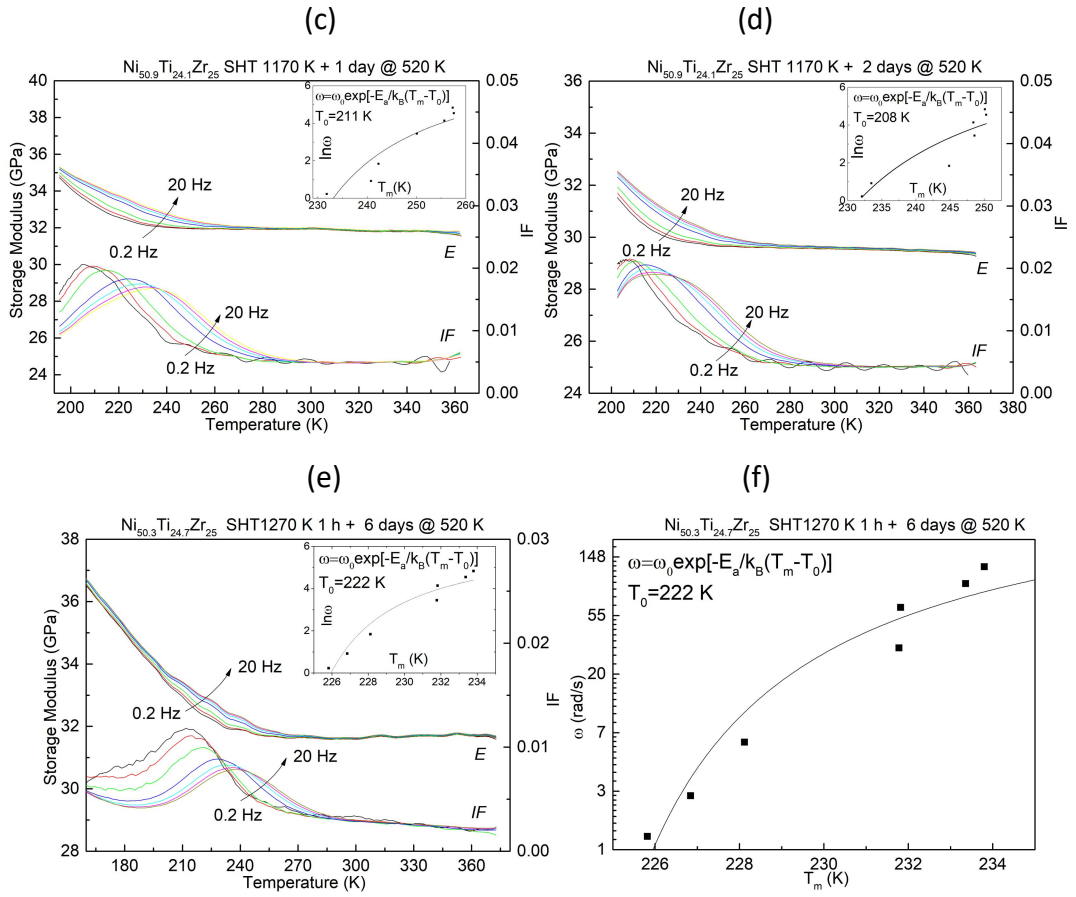

Fig. 3.2.3. DMA results of $Ni_{50.9}Ti_{24.1}Zr_{25}$ alloy for different thermal treatments: (a) solution heat treated at 1270 K sample, and (b) SHT 1170 K, followed by additional ageing at 520 K in air for (c) 1 day and (d) 2 days; (e) $Ni_{50.3}Ti_{24.7}Zr_{25}$ SHT 1270 K and ageing for 6 days at 520 K in air, (f) Vogel-Fulcher relationship fit expressed in ω-T_m.

3.2.3 Microstructure

Fig. 3.2.4 presents the TEM results of the $Ni_{50.3}Ti_{29.7}Zr_{20}$ alloy solution heat treated at 1170 K for 1 h; (a) is a bright field image of the matrix, and (b) is the corresponding SADP in the $[111]_{B2}$ zone axis. The matrix at room temperature is in the austenite phase, as its normal MTT is lower than room temperature (Fig. 3.2.1 (a)). It shows clearly B2 cubic structure (with space group Pm-3m, No. 221). The BF image shows no sign of precipitates but a slight mottled contrast under the two beam condition. The details of B2 austenite structure have been discussed in the introduction chapter and is shown in Fig. 1.1.9.

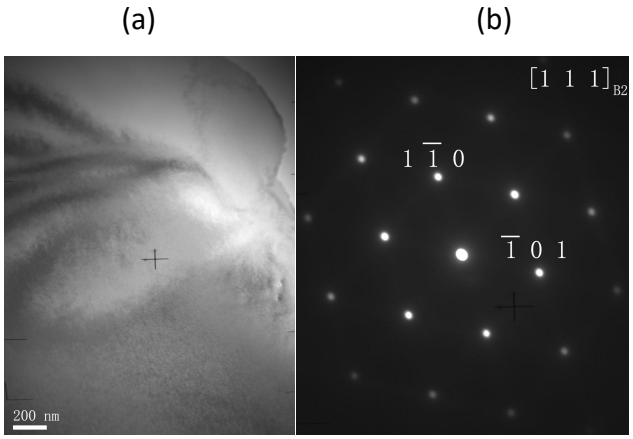

Fig. 3.2.4. TEM results of $Ni_{50.3}Ti_{29.7}Zr_{20}$ SHT 1170 K 1 h alloy: (a) bright field image of the matrix ; (b) corresponding selected area electron diffraction pattern (SADP).

The observations of the $Ni_{50.3}Ti_{29.7}Zr_{20}$ SHT alloy with additional ageing at 520 K for 14 days (treatment that induces the SG state in this material) are summarized in Fig. 3.2.5. Panels (a) to (d) were obtained under room temperature and (e), (f) at 120 K, using the *in-situ* cooling holder. A few dislocations in the austenite matrix can be observed in the bright field images taken at room temperature (panels (a), (b)). However, unlike the specimen with only SHT (Fig. 3.2.4), extra diffuse scattering rings appear between the fundamental B2 spots in the SADP obtained after ageing (Figs. 3.2.4 (b), (d)), indicating a short range reordering process. It has been discussed in the introduction chapter that similar diffuse streaks were reported by Sandu *et al*. in $Ni_{52}Ti_{42}Zr_6$, which were ascribed to short range ordering of the Zr atoms corresponding to the pre-formation of precipitates observed after ageing at higher temperatures [113, 114]. In those papers, the structure of the precipitates (H phase) was not yet identified. The diffuse streaks are close to the position of the 1/3[110] and 1/4[210]-type satellite spots characteristic of the H phase, which have been marked in Fig. 3.2.5 (d) by blue and red spots for one orientation variant of the H phase. The H-phase precipitates grow in multiple orientation variants and produce satellites along all the equivalent directions of the $<110>_{B2}$, $<210>_{B2}$ and $<111>_{B2}$ families in the diffraction patterns. As shown in Fig. 3.2.5 (d), the diffuse streaks observed after 14 days ageing at 520 K are not coincident with the positions of the H-phase superlattice spots, but rater close to them. This suggests that the limited diffusion at 520 K only permits short range processes that can be considered as the preliminary stages of the Zr and Ti redistribution towards the H phase, in agreement with the suggestion made by Sandu *et al* [113, 114]. Taking into account that the H phase is richer in Zr, lean in Ti and slightly richer in Ni, compared to the B2 austenite, the process at 520 K likely consists of a short range segregation of Zr and Ti atoms leading to the formation of very small domains with modified composition (roughly nanometric in size), but till too small for the complete development of the H phase superstructure with 3-fold and 4-fold periodicities (note that one lattice parameter of the H phase unit cell is as large as ~2.6 nm [57]). These precursor H-phase nuclei would generate a very fine spatial heterogeneity with random strain fields that

suppress the normal martensitic transformation and create the strain glass state. Figs. 3.2.5 (e), (f) demonstrate that the aged $Ni_{50.3}Ti_{29.7}Zr_{20}$ alloy globally remains in austenite phase at 120 K, but the bright field image shows an intense mottled contrast and the diffuse scattering in the SADP forms more prominent diffuse spots around the fundamental B2 spots compared to room temperature. Some of the diffuse spots are marked by arrows in Fig. 3.2.5 (f). Therefore, the TEM observations are consistent with the former DMA tests indicating the well-developed strain glass state in the long term aged $Ni_{50.3}Ti_{29.7}Zr_{20}$ alloy.

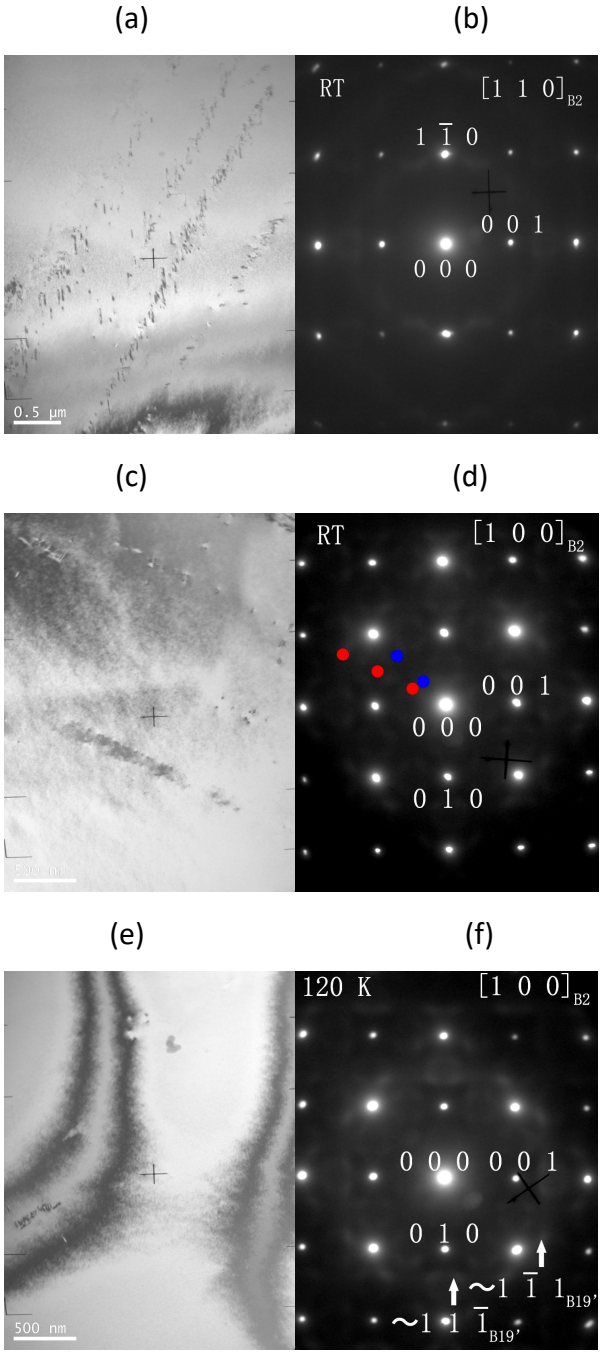

Fig. 3.2.5. TEM results of $Ni_{50.3}Ti_{29.7}Zr_{20}$ SHT 1170 K for 1 h and additional ageing at 520 K for 14 days alloy: (a) BF image of the matrix at room temperature, (b) corresponding SADP in the $[110]_{B2}$

zone axis; (c) BF image of another zone at room temperature, (d) corresponding SADP of (c) in the $[100]_{B2}$ zone axis; (e) BF image of the matrix taken at 120 K and (f) corresponding SADP in the $[100]_{B2}$ zone axis.

Fig. 3.2.6 presents the TEM observations of $Ni_{50.9}Ti_{24.1}Zr_{25}$ alloy solution heat treated at 1170 K for 1 h, also with well induced strain glass state, as shown by DMA results. Panels (a) and (b) are the SADPs of the matrix in the $[100]_{B2}$ zone axis taken at room temperature and at 140 K, respectively. Panel (c) is the corresponding BF image of (b), whereas panel (d) is from another area and shows a big carbide particle in the center, indicating that SHT cannot eliminate this type of particles. Again, diffuse streaks appear between the fundamental B2 spots and become more prominent at low temperature, forming diffuse spots around the B2 reflections (marked by arrows in Fig. 3.2.6 (b)), which is accompanied by intense mottled contrast in the bright field image (Fig. 3.2.6 (c)). The positions of the diffuse spots have been analyzed by the "Crystal" simulation software, taking into account the relationships between B2 and B19' lattices, *i.e.*, $(001)_{B2}||(100)_{B19'}$ and $[011]_{B2}||[010]_{B19'}$, and it can be found that the $[010]_{B2}$ zone axis is close to the $[011]_{B19'}$ zone axis considering some distortion. It is concluded that the diffuse spots positions in Figs. 3.2.5 (f) and 3.2.6 (b) are actually close to the (11-1) and (1-11) planes of B19' martensite. Therefore, this analysis indicates the formation of B19' martensitic-like nuclei in the strain glass state. This is at difference with many Ni-rich Ni-Ti-based alloys with strain glass, for which the martensitic-like nuclei are of the R phase instead of B19' martensite [34, 36]. However, existence of B19'-type SG was also reported in binary $Ni_{50.8}Ti_{49.2}$ alloys after cold rolling with thickness reduction levels of 27% or above and it was attributed to the dislocation arrays formed after cold rolling, which constitute extended defects that impose effective nanoconfinement of the B19' domains [33].

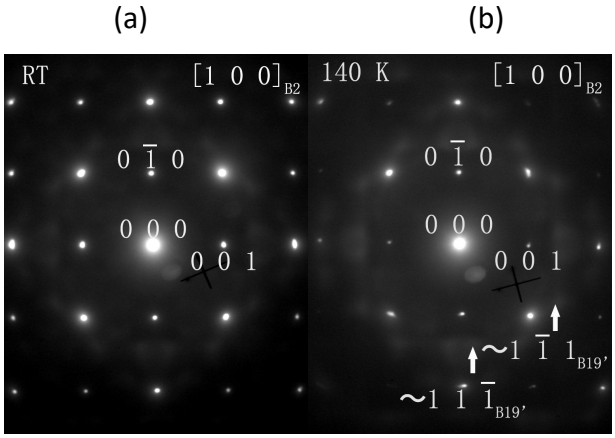

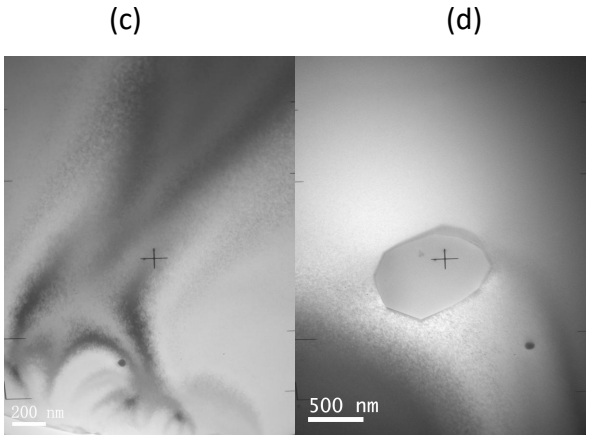

Fig. 3.2.6. TEM results of $Ni_{50.9}Ti_{24.1}Zr_{25}$ SHT at 1170 K 1 h alloy: (a) SADP of matrix at room temperature, (b) the same area at 140 K, (c) the corresponding BF at 140 K and (d) another area with a big carbide particle.

The as-received ingot of the $Ni_{50.9}Ti_{24.1}Zr_{25}$ alloy was in the state after casting and hot extrusion at 1170 K and, according to the DSC results in Fig. 3.2.1 (b), it showed the martensitic transformation. The microstructure is presented in Fig. 3.2.7 and consists of martensite variants, possible residual austenite, large carbide particles and a big amount of nano-sized H-phase precipitates. Hence, complex SADPs like that of Fig. 3.2.7 (b) were observed in these samples. The pattern corresponds to the $[110]_{B19'}$ zone axis, nearly parallel to $[111]_{B2}$, and shows two martensite variants (A and B) and additional spots with cubic symmetry, marked in red labels, corresponding to 110_{B2}-type reflections, coincident with the fundamental spots of the H phase in the $[210]_H$ zone axis (according to the relationships between B2 and H phase superlattice [56, 57]. Small H-phase precipitates are formed after hot extrusion, with length about 30 - 100 nm, as shown in Figs. 3.2.7 (c), (d). In this case, the slow cooling process after extrusion gives enough time for the formation of well-developed H phase precipitates, which avoids the strain glass state. Instead, for the solution heat treated samples only small nuclei of the precipitates can be formed upon quenching from 1170 K, which leads to the suppression of the martensitic transformation and development of the strain glass state.

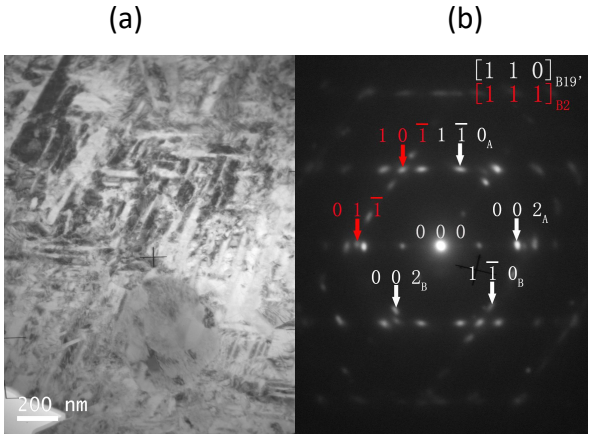

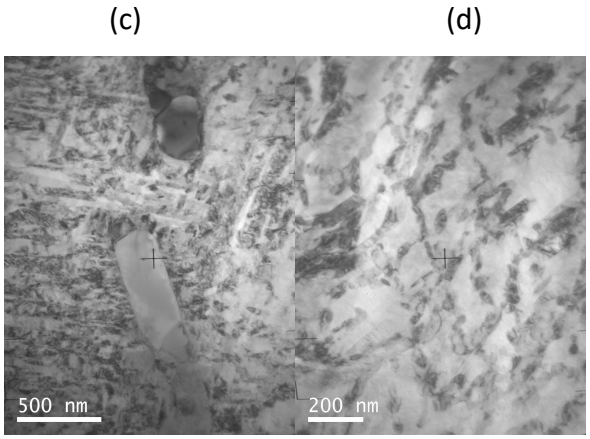

Fig. 3.2.7. TEM observations of $Ni_{50.9}Ti_{24.1}Zr_{25}$ as-extruded alloy: (a) BF of martensite matrix and (b) corresponding SADP under $[110]_{B19'}$ zone axis of (a); (c) BF of matrix with big carbide particles, (d) matrix with nano-sized precipitates.

Cooling experiments in the X-ray diffractometer were also performed for global structural determinations of different samples, the results are shown in Fig. 3.2.8. The $Ni_{50.3}Ti_{29.7}Zr_{20}$ SHT alloy presents austenite phase at room temperature and B19' martensite peaks are observed after cooling down to 120 K, as shown in Fig. 3.2.8 (a). However, a rather high 110_{B2} peak from austenite phase still appears in the XRD pattern at 120 K. Moreover, the enthalpy change of direct and reverse transformation, measured by DSC, is only about 6.5 J/g and 9.3 J/g, respectively, which is a low value for Ni-Ti-based shape memory alloys. Then, these observations indicate an incomplete martensitic transformation in $Ni_{50.3}Ti_{29.7}Zr_{20}$ SHT specimens leaving residual austenite after cooling. Fig. 3.2.8 (b) presents the XRD patterns in a narrow angular interval around 40° of the $Ni_{50.3}Ti_{29.7}Zr_{20}$ SHT alloy with additional ageing at 520 K for 5.5 h. This treatment presents reduced transformation peaks in the DSC (Fig. 3.2.1 (a)). Consequently, the intensity of the 110_{B2} peak is practically not changed upon cooling and only a very tiny $002_{B19'}$ peak is visible in this angular range. Fig. 3.2.8 (c) shows the results of $Ni_{50.9}Ti_{24.1}Zr_{25}$ SHT alloy, with strain glass. The different spectra only contain two tiny ZrC peaks and several austenite B2 peaks for all temperatures down to 120 K, confirming that this is the average structure of the material at low temperature. A remarkable result of Figs. 3.2.8 (b) and (c) is the constant positions of the B2 peaks in the spectra recorded at different temperatures. In Fig. 3.2.8 (b), the 110_{B2} peak position only changes from 295 K to 180 K and then remains constant down to 120 K, while in Fig. 3.2.9 (c) the peak positions are constant in the whole temperature range. This indicates a nearly zero thermal expansion or the "invar effect" in these samples with incipient and well-established strain glass. However, this should be confirmed with specific measurements of thermal expansion coefficient, not performed in the present work.

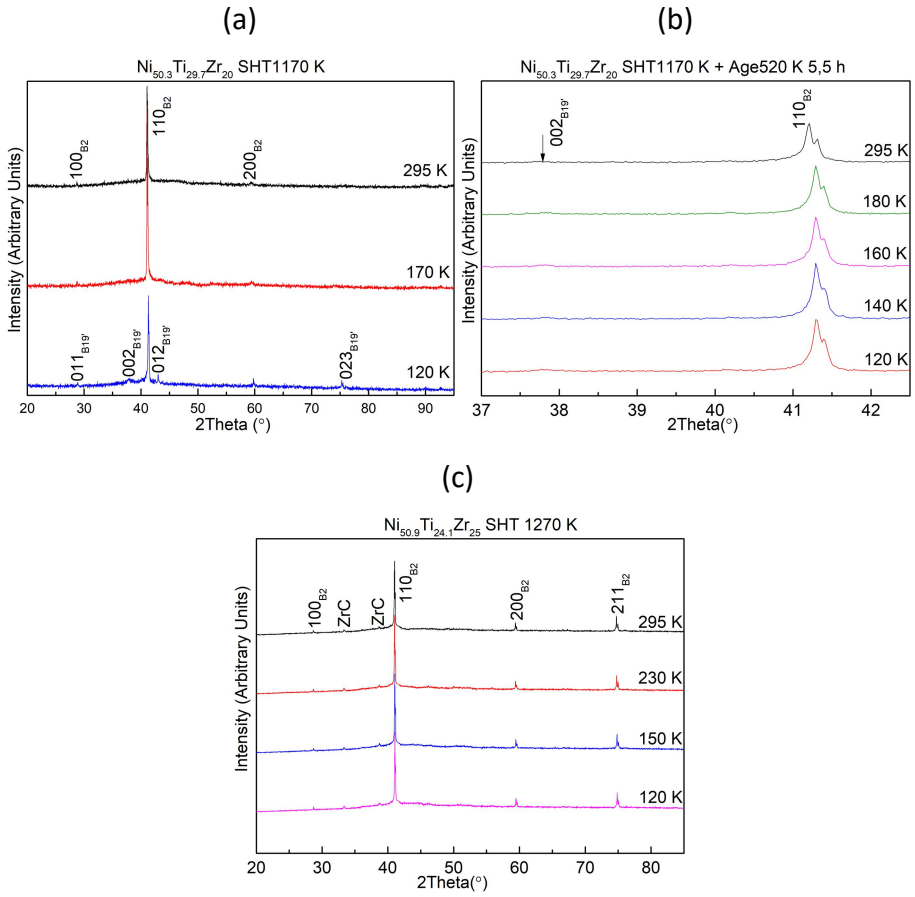

Fig. 3.2.8. XRD spectra at different temperatures for: (a) $Ni_{50.3}Ti_{29.7}Zr_{20}$ SHT alloy, (b) $Ni_{50.3}Ti_{29.7}Zr_{20}$ SHT alloy and additional ageing at 520 K for 5.5 h, (c) $Ni_{50.9}Ti_{24.1}Zr_{25}$ SHT alloy.

3.2.4 Mechanical Experiments

As it has been discussed in Chapter 1, some alloys with strain glass demonstrate the stress-induced martensitic transformation and superelasticity effect [44-46]. Therefore, the superelasticity effect has been investigated in the $Ni_{50.3}Ti_{29.7}Zr_{20}$ alloy, and the results are shown in Fig. 3.2.9. The solution heat treated specimen shows normal martensitic transformation in the DSC and a good superelasticity response with 5% recoverable strains at temperatures above A_f, from 310 K to 370 K (Fig. 3.2.9 (a)), with less than 0.2% irrecoverable strain. Moreover, the initial elastic deformation shows basically overlapped curves for all temperatures due to the low temperature dependency of the elastic modulus, as will be shown in the next section. The critical stress for transformation shows a clear temperature dependence. It is also worth to note the high strength of this material, being able to resist stress levels above 1 GPa.

Figs. 3.2.9 (b) and (c) present the stress-strain curves for samples with additional ageing at 520 K for 10 days and 14 days, respectively. Based on the DMA tests in Fig. 3.2.2, the specimen aged for 10 days has not formed the strain glass yet but possesses a microstructure that suppresses the normal martensitic transformation, for which it is considered as an intermediate state. It still demonstrates the stress

induced martensitic transformation, as shown in Fig. 3.2.9 (b), with more inclined plateau, narrow hysteresis upon loading-unloading cycles and a lower temperature dependence compared to SHT specimen. On its turn, the sample aged for 14 days at 520 K shows the strain glass state with an ideal T_0 temperature of 230 K, as measured by DMA in Fig. 3.2.2 (f). Hence, the mechanical test temperatures have been selected in the unfrozen state above T_0 up to 295 K, as shown in Fig. 3.2.9 (c). The sample shows smooth σ - ε loops with no plateau and 4% recoverable strain, relatively slim hysteresis and very little temperature dependence, mostly visible only at the end of the loading curves. The inclined stress-strain curves can be interpreted in terms of the microstructure of unfrozen strain glass which contains disordered internal stress fields induced by nano-domains that need to be overcome by extra external stress, resulting the smooth hysteresis loops with reduced hysteresis [27]. This argument will be further developed in the next paragraphs.

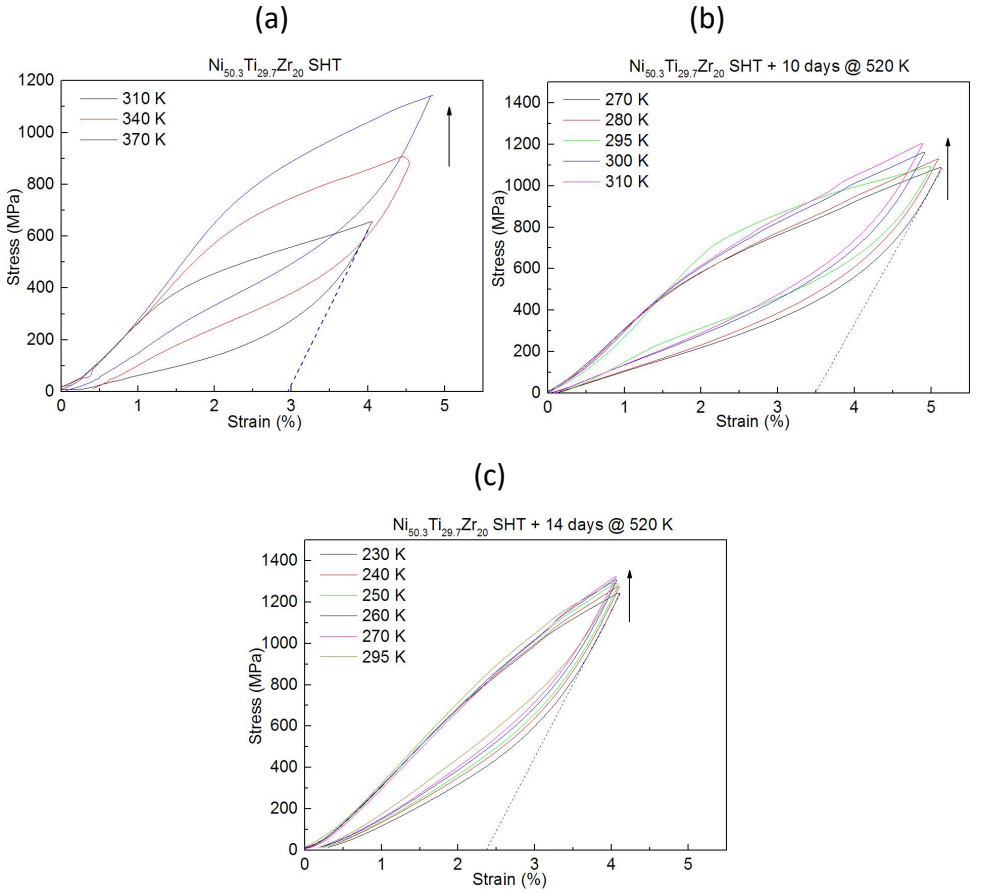

Fig. 3.2.9. Stress-strain curves of $Ni_{50.3}Ti_{29.7}Zr_{20}$ alloy for different thermal treatments: (a) solution heat treated at 1170 K for 1 h, (b) additional ageing for 10 days at 520 K, (c) additional ageing for 14 days at 520 K.

The shapes of the σ - ε curves of strain glasses reported in literature show wide variability. For some cases corresponding to SG induced in binary NiTi alloys by high Ni doping [17, 44] or Ni_4Ti_3 nanoprecipitates [46], curves with a sharp plateau and large recoverable strains above 6% are reported, which are attributed to the

reversible stress-induced transition to B19’ martensite. In these cases, the yield stress exhibits temperature dependence. In contrast, for the SG induced by cold rolling in $Ni_{50.8}Ti_{49.2}$ [33], composed of B19’-type nanodomains, smooth σ - $\mathcal{E}$ loops with no plateau and very little dependence on temperature are obtained. This is the same behavior observed in the present Ni-Ti-Zr alloys with strain glass created by the precursor H phase. The quasilinear deformation suggests the existence of a broad spectrum of defects responsible for the SG (either dislocations networks with different size/density or precursor H-phase nanodomains with different size, local composition, inter-domain distance and strain fields in the surrounding B2 matrix) that create a broad distribution of local M_s values for the martensitic transformation (and σ_s values for the stress-induced transition) in the B2 matrix at a fine scale. As a result, an increasing number of B19’-like nanodomains would be formed upon cooling. The microstructure of the present Ni-Ti-Zr alloys in the SG state is schematized in Fig. 3.2.10 for three levels of increasing stress, $0 < \sigma_1 < \sigma_2$. The black ellipses represent the precursor H-phase nanodomains responsible for the SG state, while the B19’-like nanodomains are represented by ellipses of red, yellow, blue, and green, corresponding to different orientation variants. Application of stress causes two effects: i) growth of the nanodomains of the variant favored by the direction of the applied stress, represented in red color in Fig. 3.2.10, which implies the stress-induced transformation of the surrounding B2 matrix, and ii) reorientation of the other nanodomains towards the favored variant. The precursor H phase and martensitic nanodomains of other variants limit the stress-induced growth of red domains to the low spatial scale, even under the highest stress levels (as schematized in Fig. 3.2.10), which reduces the macroscopic strain to ~4% in the present case (Fig. 3.2.9 (c)), below the maximum strain levels achieved in the normal B2-B19’ transition (~6 - 10%).

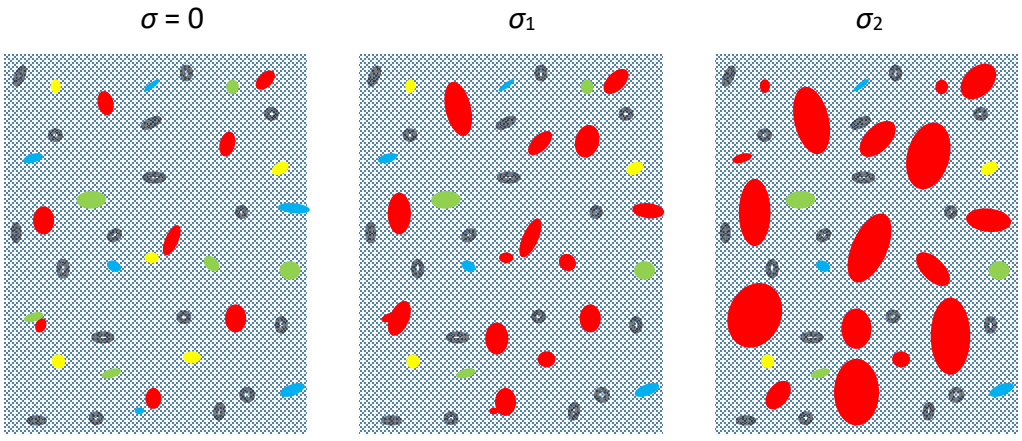

Fig. 3.2.10. Schematic diagram of microstructural evolution related to an increase of applied external stress ($0 < \sigma_1 < \sigma_2$).

To understand the structural evolution under stress at different temperatures, we may consider the typical temperature dependence of the apparent yield stress (onset of inelastic deformation) shown by alloys with normal martensitic transformation,

schematized in Fig. 3.2.11 (a). Above the Ms temperature, the stress increases linearly with temperature according to the Clausius-Clapeyron equation for the stress-induced transformation (red line in Fig. 3.2.11 (a)). Below the transition point, there is usually a lower temperature dependence with negative slope, related to the variant reorientation process in martensite (also referred to as detwinning) [13, 189], represented by the blue line. Assuming a broad distribution of local M_s values at a fine spatial scale, the phase diagram takes the form shown in Fig. 3.2.11 (b), where a discrete set of transformation/reorientation lines corresponding to different local M_s values (M_{s1}, M_{s2}..., M_{s7}) are drawn. The distribution of local M_s values is schematically represented by the green Gaussian-type curve. The transformation/reorientation lines corresponding to local M_s values located at the tails of the distribution curve are drawn in thinner lines, to visualize the fact that they have low "populations" and, then, involve a low volume fraction of material. A mechanical test performed at a certain temperature can be represented by a vertical line. In such a phase diagram, the vertical lines continuously intersect red or blue lines, producing either growth of favored martensitic nanodomains or reorientation of non-favored ones, respectively. These events develop discrete amounts of strain proportional to the population of their local M_s value in the broad distribution. As a result, the macroscopic σ - $\mathcal{E}$ curves are quasilinear in shape with no plateau. Moreover, for a temperature interval located around the center of the distribution, represented by the vertical lines at temperatures T_1 and T_2 in Fig. 3.2.11 (b), most of red/blue lines intercepted in a wide stress range correspond to local M_s values with similar populations, producing similar amounts of macroscopic deformation. Therefore, macroscopic σ - $\mathcal{E}$ curves with little temperature dependence can be expected from this qualitative model, as observed in the present Ni-Ti-Zr alloys (Fig. 3.2.9 (c)). It is worth noting that at high temperatures (around T_2), the reorientation events only play a significant role for low stress levels and the transformation process is dominating at high stresses. However, as temperature decreases and approaches T_1, the contribution of the reorientation process extends to higher stress levels whereas the transformation events at high stresses become less significant, as they involve low local M_s values with lower population.

As stated above, the $Ni_{50.3}Ti_{29.7}Zr_{20}$ SHT alloy aged for 10 days at 520 K represents an intermediate situation between strain glass and normal transformation. The precursor H-phase nuclei are not yet well developed and, then, they create a narrower distribution of M_s temperatures in in this sample, which leads to σ - $\mathcal{E}$ curves with intermediate characteristics compared to the other two extreme cases.

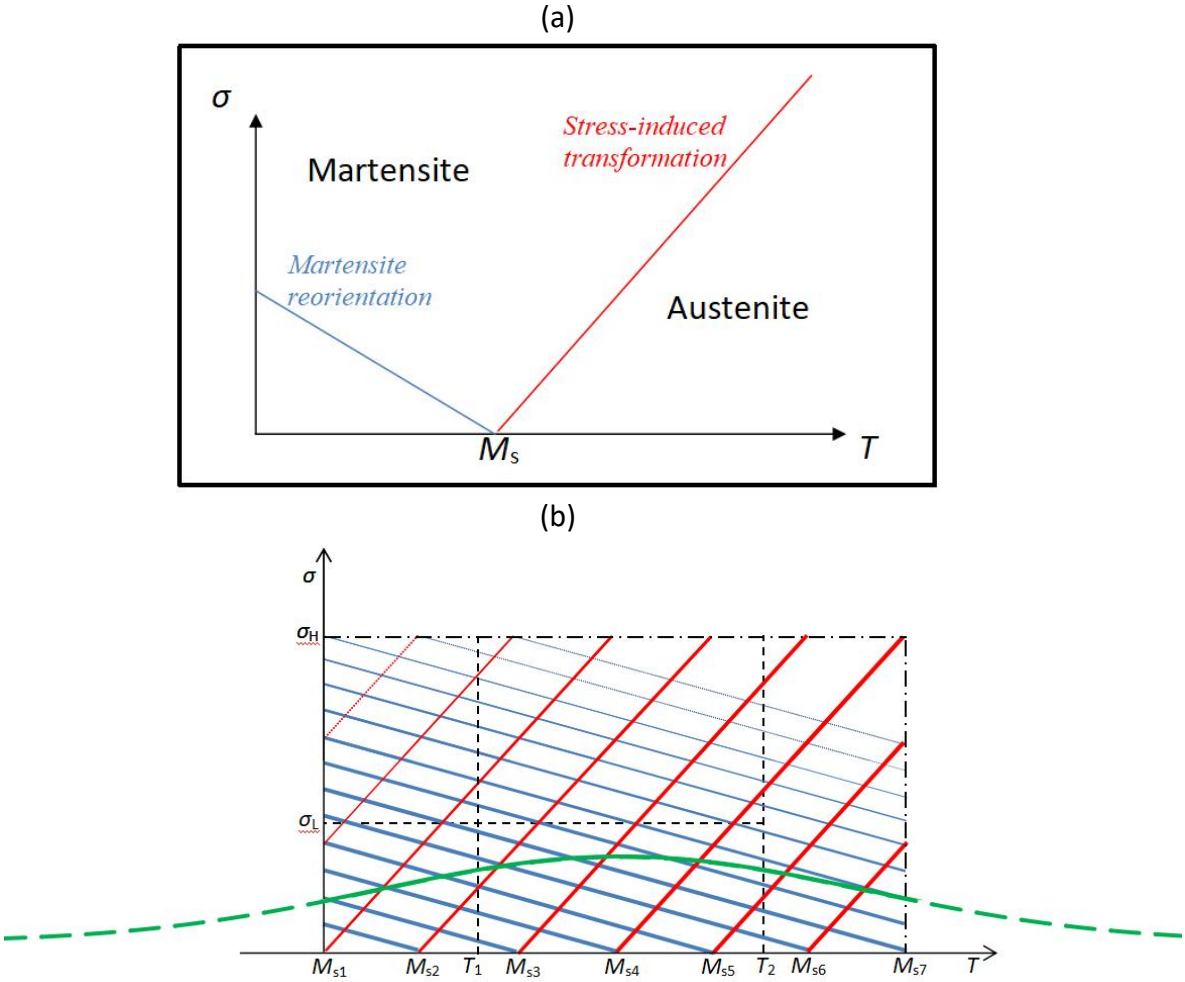

Fig. 3.2.11. (a) Schematic plot of the critical stress for martensite reorientation (blue line) and stress-induced transformation (red line) in an alloy with normal martensitic transformation. (b) Schematic diagram of temperature-stress relationship for stress induced MT and martensite reorientation with a broad local M_s distribution above T_0.

3.2.5 Resonant Ultrasonic Techniques and Electric Resistivity Measurement Supplementary Experiments

The resonant ultrasonic experiments were performed on the $Ni_{50.9}Ti_{24.1}Zr_{25}$ SHT alloy, $Ni_{50.3}Ti_{24.7}Zr_{25}$ aged 6 days (both with strain glass state) and $Ni_{50.3}Ti_{29.7}Zr_{20}$ SHT alloy (with normal transformation) in order to provide more accurate data of elastic modulus and internal friction compared to DMA measurements. In addition, electric resistivity tests were used to determine the possibility of residual martensitic transformation. As it is already known, the DSC has limited capacity to detect clear signal when the thermal effect released by the sample is very low, as it is the case for a MT extended over a large temperature range.

The resonant ultrasonic technique uses a resonator composed of two quartz crystals

rigidly attached to the sample to test [190]. An AC voltage of controllable frequency and amplitude is applied to one of the quartz crystals (drive crystal) to excite the corresponding vibration in the whole system, while the other quartz crystal (gauge crystal) is used to measure the vibration amplitude of the system. The excitation frequency is scanned over a certain interval to measure the resonant frequency of the whole system, f_t (frequency giving the maximum of the vibration amplitude). Then, resonant conditions are kept during all the measurements through a positive feedback loop on the gauge voltage. The damping of the whole system, δ_t, is determined from ratio of drive and gauge voltages. The *E* modulus and *IF* of the sample can be obtained based on the equations below:

$$E = 4\rho l^2 f_s^{\,2} \quad \text{(Eq. 3.2.3)}$$

$$f_s = \frac{(m_s + m_q) f_t - m_q f_q}{m_s} \quad \text{(Eq. 3.2.4)}$$

$$\delta_s = \frac{(m_s + m_q)\delta_t - m_q \delta_q}{m_s} \quad \text{(Eq. 3.2.5)}$$

$$IF(\tan\theta) = \frac{\delta}{\pi} \quad \text{(Eq. 3.2.6)}$$

The elastic modulus *E* is calculated from Eq. 3.2.3, where ρ is the density of the tested sample (about 6.81 g/cm^3), l is the sample length and f_s is the resonant frequency of the sample. Eq. 3.2.4 allows to extract the frequency of the sample (f_s) from the frequency of the whole resonator (f_t) measured by the device, which depends on the mass of the sample (m_s), the mass of the quartz crystals (m_q) and the intrinsic frequency of the quartz crystals (f_q = 91400 Hz). The quartz crystals have the mass of 1 g each. In the same way, Eq. 3.2.5 is used to extract the damping of the sample (δ_s) from the total damping (δ_t) measured by the equipment. Damping of the quartz crystals (δ_q) is negligible. Finally, Eq. 3.2.6 relates the damping (δ) with the *IF* ($\tan\theta$) measured by the DMA, where θ is the phase shift between the stress and strain sinusoidal functions. It should be noted that the quartz used in the resonator cannot endure temperatures above 350 K. Hence, two testing chambers have been used for measurements above room temperature (high temperature chamber) or below it, down to 170 K (low temperature chamber). In the high temperature chamber, an additional intermediate quartz rod tolerating high temperature is used to separate the measuring quartz crystals from the hot sample and transmit the vibration between them. However, this additional quartz possesses the intrinsic resonant frequency varying with temperature. Therefore, an initial scan with only the quartz crystals (resonator and additional high temperature quartz) without sample has to be measured first, to determine the temperature dependence of f_q. The same configuration is also used in the low temperature chamber to keep consistency. The measurements were made with a constant strain amplitude around 10^{-5} - 10^{-4} and

cooling/heating rate of 2 K/min.

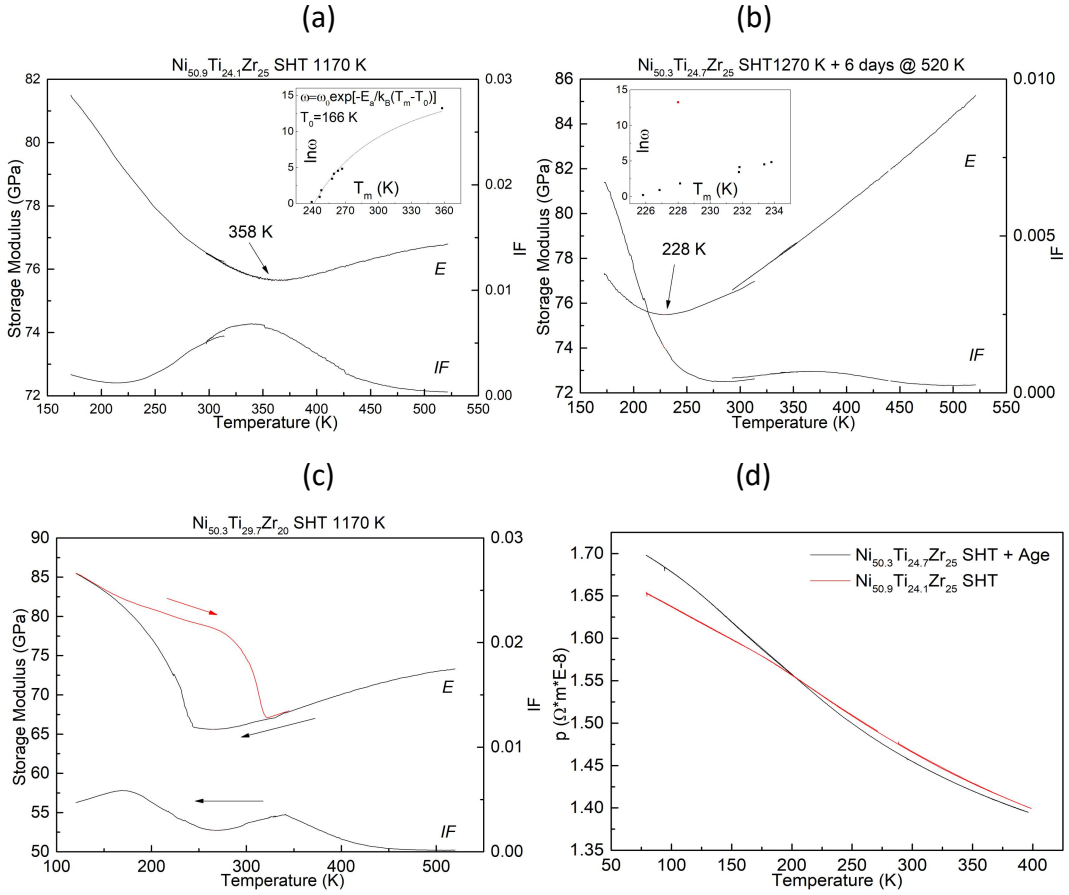

Fig. 3.2.12. resonant ultrasonic measurement of (a) $Ni_{50.9}Ti_{24.1}Zr_{25}$ SHT 1170 K for 1 h specimen, and (b) $Ni_{50.3}Ti_{24.7}Zr_{25}$ SHT 1270 K for 1 h with additional ageing at 520 K for 6 days specimen, and (c) $Ni_{50.3}Ti_{29.7}Zr_{20}$ SHT 1170 K for 1 h specimen. (d) Electric resistivity of the two alloys under cooling heating cycle.

Figs. 3.2.12 (a), (b), and (c) present the *E* modulus and *IF* (damping) values measured by resonant ultrasonic technique, which is a much accurate test method in comparison with DMA. The slight discontinuity that can be observed in the *E* modulus and *IF* curves around 300 K (or 330 K) is caused by the change of testing chamber. Fig. 3.2.12 (d) exhibits the electric resistivity measurement of the $Ni_{50.9}Ti_{24.1}Zr_{25}$ and aged $Ni_{50.3}Ti_{24.7}Zr_{25}$ specimens with suppressed martensitic transformation in the DSC. The resistivity continuously increases during cooling without sudden drop of value and there is no hysteresis after heating up, which further proves the absence of martensitic transformation in these samples. In addition, the different slopes of the two samples may reflect small differences in the microstructure of both alloys.

Similar to the DMA results, the $Ni_{50.9}Ti_{24.1}Zr_{25}$ SHT specimen presents an *E* modulus dip and a corresponding *IF* peak during cooling in the resonant ultrasonic measurement shown in Fig. 3.2.12 (a). However, as the result of frequency

dependence and the high frequency levels used in this technique (close to 90 kHz), the peak temperature of *IF* and dip temperature of *E* modulus shift to higher values about 358 K, marked by an arrow in Fig. 3.2.12 (a). The corresponding resonant frequency of the specimen is 88490 Hz, and the absolute value of the *IF* peak is decreased in comparison with DMA results. In addition, the levels of *E* modulus measured by the resonant technique, above 78 GPa, are significantly larger than those measured by DMA. The dip temperature in the elastic modulus is combined with the results of DMA measurement, and again is plotted based on the Vogel-Fulcher relationship in the inset of Fig. 3.2.12 (a). The plot presents a good fit with the relationship, which confirms the exponential dependency between frequency and temperature over a wide frequency range up to 10^5 Hz and completely rules out a linear relationship, although the new T_0 temperature obtained, 168 K, is changed in relation to the value fitted only with DMA data. Moreover, the *E* modulus only presents a small drop of about 1.2 GPa when cooling from 522 K to 358 K, which gives a very low slope of 0.0073 GPa/K. Therefore, the highly accurate resonant ultrasonic technique confirms the low temperature dependence of storage modulus observed by DMA and still indicates the “elinvar”-like effect appearing in the $Ni_{50.9}Ti_{24.1}Zr_{25}$ SHT alloy with SG state.

Fig. 3.2.12 (b) shows the results of $Ni_{50.3}Ti_{24.7}Zr_{25}$ SHT alloy with additional ageing at 520 K for 6 days, with suppressed MT. In this case, the *E* modulus presents a pronounced softening with a continuous decrease by about 9.8 GPa during cooling from 521 K to 228 K (average rate of 0.033 GPa/K) and reaches a minimum at 228 K. This is 4.5 times larger temperature dependence than the previous alloy. The *IF* shows a very small peak at about 360 K followed by a sudden rapid increase below 250 K that could be related to the *E* modulus dip. This will be further discussed below. Unlike the $Ni_{50.9}Ti_{24.1}Zr_{25}$ alloy, the modulus dip observed in the aged $Ni_{50.3}Ti_{24.7}Zr_{25}$ alloy is not shifted by the high frequency used in the ultrasonic experiments and remains in a similar temperature as the DMA results (Fig. 3.2.3 (e)). So, the new data point is located completely away from the DMA data in the $\ln\omega$ vs. T_m plot and does not fit the Vogel-Fulcher relationship, as shown in the inset of Fig. 3.2.12 (b). Hence, despite the suppressed MT in the DSC and frequency dependence observed by DMA, the new experiments would indicate that the $Ni_{50.3}Ti_{24.7}Zr_{25}$ alloy aged for 6 days at 520 K has not yet achieved a completely established SG state.

Fig. 3.2.12 (c) presents the resonant measurements of $Ni_{50.3}Ti_{29.7}Zr_{20}$ SHT specimen. This material shows the martensitic transformation in the DSC. The *E* modulus presents again an extended softening effect in austenite and decreases from about 73.3 GPa at 520 K to the minimum value about 65.6 GPa at 265 K and then it grows up to 85.5 GPa at 120 K due to the martensitic transformation. This gives an average slope of 0.030 GPa/K in the austenite state, which rules out the apparent elinvar effect shown by the DMA results (Fig. 3.2.2 (a)). Upon heating up, there is a clear reverse transformation signal in the E-modulus curve, accompanied with a wide hysteresis about 84 K. The M_s and A_f can be determined as 245 K and 323 K,

respectively; these values are similar to the DSC results (Fig. 3.2.1). It should be noted that the heating-cooling cycle was first performed in the high temperature chamber followed by cooling-heating cycle in the low temperature chamber with a crossover temperature at ~340 K, which lies just at the end of the reverse transformation in the *E* modulus signal (measured in the low temperature chamber). Concerning the *IF* signal, the combined cooling process from both temperature chambers is shown in Fig. 3.2.12 (c), and, which exhibits two peaks at about 341 K and 169 K, respectively. The peak around 350 K also appears in the other two alloys but are caused by different reasons. The peak at 169 K is close to the direct transformation observed in *E* modulus and can be related to the direct martensitic transformation. In this case, the large increase in frequency tends to reduce the transient component of the internal friction, but this is compensated by the low strain amplitude level used in the ultrasonic experiments. The peak at 341 K is close to the reverse transformation observed in the *E* modulus signal on heating, but cannot be attributed to the reverse transformation, because the *IF* peak occurs on cooling. Its origin will be discussed in the next paragraph.

It is known that the Ni-Ti-based alloys can be unintentionally contaminated by hydrogen during the water quenching from high temperature, even with samples encapsulated in quartz ampoules. This is due to a chemical reaction of water with Ti [191]. The *IF* curves of these alloys are sensitive to the hydrogen content and usually present a relaxation peak (additional to other peaks originated from phase transformations) related to the interaction of hydrogen atoms with moving defects under the oscillatory stress (typically the martensite twin boundaries or austenite-martensite interfaces) [191-194]. The hydrogen relaxation peak appears at different temperatures, depending on the alloy composition: ~150 K for binary Ni-Ti [193], ~250 K for Ni-Ti-Cu [191] or below 100 K for Ti-Ni-Fe [192]. Mazzolai *et al*. [193] studied the $Ni_{52}Ti_{48}$ alloy with suppressed martensitic transformation and found a frequency dependent *E* modulus dip fulfilling the Vogel-Fulcher relationship (corresponding to the strain glass freezing), together with a frequency dependent *IF* peak at temperatures very close to the *E* modulus dip. However, the authors did not attribute the *IF* peak to the strain glass, but to the effect of hydrogen, since the frequency dependent *IF* peak only appeared in H-doped samples and was absent in H-free samples (annealed at high temperature under high vacuum to release the hydrogen). This H-related *IF* peak was shifted to higher temperatures and decreased in height with increasing frequency [193]. These are the same features exhibited by the DMA results in the present Ni-Ti-Zr alloys with strain glass (Figs. 3.2.2 (f) - (h) and 3.2.3). Therefore, the *IF* results obtained by DMA and ultrasonic measurements need to be reconsidered in terms of the effect of hydrogen.

The *IF* peak detected by DMA in $Ni_{50.9}Ti_{24.1}Zr_{25}$ SHT alloy between 200 K and 240 K reaches values *IF* > 0.02 (Figs. 3.2.3 (a) - (d)) and shifts to ~350 K in the ultrasonic measurements, together with the *E* modulus dip, while for the other alloys with suppressed transformation, the peak values detected by DMA are only *IF* ~0.01.

Therefore, for $Ni_{50.9}Ti_{24.1}Zr_{25}$ the *IF* peaks observed by DMA and ultrasonic experiments may be composed of two parts, one related to the strain glass freezing (following the Vogel-Fulcher relationship up to ultrasonic frequencies) and the other arising from the effects of hydrogen. The latter seems to have a similar frequency dependence as the strain glass freezing and also shifts to ~350 K at ultrasonic frequencies. Instead, the $Ni_{50.3}Ti_{24.7}Zr_{25}$ SHT alloy with additional ageing at 520 K for 6 days presents a complex behavior. It shows a suppressed transformation in the DSC, but the *E* modulus dip observed by DMA and ultrasonic experiments does not represent a complete freezing of the martensitic-like nanodomains, as it does not follow the Vogel-Fulcher relationship up to ultrasonic frequencies. Then, the *IF* peaks obtained by DMA around 220 K would contain both, a contribution related to the dip in the *E* modulus and the effect of hydrogen, while the *IF* at ultrasonic frequencies splits into an incipient peak at ~200 K (not complete due to an insufficient cooling) related to the modulus dip and a small peak at ~350 K that would correspond to the hydrogen effect (Fig. 3.2.12 (b)). In the alloys with suppressed normal transformation, no large martensitic twin boundaries or parent/martensite interfaces exist, but small martensitic-like nanodomains that would be less influenced by hydrogen, producing a small hydrogen peak. Finally, for the $Ni_{50.3}Ti_{29.7}Zr_{20}$ SHT with normal transformation, the *IF* at ultrasonic frequencies shows a peak at ~350 K upon cooling (Fig. 3.2.12 (c)), coincident in temperature with the hydrogen peak of the other alloys. However, the alloy is in austenite state at this temperature and there are no austenite/martensite interfaces that may interact with hydrogen atoms. Then, it seems not plausible to assume that the ultrasonic frequencies may shift the hydrogen peak to ~350 K in this alloy. Therefore, more dedicated work is needed to completely understand the anelastic behavior of these alloys, influenced by hydrogen, which is out of the scope of this thesis.

3.3 Summary of Ni-Ti-Zr alloys

(1) $Ni_{50.3}Ti_{24.7}Zr_{25}$

As it is known, the ageing induced H-phase precipitates with proper sizes can elevate the transformation temperature in Ni-rich Ni-Ti-Hf and Ni-Ti-Zr alloys and generate good shape memory response [57, 121, 140, 141]. The composition of matrix is changed as the result of long range atomic diffusion during ageing, where the excess Ni atoms tend to incorporate into the precipitates leaving a Ni-lean matrix with higher transformation temperatures. The mechanical properties are improved due to the coherency between the H phase and the B2 austenite [57]. When small precipitates (few tens of nm in size) are embedded in austenite with good coherency, the surrounding strain fields caused by the martensitic transformation can be easily accommodated, and the martensite plates can absorb many precipitates inside them (Fig. 3.1.5). However, over developed precipitates with no coherency, like the furnace cooled sample shown in Fig. 3.1.6, cannot be absorbed by individual martensite plates and strongly restrict the growth of the martensite plates to the areas between

the big particles. These characteristics have been reproduced in this work on the $Ni_{50.3}Ti_{24.7}Zr_{25}$ alloy.

The previous studies of $Ni_{50.3}Ti_{29.7}Zr_{20}$ or $Ni_{50.3}Ti_{29.7}Hf_{20}$ concluded that ageing at 770 K or 820 K for 3 h produces the best thermomechanical response at rather high temperatures, around 400 K. These treatments have been investigated here for $Ni_{50.3}Ti_{24.7}Zr_{25}$ and the thermomechanical response increases in temperature up to ~450 K due to the increase of Zr content. The functional properties are very similar for both thermal treatments and give total transformation strain values in compression around 1% under applied stresses in the range 400 - 600 MPa, but only ~0.8% recoverable strain, due to a significant amount of irrecoverable strain, ~0.2%, and hysteresis about 75 - 90 K. This is a worse behavior compared to the alloy with 20 at.% Zr, which shows 1.6% transformation strain under 300 MPa in tension with practically negligible irrecoverable strain [140]. In turn, the alloy with 20 at.% Hf still presents better properties, with 3.3% recoverable strain in compression and low hysteresis, ~25 K. For the thermal treatments studied, the size and morphology of the H-phase precipitates formed in $Ni_{50.3}Ti_{24.7}Zr_{25}$ is similar to $Ni_{50.3}Ti_{29.7}Zr_{20}$. The main difference comes from the number of precipitates, which is much higher in $Ni_{50.3}Ti_{24.7}Zr_{25}$. Therefore, the excessive precipitation induced by the increment in Zr content hinders the functional properties of the alloy, in the sense to reduce the recoverable transformation strain and increase the hysteresis.

(2) Strain glass

The experimental results prove that strain glass transition can exist in the Ni-Ti-Zr alloys with adequate thermal treatment, which is associated with the early stage of formation of H-phase precipitates. As commented in the Introduction chapter, the H phase is actually a superstructure derived from the B2 austenite phase but with redistribution of Ti and Zr atoms in their sublattice [57]. This requires a significant diffusion of these atoms and, normally, the H phase can be only induced by thermal treated above 720 K. Therefore, ageing the $Ni_{50.3}Ti_{29.7}Zr_{20}$ alloy at 520 K gives no sign of developed H-phase precipitates (Fig. 3.2.5) but only B2 fundamental spots with diffuse scattering in DP, indicating that atoms can only move in short range due to the limited thermal diffusion at 520 K. The diffuse streaking is close, but not coincident, to the positions of H phase superlattice reflections, which can be interpreted as the locally reordered Ti and Zr atoms would concentrate to form the precursor nuclei of H phase. Such a nanoscale heterogeneity generates the random strain fields that suppress the martensitic transformation, substituted by B19'-like nanodomains in coexistence with the precursor nuclei of H phase.

The ability to from SG states depends on the alloy composition: $Ni_{50.9}Ti_{24.1}Zr_{25}$ is in SG state just after the solution heat treatment, $Ni_{50.3}Ti_{24.7}Zr_{25}$ needs additional ageing at 520 K for 6 days and $Ni_{50.3}Ti_{29.7}Zr_{20}$ needs 14 days. So, the SG state is easier in compositions with enhanced Ni and Zr content. On its turn, the H phase is rich in Ni,

Zr and lean in Ti in comparison with B2 matrix [57], so the ability to form SG is perfectly correlated with the tendency to increase the H-phase precipitation. This observation supports the idea of the precursor H-phase precipitation as origin of the SG state observed in Ni-rich Ni-Ti-Zr alloys, explained in the previous paragraph. For the $Ni_{50.9}Ti_{24.1}Zr_{25}$ alloy, the atomic redistribution to form the precursor H-phase nuclei takes place during the water quench after SHT, with no need of further ageing.

The $Ni_{50.3}Ti_{29.7}Zr_{20}$ alloy in the unfrozen strain glass state presents remarkable mechanical properties: 4% recoverable strain with relatively low hysteresis, high strength above 1 GPa and nearly temperature independent σ - $\mathcal{E}$ curves. This can be suitable properties for applications in devices working at different temperatures that need a precise mechanical response.

Moreover, the alloys with 50.3 at.% Ni show an incubation period with suppressed martensitic transformation in the DSC, but not yet well established strain glass state. The details of this intermediate state of the alloys constitutes an interesting subject to be further studied in the future.

(3) Elinvar effect

The DMA results (Figs. 3.2.2 and 3.2.3) present a basically unchanged elastic modulus in a wide temperature range upon cooling for the three studied alloys, $Ni_{50.3}Ti_{29.7}Zr_{20}$, $Ni_{50.9}Ti_{24.1}Zr_{25}$ and $Ni_{50.3}Ti_{24.7}Zr_{25}$, after specific thermal treatment. This behavior of *E* modulus is called “elinvar” effect. For most of the solid materials, the elastic modulus increases during cooling because of the hardening effect derived from anharmonic atomic vibration. However, it is well known that alloys with thermoelastic martensite may exhibit the opposite behaviour, *i.e.*, gradual elastic modulus softening previous to the transformation during cooling arising from different premartensitic effects, which is stronger than the normal hardening effect resulting in an effective decrease of the elastic modulus on cooling. Liangxiang Zhang *et al*. [195] suggest a mechanism to explain this barely temperature independence of *E* modulus behavior in the alloys with strain glass transition instead of MT. It takes into account the formation of martensitic-like nano domains in a wide temperature range, which creates a limited and gradual softening of *E* modulus that compensates the normal modulus hardening due to anharmonic atomic vibration, resulting in a wide temperature range of stable *E* modulus [195].

The resonant ultrasonic technique used to accurately measure the *E* modulus only shows a nearly elinvar effect in the $Ni_{50.9}Ti_{24.1}Zr_{25}$ SHT alloy with SG transition, which only presents 1.5% change in a temperature interval of 162 K. In comparison, the $Ni_{50.3}Ti_{24.7}Zr_{25}$ with not well developed SG transition and the $Ni_{50.3}Ti_{29.7}Zr_{20}$ SHT alloy with normal MT show stronger temperature dependence of *E* modulus (softening) and absence of elinvar effect. These results are in line with the interpretation of the elinvar effect given above.

Chapter Ⅳ Ni-Mn-Ga-Cu/Sn

Ni-Mn-Ga polycrystalline ternary alloys show a high level of brittleness at the grain boundaries, as it was already explained in Chapter 1, being a potential problem to apply them as HTSMAs. A possible strategy to face this difficulty is introducing additional elements to induce precipitates of a ductile second phase, especially at the grain boundaries, with the purpose of improving the mechanical properties of these alloys. Cu is a promising candidate to alloy ternary Ni-Mn-Ga as it is relatively cheap, has a high intrinsic ductility, and not only can increase MTT proportional to the *e*/*a* value of the matrix [168], but also the resulting alloys present good mechanical properties [169]. Previous reports [58, 59, 196] have already investigated the functional properties of Ni-Mn-Ga-Cu alloys with high amount of Cu addition and different thermal treatments, and they reported very stable compositions. However, after prolonged ageing treatments, some alloys can develop a strong and quick precipitation, harming the thermal stability and reducing the MTT, especially in high Cu content alloys with ordered γ' phase [58]. Hence, in this chapter, the effect of low additions of Cu to Ni-Mn-Ga is investigated. One of the objectives is to investigate the possibility to induce nanometric precipitates of the second phase by proper thermal treatments, which normally improves the mechanical properties of the alloys. A second objective is to investigate the thermomechancial properties of quaternary alloys with low Cu content, which has not been studied yet. Furthermore, alloying with Sn has also been initially explored to obtain a potential candidate of Ni-Mn-Ga-X HTSMA.

4.1 Ni-Mn-Ga-Cu Characterization

4.1.1 Calorimetric Analysis

Table 4.1 presents the nominal composition of the Ni-Mn-Ga and Ni-Mn-Ga-Cu polycrystalline alloys studied in this thesis and their nominal electron valence per atom (*e*/*a*), together with the forward and reverse martensitic transformation peak temperatures, hysteresis, and average enthalpy change obtained from DSC thermograms. All the ingots were homogenized at 1295 K for 96 h, and slow cooled to room temperature inside the furnace: this treatment is denoted as "*as-treated*" specimens hereafter. As it can be seen, H1 and H2 are slightly Ni-rich ternary Ni-Mn-Ga alloys, while H3 - H5 are quaternary Ni-Mn-Ga-Cu alloys with the same Cu content (1 at.%), showing all of them a relatively small hysteresis (around 10 K), determined from the DSC thermograms as A_p–M_p. From the quaternary alloys, H3 and H4 exhibit the highest transformation temperatures, *e*/*a* ratio and enthalpy change, as well as the highest Ni content, which should enhance precipitation, and

therefore, these alloys were chosen for the present investigation. Finally, it should be noted that single crystals from H2 and H5 alloys have been previously studied by C. Picornell, *et al*. reporting very good superelasticity and shape memory effect (work presented at the International Conference on Ferromagnetic Shape Memory Alloys - ICFSMA '13 - in Boise, USA, with title “Superelasticity and shape memory properties of Ni-Mn-Ga high temperature SMA single crystals”).

Table 4.1. Nominal composition, nominal valence electron concentration (*e/a)*, experimental DSC peak temperatures of the forward and reverse martensitic transformation, hysteresis and average enthalpy change for the as-treated Ni-Mn-Ga and Ni-Mn-Ga-Cu alloys.

Alloy	Nominal composition	*e/a*	M_p /K	A_p /K	Hysteresis /K	Δ*H* / J/g
H1	$Ni_{51.2}Mn_{31.1}Ga_{17.7}$	7.828	493	504	11	15.2
H2	$Ni_{50.8}Mn_{31.5}Ga_{17.7}$	7.816	474	484	10	15.8
H3	$Ni_{50.3}Mn_{31.0}Ga_{17.7}Cu_{1.0}$	7.841	515	525	10	17.9
H4	$Ni_{50.5}Mn_{30.5}Ga_{18.0}Cu_{1.0}$	7.835	479	488	9	17.0
H5	$Ni_{50.0}Mn_{31.0}Ga_{18.0}Cu_{1.0}$	7.820	455	469	14	15.2

Fig. 4.1.1 shows the relationship between the transformation peak temperatures and the nominal *e/a* ratio from the alloys in Table 4.1. It can be seen from the overall tendency that the alloys with higher *e/a* ratio exhibit higher transformation peak temperatures, and vice versa. However, it should be noted that the transformation peak temperatures of studied alloys do not strictly follow a linear relationship as a function of *e/a* ratio, as a result of the difference between the real and nominal compositions. It is worth noting that the compositions of studied alloys are very close to each other and cause less than 0.04 difference in *e/a* ratio. Then, any small deviation during experimental alloy preparation produces visible effects in the highly magnified plot of Fig. 4.1.1. Furthermore, the Cu addition could influence the electron configuration of the alloy system, which could lead to separated *T* - *e/a* paths of alloys without (H1 - H2) and with Cu addition (H3 - H5), as seen in Fig. 4.1.1.

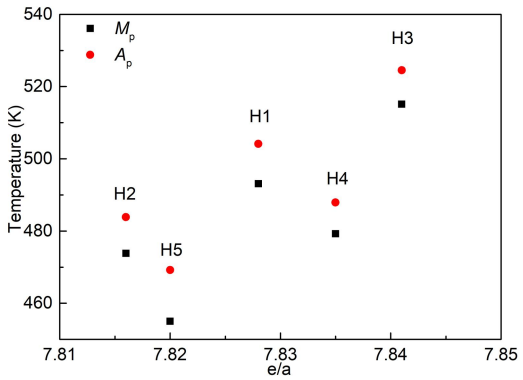

Fig. 4.1.1. Direct and reverse transformation peak temperatures as a function of the nominal valence electron concentration (*e/a*) of the as-treated alloys.

Ni-Mn-Ga-Cu H3 as-treated specimens from adjacent regions of the ingot were

encapsulated in quartz with partial Ar atmosphere and solution heat treated (SHT) at 1270 K for 1 h followed by water quench without breaking the quartz. Then, some specimens were aged at 670 K for either 24 h or 408 h followed by water quench. Fig. 4.1.2 (a) shows two consecutive DSC cycles of the aforementioned specimens, demonstrating that the H3 alloy has very high thermal stability under ageing at 670 K with little difference in M_p for the as-treated, aged 24 h and aged 408 h (515, 507, and 513 K, respectively). The average enthalpy change is also very stable, with 17.9 J/g, 17.2 J/g and 17.3 J/g, respectively.

Ni-Mn-Ga-Cu H4 as-treated specimens were subjected to a furnace cooling treatment, consisting of SHT at 1270 K for 1 h and, immediately afterwards, putting the sample directly into another furnace at 1070 K to be cooled down to 470 K in the furnace for 72 h, and finally water quenching. Despite that the prolonged ageing at so high temperatures should enhance precipitation processes, the DSC measurements after this thermal treatment (Fig. 4.1.2 (b)) exhibits basically the same peak transformation temperature (M_p = 482 K) and average enthalpy change (16.8 J/g) than the H4 as-treated state (Table 4.1), indicating that most probably no precipitates are formed.

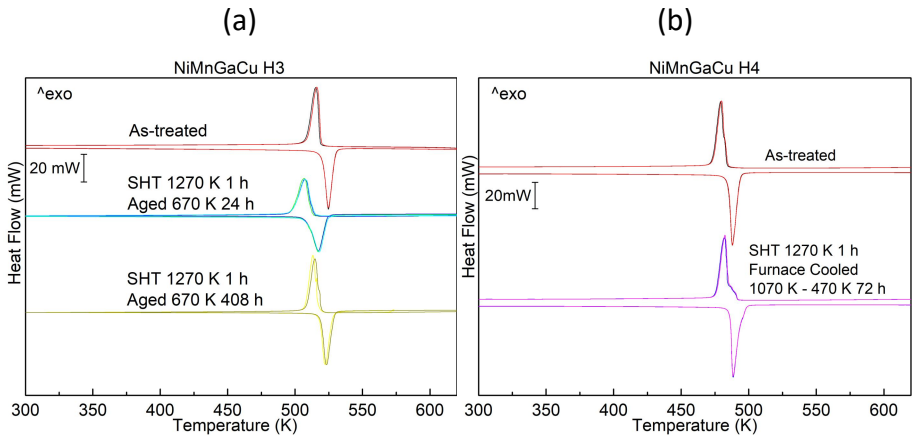

Fig. 4.1.2. DSC thermograms of (a) Ni-Mn-Ga-Cu H3 specimens, and (b) Ni-Mn-Ga-Cu H4 specimens after different thermal treatments.

4.1.2 XRD Analysis

The phase transformation of the Ni-Mn-Ga-Cu H3 as-treated alloy upon heating was monitored by *in-situ* XRD analysis, and Fig. 4.1.3 (a) shows a three-dimensional plot with the intensity as a function of 2theta and temperature. It should be noted that the patterns from 500 K to 550 K were obtained with a smaller 2theta range (35° - 60°), but including the major peaks, and with a smaller temperature interval (5 K or 10 K) in order to better track the transformation region, according to DSC results, without increasing too much tested time. However, the normalized XRD patterns show a clear development of the $220_{b.c.c.}$ austenite peak around 450 K (Fig. 4.1.3 (b)), which is about 50 K lower than the A_s obtained by DSC (Fig. 4.1.2 (a)). This difference

could be ascribed either to a partial transformation of the surface of the specimen (attributed to a lower A_s due to induced stresses introduced during polishing), or to an error of the temperature control system of the XRD. Fig. 4.1.3 (b) shows that the non-modulated b.c.t. martensite phase clearly exists from RT to 470 K in the H3 as-treated specimen, although the intensity of the martensite peaks are decreasing with increasing temperature due to the reverse martensitic transformation. Fig. 4.1.3 (b) also demonstrates that the $220_{b.c.c.}$ austenite peak starts to appear at 410 K, and becomes as high as $202_{b.c.t.}$ martensite peak at 450 K, which not necessarily means that the transformation is just in the middle.

Using the patterns in Fig. 4.1.3 (a), both the lattice parameters of martensite and austenite were obtained by the procedure detailed in Chapter 2 and plotted as a function of temperature in Fig. 4.1.3 (d). In this figure, the increase in a and a_0 with temperature is due to the thermal expansion, while c and the tetragonality (c/a) are decreasing with temperature because of the reverse transformation upon heating. Fig. 4.1.3 (e) presents the evolution of c/a_0 and a/a_0 ratios with temperature, clearly showing that both tend to 1 upon heating, *i.e.*, the difference between the martensite and the austenite lattice parameters reduces with temperature. In the region where austenite and martensite coexist, the $202_{b.c.t.}$ and $220_{b.c.c.}$ peaks are overlapped (see Fig. 4.1.3 (c) as an example), so the “psdvoigt” fitting method were used to deconvolute the multiple peaks and obtain the proper lattice parameters.

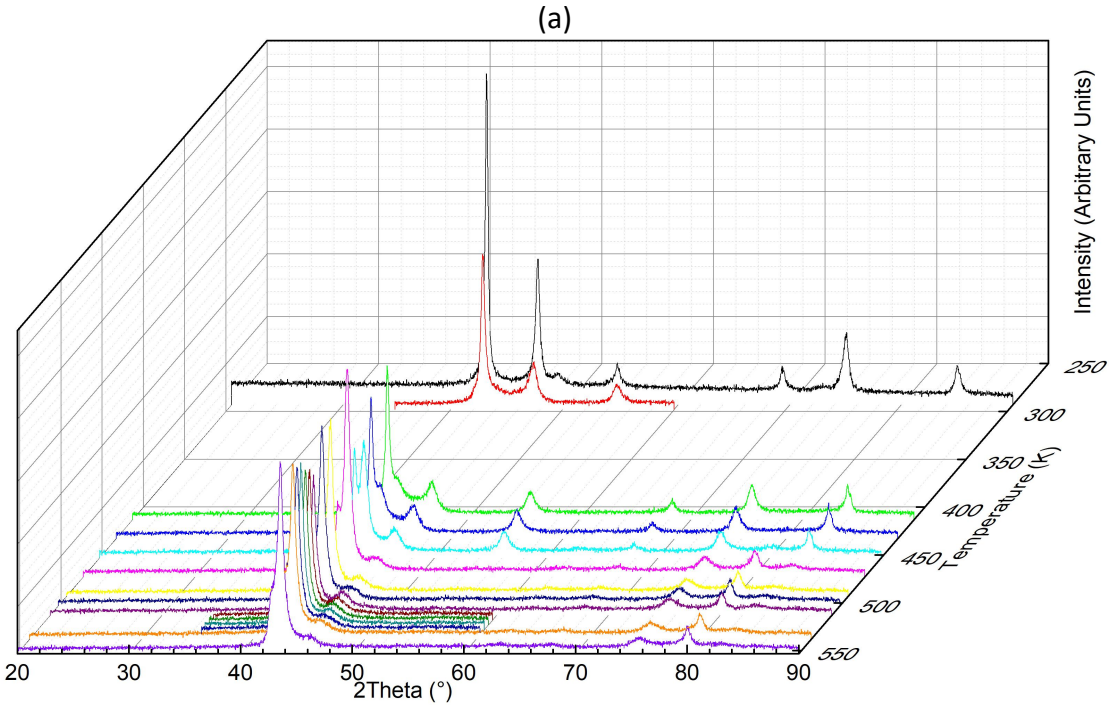

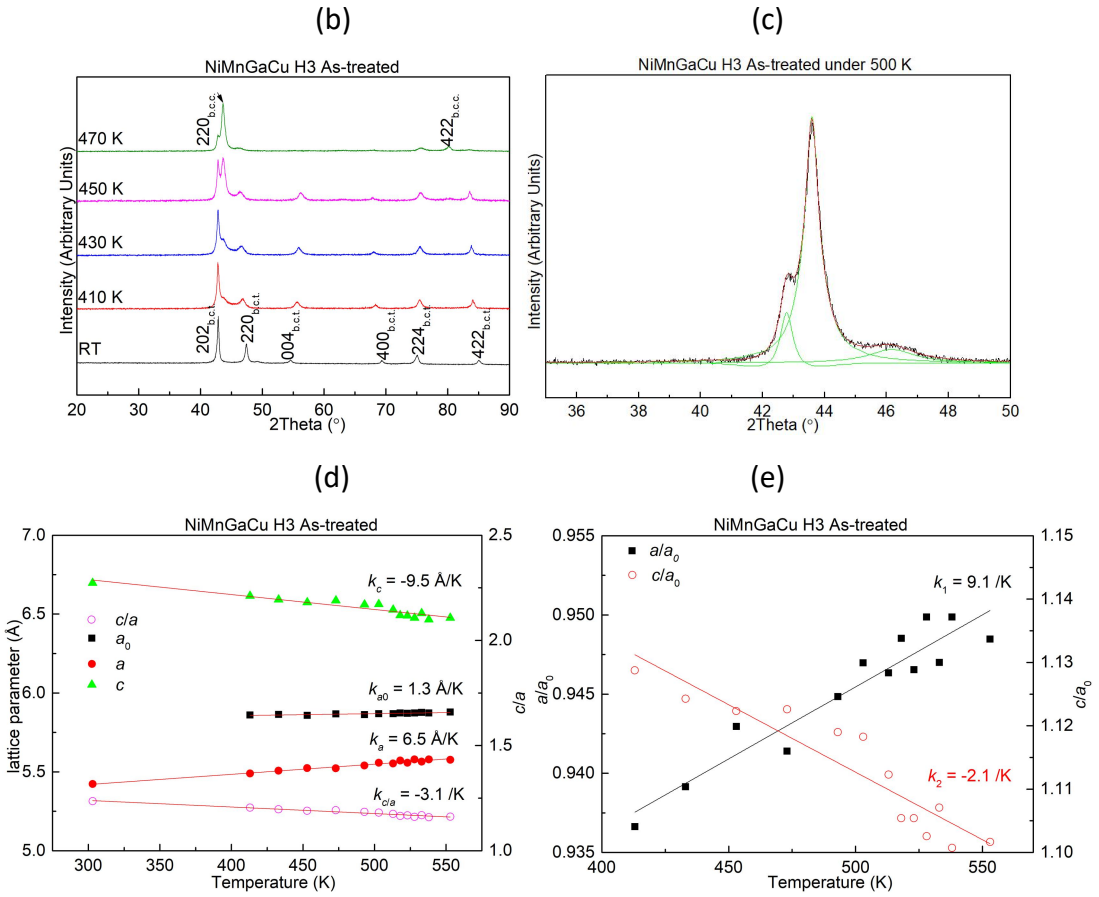

Fig. 4.1.3. (a) *In-situ* XRD analysis on Ni-Mn-Ga-Cu H3 as-treated alloy; (b) XRD patterns selected from the temperature region in (a) where the martensitic transformation occurs; (c) example of fitting in a peak with overlapped contributions from martensite and austenite; (d) lattice parameters of martensite and austenite as a function of temperature; (e) lattice parameters ratios between the two phases (a/a_0 and c/a_0).

4.1.3 Microstructure

The morphology of both alloys after the different thermal treatments has been observed by optical microscopy. Micrographs from the H3 as-treated alloy, aged at 670 K for 24 h and aged at 670 K for 408 h are shown in Figs. 4.1.4 (a), (b), and (c), respectively, whereas a micrograph from the H4 furnace cooled alloy is presented in Fig. 4.1.4 (d). The H3 as-treated specimen (Fig. 4.1.4 (a)) exhibits multiple martensite variants, with grains sizes from about 50 µm up to over 500 µm. The specimens (Figs. 4.1.4 (a), (b) and (c)) exhibit relatively large grains, all of them above several hundreds of microns, with some of them even larger than the size of the image. Moreover, some wide grain boundaries can be observed in aged 408 h specimens after etching (Fig. 4.1.4 (c)), which may indicate the initial steps of an early-stage fracture. On its turn, the furnace cooled H4 specimens exhibit some large grains with sizes over ~600 µm (Fig. 4.1.4 (d)). Besides the martensite variants, there are black spots in all the alloys, considered as carbide/oxides inclusions and/or the small holes associated to them after etching. However, no signs of precipitates have been

observed in the optical microscope for any of the Ni-Mn-Ga-Cu H3 and H4 alloys.

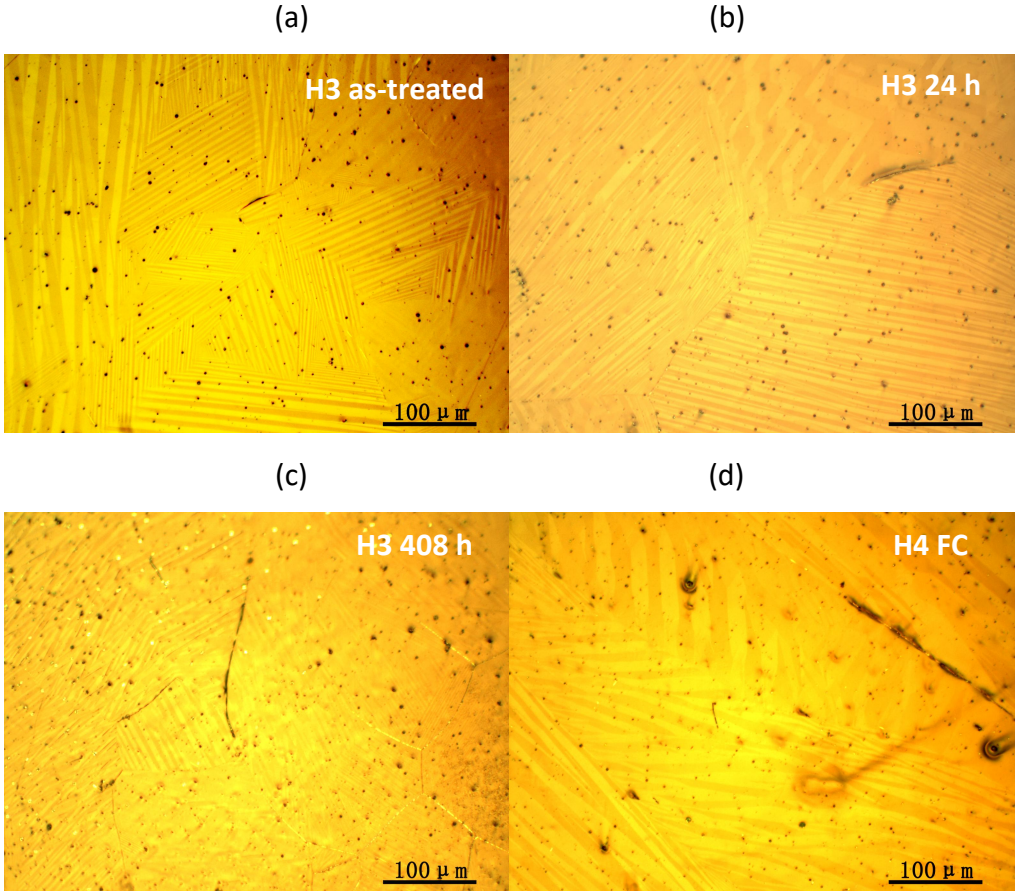

Fig. 4.1.4. Optical micrographs from Ni-Mn-Ga-Cu H3 alloys: (a) H3 as-treated; H3 after SHT 1270 K for 1 h and aged at 670 K for (b) 24 h and (c) 408 h; (d) H4 furnace cooled.

The Ni-Mn-Ga-Cu H3 as-treated alloy has been also observed in the TEM at room temperature, confirming that the entire samples are in martensite. Fig. 4.1.5 (a) shows a bright field image of one region of the matrix with internal twins at the left part of the image, and a large martensite variant at the right side of the image. Fig. 4.1.5 (b) presents a bright field (BF) image of another region, with fine martensite twins in both grains, and Fig. 4.1.5 (c) shows the corresponding selected area diffraction pattern (SADP) along the $[111]_{b.c.t.}$ zone axis confirming $(-202)_{M,T}$ as the internal twinning plane. All the diffraction patterns have been indexed as the non-modulated body centered tetragonal martensite, confirming the XRD analysis from the previous section. After ageing the alloy at 670 K for 408 h, the microstructure is essentially the same as the as-treated samples, as shown in Fig. 4.1.5 (d). The similar microstructures of the as-treated and aged samples is in agreement with the DSC results shown in Fig. 4.1.2 (a), where it was demonstrated that the transformation is stable after prolonged ageing at that temperature. Some particles like the transparent one in the center of Fig. 4.1.5 (d) are carbides or oxides, and they have been observed in all the studied alloys with any thermal treatment. These particles are not expected to play any important role in the martensitic

transformation. Finally, Fig. 4.1.5 (e) is a bright field image observed under two-beam condition from another zone of an aged specimen that was previously thermal cycled, showing a large amount of dislocations, which could be derived from the former step of DSC cycles.

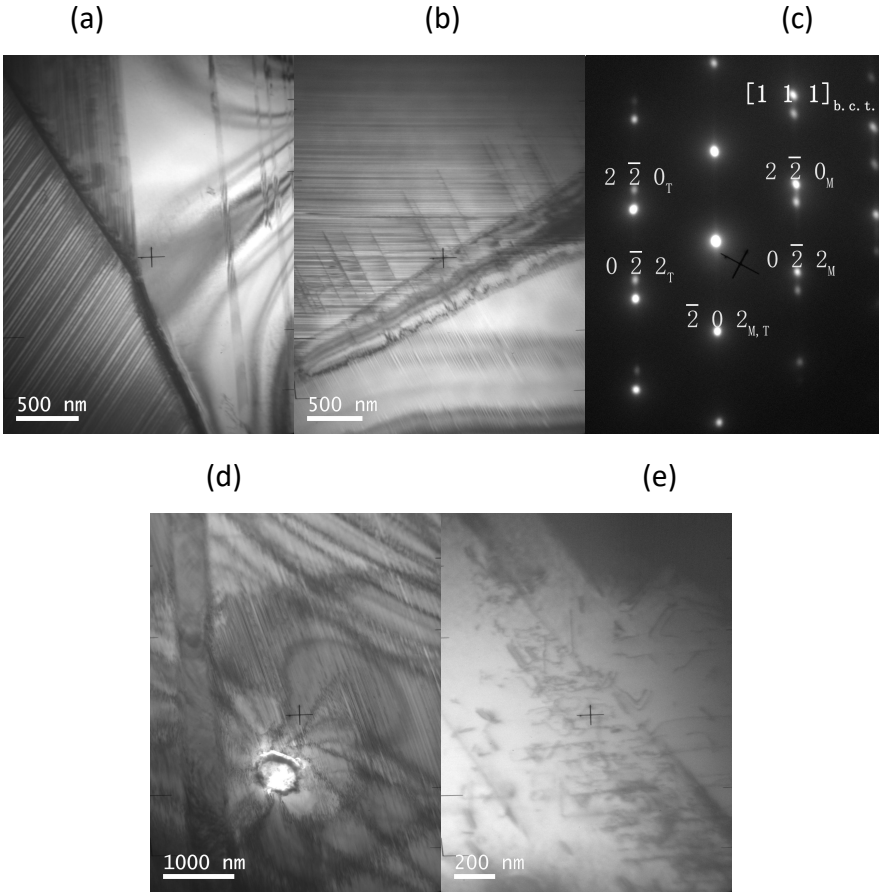

Fig. 4.1.5. TEM results of the Ni-Mn-Ga-Cu H3 alloy: (a) and (b) bright field images of the H3 matrix after 1270 K for 1 h; (c) selected area diffraction pattern from (b); (d) and (e) bright field images of the matrix after 1270 K for 1 h and subsequent ageing at 670 K for 408 h, the latter one obtained under two-beam condition to better show the presence of dislocations.

The Ni-Mn-Ga-Cu H4 furnace cooled alloy has also been observed in the TEM at room temperature. Fig. 4.1.6 (a) shows a BF image of the matrix with internal twins, which can range from several nanometers up to ~40 nm width. Fig. 4.1.6 (b) is the corresponding SADP, again confirming the presence of the non-modulated body centered tetragonal martensite in all the observations. The absence of precipitates after furnace cooling is related with the high stability of the DSC results shown in Fig. 4.1.2 (b).

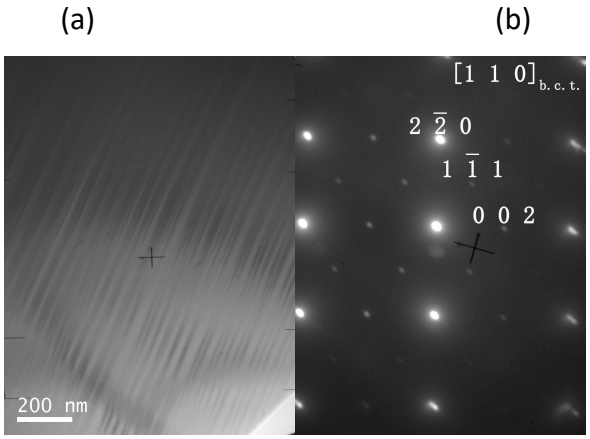

Fig. 4.1.6. TEM observations of the Ni-Mn-Ga-Cu H4 furnace cooled alloy: (a) BF image of a region of the matrix; (b) corresponding SADP.

4.1.4 Thermomechanical Experiments

The former results have shown the excellent thermal and microstructural stability of the Ni-Mn-Ga-Cu H3 and H4 alloys upon prolonged ageing at 670 K, so the thermomechanical behavior of only the as-treated alloy was investigated. Fig. 4.1.7 (a) presents the cooling-heating cycles of the Ni-Mn-Ga-Cu H3 as-treated alloy under different constant applied compression stresses ranging from 20 MPa up to 300 MPa. Then, the total, irrecoverable and recoverable strains together with the hysteresis have been obtained from each curve and plotted as a function of the applied stress in Fig. 4.1.7 (b). It has to be noted that the data for the 300 MPa curve has not been included in Fig. 4.1.7 (b) because the reverse transformation is not completed upon heating. Both figures show that the recoverable strain rises from 0.48% at 20 MPa to 1.85% at 200 MPa, which are obviously lower strains than those obtained from single crystals (*e.g.*, H2 [001] oriented single crystal shows around 4% recoverable strain under 200 MPa reported by C. Picornell, *et al*). As it is well known, during thermomechanical cycling, the martensite variants are activated by temperature, and the number of variants favorably oriented in respect to the biased applied stress increases with the external stress. However, the tested specimen H3 cracked after cycling at 300 MPa, so the maximum recoverable strain is clearly influenced by this limitation. Figs. 4.1.7 (a) and (b) show that the irrecoverable strain also increases with the applied stress, from 0.07% at 20 MPa to 1.08% at 200 MPa as a result of the increasing number of dislocations produced during thermomechanical cycling, together with some retained martensite remaining at the upper cycle temperature under stress. Moreover, the dislocations hinder the movement of the austenite and martensite internal boundaries, leading to an extra frictional work and, therefore, they are responsible of the growth of the hysteresis with the applied stress [197].

Fig. 4.1.7 (c) shows the thermomechanical tests of the Ni-Mn-Ga-Cu H4 alloy for the different constant applied stress in compression, ranging from 20 MPa to 200 MPa, and the corresponding strains and hysteresis were extracted and plotted as a

function of the stress in Fig. 4.1.7 (d). In this case, the tested specimen cracked after the 200 MPa cycle. Regarding the H4 alloy, the recoverable strain increases as a function of the applied stress from 0.74% at 20 MPa to 1.80% at 200 MPa, whereas the irrecoverable strain grows from 0.07% to 2.47% in the same stress range. It is clear that the recoverable strain due to the transformation saturates at 100 MPa (*i.e.*, 2.08%), and further loading does not contribute to increase the recoverable strain. Hence, the recoverable strain at a particular applied stress is higher in the H4 alloy, but this alloy generates more irrecoverable strain than H3 for the same external compressive stress (0.67% and 0.33% at 100 MPa, respectively). Finally, similar to the H3 alloy, the hysteresis of the H4 alloy increases with the applied stress due to the generation of dislocations, but in the latter alloy the hysteresis values are higher at the same stress level, matching the fact that more plastic deformation is generated in H4 during thermomechanical cycling.

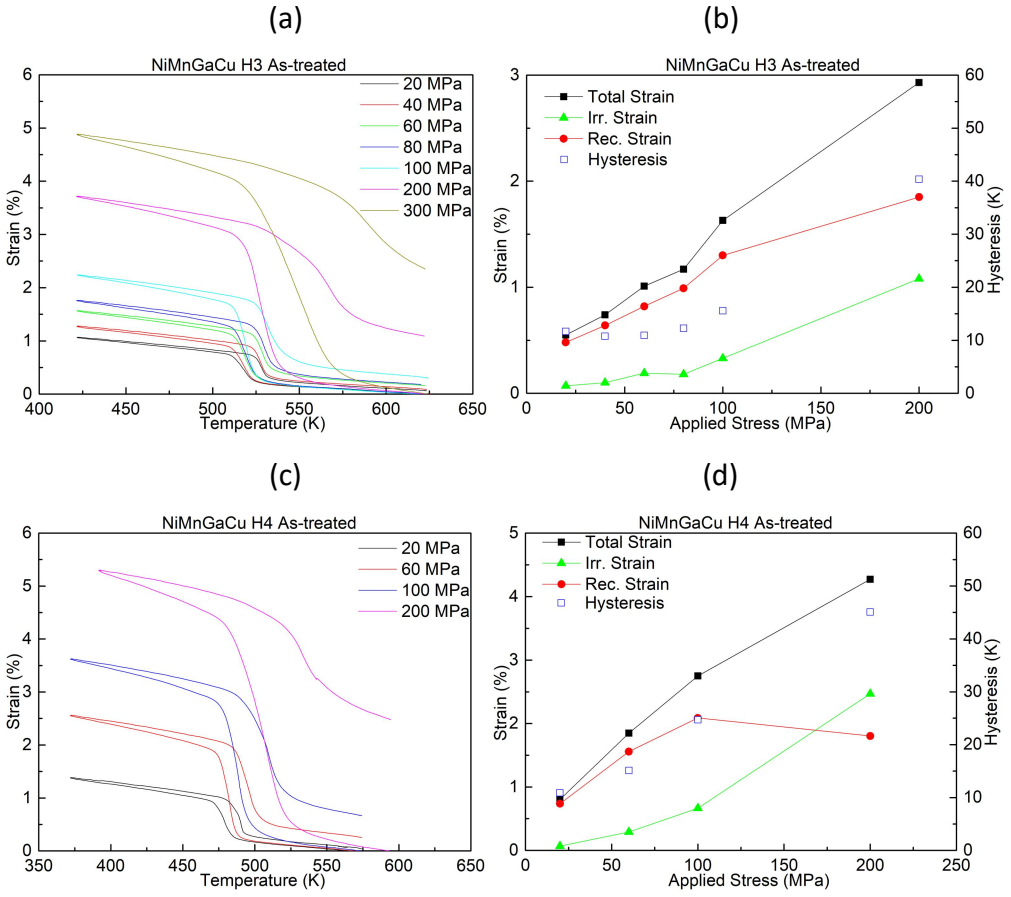

Fig. 4.1.7. (a) Thermomechanical cycling of Ni-Mn-Ga-Cu H3 alloy under constant applied compression stress; (b) total, irrecoverable, and recoverable strains and hysteresis as a function of applied stress, extracted from (a); (c), (d) equivalent plots for H4 alloy.

Figs. 4.1.8 (a) and (b) show the relationship between the transformation temperatures (M_s, M_f, A_s, and A_f) and the applied stress for H3 and H4 alloys, respectively. Both alloys show growing transformation temperatures with the applied stress (*i.e.*, positive slope value from the Clausius-Clapeyron type equation (Eq.

1.1.1)). However, in both alloys the slopes obtained from the direct transformation are notably higher than those from the reverse one, which is another way to visualize how the increase in the hysteresis with the external stress is obtained. Moreover, the H4 alloy shows smaller slopes than the H3 alloy, *e.g.*, the slopes of M_f are 12.5 MPa/K and 26.0 MPa/K for H4 and H3, respectively.

It is worth to note that the H3 alloy under low applied stresses (especially below 60 MPa (Fig. 4.1.8 (a)) seems to have a negative slope between consecutive data instead of following the overall tendency (Fig. 4.1.8 (a)). This deviation from the general behavior has been attributed to the internal stresses, which may compensate the low external applied stress, and therefore, an additional stress is needed to activate the martensitic transformation. Therefore, the transformation temperatures deviate from the expected location and do not strictly follow the Clausius-Clapeyron relationship. In comparison, the H4 alloy shows much better linear fitting, including the region at low stresses (although fewer tests were obtained in this case), which could be correlated with fewer defects and less internal stress fields. The internal stresses existing in H3 alloy would, then, be responsible of the lower transformation strain levels measured for this alloy in relation to H4.

.

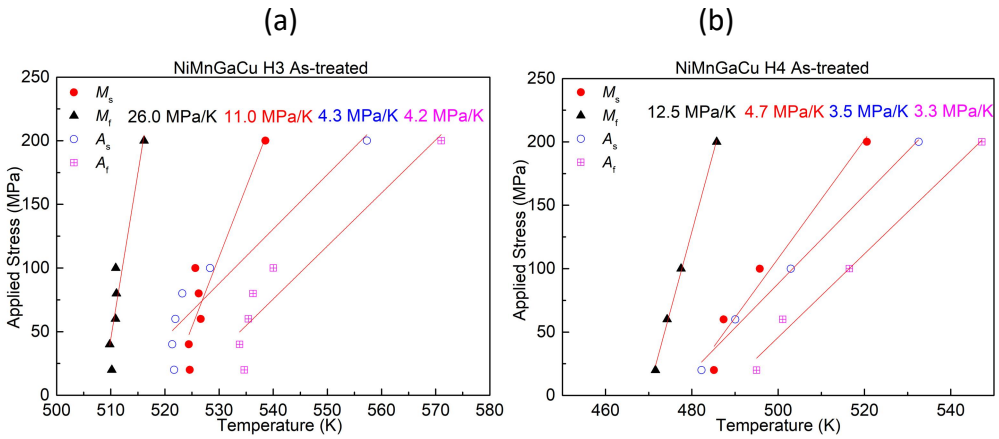

Fig. 4.1.8. Evolution of the transformation temperatures with the applied compression stress together with the Clausius-Clapeyron slopes of as-treated (a) Ni-Mn-Ga-Cu H3 and (b) Ni-Mn-Ga-Cu H4 alloys.

As thermomechanical cycling are experiments quite similar to the way a real actuator is working, it is interesting to calculate the work output generated by the material, which is obtained multiplying the recoverable strain extracted from the thermomechanical curves by the applied stress (Eq. 3.1.3). Figs. 4.1.9 (a) and (b) show the work output as a function of the applied compression stress for the Ni-Mn-Ga-Cu H3 and H4 alloys, respectively. The maximum work output delivered by H3 and H4 alloys are almost the same (3.7 and 3.6 J/cm^3, respectively), both obtained at 200 MPa, though the H4 alloy exhibits higher work output at lower applied stress (*e.g.*, 2.1 and 1.3 J/cm^3 at 100 MPa for H4 and H3, respectively), since the recoverable strain is higher. However, no signs of saturation are observed for the

H3 alloy, while for the H4 alloy the maximum work output seems to be close to 200 MPa. Despite the maximum work output in these experiments is obtained at 200 MPa, the large irrecoverable strains generated in both alloys above 100 MPa (Fig. 4.1.7) suggest the latter stress as the best compromise between work output and irrecoverable strain for potential applications of these polycrystals.

It should be noted that the significant differences of thermomechanical properties between H3 and H4 alloys may not necessarily come from the intrinsic quality of alloys, considering the quite small changes in composition. Probably, a different texture was induced in both ingots during the alloy preparation and it generates different volume fraction of stress-favored martensite variants in each sample. Considering the big grain size (about 500 μm) and the cross section area of the tested samples (about 10 - 12 mm^2), the number of grains in the cross section is about 40 - 50, thus, different preferred orientations may cause significant changes in the thermomechanical properties.

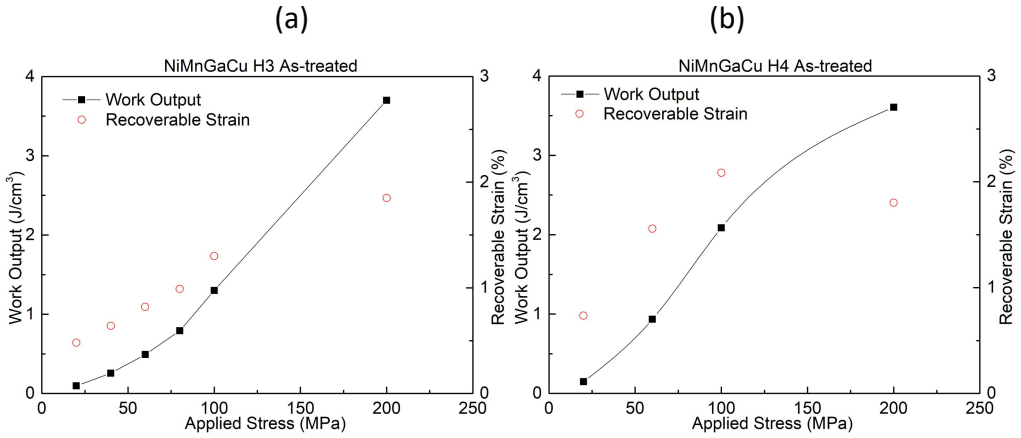

Fig. 4.1.9. Work output as a function of the applied compression stress for (a) Ni-Mn-Ga-Cu H3 and (b) Ni-Mn-Ga-Cu H4 alloys.

After analyzing the previous results, thermomechanical training experiments were performed on the Ni-Mn-Ga-Cu H3 alloy under 100 MPa. The same specimen was first cycled 10 times between 420 K and 620 K (Fig. 4.1.10 (a)), then one more time under a larger temperature range between 370 K and 670 K (Fig. 4.1.10 (b)), and finally, 6 more cycles using the same temperature range as the initial 10 cycles (Fig. 4.1.10 (c)). Figs. 4.1.10 (d) and (e) show the evolution of the total and irrecoverable strains and transformation temperatures, respectively, as a function of the cycle number. During the first 10 cycles (Fig. 4.1.10 (a)), the sample was removed from the testing machine every two cycles, and cooled down to room temperature for a dimension measurement. This was made to check the accuracy of the strain measurement in the testing machine. In general, good agreement was obtained for the irrecoverable strain measured in the machine and the sample dimension data. Thereafter, the specimen was put back into the testing machine, heated up to the same target temperature (620 K), and loaded with 100 MPa in compression.

During the events of cooling-heating cycle without stress made every two cycles, some retained martensite could transform into austenite again, eventually accompanied by partial thermal recovery of dislocations, which releases part of the accumulated irrecoverable strain. However, that part of retained martensite seems to appear again after the subsequent thermomechanical cycle (3^{rd} / 5^{th} / 7^{th} / 9^{th} cycle) and is added to the irrecoverable strain of the cycle, resulting in a small fluctuation of the strains curves every 2 cycles (Fig. 4.1.10 (d)). For example, after the 1^{st} cycle, a part of the irrecoverable strain corresponds to retained martensite that could not transform into austenite by heating up to 620 K under stress. During the 2^{nd} cycle, made immediately after the first without releasing the stress, the retained martensite does not transform, and therefore, it does not appear neither as recoverable strain nor as irrecoverable strain. Thus, in the 2^{nd} cycle the irrecoverable strain is reduced, but the recoverable strain is increased due to the training effect, leading to almost unchanged total strain in respect to the first cycle. Then, before the 3^{rd} thermomechanical cycle, the specimen is unloaded and removed from the machine to measure the sample dimensions and subsequently installed again in the machine and heated up to 620 K without stress. During such processes, the martensite retained after the previous thermomechanical cycles can retransform to austenite and be ready to transform again in the next cycle. Therefore, the total strain recorded in the 3^{rd} cycle increases in relation to the 2^{nd} cycle, but new retained martensite is induced again, resulting in larger irrecoverable strain than in the 2^{nd} cycle. This procedure was repeated up to the 10^{th} thermomechanical cycle and produces the 2-cycles oscillations visible in Fig. 4.1.10 (d).

The 11^{th} cycle was performed under an extended temperature range (370 K - 670 K) to test the effect on the transformation strains, as shown in Fig. 4.1.10 (b). It demonstrates a significant increase of the total strain compared to the previous cycle made with an initially unloaded sample (e.g., the 9^{th} cycle, as seen from Fig. 4.1.10 (b)). This can be attributed to additional stabilized martensite that can retransform during the extended overheating and becomes activated again for the subsequent cooling under stress in the 11^{th} cycle. Finally, the last 6 cycles (12^{th} - 17^{th}) were recorded continuously, without removing the sample from the machine, in the normal temperature range 420 - 620 K (the 12^{th} cycle started with the sample in unloaded condition). Therefore, no 2-cycle oscillations occur in the irrecoverable strain, which shows a continuous decreasing tendency down to ~0.05% due to the training effect.

It is worth to note that the total strain experiences an overall increasing tendency during the first ten thermomechanical cycles due to the training effect. Moreover, the total strain achieved in the last 6 cycles (12^{th} - 17^{th}) is significantly increased in relation to the first ten cycles, as a consequence of the 11^{th} cycle performed in the extended temperature range. The small fluctuations observed in Fig. 4.1.10 for the 13^{th} - 17^{th} cycles may result from the intrinsic error of the tangent method used to determine the total transformation strain. Instead, the irrecoverable strain has much

less error because it is directly measured from the recorded data. The training effect of the first cycles arises from the dislocations introduced during each thermal cycle under stress, which relax the system and facilitates the transformation of higher fraction of oriented martensite variants under stress. This causes a small and progressive (cycle by cycle) “unblocking” of the oriented martensite variants. From the results of Fig. 4.1.10 (d), this effect appears to saturate at the 12th thermomechanical cycle.

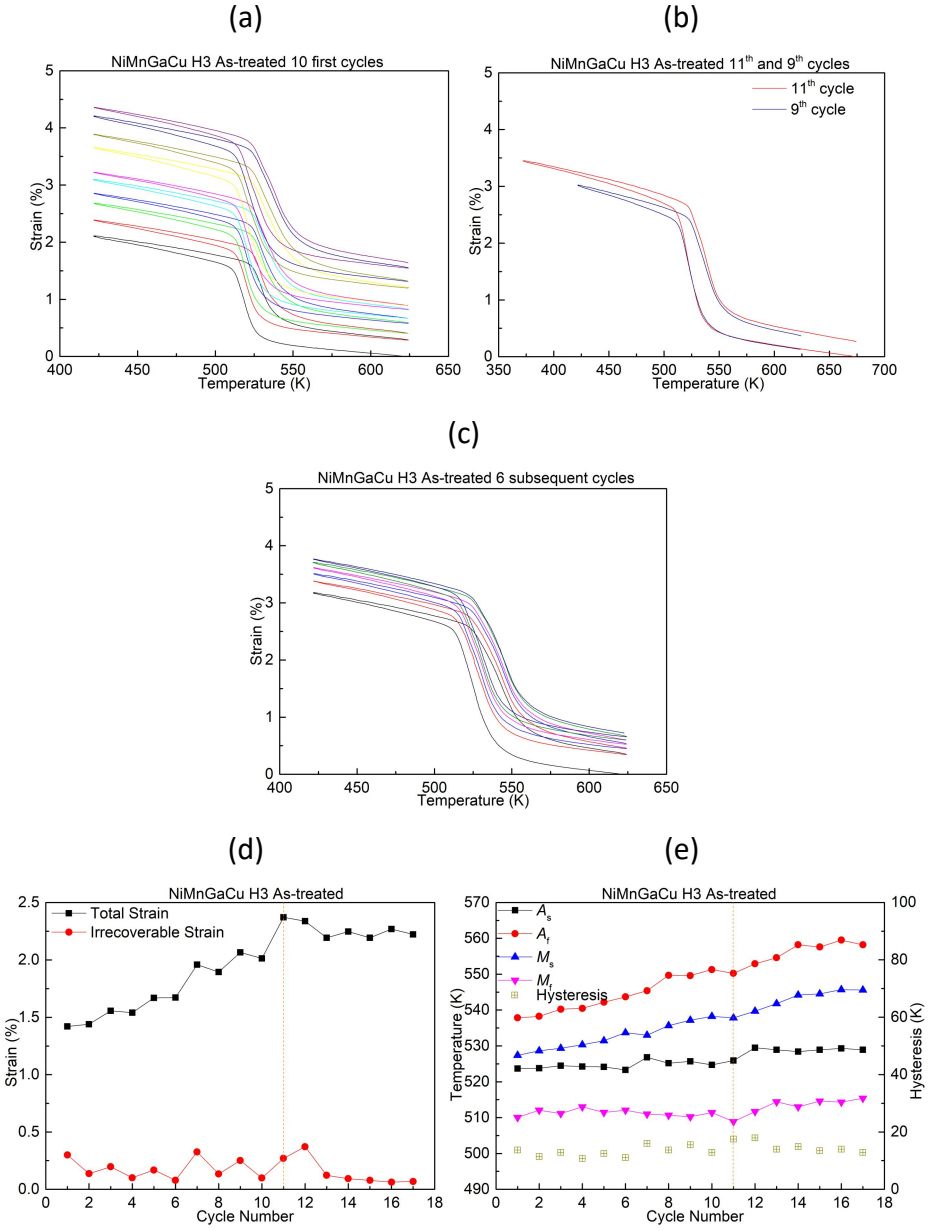

Fig. 4.1.10. Thermomechanical cycling of Ni-Mn-Ga-Cu H3 as-treated alloy under 100 MPa, (a) removing the sample from the testing machine every two cycles for a dimension measurement and (c) continuous cycling for 6 times without removing the sample; (b) is the middle 11th cycle with enlarged temperature interval compared to the 9th cycle with ordinary small one. Plots of the total and irrecoverable strains (d) and transformation temperatures (e) as a function of cycle number.

During the thermomechanical cycling, the transformation temperatures grow as a function of the cycle number due to the effect of training. However, there are some fluctuations disrupting the linear tendency, considered to arise from tangent measurement error. From the 12^{th} cycle to 17^{th} cycle (Fig. 4.1.10 (e)) the evolution of the transformation temperatures and strains with the cycle number becomes more stable due to the saturation effect discussed in the previous paragraph.

4.1.5 Mechanical Experiments

Fig. 4.1.11 presents three mechanical tests of a Ni-Mn-Ga-Cu H3 as-treated polycrystalline specimen performed at different temperatures (A_f, A_f + 20 K and A_f + 40 K). In the left side curve, obtained at 530 K, there is a clear plateau when loading above 220 MPa due to the gradual stress-induced martensitic transformation in the polycrystalline alloy. However, no reverse transformation upon unloading is observed because of low temperature of the test. After this cycle, the specimen was heated in the same testing machine up to 650 K under low stress (3 MPa), obtaining about 2.2% recoverable strain (marked with a red arrow in Fig. 4.1.11).

In the middle curve, obtained at 550 K, the yield stress is higher and the plateau associated to the stress-induced martensitic transformation is more inclined due to the higher ambient temperature. The reverse transformation appears during unloading, obtaining 1.9% of recoverable strain and 1.1% of irrecoverable strain (both marked with black arrows in Fig. 4.1.11). After the mechanical test, the same heating procedure as in the previous cycle was applied, obtaining only 0.4% of additional recoverable strain (marked with red arrow in Fig. 4.1.11) and 0.7% of remaining irrecoverable strain. Therefore, in total, the total recoverable strain at 550 K (1.9% + 0.4%) is practically the same as the one obtained at 530 K.

Finally, in the right side curve obtained at 570 K, the martensitic transformation cannot be induced up to 350 MPa and a quasilinear loop with relatively smaller hysteresis is obtained in the mechanical test. The subsequent heating process up to 650 K generates only 0.2% recoverable strain (marked with red arrow in Fig. 4.1.11), probably due to the retransformation of some stabilized martensite. Therefore, the mechanical tests demonstrate a very poor, practically absent, superelasticity in this polycrystalline sample.

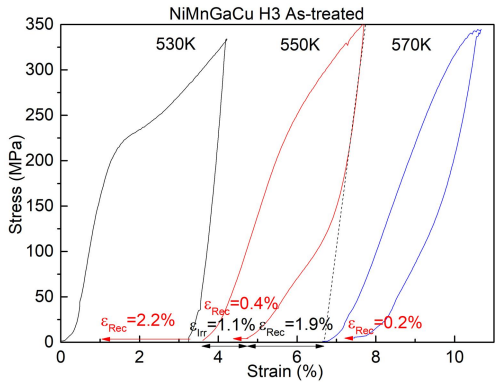

Fig. 4.1.11. Mechanical tests of the Ni-Mn-Ga-Cu H3 alloy at different temperatures. Recoverable strains from the after heating procedure are marked with red arrows for all the experiments.

4.2 Ni-Mn-Ga-Sn Characterization

To the author's knowledge, the quaternary Ni-Mn-Ga-Sn alloy system has been studied as a candidate for the giant magneto-caloric effect (MCE). Chatterjee *et al*. [79] reported big MCE (12.8 J/(kgK)) at 274 K by adding Ga into the Ni-Mn-Sn Heusler system. Doping Sn into the Ni-Mn-Ga system strongly reduces the martensitic transformation temperatures and affects the magnetic properties [175]. However, all the alloys studied were conceived to obtain the martensitic transformation below room temperature. Therefore, doping the Ni-Mn-Ga system with Sn to obtain HTSMA has been explored in the present work.

4.2.1 Calorimetric Analysis

A ternary Ni-Mn-Ga alloy with high transformation temperatures is designed starting from the Ni-Mn-Ga H1 alloy composition (Table 4.1) and using the Ni-Mn-Ga equilibrium phase diagram [71]. For that ternary alloy, the Ni content was increased up to 53 at.% to compensate the negative effect of doping with Sn on the transformation temperatures and kept constant for all the alloys. Then, Sn was introduced equally replacing Mn and Ga. Therefore, a series of three compositions ($Ni_{53.0}Mn_{30.0Z}Ga_{17.0Z}Sn_X$, with Z = (47-X)/47 and X = 0, 2, 4), was cast by induction melting starting from pure elements (Ni 99.99+ wt.%, Mn 99.99 wt.%, Ga 99.9999 wt.%, Sn 99.99 wt.%).

Table 4.2 presents the nominal composition of the three Ni-Mn-Ga-Sn cast alloys and their nominal valence electron concentration (e/a), together with the forward and reverse martensitic transformation peak temperatures, hysteresis, and average enthalpy change obtained from the DSC. The thermograms of the three Ni-Mn-Ga-Sn alloys solution heat treated at 1170 K (Sn0) or 1270 K (Sn2 and Sn4) for 48 h are plotted in Fig. 4.2.1, clearly showing a serious deterioration of the martensitic transformation as a consequence of doping with Sn. As it is shown in Table 4.2, M_p

decreases from 590 K to 314 K, and the enthalpy change drops from 14.3 J/g to 8.4 J/g. Moreover, the transformation becomes more diffuse, increasing the temperature range of the peaks from ~30 K in Sn0 up to over ~100 K in Sn4. However, the hysteresis is largely reduced from 38 K to 9 K with only 2 at.% Sn, which could be attributed to the change of the matrix composition and compatibility between the austenite and martensite crystal lattices. This situation is very similar to the Ni-Mn-Ga-Hf/Zr alloys that will be discussed in the Chapter 6.

Table 4.2. Nominal composition, nominal valence electron concentration (*e*/*a*), experimental DSC peak measurements of the forward and reverse martensitic transformation, hysteresis and average enthalpy change for the solution heat treated Ni-Mn-Ga-Sn alloys.

Alloy	Nominal composition	*e*/*a*	M_p /K	A_p /K	Hysteresis /K	Δ*H* / J/g
Sn0	$Ni_{53.0}Mn_{30.0}Ga_{17.0}$	7.910	590	628	38	14.3
Sn2	$Ni_{53.0}Mn_{28.7}Ga_{16.3}Sn_{2.0}$	7.877	446	455	9	15.9
Sn4	$Ni_{53.0}Mn_{27.4}Ga_{15.6}Sn_{4.0}$	7.846	314	322	8	8.4

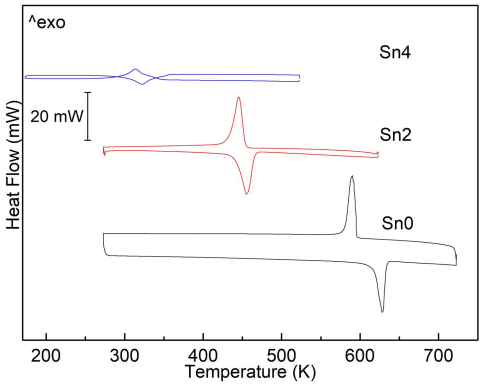

Fig. 4.2.1. Thermograms of the of Ni-Mn-Ga-Sn alloys. Sn2 and Sn4 were solution heat treated at 1170 K for 48 h, and Sn0 at 1270 K for 48 h.

One Sn2 additional sample, adjacent to the previous one and SHT at 1170 K for 48 h, was subjected to thermal cycling 20 times in the DSC using temperature range from RT to 570 K (Fig. 4.2.2 (a)). The specimen shows very high thermal cycling stability, except for the first reverse transformation, which shows slightly higher temperatures than the rest of the cycles. As the cycling series start with heating from RT, this difference in temperature could be attributed to the martensite stabilization by quenched-in defects and/or atomic reordering of the matrix [198, 199]. In any case, the effect is very low. The transformation temperatures and enthalpy change of the direct and reverse transformations were extracted from the thermograms in Fig. 4.2.2 (a) and plotted in the Fig. 4.2.2 (b). It is clear that both transformation temperatures and enthalpy change are quite stable with cycling, except for the small variation in the reverse transformation temperatures from the first to the second cycles. The small oscillations of the enthalpy change are irrelevant for the overall behavior, and they are within the experimental error.

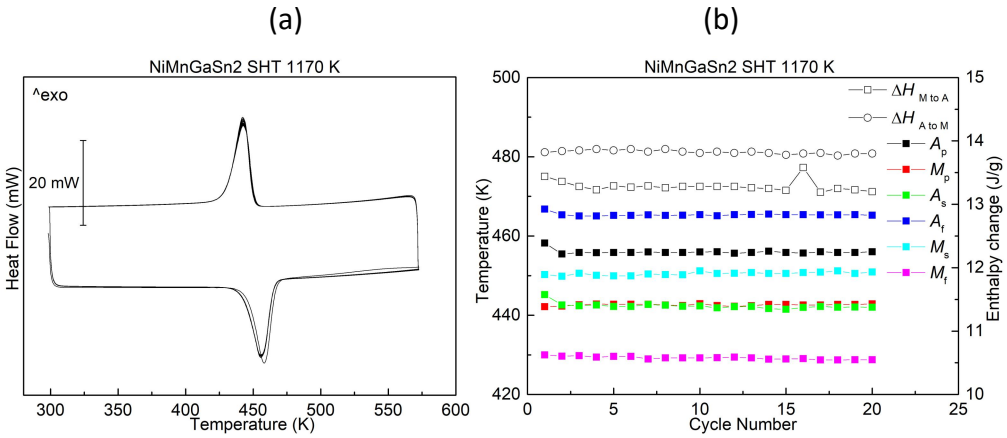

Fig. 4.2.2. (a) Thermal cycling 20 times in the DSC of the Sn2 alloy SHT at 1170 K for 48 h, (b) transformation temperatures and enthalpy change as a function of the cycle number extracted from thermogram (a).

4.2.2 Microstructure

The microstructure of Sn2 and Sn4 alloys after SHT at 1170 K for 48 h was observed by SEM (Figs. 4.2.3 (a) and (b)) and TEM (Figs. 4.2.3 (c) and (d)). The Sn2 alloy (Fig. 4.2.3 (a)) shows a matrix completely transformed into martensite variants along with some inclusions (carbides and/or oxides). No signs of γ phase precipitation have been detected in the SEM observations as it has been reported for other Ni-Mn-Ga-X quaternary alloys [161, 165]. The Sn4 alloy not only exhibits the normal martensite variants and inclusions but also a large amount of tiny holes in the matrix (Fig. 4.2.3 (b)), which makes this material extremely brittle even for the normal sample preparation procedure. Actually, some porosity can be found in a lot of Ni-Mn-Ga ternary and Ni-Mn-Ga-X quaternary alloys produced by induction melting. However, the number of holes observed here for the Sn4 alloy is unusual and could be a consequence of the induction melting process or impurities (oxides, carbides, etc …) removed during sample preparation. The study of the origin of these holes is beyond the scope of the present work and it was not analyzed deeper.

A bright field image of the Sn2 alloy and the corresponding SADP are presented in Figs. 4.2.3 (c) and (d) respectively, showing the common martensite variants with internal twins and confirming that the martensitic structure of the Sn2 alloy is the non-modulated body centered tetragonal. Fig. 4.2.3 (d) is obtained along the $[100]_{b.c.t.}$ zone axis and shows the typical internal twining along (022) planes. Nevertheless, the diffuse line along the <022> direction observed between the fundamental b.c.t. martensite spots (Fig. 4.2.3 (d)) could indicate that inside the microtwinned variants (Fig. 4.2.3 (c)) there exist some precursor or even variants from one or more modulated martensites.

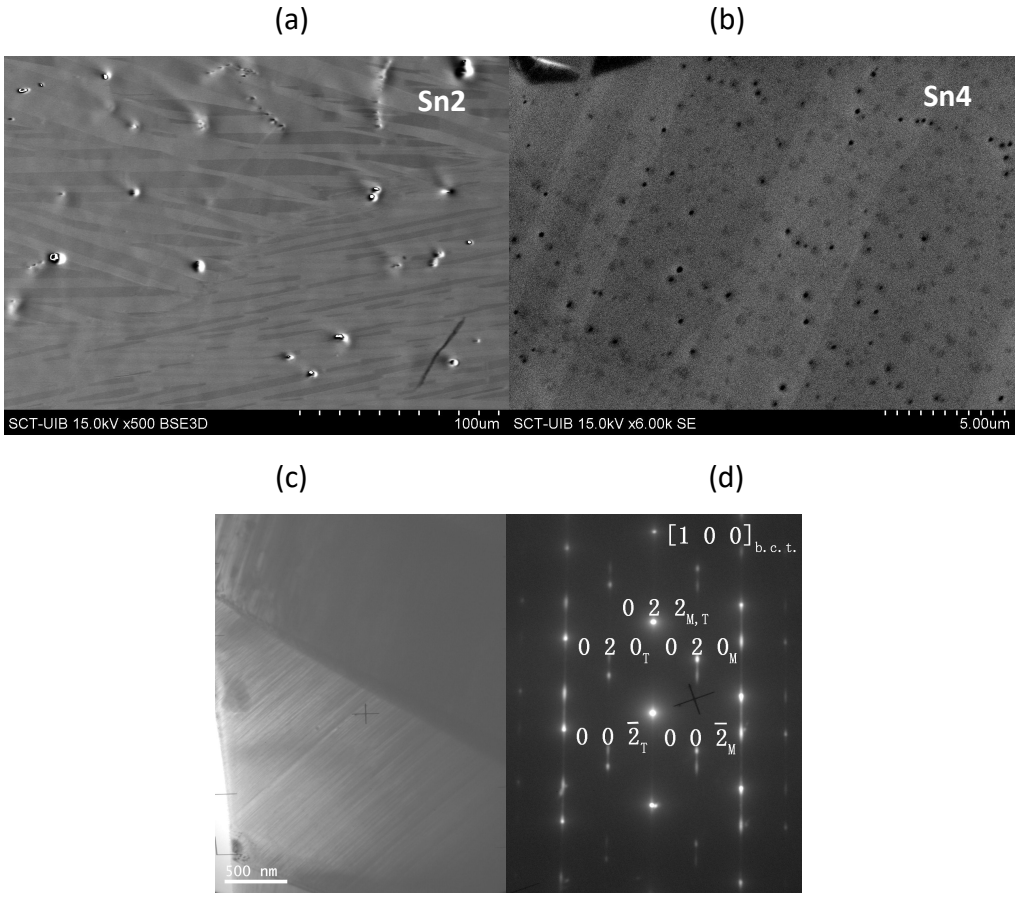

Fig. 4.2.3. Microstructural observations of Sn2 and Sn4 alloys after SHT at 1170 K for 48 h: (a) general view in the SEM of the Sn2 matrix, (b) enlarged view in the SEM of the Sn4 matrix; (c) TEM BF image of the Sn2 matrix, and (d) corresponding SADP from (c).

4.3 Summary of Ni-Mn-Ga-Cu/Sn Alloys

1. The thermal evolution of the martensitic transformation was investigated for two Ni-Mn-Ga-Cu quaternary polycrystalline alloys slightly rich in Ni and with 1 at.% of Cu (H3 and H4) were investigated. Both compositions show a single and sharp step transformation from b.c.c. austenite to b.c.t. martensite and a complete absence of precipitation after any of the studied thermal treatments, demonstrating a high thermal stability upon long ageing at 670 K or furnace cooling treatments. These results together with previous reports on compositions with higher Cu content seem to prove the impossibility to induce nanometric precipitates in the Ni-Mn-Ga-Cu system, which were expected to improve the mechanical properties of these alloys.

2. *In-situ* heating XRD experiments were performed on Ni-Mn-Ga-Cu H3 specimens, showing that both lattice parameters of the tetragonal martensite (*a* and *c*) approach to the lattice parameter of the austenite (a_0) upon heating. A good compatibility between the two phases could be related to the low thermal hysteresis of this alloy. All the significant peaks could be indexed with these two phases.

3. Thermomechanical tests in compression were applied to the as-treated Ni-Mn-Ga-Cu H3 and H4 alloys. Higher recoverable strains were achieved in H4 respect to H3 at any particular applied stress, and consequently the work output was larger for the H4 alloy than for the H3 (*e.g.*, 2.1 J/cm^3 vs. 1.3 J/cm^3 at 100 MPa). However, H4 broke at 200 MPa whereas H3 failed at 300 MPa. The large irrecoverable strains generated in both alloys above 100 MPa suggest the latter stress as the best compromise between work output and irrecoverable strain for potential application as thermal actuators. Thermomechanical cycling was also applied to the Ni-Mn-Ga-Cu H3 alloy, showing a slightly and continuous growth of the recoverable strain with cycling due to the training effect, although evidences of the presence of stabilized martensite under stress have also been found. The training effect saturates after ~ 12 thermomechanical cycles.

4. The Ni-Mn-Ga-Cu H3 alloy exhibits a poor superelasticity effect under mechanical test in compression, showing about 1.9% of recoverable strain at 550 K, but 1.1% of irrecoverable strain in the same test (of which 0.4% strain is from stabilized martensite). The superelastic window of this alloy is extremely narrow, being 530 K too low to complete the transformation and 570 K too high to achieve a significant recoverable strain.

5. The effect of doping Ni-Mn-Ga with Sn was also investigated, demonstrating that Sn strongly reduces the transformation temperatures (4 at.% of Sn shifts the transformation to RT). The Ni-Mn-Ga-Sn alloy with 2 at.% Sn shows narrow hysteresis and high thermal stability under DSC cycling due to the good compatibility between austenite and martensite lattices. However, the alloy with 4 at.% of Sn shows a high brittleness due to the appearance of a significant number of holes in the matrix even after annealing. The origin of these holes is probably related to the induction melting process or impurities, but further study is beyond the scope of the present work. The high brittleness of the material and the sharp decrease in the transformation temperatures are strong reasons to rule out the Ni-Mn-Ga-Sn system as HTSMA.

Chapter Ⅴ Ni-Mn-Ga-Hf

As it has been discussed in the introduction, one of the solutions to reduce the brittleness from grain boundaries is to grow a ductile second phase by introducing a fourth element in polycrystalline Ni-Mn-Ga alloy system. The martensitic transformation temperature (MTT) can be inevitably changed as the result of the changing valence electron concentration (*e*/*a*) and/or cell volume effect. In the mean time, the vital mechanical behavior can also be changed due to the microstructural variation. Most of the possibilities in periodic table have been studied. Among them, several works have reported that Ti not only can enhance the shape memory effect attributed to the presence of Ni_3Ti precipitates [177, 178], but also it brings about an increase in MTT due to the energy difference when Ga sites are occupied by Ti [179]. However, to the author's knowledge, additions of Hf or Zr (elements located in the same column of the periodic table as Ti) to Ni-Mn-Ga are practically unexplored in literature. No researches have been found on the addition of Hf, whereas addition of Zr to replace Cu in Ni-Mn-Ga-Cu alloy system causes dual-phases microstructure and changing of MTT with different thermal treatments [182-184]. However, the functional properties like SME were not reported, and the structure of the second phase was not investigated. Furthermore, no researches have been found on the addition of Hf that is in the same column as Ti and Zr. Therefore these additions will constitute the subject of the rest of this thesis.

In this chapter we present the effect of Hf addition to Ni-Mn-Ga high temperature shape memory alloys in polycrystalline form. Based on the Ni-Mn-Ga equilibrium phase diagram [71], the nominal composition for the ternary alloy has been chosen as $Ni_{53.0}Mn_{30.0}Ga_{17.0}$, which presents high martensitic transformation temperatures, around 600 K, and more tendency to form the β + γ dual phases. For the quaternary alloys, the elevated Ni content has been kept constant to facilitate the precipitation of γ phase, and Hf has been added to substitute both Mn and Ga in the same ratio. Keeping this rule, a set of Ni-Mn-Ga-Hf polycrystalline alloys were prepared by induction and arc melting with these nominal compositions: $Ni_{53.0}Mn_{31.1Z}Ga_{17.7Z}Hf_X$, with Z = (47-X)/48.8 and X = 0, 0.5, 1, 2, 3, 4. The nominal compositions of the six alloys studied are shown in Table 5.1. The alloys were encapsulated in evacuated quartz ampoules under partial Ar atmosphere and solution heat treated at 1270 K for 48h followed by water quenching with breaking the ampoules.

5.1 Results of Analysis and Observation

5.1.1 Calorimetric Analysis

Fig. 5.1.1 shows the results of DSC measurement for the studied alloys with different Hf contents. All specimens were subjected to cooling and heating thermal cycles in the same tested temperature range (270 K - 720 K) and they show a single peak corresponding to the martensitic transition. From the curves it can be observed that the peaks for low Hf contents (Hf0.5 and Hf1) become broader than the others, which may be a result of their inhomogeneous matrix composition. Moreover, the transformation peaks continuously shift to lower temperatures as the Hf content increases, *e.g.,* the peak temperature M_p decreases from 590 K for Hf0 to 412 K for Hf4. At the same time, the reverse transformation peak approaches the direct transformation, producing a significant reduction of the transformation hysteresis.

Table 5.1 shows the nominal compositions of all the alloys and the characteristics of the martensitic transformation obtained from the DSC results. The valence electron concentration has been calculated from the nominal composition. Peak temperatures of direct and reverse transformations (M_p, A_p, respectively) are extracted from the DSC thermograms. The transformation hysteresis, which is defined as the difference $A_p - M_p$, decreases from 46 K for Hf0.5 to 8 K of Hf3 and Hf4. Moreover, the enthalpy change, corresponding to the average value for the direct and reverse transformations, also decreases with the increase of Hf. The data obtained for a ternary alloy NMG1 of nominal composition $Ni_{53.2}Mn_{25.0}Ga_{21.8}$ (selected after the results reported by Ma Y *et al*. [150]) is also included in the table. This alloy presents similar transformation temperatures to the quaternary alloys Hf3 and Hf4, and will be used to compare some of their properties.

Table 5.1. Nominal composition and values of the valence electron concentration (e/a), DSC peak temperatures for the direct and reverse transformation (M_p, A_p, respectively), hysteresis (calculated as $A_p - M_p$) and average enthalpy change (ΔH) for the investigated alloys after solution heat treatment at 1270 K.

Alloy	Nominal composition	e/a	M_p /K	A_p /K	Hysteresis /K	ΔH / J/g
Hf0	$Ni_{53.0}Mn_{30.0}Ga_{17.0}$	7.91	590	628	38	14.3
Hf0.5	$Ni_{53.0}Mn_{29.6}Ga_{16.9}Hf_{0.5}$	7.90	595	641	46	14.5
Hf1	$Ni_{53.0}Mn_{29.3}Ga_{16.7}Hf_{1.0}$	7.89	536	556	20	10.3
Hf2	$Ni_{53.0}Mn_{28.7}Ga_{16.3}Hf_{2.0}$	7.88	465	478	13	10.4
Hf3	$Ni_{53.0}Mn_{28.0}Ga_{16.0}Hf_{3.0}$	7.86	431	439	8	10.7
Hf4	$Ni_{53.0}Mn_{27.4}Ga_{15.6}Hf_{4.0}$	7.85	412	420	8	9.3
NMG1	$Ni_{53.2}Mn_{25.0}Ga_{21.8}$	7.73	394	413	19	13.2

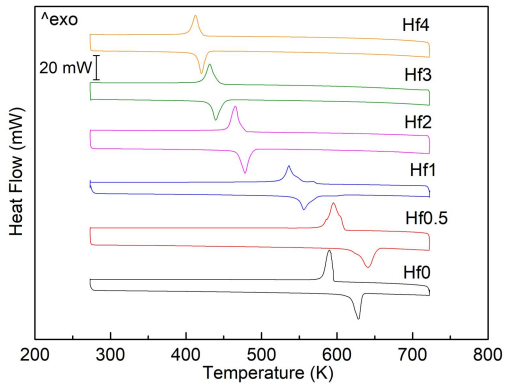

Fig. 5.1.1. DSC analysis of solution heat treated 1270 K for 48 h Ni-Mn-Ga-Hf_X (X = 0, 0.5, 1, 2, 3, 4) alloys.

The stability of the martensitic transformation upon ageing in austenite phase and thermal cycling through the martensitic transformation has been also studied. Fresh samples cut from neighbor areas in the initial ingots of Hf2 and Hf3 alloys were encapsulated and aged at 870 K for different times, followed by water quenching. The neighbor samples are considered to have similar initial states (composition, microstructure, transformation temperatures, …), which can better reveal the behavior of ageing. Figs. 5.1.2 (a), (b) present the DSC thermograms obtained. For each alloy and ageing treatment, two consecutive thermal cycles were recorded in the DSC and they are plotted in Fig. 5.1.2. As it is shown, all samples of Hf2 and Hf3 alloys present a single stage transformation with perfect reproducibility of the two cycles performed in the DSC. They also present a very low evolution upon ageing at 870 K. For the Hf2 alloy (Fig. 5.1.2 (a)) a slight shift of the direct and reverse transformation peaks to lower temperatures can be observed after 48 h ageing at 870 K, varying from 481 K to 468 K for M_p and from 493 K to 477 K for A_p temperatures. The average enthalpy change also decreases slightly from 10.6 J/g to 9.3 J/g after 48 h ageing. In addition, the small “shoulder” of the peaks existing in the high temperature side of the SHT sample is progressively diminished upon ageing, indicating that a more homogeneous microstructure has been reached after ageing. As for the Hf3 alloy (Fig. 5.1.2 (b)), it also shows a stable martensitic transformation; the peak temperatures slightly decrease from 431 K to 423 K (M_p) and from 439 K to 430 K (A_p), while the average enthalpy change drops from 10.8 J/g to 9.0 J/g after 72 h ageing. Therefore, the quaternary Hf2 and Hf3 alloys demonstrate a good thermal stability upon ageing at 870 K. Fig. 5.1.2 (c) presents the thermograms of the ternary Hf0 alloy SHT with additional ageing treatments at 920 K (austenite state) up to 72 h in order to compare and elucidate the effect of Hf addition. The overall tendency shows that the ageing treatment has also a very little effect on the transformation for this alloy composition, similar to the Hf2 and Hf3 alloys. However, in contrast to the Hf containing alloys, for the ternary Hf0 alloy the peak temperatures (1^{st} cycle) increase slightly from 590 K for SHT to 601 K (M_p) K and from 624 K to 625 K (A_p) after aged 72 h at 920 K. Moreover, Fig. 5.1.2 (c) also reveals a lack of reproducibility of the two thermal cycles performed on each ageing stage. It is remarkable the behavior of

the SHT sample, which shows a notable difference between the first and second reverse transformation peaks, while the direct transformation peaks are practically coincident. This can be linked to a small martensite stabilization effect induced by water quenching after the solution treatment at 1270 K, as will be further discussed in the next paragraph. Instead, for the ageing treatments at 920 K there is a shift of both the forward and reverse transformation peaks in two consecutive cycles, which is indicative of the existence of thermal cycling effects in the ternary Hf0 alloy.

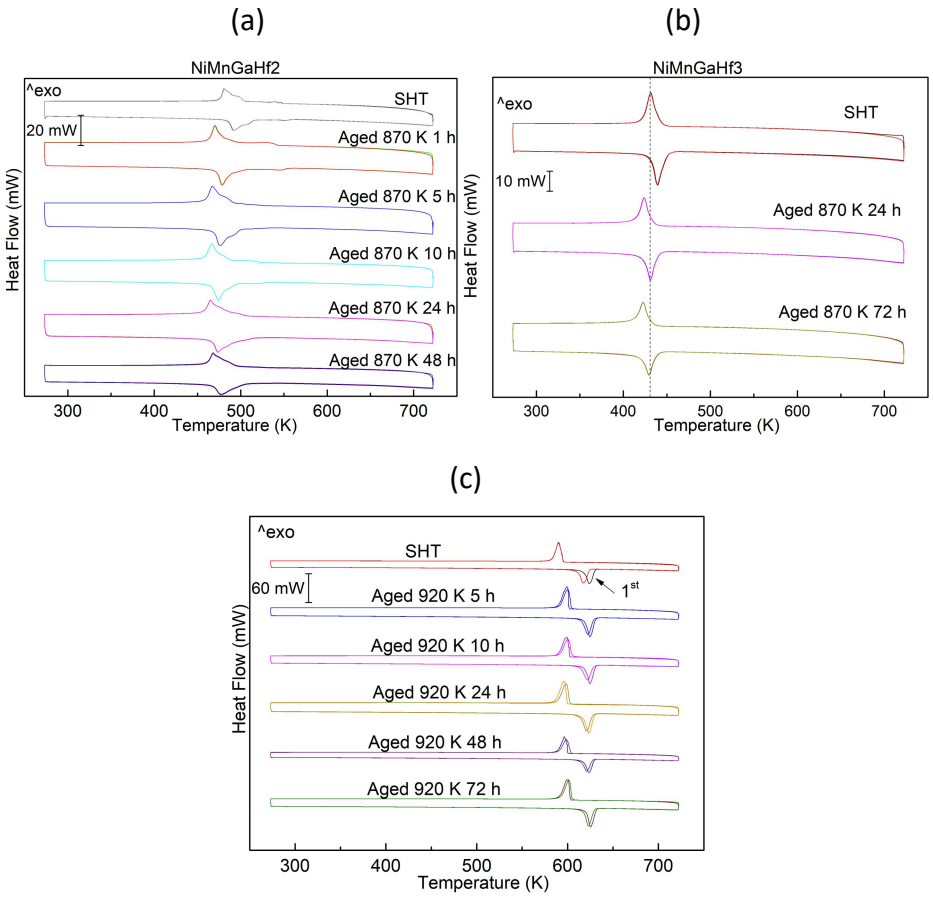

Fig. 5.1.2. DSC measurements of (a) NiMnGaHf2 SHT 1270 K for 1 h with additional ageing at 870 K for 1 h, 5 h, 10 h, 24 h, 48 h; (b) NiMnGaHf3 SHT 1270 K for 1 h with additional ageing at 870 K for 24 h, 72 h; (c) NiMnGaHf0 SHT 1270 K for 1 h with additional ageing at 920 K up to 72 h.

From the results of the previous paragraph, the effect of thermal cycling through the martensitic transformation has been studied up to 20 consecutive cycles in the DSC, performed on SHT samples at a heating/cooling rate of 10 K/min. The results are shown in Fig. 5.1.3. The ternary Hf0 alloy shows a significant degradation of the martensitic transformation upon cycling, with progressive shift to lower temperatures and broadening of the DSC peaks (Fig. 5.1.3 (a)). The transformation temperatures of Hf0 are plotted as a function of the cycle number in Fig. 5.1.3 (b) showing, essentially, a linear decrease. It is worth noting that M_s and A_s lines cross at the 15th cycle. Moreover, the figure reveals a larger drop of the reverse transformation temperatures between the first and second cycle. This is indicative of

the martensite stabilization effect occurring after quenching to martensite state, as also revealed in Fig. 5.1.2 (c). This effect was observed in Cu-based shape memory alloys and deeply studied. This is a transient phenomenon that occurs either by short range reordering processes occurring in the martensite lattice or by pinning of the martensite/austenite interfaces induced by the quenched-in defects (or a combination of both effects), which result in the shift of the reverse transformation to higher temperatures. However, the effect is neutralized after the first reverse transformation by the rapid diffusion existing in the austenite phase and the subsequent transformation events occur in the normal temperatures [198–200]. For the present Hf0 alloy, the difference between the first and second reverse transformation is of only ~5 K, which is very moderate compared to other alloys with hiperstabilization effects [201, 202].

Fig. 5.1.3 (c) presents the results of the Hf3 quaternary alloy solution heat treated at 1270 K. As shown in the figure, the thermograms of all the 20 thermal cycles are perfectly reproducible, indicating an absolute lack of evolution of the martensitic transformation parameters over 20 cycles and no martensite stabilization effect at all. The forward and reverse peak temperatures are 431 K and 440 K, respectively, *i.e.*, a quite small hysteresis of 9 K, compared to 30 K for Hf0 alloy in the 1st cycle. The average enthalpy change for direct and reverse transformations is 10.0 J/g. Another neighbor bar of Hf3 alloy was solution heat treated at 1320 K (close to the melting point) in order to retain a higher amount of quenched-in vacancies and trying to enhance the thermal cycling effects. However, as shown in Fig. 5.1.3 (d), the perfect reproducibility over 20 cycles is also observed for this sample, which presents 432 K and 440 K for M_p and A_p, respectively, and average enthalpy change of 9.8 J/g. These are almost identical transformation parameters as the previous sample, treated at 1270 K. As will be shown in the next section, the quaternary alloys with Hf content above 1% present a dual phase structure. This microstructure, together with the low hysteresis observed in this alloy are responsible of the high stability.

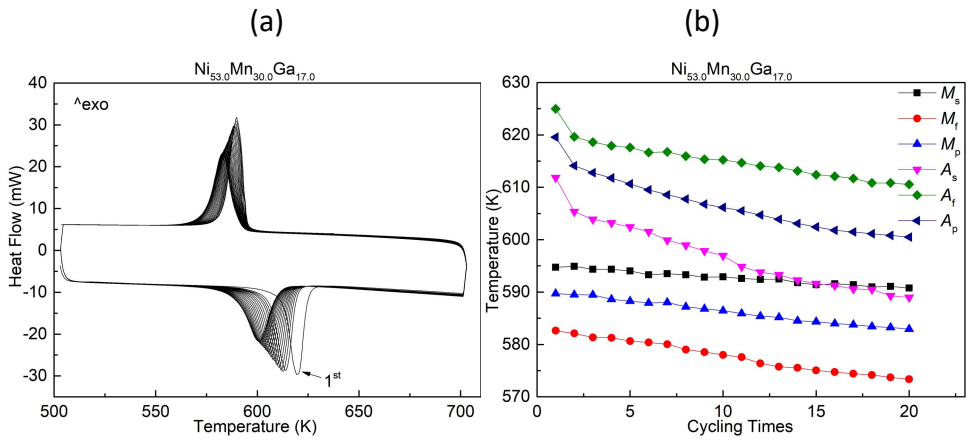

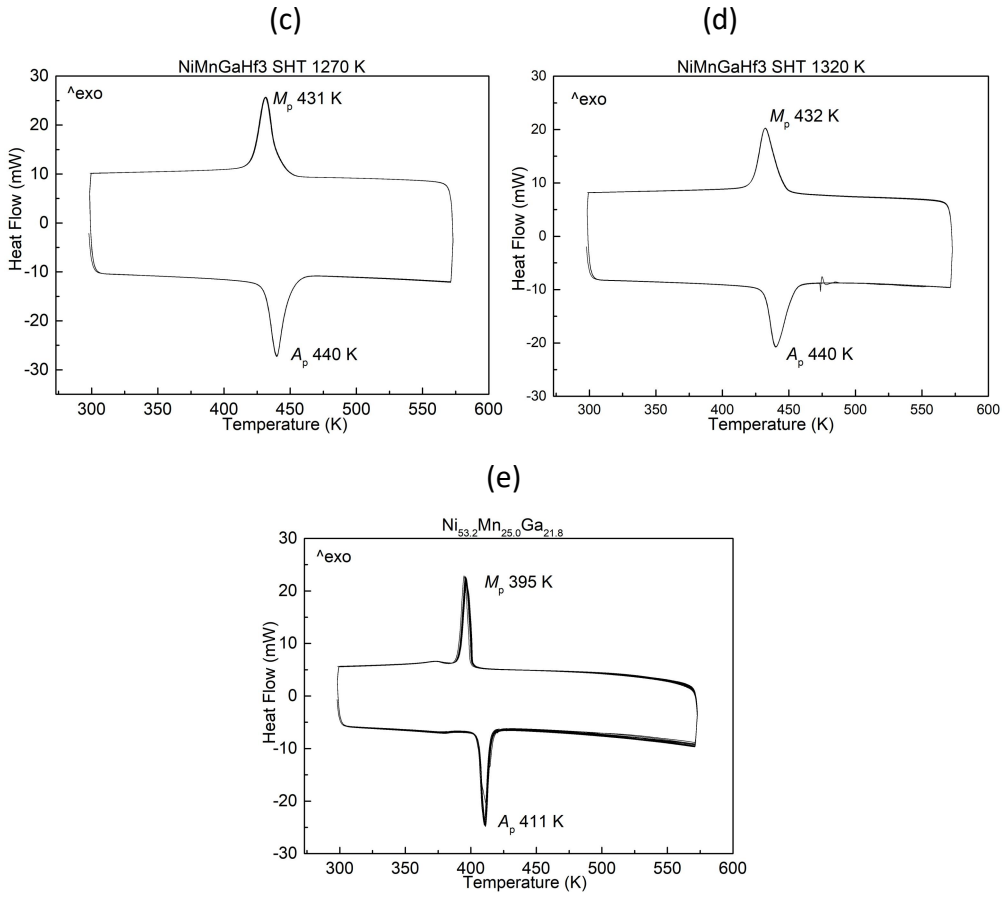

Fig. 5.1.3. DSC thermal cycling 20 times results of (a) NiMnGaHf0 SHT 1270 K for 48 h alloy, (b) corresponding transformation temperatures tendency extracted from (a); and 20 cycles of (c) NiMnGaHf3 SHT 1270 K for 48 h alloy, (d) NiMnGaHf3 SHT 1320 K for 48 h alloy; 20 cycles of (e) $Ni_{53.2}Mn_{25.0}Ga_{21.8}$ (NMG1) SHT 1270 K for 48 h alloy.

It is known that the cycling effects can be derived from the growth of dislocation density and their internal stress fields with increasing number of cycles. Moreover, thermal cycles combined with pre-strain can even lead to fracture [203]. In this sense, the generation of dislocations upon cycling could be responsible of the transformation evolution observed in the ternary alloy Hf0 (Figs. 5.1.3 (a), (b)). However, it should be noted that this alloy has been cycled up to temperatures as high as 700 K, while for the Hf3 alloy the upper temperature was reduced to 570 K, due to their lower transformation temperatures. Presuming ageing effects occurring at high temperatures in austenite state during each thermal cycle could have an influence on the subsequent cycles and could be also responsible of the large evolution observed in Hf0. In fact, such step-by-step ageing effect was reported in Cu-based HTSMAs [204]. However, the ageing treatments at 920 K performed on this alloy show no big effects on the transformation temperatures, as seen from Fig. 5.1.2 (c). Such treatments involve far longer duration at high temperature than the step-by-step ageing effect concomitant with thermal cycling, which is contradictory to this assumption. To obtain further information for clarifying this point, a new ternary alloy NMG1 of nominal composition $Ni_{53.2}Mn_{25.0}Ga_{21.8}$ and lower

transformation temperatures than Hf0 was produced and thermally cycled within the same temperature range used for the Hf3 alloy (300-570 K). The results are shown in Fig. 5.1.3 (e). As it is shown, the evolution of the transformation peaks is strongly diminished in relation to Hf0 alloy. Moreover, the hysteresis of transformation of NMG1 (19 K) is half of Hf0 alloy (38 K), as shown in Table 5.1. Hence, it can be concluded that the deterioration of Hf0 alloy upon cycling is mainly caused by the generation of lattice defects (mainly dislocations) upon thermal cycling. The large transformation hysteresis of this alloy reveals the existence of higher irreversibility due to a bigger incompatibility between austenite and martensite phases. Together with the high temperature of the transformation, the material is quite soft and microplastic deformation becomes easier to occur at each transformation cycle. It is also worth noting that the hysteresis of Hf3 alloy is very low (8 K) and, then, a negligible generation of dislocations can be expected, resulting in a perfect reproducibility of the transformation during thermal cycling.

5.1.2 XRD Analysis

Different polycrystalline samples have been studied by X-ray diffraction (powder method) to investigate their structural state at room temperature. Unless otherwise specified, all samples were previously solution heat treated at 1270 K for 48h and water quenched. The results are shown in Fig. 5.1.4. For the ternary Hf0 alloy, the XRD spectrum only presents four peaks, consistent with the non-modulated martensite (Fig. 5.1.4 (a)). The peaks are indexed as $200_{b.c.t.}$, $202_{b.c.t.}$, $004_{b.c.t.}$ and $400_{b.c.t.}$, according to the body centered tetragonal (b.c.t.) unit cell in the crystallographic axes parallel to those of the $L2_1$ austenite phase, as shown in Fig. 1.1.11. The low number of detected peaks is attributed to a combination of a relatively low number of grains, in comparison to a powder sample, together with the typical texture developed during solidification of b.c.c. and f.c.c. metals , as it will be discussed later. For the Hf0.5 alloy, additional small peaks consistent with the hafnium carbide (HfC) phase are obtained, together with martensitic b.c.t. peaks (Fig. 5.1.4 (b)). The hafnium carbides (and also oxides, HfO_2, detected in Hf3 sample, Fig. 5.1.4 (f)) are inevitably introduced during the arc melting procedure and are present in all the quaternary alloys. Increasing the Hf addition, a bunch of new peaks appear in Hf1, Hf2, Hf3 and Hf4 alloys, indicative of the formation of a precipitated second phase, marked with P in the XRD patterns (Figs. 5.1.4 (c) to (h)). Analysis of the additional peaks (together with the information from electron diffraction in the TEM that will be presented in the next section) allow to identify a face-centered cubic structure (f.c.c.) of the precipitated second phase. The second phase peaks appear in the SHT samples and also in samples just arc-melted with no additional thermal treatment, as shown in Fig. 5.1.4 (d) for Hf2 alloy as an example. Therefore, the solution heat treatment at 1270 K for 48 h cannot dissolve the f.c.c second phase, which indicates that this phase is stable at very high temperatures. Probably, it precipitates from austenite just after solidification, or it forms during solidification together with the austenite phase.

Figs. 5.1.4 (e) to (g) present the XRD spectra obtained in two orientations of the sample surface, parallel and perpendicular to the arc flame, for the Hf2, Hf3 and Hf4 alloys. Clear differences in the number of detected peaks and their intensities can be observed for the two orientations of the samples. For example, in Fig. 5.1.4 (e), corresponding to the Hf2 alloy, the 111_P and 222_P peaks only appear in the orientation parallel to the arc flame, while the 422_P peak is only visible in the perpendicular orientation. Also, the relative intensity of the $220_{b.c.t.}$ peak with respect to the most intense peak $202_{b.c.t.}$ is much higher in the direction parallel to the flame, while $224_{b.c.t.}$ peak shows higher intensity in the orientation perpendicular to the arc flame. Hence, the orientation of the martensite variants and of the precipitates are not randomly distributed but with some preference, which is indicative of a significant texture existing in the arc-melt ingots with the assistance of large temperature gradient.

The relative intensity of the peaks corresponding to the f.c.c. precipitated phase increases with the Hf content. This is particularly evident from comparison of Hf3 (Fig. 5.1.4 (f)) with Hf2 or Hf1 (Figs. 5.1.4 (e), (c)) through the relative intensity of the major peaks of martensite, $202_{b.c.t.}$, and precipitates, 311_P. Even, the intensity of precipitates peaks are far higher than those of martensite in the orientation parallel to arc flame of Hf3. These observations suggest an increase of the precipitate volume fraction with the Hf content in the alloy. This is confirmed by the microstructural observations that will presented in the next section.

For the Hf4 alloy, Fig. 5.1.4 (g) presents additional peaks from another phase different than b.c.t. martensite and precipitates. With the support of electron diffraction (presented in the next section) these additional peaks can be indexed as 14M modulated martensite structure. This structure has been described in the introduction chapter seen and can be visualized from Fig. 1.1.12. Multiple peaks are concentrated in the angular range of 40 - 50°, so an enlarged spectrum of this zone is presented in the Fig. 5.1.4 (h). The lattice parameters of the 14M are a = 4.3074 Å, b = 5.4462 Å, c = 29.7231 Å and β = 94.41°, which are refined by MAUD software. As shown, there are five major peaks in this range corresponding to non-modulated b.c.t. martensite, modulated 14M martensite and precipitates. In addition, some of the peaks are common for two different phases, as shown with arrows and indices in the figure.

In summary, the XRD study indicates that all the studied alloys present the non-modulated body centered tetragonal martensite at room temperature, though Hf4 alloy also presents coexistence of 14M martensite. Addition of 1 at.% or higher amount of Hf to Ni-Mn-Ga induces the formation of an f.c.c. phase which persists after the solution heat treatment at 1270 K. The microstructural details of the alloys are presented in the next section.

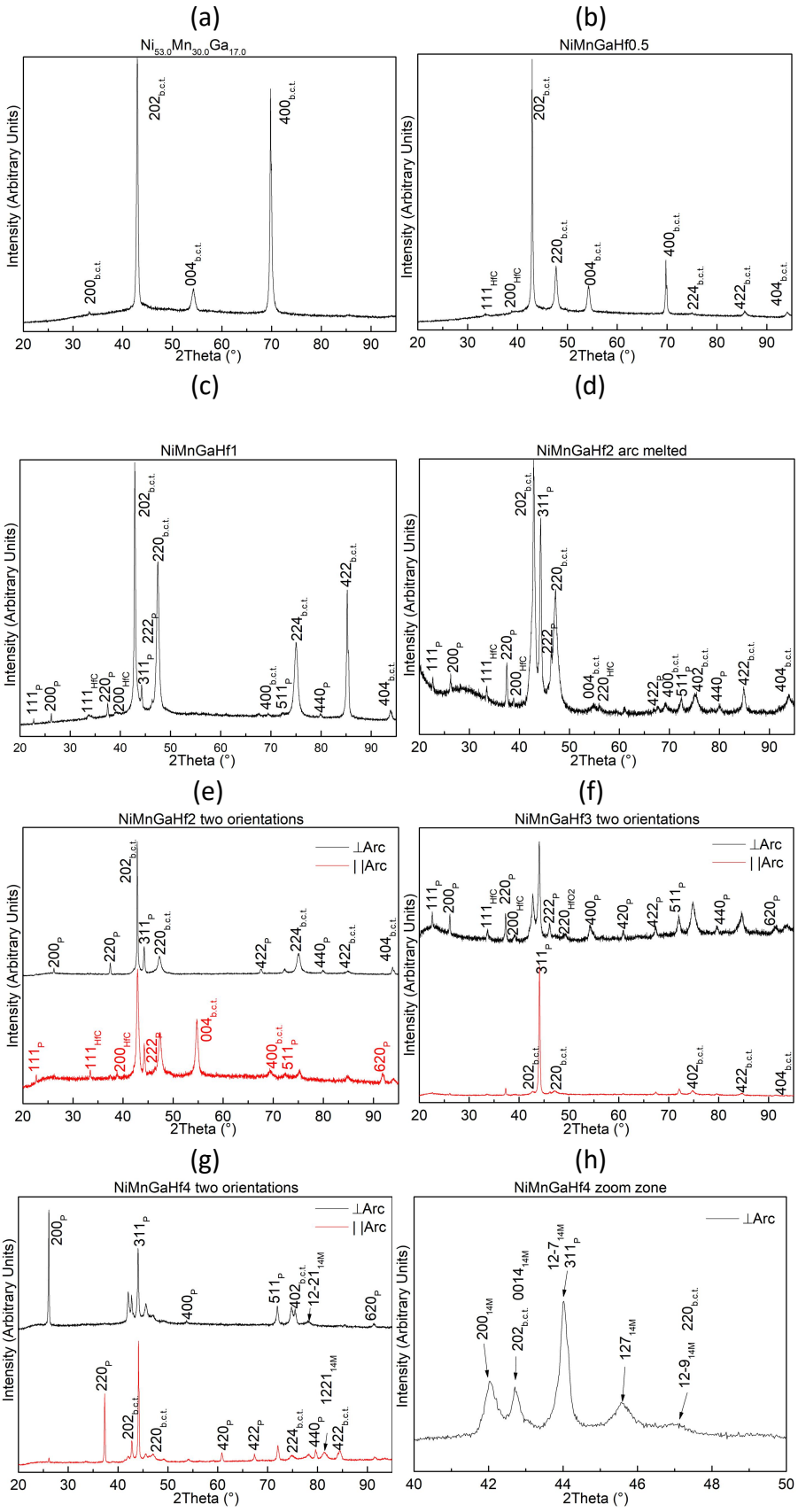

Fig. 5.1.4. XRD analysis of Ni-Mn-Ga-Hf$_X$ alloys SHT 1270 K for 48 h: (a) ternary alloy (Hf0), (b) Hf0.5, (c) Hf1, (e) Hf2 with two orientations, (f) Hf3 with two orientations, (g) Hf4 with two orientations, (h) Hf4 zoom zone, and (d) Hf2 arc melting without SHT.

5.1.3 Microstructural observations

Optical microscopy and SEM observations

Fig. 5.1.5 shows SEM images of the studied alloys taken at room temperature after a solution heat treatment at 1270 K. The Hf0 and Hf0.5 alloys exhibit the single martensite phase with some small pores and isolated particles inside the matrix, and the width of the martensite variants are between ~5 and ~25 μm (Figs. 5.1.5 (a), (b)). The particles that emerge from the matrix turn out to be rich in Hf, from the EDX analysis and correspond to hafnium carbide and/or oxide, as also detected in XRD patterns in Fig. 5.1.4. The f.c.c. second phase starts to appear not only at grain boundaries (big particles) but also randomly inside the grains (small ones) when Hf concentration is equal to or higher than 1 at.%, as shown in Figs. 5.1.5 (c) - (f) in white contrast. This is, again, in good correspondence with the XRD results. The second phase is rich in Ni and Hf, as measured by EDX. It is obvious that with the increase of Hf addition the alloy changes from single phase to dual phase and the second phase particles grow in number (Fig. 5.1.5 (d)) and subsequently in size (Fig. 5.1.5 (e)). The Hf4 alloy shows the highest number and relatively big size of particles. The proportion of area occupied by the second phase has been measured through the PS software obtained from the SEM images in Fig. 5.1.5 to be 2%, 8%, 16% and 21% for Hf1, Hf2, Hf3 and Hf4, respectively.

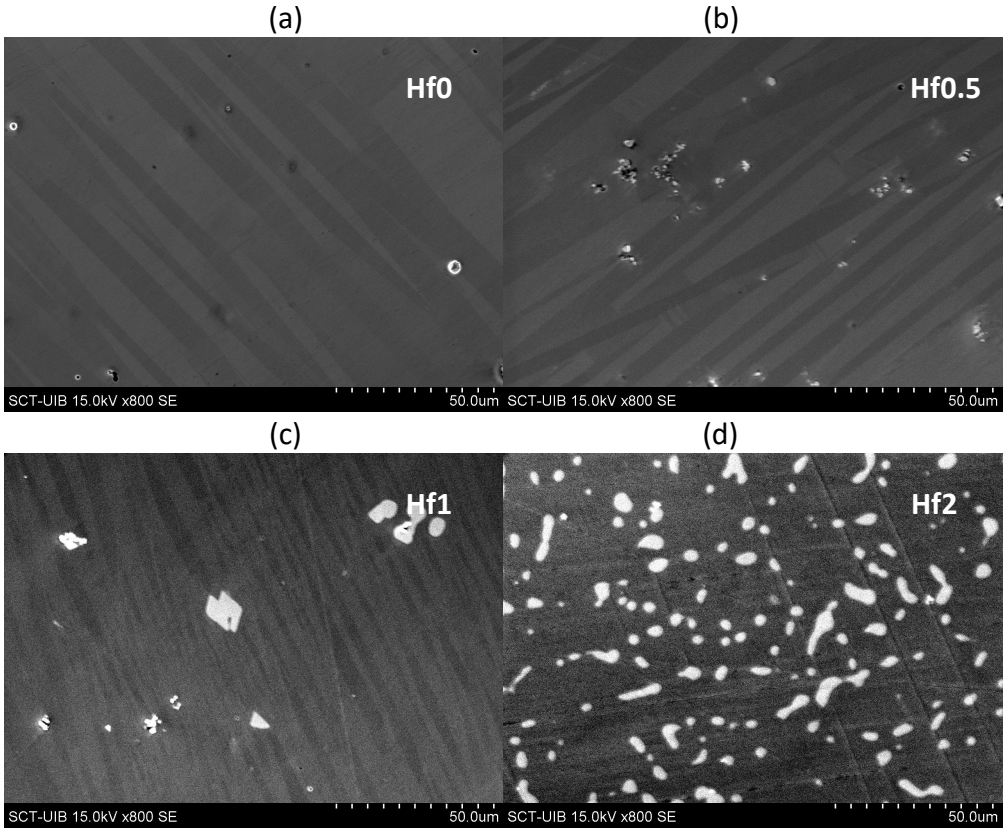

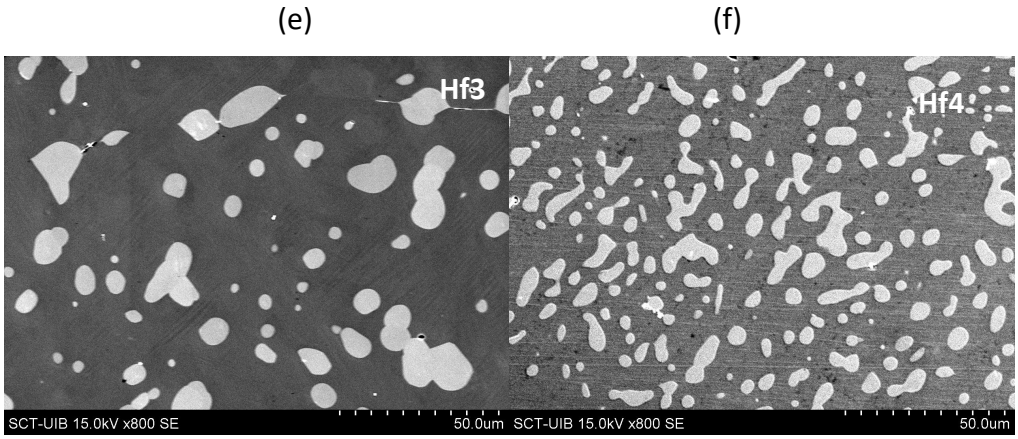

Fig. 5.1.5. SEM images of solution heat treated 1270 K for 48 h Ni-Mn-Ga-Hf_X alloys: (a) Hf0, (b) Hf0.5, (c) Hf1, (d) Hf2, (e) Hf3, (f) Hf4.

However, the precipitates are not always evenly distributed in the matrix and SEM observation with big magnification sometimes cannot reflect the whole picture. Therefore, the optical microscopy is necessary for the investigation at lower magnification with relatively larger scale shown in Fig. 5.1.6. As it is shown in Fig. 5.1.6 (a), Hf1 alloy possesses some discontinuous precipitates along the grain boundaries, while some tiny ones are scattered inside of the big grains. The low fraction of precipitates allows to visualize large martensite plates in the optical microscopy image. Figs. 5.1.6 (b) and (c) were captured from two zones of the same Hf2 sample, but show different precipitates layout. More evenly distributed precipitates are visible in Fig. 5.1.6 (b), while Fig. 5.1.6 (c) presents more precipitates located at grain boundaries. It seems that precipitates prefer to concentrate at the grain boundaries first and then inside the grains, when the boundaries are basically occupied. Fig. 5.1.6 (e) corresponds to a Hf3 SHT specimen and it presents bigger number of precipitates with narrower separation distance compared to Hf2 specimen. Although precipitates in Hf3 alloy can also be sparsely distributed in some zones with relatively large intermediate distance, the clean matrix spaces are smaller than in Hf2 sample. Finally, the Hf4 alloy shows dense and relatively big sized particles with round shape, as shown in Fig. 5.1.6 (f).

One sample of NiMnGaHf2 was solution heat treated at 1370 K for 48 h, to try to dissolve the second phase particles. The optical microscopy image, shown in Fig. 5.1.6 (d) shows a dendritic microstructure with connected net structure of the second phase, which is the typical structure of over-burning. Therefore, this heat treatment temperature is too high and the sample re-melts and solidifies during this process. After this result, all the solution heat treatments were normally performed at 1270 K or lower temperature. As commented in previous sections, this observation confirms that the f.c.c. second phase is stable up to very high temperatures, close to the melting point, and cannot be dissolved in the matrix.

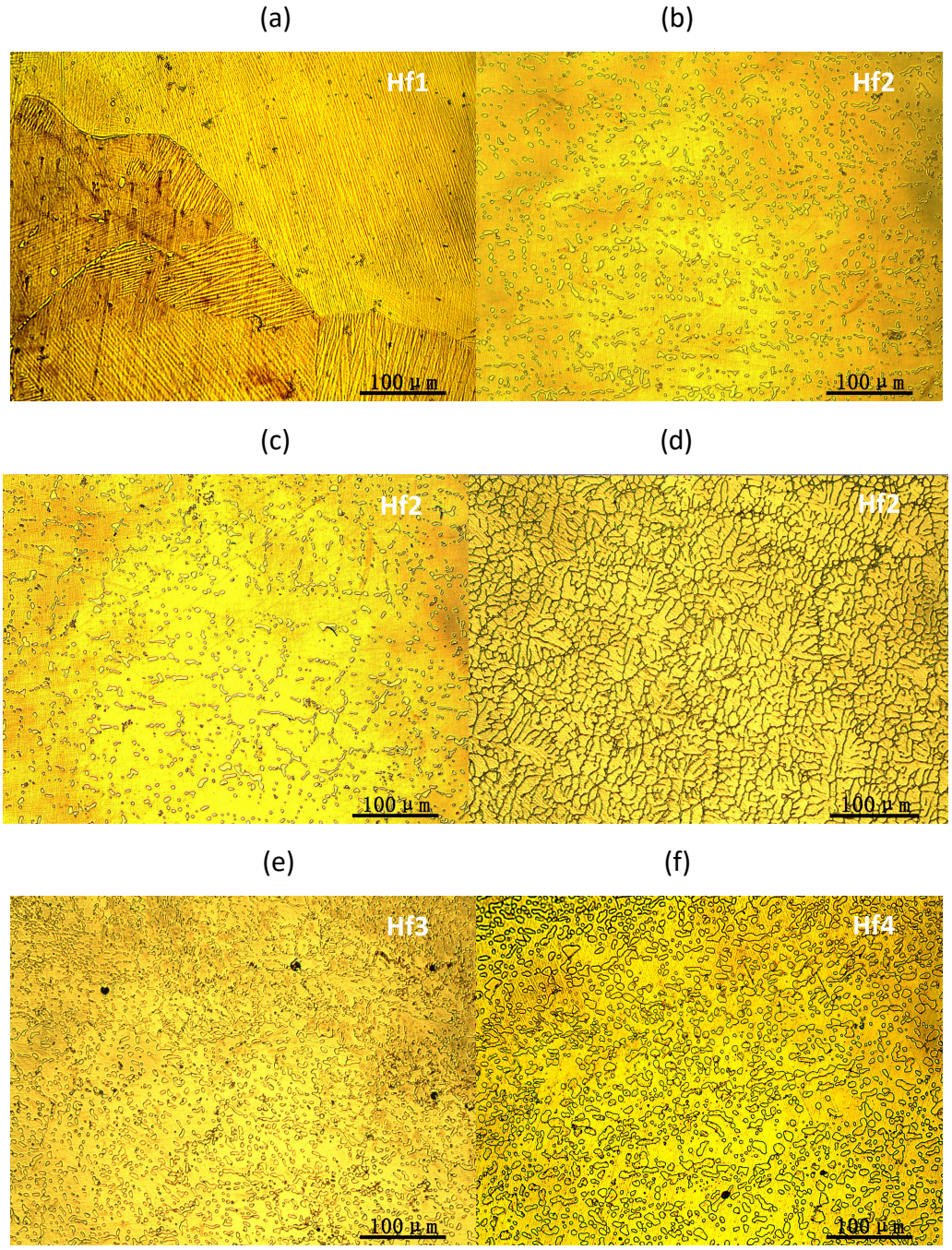

Fig. 5.1.6. Optical observation images of Ni-Mn-Ga-Hf_X alloys: (a) Hf1 SHT 1270 K for 48 h, (b) Hf2 SHT 1270 K for 48 h and another zone from the same sample (c), (d) Hf2 SHT 1370 K for 48 h, (e) Hf3 SHT 1270 K for 48 h, (f) Hf4 SHT 1270 K for 48 h.

Large differences have been found in previous section in XRD results for two different orientations of the sample surface, *i.e.*, parallel or perpendicular to the arc-melting flame. Then, the microstructural differences in both orientations have also been studied by optical microscopy and SEM. The images shown in Fig. 5.1.5 and Fig. 5.1.6 for all the studied alloys correspond to the orientation parallel to the arc flame. Fig. 5.1.7 presents the microstructure in the perpendicular orientation for Hf2, Hf3 and Hf4 alloys. It is clear that the irregular shape of the precipitates are more or less

similar for both orientations. However, some differences come from the number and distribution of precipitates. In the perpendicular orientation, the Hf2 alloy demonstrates in some zones (Fig. 5.1.7 (a)) distributions of precipitates similar to the orientation parallel to arc flame seen in Figs. 5.1.6 (b) and (c), while there are other zones that show incomplete precipitates network with large internal distance (Fig. 5.1.7 (b)).

In the perpendicular orientation of Hf3 alloy, shown in Fig. 5.1.7 (c), the images present a well-formed precipitates network concentrated at grain boundaries, but show a lower number of particles (mainly inside the grains) and relative bigger interspace compared to the parallel orientation seen in Fig. 5.1.6 (e). Nonetheless, Hf4 alloy demonstrates a consistent precipitates arrangement in both orientations of perpendicular (Fig. 5.1.7 (d)) and parallel to arc flame (Fig. 5.1.6 (f)), which exhibit comparatively bigger and more compacted precipitates than the other alloys. Figs. 5.1.7 (e) and (f) present SEM images of Hf2 and Hf3 alloys, however, considering the heterogeneous distribution effect, SEM may not necessarily be fully representative of the whole alloy due to the large magnification. In any case, the precipitates grain refinement effect can be observed through SEM images.

It can be concluded by comparing the images in the two orientations (Fig. 5.1.6 and Fig. 5.1.7) that the precipitates tend to form first a network at the grain boundaries and then they grow inside the grains. The grain boundaries are first saturated in the orientation parallel to the arc flame than in the other. Furthermore, the precipitates grow in number and/or size with increase of Hf content. As the f.c.c. second phase forms just after solidification (or during this process), the increase in precipitates number and size reduces the grain growth and causes a grain refinement effect.

(a) (b)

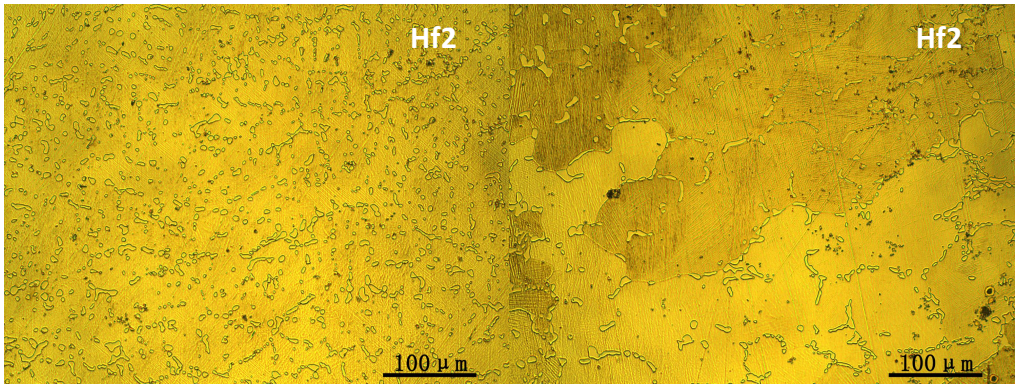

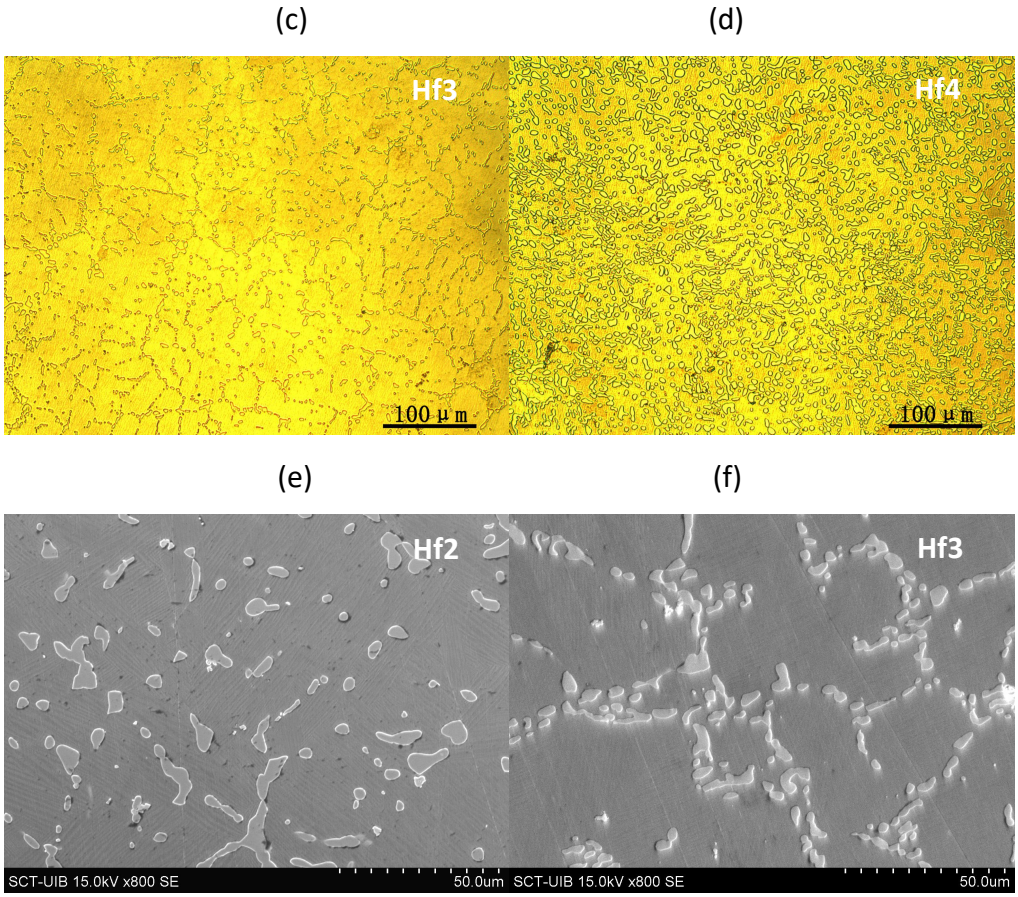

Fig. 5.1.7. Images of the other orientation, perpendicular to arc flame, of the specimens solution heat treated at 1270 K for 48 h: (a) NiMnGaHf2 and another zone (b), (c) NiMnGaHf3, (d) NiMnGaHf4; SEM images of (e) NiMnGaHf2, (f) NiMnGaHf3.

As shown in section 5.1.1, the Hf2 and Hf3 alloys present an excellent stability of the martensitic transformation upon ageing at 870 K for 48 h or 72 h, respectively. The microstructural evolution of Hf2 samples, observed by optical microscopy and SEM, is presented in Fig. 5.1.8. Neighbor samples from the same SHT bar were chosen to eliminate the heterogeneity induced during the manufacturing process and were aged at 870 K for different times. It is obvious that the high temperature ageing has no influence on the size nor the amount of the second phase indicating good thermal stability upon ageing, in agreement with the DSC results of Fig. 5.1.2. It should be noted that all the observed area of neighbor samples are parallel to the arc flame which have close relation to the second phase orientation. Fig. 5.1.9 presents the images of Hf3 SHT samples with additional ageing at 870 K for 24 h (a) and 72 h (b) obtained by optical microscopy, respectively. Again, the microstructure after ageing is basically identical to that observed before ageing, shown in Fig. 5.1.6 (e).

(a) (b)

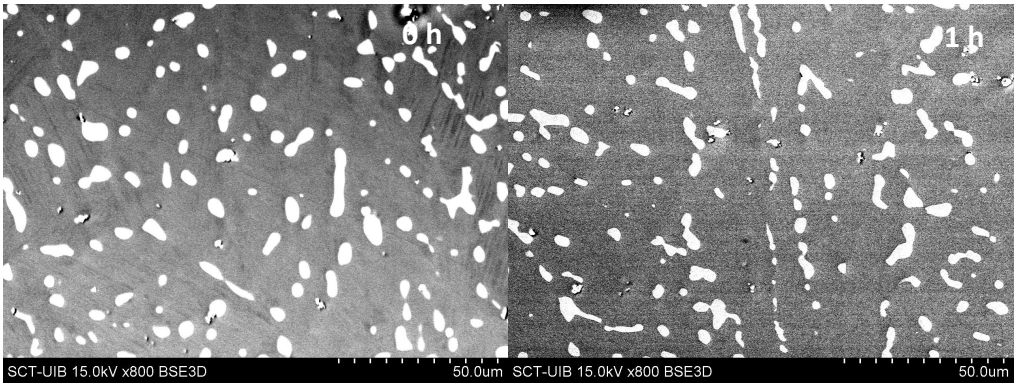
0 h
1 h
SCT-UIB 15.0kV x800 BSE3D
50.0um
SCT-UIB 15.0kV x800 BSE3D
50.0um

(c) (d)

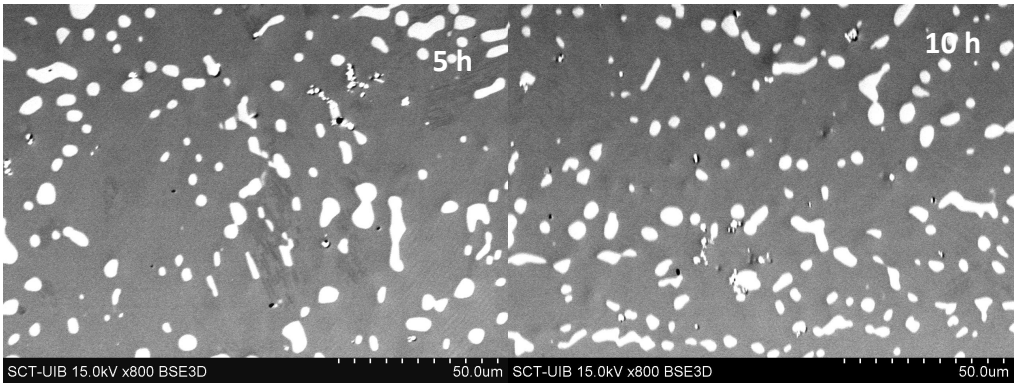
5 h
10 h
SCT-UIB 15.0kV x800 BSE3D
50.0um
SCT-UIB 15.0kV x800 BSE3D
50.0um

(e) (f)

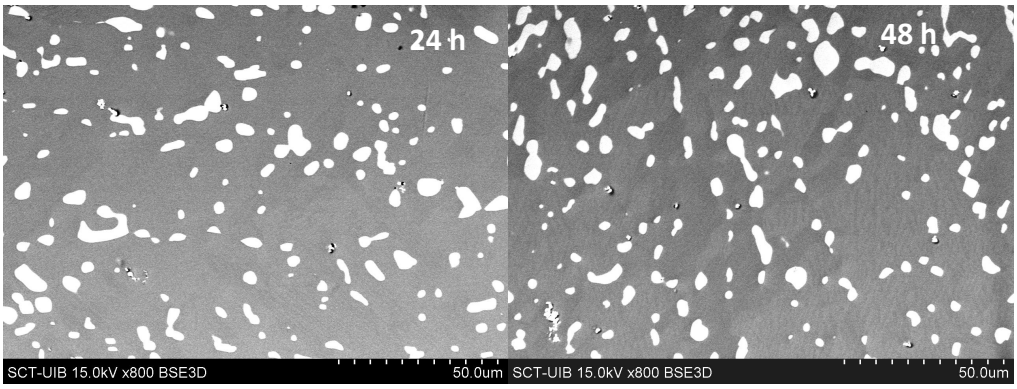
24 h
48 h
SCT-UIB 15.0kV x800 BSE3D
50.0um
SCT-UIB 15.0kV x800 BSE3D
50.0um

(g) (h)

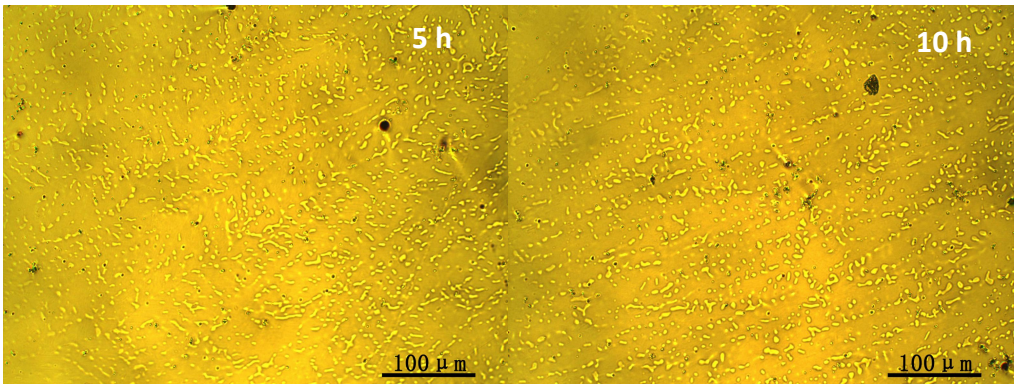
5 h
10 h
100 μm
100 μm

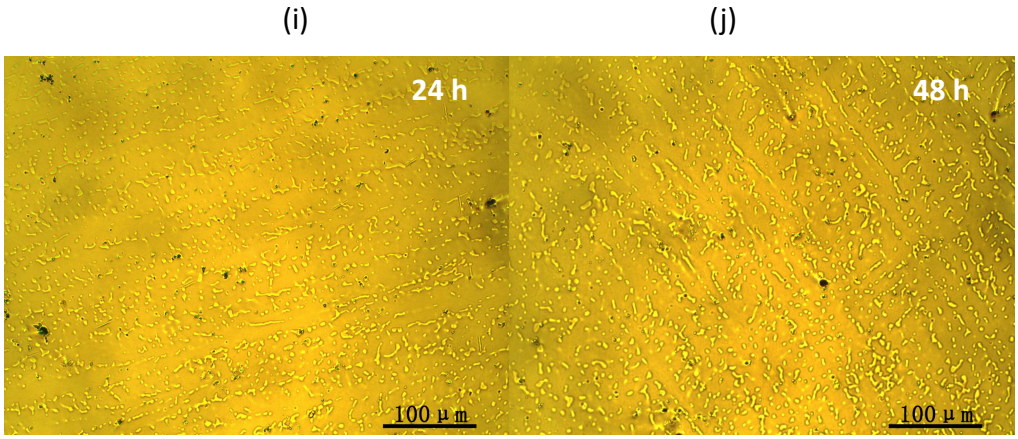

Fig. 5.1.8. SEM images of NiMnGaHf2 alloy SHT 1270 K for 48 h with additional ageing treatment at 870K for (a) 0 h, (b) 1 h, (c) 5 h, (d) 10 h, (e) 24 h, (f) 48 h; and optical microscopy observations aged for (g) 5 h, (h) 10 h, (i) 24 h, (j) 48 h.

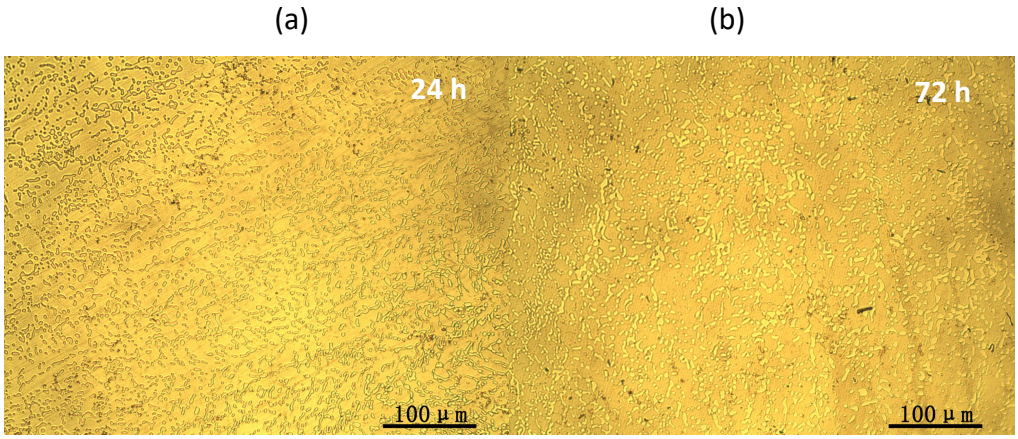

Fig. 5.1.9. Optical observation images of NiMnGaHf3 alloy SHT 1270 K for 48 h with additional ageing at 870K for (a) 24 h, and (b) 72 h.

Considering the whole set of SEM and OM images presented so far we may infer the 3D shape of the second phase particles (the images only show 2D cuts on the observation plane). From the author's perspective, the images of the second phase particles could be roughly separated into two major shapes: long bar and ellipse-like shapes (except the very small white particles which are proved to be HfC). The sizes of the two main shapes have been measured for the SEM images in Fig. 5.1.8 and are shown in Table 5.2. It can be seen that the widths of both main shapes are very similar to each other. This suggests that some of the observed ellipses could correspond to cuts of the long bar on planes at different angles to the transversal plane of the bar. Therefore, from this preliminary inspection it seems that two different types of 3D shapes exist in the second phase particles: long bars with nearly circular cross section and shorter particles with ellipsoidal shape. Both shapes develop a discontinuous network of second phase domains.

Table 5.2. Thermal treatment and second phase sizes of NiMnGaHf2 SHT alloy.

Alloy	**Ageing at 870 K**	**Long Bar**		**Ellipse-like**	
		Length µm	Width µm	Length µm	Width µm
NiMnGaHf2 SHT 1270 K	0 h	8 - 22	2 - 4	2 - 8	1 - 5
	1 h	9 - 15	1 - 4	1 - 10	1 - 4
	5 h	5 - 24	2 - 6	2 - 10	1 - 7
	10 h	9 - 18	2 - 5	2 - 9	1 - 7
	24 h	6 - 16	2 - 5	2 - 11	2 - 6
	48 h	6 - 17	1 - 6	2 - 12	1 - 8

Compositional study by EDX

Besides the microstructure, the change of composition with certain thermal treatment and addition of Hf has been also studied by EDX, attached to the scanning electron microscope. As observed before in XRD (Fig. 5.1.4) and SEM (Fig. 5.1.5), f.c.c. precipitates and carbides are formed along with the Hf addition. However, the EDX technique limits the accuracy to identify carbides, since the light elements can only yield logarithmically small *K* shell fluorescence compared with high *Z* number elements. It means that small peak form in the EDX spectra even if there is a high concentration of light elements, which could be easily disrupted by background signal noise. Therefore, light elements like C, O are excluded in the EDX quantification of the matrix and f.c.c. precipitates in the studied alloys, but they must be maintained for the characterization of carbide or oxide particles. It could be assumed that the carbides form an outer layer and cover the pure Hf inside, which cannot go to the matrix and f.c.c. precipitates, so two different sample preparation methods have been used to identify it. The first one is to quantify the carbides on the cracked sample surface without polishing in order to maintain the three dimensional shape of particles. The back scattered electrons image is presented in Fig. 5.1.10 (a). The particles with the highest white contrast are the carbide/oxide particles, and the corresponding EDX spectrum is shown in Fig. 5.1.10 (b). The composition measured by EDX is Ni 8.7 at.%, Mn 8.2 at.%, Ga 4.2 at.%, Hf 14.3 at.% and C 64.6 at.%. In addition, the f.c.c. precipitates can be also observed with less contrast, and the EDX pattern is presented in Fig. 5.1.10 (c). The composition measured by EDX is Ni 62.0 at.%, Mn 17.7 at.%, Ga 6.0 at.% and Hf 14.3 at.%. The other way is to obtain the EDX patterns from polished specimens. The compositions obtained with these samples are shown in Table. 5.3, using red bold font for the carbide particles and standard black font for the martensitic matrix and f.c.c. precipitates. It can be observed that the polished carbides contain relatively more Ni and less carbon in comparison with unpolished ones, which could support our assumption. However, the accuracy of composition is limited, because the measured signal can also include a fraction of matrix surrounding the particles. Therefore, the minor differences observed are actually in the margin of test error and no clear conclusions can be drawn. The

specific structure and components of carbide particles need further investigations, out of the scope of this work. Since the differences of both sample preparation methods are not significant, the rest of EDX analysis of the studied alloys are performed on polished samples for other conveniences.

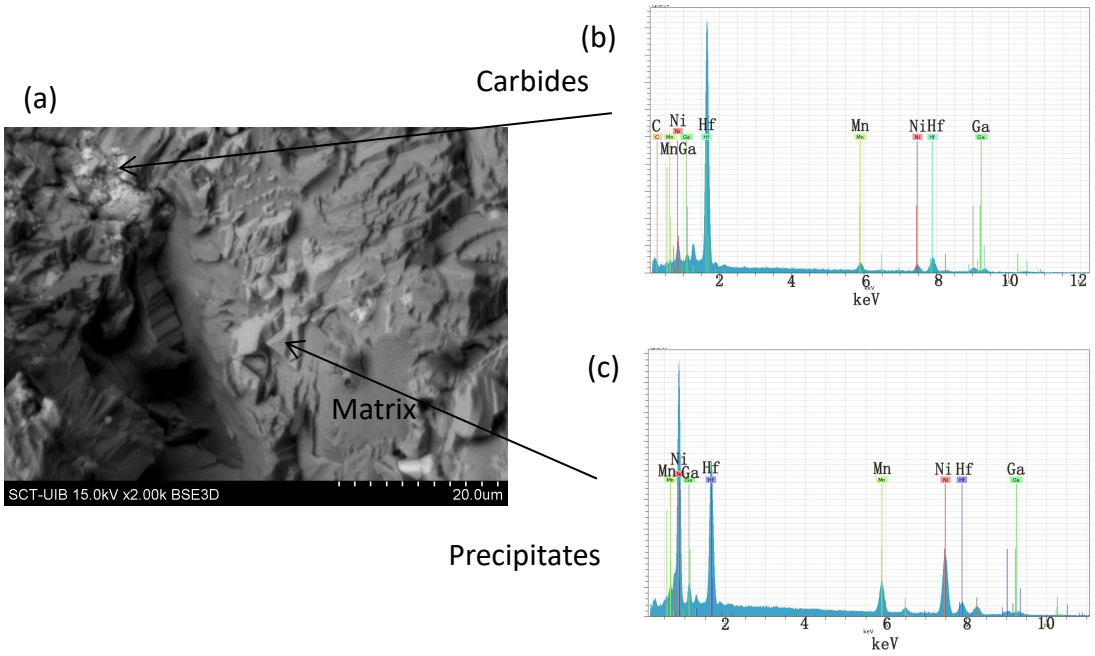

Fig. 5.1.10. SEM image of (a) NiMnGaHf1 SHT 1270 K 48h cracked sample without polishing; EDX analysis patterns of (b) carbides and (c) precipitates.

It should be noted that carbides exist in all Hf additions and their composition is very similar in all alloys, whereas the f.c.c. precipitates start to appear with over 1 at.% Hf addition. So, Table 5.3 only shows the carbides composition for Hf0.5, Hf1 and Hf2 SHT samples. For the Hf2 alloy, the compositional changes of the matrix upon ageing at 870 K show that the Ni content first decreases slightly then it grows again, while the matrix of Hf3 alloy shows a small decrease of Ni but a relatively constant value of Hf after ageing. Furthermore, the f.c.c. precipitates are richer in Ni and Hf in relation to the matrix and show irregular compositional variation upon ageing at 870 K, as seen from Table 5.3. The slight compositional changes to reach equilibrium at 870 K could be responsible of the small decrease of transformation temperatures with ageing observed in the DSC results (Figs. 5.1.2 (a) and (b)). However, it should be noted that the detected variations are of less than one unit percent and lie within the experimental uncertainty of the technique, therefore, they cannot be considered as really significant changes.

It is also worth to note in Table 5.3 that the compositions of the matrix for Hf2, Hf3 and Hf4 SHT alloys are rather similar to each other, in particular for the Hf content. For the f.c.c precipitates, the Ni content seems to decrease as a function of Hf addition (the composition of precipitates in Hf1, not shown in the Table, is: Ni 62.3 at.%, Mn 17.4 at.%, Ga 5.8 at.%, Hf 14.5 at.%). Moreover, the results indicate that the

maximum Hf content that can be dissolved in the matrix Heusler structure (which transforms to martensite at the transition temperature) is around 1 at.% and the excess Hf goes to the f.c.c. precipitates. This explains the large increase in size and number of f.c.c. precipitates observed in Hf3 and Hf4 alloys.

Table 5.3. Composition of Ni-Mn-Ga-Hf alloys with thermal treatment SHT and additional ageing at 870 K, measured by EDX for the matrix, precipitates and carbides. Red bold font is for carbides (the difference to 100 at.% is the C content) and black standard font is for precipitates.

Alloy	**Treatment**	**Martensite**				**Precipitates (or Carbides)**			
		Ni at.%	Mn at.%	Ga at.%	Hf at.%	Ni at.%	Mn at.%	Ga at.%	Hf at.%
Hf0.5	SHT 1270 K 48 h	52.9	30.8	16.0	0.3	**13.3**	**9.3**	**4.4**	**22.2**
	SHT 1270 K 96 h	52.8	30.4	16.5	0.3	**6.3**	**4.1**	**2.4**	**30.7**
Hf1	SHT 1270 K 48 h	52.3	30.3	16.8	0.6	**5.4**	**3.9**	**2.3**	**32.8**
Hf2	SHT 1270 K 48 h	52.5	29.2	17.5	0.8	**12.1**	**7.1**	**3.5**	**25.7**
	Aged 870 K 1 h	51.5	32.1	15.5	0.9	63.1	18.7	4.8	13.4
	Aged 870 K 10 h	51.3	30.4	17.5	0.8	61.1	19.4	6.7	12.8
	Aged 870 K 24 h	50.4	30.6	18.2	0.8	61.7	17.7	6.4	14.2
	Aged 870 K 48 h	52.1	30.3	16.8	0.8	61.0	18.5	6.3	14.2
Hf3	SHT 1270 K 48 h	51.2	30.9	16.9	1.0	59.6	19.3	7.2	13.9
	Aged 870 K 72 h	51.1	31.1	16.9	0.9	59.2	20.3	7.5	13.0
Hf4	SHT 1270 K 48 h	50.3	31.2	17.5	1.0	58.8	19.4	8.3	13.5

TEM observations

At this point, the main results of the TEM investigation performed on these alloys will be presented. Fig 5.1.11 shows micrographs ((a) and (c)) and their corresponding selected area electron diffraction patterns (SADP) of Hf0.5 and Hf1 alloys at room temperature. The diffraction patterns confirm the non-modulated martensite in both alloys, indexed according to the body centered tetragonal (b.c.t.) structure (Figs. 5.1.11 (b), (d)), with (022)-type internal twinning plane. The bright field images show fine and rather regular internal twins with similar spacing distance of few nanometers. Moreover, no second phase precipitates were observed in these specimens, even after prolonged homogenization thermal treatments (up to 4 days), in agreement with the XRD and SEM results.

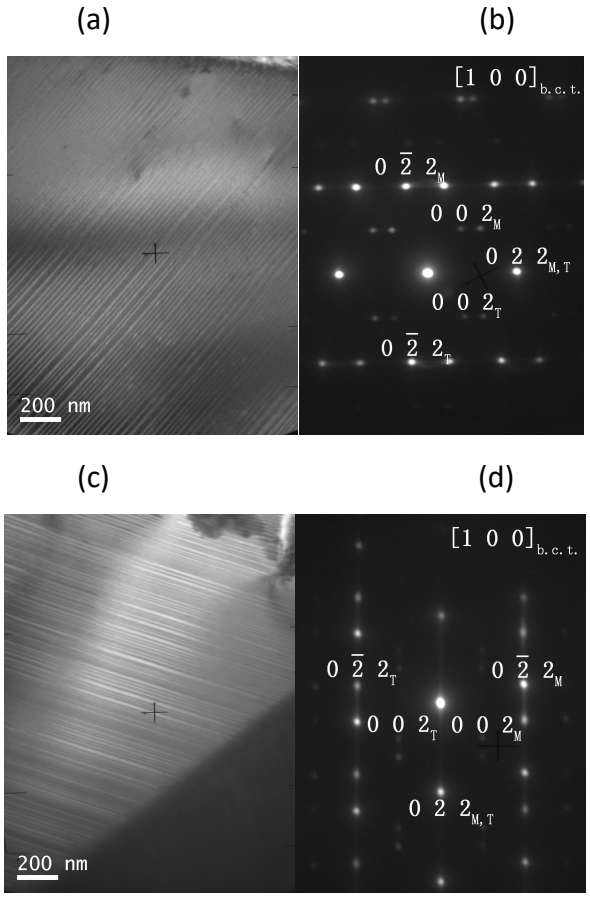

Fig. 5.1.11. TEM observation of NiMnGaHf0.5 SHT 1270 K for 4 days alloy: (a) bright field image, (b) corresponding selected area diffraction pattern; and NiMnGaHf1 SHT 1270 K for 4 days (c) bright field image, (d) corresponding selected area diffraction pattern.

Fig. 5.1.12 shows the bright field images (a), (c) and SADPs (b), (d) of Hf2 alloy at room temperature. The bright field micrographs show second phase particles embedded in the b.c.t. non-modulated matrix. The particles are marked with a label "P". A higher amount of bending contours appear on the matrix and precipitates compared to Hf0.5 (Fig. 5.1.11 (a)) and Hf1 (Fig. 5.1.11 (c)), as a result of the internal stresses arising from the accommodation of both phases. The SADPs of Figs. 5.1.12 (b) and (d) correspond to the precipitates and are indexed according to the f.c.c structure in two different zone axes, $[110]_P$ and $[211]_P$, respectively. The γ phase with f.c.c. structure is well known to form in Ni-Mn-Ga alloys. However, there is a big difference in lattice parameter of the present SADPs compared to the γ phase reported from the literature. For example, Ma YQ *et al*. [62] obtained an almost constant lattice parameter of γ phase, a = 3.614 Å, for different Cr content. With such a lattice parameter, the distance between spots in the diffraction patterns should be, approximately, double than the distance observed in the present patterns given in Figs. 5.1.12 (b) and (d). Hence, the precipitates induced by Hf addition must have a different structure than the normal γ phase, and the detail of the structure will be investigated in the discussion section.

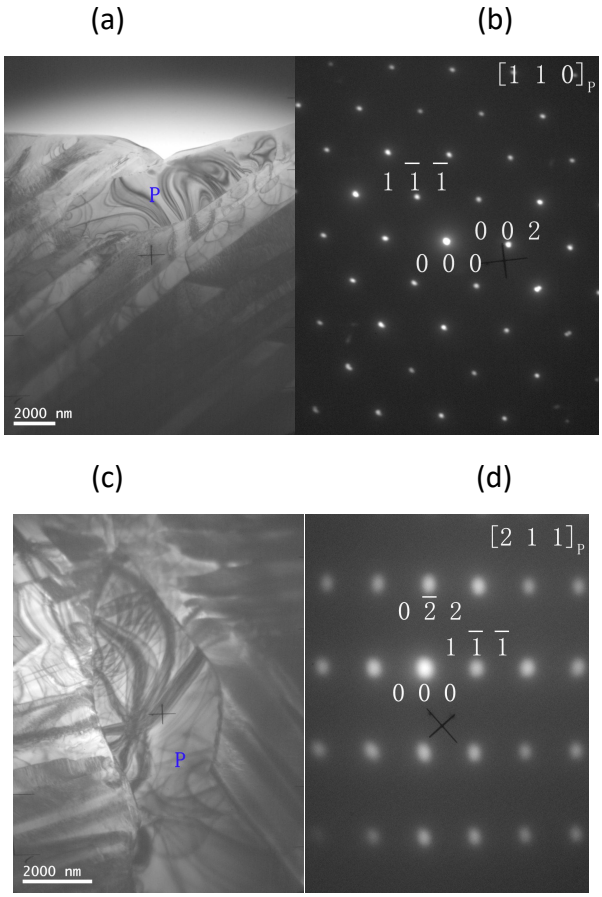

Fig. 5.1.12. TEM observations of NiMnGaHf2 SHT 1270 K for 48 h alloy: (a) bright field image (b) corresponding selected area diffraction pattern of precipitates; (c) BF image of another zone, (d) corresponding SADP of precipitates under another zone axis.

Fig. 5.1.13 present the TEM observation of Hf4 alloy SHT at 1270 K for 48 h, which contains a big amount of precipitates (a) - (c), non-modulated body centered tetragonal martensite plates (d) - (e) and modulated 14M martensite (f) - (g). The precipitates exhibit the same cubic structure with similar lattice parameter as the precipitates observed in Hf2 alloy. Another zone axis, $[301]_P$ consistent with the f.c.c. structure, is shown in Fig. 5.1.13 (c). More precipitates, marked with label "P", appear in this alloy compared to Hf2 alloy, and they show more transparency than the surrounding martensite variants as a result of preferential electro-polishing. Non-modulated martensite plates are visible with thin (022)-type internal twins, like in the other Ni-Mn-Ga-Hf alloys. However, an unexpected structure is also displayed by Hf4 alloy, which has not been observed in the rest of studied alloys and is not typical for high temperature Ni-Mn-Ga alloys. The SADPs reveal the so-called 7-layered or 14M structure of martensite (Fig. 5.1.13 (g)), with the characteristic six extra spots along the $[001]_{14M}$ direction (corresponding to a <011> direction of $L2_1$ austenite) [64, 67]. Actually, the bright field image of 14M structure (Fig. 5.1.13 (f)) shows much lower thickness of the internal twins in comparison with the non-modulated b.c.t. martensite. For the ideal 14M structure, the internal twin thicknesses are of only 5 and 2 atomic planes [64]. Probably, the enhanced internal

stress fields caused by the larger amount of f.c.c precipitates causes the twin thickness refinement and development of the 14M structure.

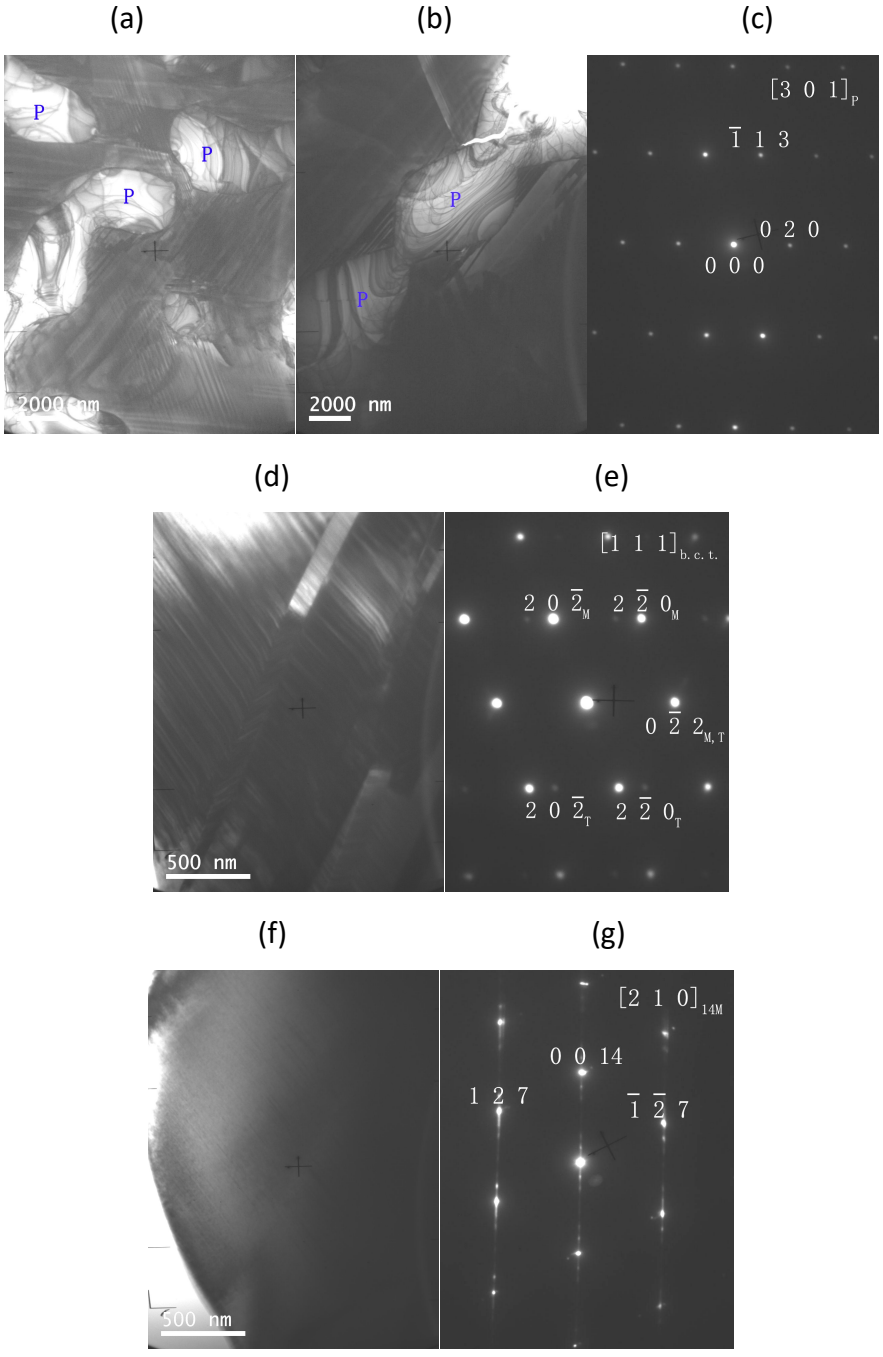

Fig. 5.1.13. TEM observation of NiMnGaHf4 SHT 1270 K 48 h alloy: (a) BF image of precipitates and matrix, (b) another zone of matrix and precipitates and (c) corresponding SADP of the precipitates of (b); (d) BF image of matrix and (e) corresponding SADP of non-modulated martensite in the $[111]_{b.c.t.}$ zone axis; (f) BF image of matrix and (g) corresponding SADP of modulated 14M martensite in the $[210]_{14M}$ zone axis.

5.1.4 Thermomechanical Experiments

Fig. 5.1.14 presents the results of thermomechanical tests (cooling/heating under different levels of compressive stress) performed on Ni-Mn-Ga-Hf SHT alloys to characterize their shape memory effect. All graphs are adjusted to the same scale of temperature (**X**-axis) and strain (**Y**-axis), to facilitate the visualization of the evolution of the mechanical response with the Hf addition. A clear trend shown in the Fig. 5.1.14 is that the thermomechanical response related to the martensitic transformation is shifting to lower temperatures as a result of Hf addition, which is consistent with the DSC results in Fig. 5.1.1. Furthermore, the hysteresis of the thermomechanical cycles is becoming slimmer with the increase of Hf, *e.g.*, Hf0 exhibits ~52 K hysteresis under 300MPa while Hf3 only has ~8 K hysteresis under the same stress level. As typical in all shape memory alloys, the total strain developed upon cooling increases with the applied compressive stress and so does the irrecoverable strain. For instance, Hf0 alloy exhibits 0.62% or 2.77% total strain and 0.06% or 0.73% irrecoverable strain under 20MPa or 300MPa, respectively (Fig. 5.1.14 (a)).

Tables of different parameters of the thermomechanical cycles can be found in the Appendix section (Tables A1 to A5), which show the direct and reverse transformation temperatures, hysteresis, total strain, irrecoverable strain and ratio of both strains, obtained through the way mentioned in the introduction chapter. The tendency of the aforementioned parameters will be further analyzed in the following part.

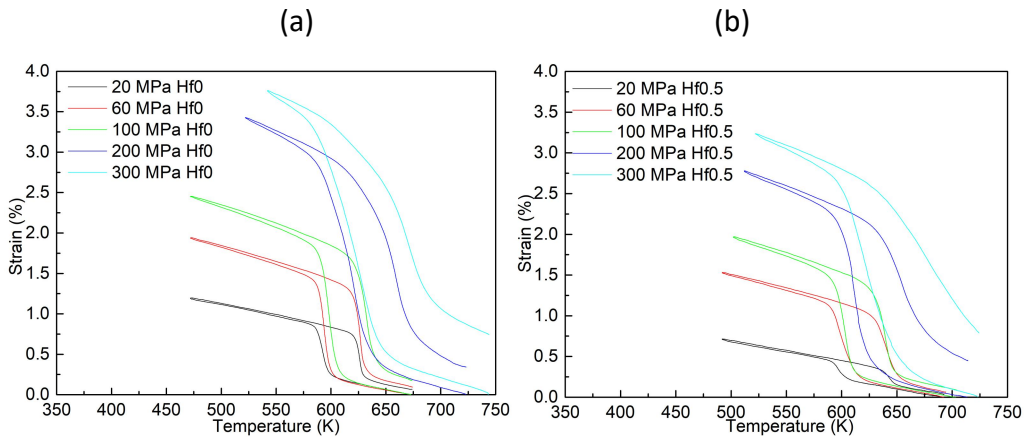

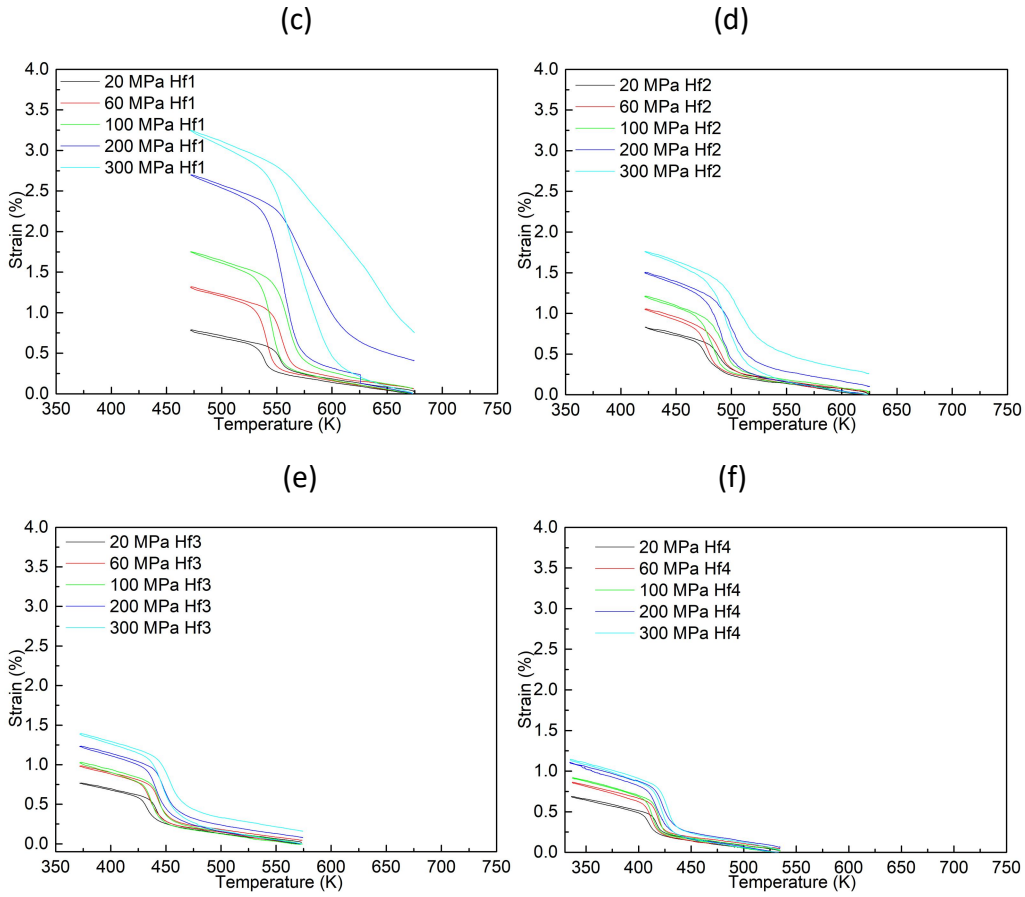

Fig. 5.1.14. Thermomechanical tests of Ni-Mn-Ga-Hf$_X$ SHT 1270 K for 48 h alloys: (a) Hf0, (b) Hf0.5, (c) Hf1, (d) Hf2, (e) Hf3, under the constant compression stress from 20 MPa up to 300 MPa.

Figs. 5.1.15 (a) and (b) present the evolution of the total and irrecoverable strains as a function of the applied stress for the Ni-Mn-Ga-Hf alloys, extracted from the thermomechanical tests shown in Fig. 5.1.14. It is obvious that the total strain follow an increasing tendency with the compression stress, indicating the increase in the proportion of stress induced martensite variants favored by the applied external stress. For Hf0 and Hf0.5 alloys, the growth rate of total strain is gradually decreasing as a result of saturation of stress assisted preferred variants, but for higher Hf content the curves are almost linear, which means that more preferred variants could be activated with further stress increment. On the contrary, the slope of irrecoverable strain keeps growing continuously in all alloys. It can be seen that there is a large gap between 1 at.% and 2 at.% Hf curves for both strains, due to the increase in the amount of non-transformable precipitates, *i.e.*, the volume fraction of austenite/martensite matrix reduces, which contributes to decrease the strain value. For example, under 200MPa the total strain decreases from 2.45% to 0.72% for Hf0 to Hf3, respectively, while the irrecoverable strain drops from 0.34% to 0.08%.

Fig. 5.1.15 (c) exhibits the ratio between irrecoverable strain and total strain as a function of the applied stress, which shows a small drop in the stress range 60 - 100 MPa followed by a continuous increase for higher stresses up to 300 MPa. This

situation is the result of the low and almost constant values of irrecoverable strain below 100 MPa, which indicates that plastic deformation by generation and movement of dislocations or development of retained martensite as the main factors responsible for the irrecoverable strain could be restrained by the internal stress fields of the tested specimen. However, under applied stresses above 100 MPa, the linear tendency means that the mechanisms for irrecoverable strain are activated irrespective of the internal stresses. In this sense, the Hf1 and Hf0.5 alloys (with absence or very low amount of the second phase precipitates) show a higher slope than Hf0 and attain rather large values of the $\varepsilon_{irr}/\varepsilon_{total}$ ratio, above 30%, at 300 MPa. In turn, Hf2 and Hf3 show a slightly lower slope than Hf0 and the strain ratio at 300 MPa is reduced to ~20%. For Hf4 alloy the ratio is further reduced to 10% at 300 MPa; however, the total strain developed with the martensitic transformation is reduced to only ~0.5%, due to large volume fraction of the f.c.c. second phase. Therefore, these results would indicate that Hf addition without significant generation of second phase precipitation produce a small softening of the Ni-Mn-Ga alloys, whereas the Hf additions that promote the second phase precipitation can only produce a limited strengthening effect of the material, probably due to the large size of the second phase particles.

As it is well known, the martensitic transformation temperature and applied stress are related through the Clausius-Clapeyron relationship. Fig. 5.1.15 (d) plots the M_s temperature measured under different applied stresses. As it is shown, the positive slope means the M_s temperature increases with the applied stress, as expected. However, different values of the slope below 100 MPa and above this stress level are visible in Fig. 5.1.15 (d). As discussed in the previous paragraph, the different response at low stress values can be related to the role of the internal stress fields existing in the material, that compensate the external applied stress and reduce the change in the M_s temperature. The results of Figs. 5.1.15 (c) and (d) indicate that the internal stress levels existing in these alloys are of the order of 100 MPa. For applied stresses above 100 MPa, the Clausius-Clapeyron slope values are around 5 MPa/K for low Hf addition up to 1 at.% and increase to 9.5 MPa/K, 12.9 MPa/K and 16.6 MPa/K for Hf2, Hf3 and Hf4 alloys, respectively. For the latter alloys, more applied stress is needed to elevate the M_s temperature. Actually, the applied stress is acting on the mixture of matrix and precipitates, so the external stress is partially compensated by the stress field induced by precipitates.

Fig. 5.1.15 (e) presents the work output of the different alloys, calculated from the product of recoverable strain (difference between the total and irrecoverable strains) and applied stress. As it is shown, the work output increases with the applied stress level, and it decreases with the addition of Hf due to the formation of non-transformable second phase precipitates. For example, the Hf0 alloy generates about 6.0 J/cm^3 work output while Hf3 only produces about 2.0 J/cm^3 work output under 300 MPa.

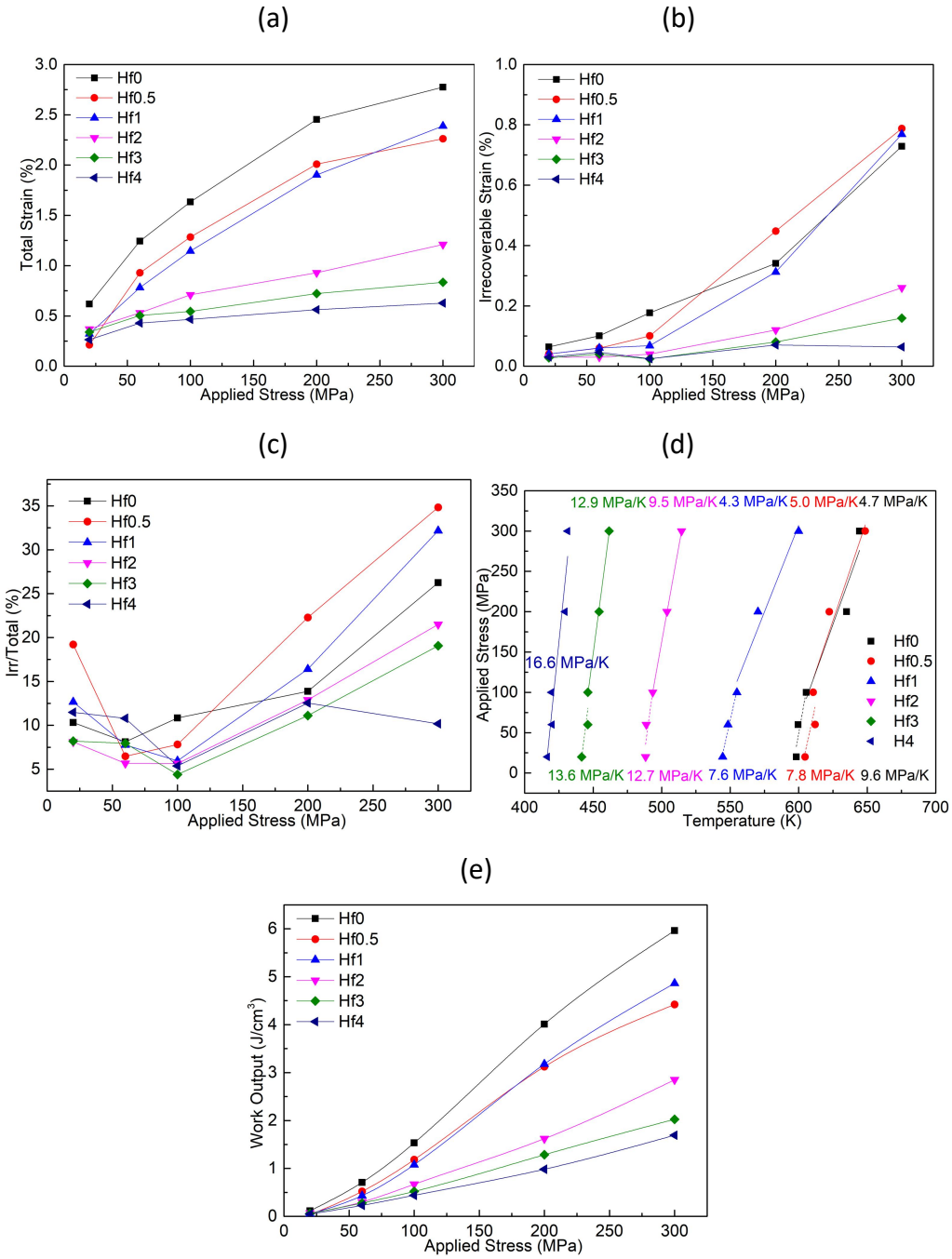

Fig. 5.1.15. Thermomechanical results of Ni-Mn-Ga-Hf alloys as the result of Hf addition: (a) total strain, (b) irrecoverable strain and (c) ratio of irr/total strain as a function of applied stress; (d) applied stress and M_s related to Clausius-Clapeyron equation; (e) work output as a function of applied stress.

5.1.5 Mechanical Experiments

Fig. 5.1.16 presents the results of mechanical tests of Ni-Mn-Ga-Hf solution heat treated alloys performed at different temperatures above A_f. For the ternary alloy without Hf addition (Fig. 5.1.16 (a)), typical stress-strain loops with an inclined plateau can be observed upon loading, but the recovered strain is very low. For

instance, for a total applied deformation of 3.4% at 680 K (at applied stress levels about 600 MPa) the material only exhibits 1.5% recoverable strain (disregarding the elastic strain) and relatively large residual irrecoverable strain (0.4%). The obtained recoverable strain is smaller than the values reported for a single crystal alloy [147], due to the stresses accumulated at the grain boundaries that induce plastic deformation. Moreover, plastic deformation is easier to take place at the high test temperatures (over 600 K) used in these experiments.

For the alloys with Hf addition containing second phase particles (Figs. 5.1.16 (b), (c) and (d)), however, no or very little superelasticity effect can be observed in the mechanical tests performed at temperatures above their A_f. Most of the stress-strain curves demonstrate slim cycles and only few ones show some recoverable strain after applied stress above 600 MPa, *e.g.*, Hf2 alloy at 540 K. The Hf4 alloy compressed at 460 K reaches a total strain above 3% at ~800 MPa applied stress, and exhibits some recoverable strain upon unloading of ~1.0% with wide hysteresis. However, the sample was fractured after this test. The crack occurrence is clearly appearing in the σ-$\mathcal{E}$ curve as sudden vertical drops of stress, marked with red circles. These results indicate that the reverse martensitic transformation upon unloading is impeded by the second phase precipitation in form of large particles of micrometric sizes exhibited by these alloys.

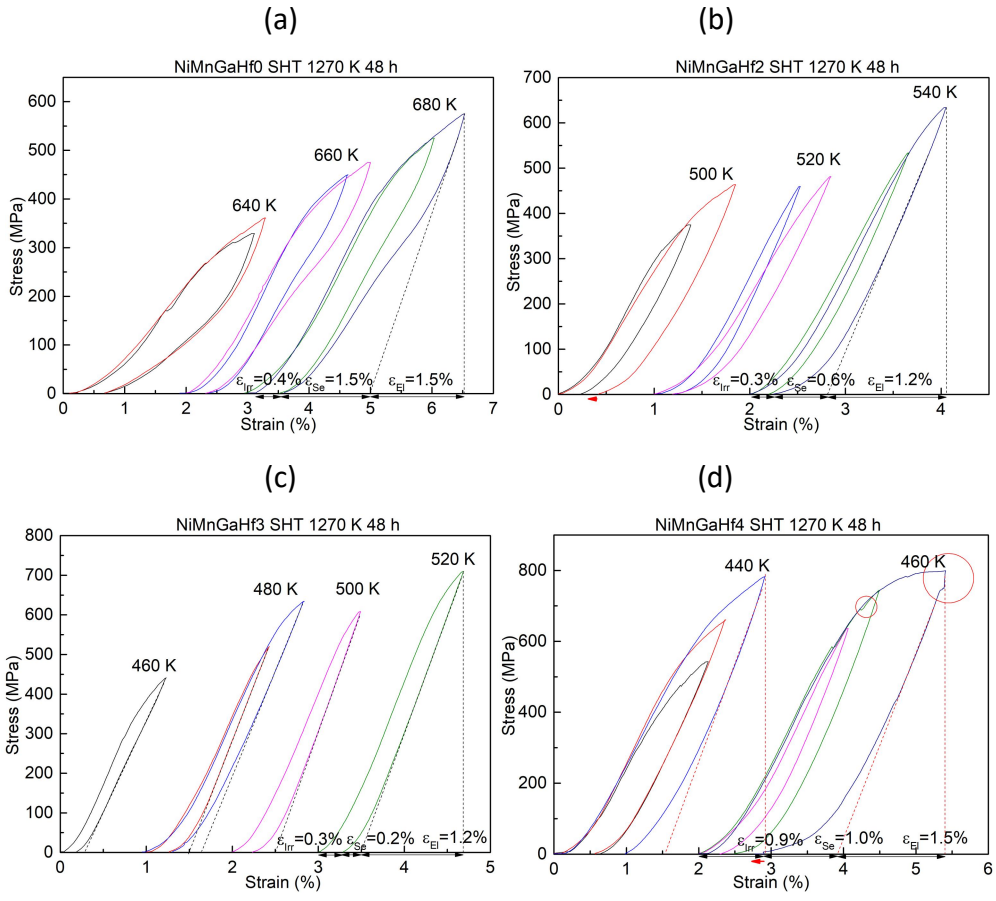

Fig. 5.1.16. Stress-strain curves of Ni-Mn-Ga-Hf SHT 1270 K alloys: (a) Hf0, (b) Hf2, (c) Hf3, (d) Hf4.

5.2 Discussion of the results

It is well known that the introduction of a fourth element in ternary alloy Ni-Mn-Ga system can extremely change the structure constitution as well as other characteristics of shape memory properties. In this chapter, the effect of Hf addition (from 0 at.% up to 4 at.%) on the martensitic transformation, microstructure and shape memory properties will be discussed combining the observations and analysis mentioned above.

5.2.1 Transformation Temperatures and Other Thermal Characteristics

The martensitic peak temperature as a function of *e*/*a* and *c*/*a* ratio is shown in Figs. 5.2.1 (a) and (b), respectively. The temperature is extracted from the DSC direct transformation peak point, and the *e*/*a* ratio is calculated from the experimental composition obtained by EDX (average data of six points). Additionally, the lattice parameters are obtained from the XRD patterns recorded in the orientation perpendicular to the arc flame (Table 5.4). As it is already discussed in the introduction section, in the Ni-Mn-Ga-X quaternary alloys the growth of MTT can be attributed to the increasing value of *e*/*a* and cell lattice effect [61, 62, 173]. In the composition design of the studied alloys, Mn and Ga are substituted by Hf in the same ratio. The former elements provide in average around 5 valence electrons per atom (7 by Mn and 3 by Ga) while Hf provides only 4 valence electrons per atom. Therefore, a drop of MTT is expected when more Hf substitutes the Mn and Ga as shown in Fig. 5.2.1 (a). Small deviations from the nominal composition in the alloy production together with the experimental error of the EDX technique causes a significant dispersion of the data, but an overall decreasing tendency is still observed and can be trustworthy since the spots are scattered in the two sides.

Fig. 5.2.1 (b) also demonstrates a clear lattice effect on the MTT variation for low addition of the fourth element (≤ 2 at.%), due to the higher atomic radius of Hf compared to the other elements. The decreasing tetragonality of the martensite reduces its stability and leads to reduction of MTT [173]. The anomalous increase of MTT of Hf0.5 alloy in relation to Hf0 can be reasonably explained from a deviation in the real composition that produces the large increase of the *e*/*a* ratio observed in Fig. 5.2.1 (a). However, for Hf2, Hf3 and Hf4 alloys there is a very little change of the martensite lattice parameters and tetragonality ratio *c*/*a* (Table 5.4), which causes the proximity of the corresponding spots in the left hand side of Fig. 5.2.1 (b). This is a consequence of the saturation in the amount of Hf (about 1 at.%) dissolved in the martensitic matrix, as shown and discussed in Table 5.3. Therefore, the effect of the higher atomic radius of Hf is also saturated for ~1 at.% Hf content. The drop of MTT observed in Hf3 and Hf4 alloys in relation to Hf2 has to be related to the increasing

amount of precipitated f.c.c. second phase, which affect to total amount of elastic energy needed to accommodate the transformation strain of the matrix surrounding the non-transformed f.c.c. particles.

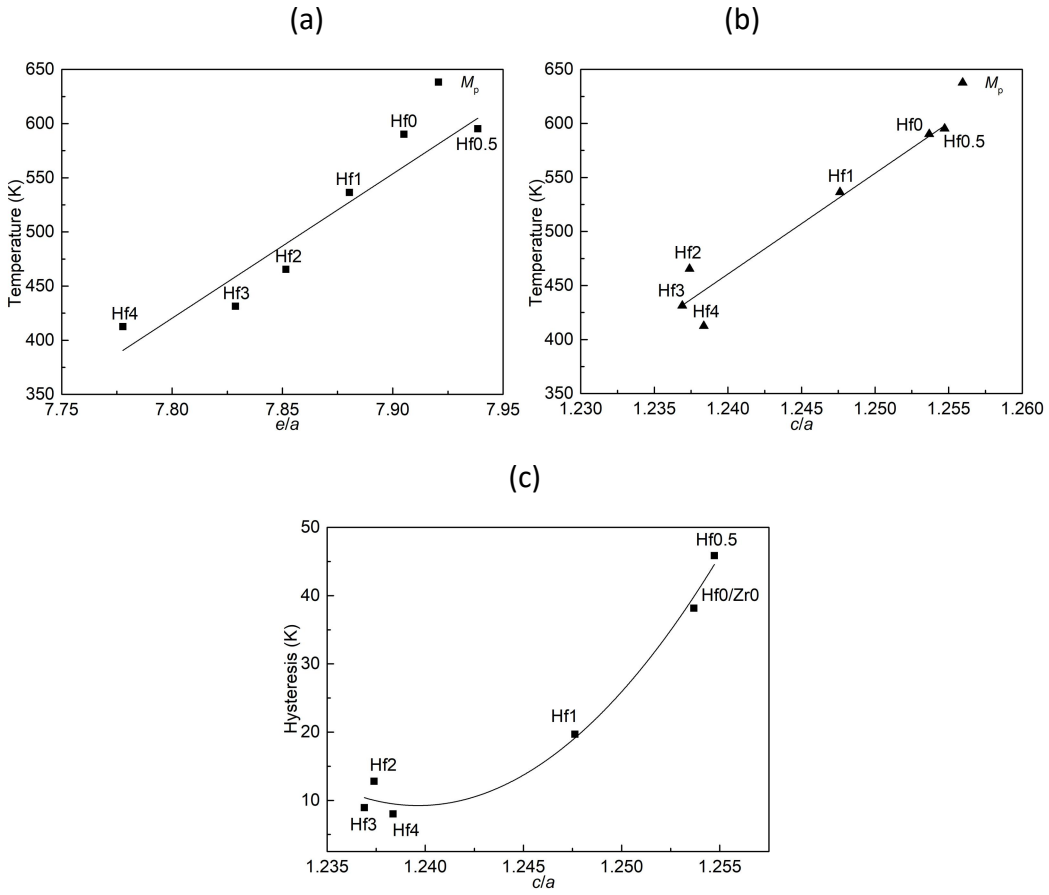

Fig. 5.2.1. Variation of the transformation peak temperature (M_p) (a) as a function of valence electron concentration per atom (*e*/*a*) and (b) as a function of tetragonality (*c*/*a*) of matrix; (c) Hysteresis variation as a function of tetragonality (*c*/*a*), for studied Ni-Mn-Ga-Hf alloys.

Table 5.1 shows the values of MTT along with the hysteresis and enthalpy change of transformation, which are both decreasing with the Hf addition. The second phase does not participate in the thermoelastic martensitic transformation [161]. Therefore, the volume fraction of precipitates is continuing increase as the result of Hf addition, leading to the decrease of martensite volume fraction and the drop of enthalpy change. The hysteresis reaches very low values (8 K) for Hf3 and Hf4 alloys. Santamarta *et al*. [58] studied Cu additions to high temperature Ni-Mn-Ga alloys and found a decrease of the transformation temperatures and hysteresis width with the *e*/*a* ratio and also suggested a dependence of hysteresis with *c*/*a*. This behavior is similar to the present results of Hf addition shown in Fig. 5.2.1 (c). It is obvious that the hysteresis decreases as a function of tetragonality with the Hf addition smaller than 2 at.%, and then remains basically unchanged with further Hf addition (2 - 4 at.%). Hf0.5 alloy shows higher tetragonality value than the Hf0 alloy, which could be attributed to the solution of Hf atoms that has been discussed before.

The second phase precipitates produce a wide variety of effects on the martensitic transformation and its hysteresis in different SMAs. In Cu-Zn-Al or Cu-Al-Mn, the so-called γ phase (with a cubic structure different from γ phase of Ni-Mn-Ga) initially forms nanometric precipitates fully coherent with the matrix and causes a decrease of the transformation temperatures and a small increase of hysteresis width. However, for larger precipitate sizes above ~1 μm, the martensite plates cannot overcome the precipitates and form a microstructure of small plates in the regions between the γ particles, which produces a large increase of hysteresis (up to 8 times larger than the normal transformation in absence of precipitates). The increase of hysteresis was attributed to the generation of dislocations around the particles and the larger friction in the movement of martensitic interfaces, related to the drastic decrease of the martensite plate size [205-207]. The same qualitative effects, but intensified in magnitude, are observed in Co-Ni-Ga single crystals containing γ' precipitates, even with nanometric sizes, due to a very strong interaction of the precipitates with the martensite [208, 209]. On its turn, the Ni_4Ti_3-type precipitates formed in Ni-rich Ni-Ti single crystals upon ageing produce first a decrease of transformation temperatures for nanometric sized precipitates and then an increase of the temperatures with further growth of the precipitates, but the thermal hysteresis is not much affected by the different precipitate sizes. The changes of transformation temperatures are attributed to the internal stresses created by the precipitates, changes in the elastic energy during the transformation, fine twinning of martensite for large precipitate sizes and compositional change of the transforming matrix [8, 210]. As mentioned in Chapter 3, H-phase precipitates form in Ni-rich Ni-Ti-Hf and Ni-Ti-Zr HTSMAs and also produce a decrease of transformation temperatures when they have nanometric size and can be absorbed by the martensite plates. However, contrary to Cu-based and Co-Ni-Ga, this is accompanied by a decrease of thermal hysteresis, attributed to the strong hardening effect of the matrix caused by the precipitates [123, 141]. For H-phase particle sizes of hundreds of nm, small martensite plates form between the precipitates, which is accompanied by a moderate increase of hysteresis, but still below the hysteresis level of the material with no precipitates [123, 141].

The hardening effect of precipitates embedded inside the matrix can impede the energy dissipation during transformation leading to the decrease of hysteresis, such as nano sized H phase in Ni-Ti-Hf [123]. However, the situation seems to be different in our alloy system Ni-Mn-Ga-Hf, as very big particles of dozens of microns in length and several microns in width are obtained (Table 5.2), not affected by thermal treatment. No hardening effect of the matrix could be expected due to these incoherent huge size precipitates. Moreover, P. La Roca *et al*. [211] report a strong increase of the hysteresis in Cu-based alloys, when the grain size diminishes from 100 μm, and especially below 20 μm, which is accompanied by a reduction of the martensite plate size. In our case, the effective grain size is reduced down to ~20 μm by the formation of networks of big particles with addition of Hf; however, the hysteresis does not increase but continuously decreases irrespective of the sizes of

particles and martensite plates, which is contradictory to the above results. From Hf0 to Hf4 alloys the drop of M_p (ΔM_p = 178 K) is lower than the drop of A_p (ΔA_p = 208 K), which causes the reduced hysteresis (A_p-M_p). A continuous decrease of M_p and A_p in the same degree is expected from the decreased e/a ratio, while the extra drop of A_p could be derived from the tetragonality (c/a) reduction.

There is another major point affecting the transformation hysteresis related to the cell lattice compatibility between the two phases. A theory developed for the cubic to orthorhombic transformation (B2-B19 phases of Ni-Ti-X alloys) provides a good guidance for the purpose to understand the small hysteresis and the reversibility during transition [212]. The theory suggests several conditions for the stretch matrix from austenite to martensite lattices, $\boldsymbol{U}$, and its eigenvalues $\lambda_1 \leq \lambda_2 \leq \lambda_3$, namely det$\boldsymbol{U}$ = $\lambda_1\lambda_2\lambda_3$ = 1 and λ_2 = 1. This represents the perfect compatibility between martensite and austenite lattices, although for most of the real SMAs λ_2 deviate from one. It has been experimentally observed that the closer to one the λ_2 is, the smaller the hysteresis is in many SMA systems [213]. A quaternary Ni-Ti-Cu-Pd was reported to possess near zero hysteresis along with enhanced thermal stability, obtained after proper composition search [214]. The transformation behavior was mainly ascribed to modification of λ_2 value by Pd addition, which is known to possess larger atom radius and have preference to occupy Ni site. Hence, it is reasonable to consider that the small hysteresis of the studied alloys is owed to the matrix composition variation when adding Hf with large atom radius, which causes a better compatibility of the lattices. This topic will be further discussed in the next chapter.

5.2.2 Microstructure Characteristics

As already shown in XRD and TEM results, the non-modulated body centered tetragonal martensite structure appears in all high temperature Ni-Mn-Ga-Hf alloys, but Hf4 alloy also contains the modulated 14M martensite structure. Moreover, a large amount of precipitates are induced as the result of Hf addition (over 1 at.%), with diffraction patterns compatible with an f.c.c. structure. However, the differences in lattice parameter prove that they are a new type of precipitates formed in Ni-Mn-Ga-Hf alloys, different than the γ phase reported in the literature. Hence, it is necessary to make a carefully analysis of the phases since they are dominating the shape memory properties. The specific structure information of b.c.c. austenite, b.c.t. martensite and standard precipitates (γ phase and γ' phase) have been introduced in chapter 1.1.3.

For the studied Ni-Mn-Ga-Hf alloys, the calculated lattice parameters of non-modulated b.c.t martensite and f.c.c. precipitates are listed in the Table 5.4 based on XRD patterns obtained in the orientation perpendicular to the arc flame. For martensite, a clear overall tendency can be observed that a is increasing while c is declining as a function of Hf addition. A small bounce back happens at Hf4, which could be related to the appearance of 14M modulated martensite phase. As a result,

the overall tetragonality decreases as a function of Hf addition associated with transformation temperature, which has been already shown in Fig. 5.2.1 (b).

Table 5.4. Lattice parameters of b.c.t. martenstie and f.c.c. precipitates in Ni-Mn-Ga-Hf SHT 1270K for 48h alloys.

Alloys	***a* C**	***c* Å**	**volume Å**	***c/a* Å**	**a_P Å**
Hf0	5.388	6.754	196.072	1.254	
Hf0.5	5.385	6.757	195.941	1.255	
Hf1	5.407	6.746	197.224	1.248	6.784
Hf2	5.430	6.719	198.110	1.237	6.788
Hf3	5.429	6.715	197.918	1.237	6.823
Hf4	5.435	6.731	198.829	1.238	6.814

It is well known that not all the martensite found in Ni-Mn-Ga/Ni-Mn-Ga-X systems are non-modulated tetragonal structure. Wang J *et al*. [196] claims that partial replacement of Ga by Cu leads to the formation of non-modulated martensite as a result of difference in atom radius, which could also happens in the substitution of Ni or Mn. Moreover, it has been reported that 14M modulated martensite was mixed with austenite with addition of high amount of Cu [59], and the tetragonal structure can swiftly turn to orthorhombic structure by adding Gd [153]. Therefore, it is not surprised to observed the 14M in the Ni-Mn-Ga-Hf alloy system as the result of big atom radius differences between the Hf and other elements.

Concerning the second phase observed by OM, SEM and TEM, at first glance, the f.c.c. structure was considered to be the so-called “γ phase” reported in the literature for Ni-Mn-Ga-X, Ni-Fe-Ga, Co-Ni-Al/Ga, … However, combined with further investigations, an unconventional f.c.c. structure will be suggested for the second phase of Ni-Mn-Ga-Hf alloys to explain the abnormal characteristics in relation to the reported γ phase. The differences obtained in comparison with the literature are listed here: (1) the special composition of precipitates measured by EXD analysis, which is about Ni (58 - 63 at.%), Mn (17 - 20 at.%), Ga (5 - 8 at.%), Hf (12 - 14 at.%) for all the studied Hf additions; (2) the close distance of the diffraction spots in the electron diffraction patterns, which reveals that the lattice parameter “a_p” should have about double value than the normal γ phase formed in Ni-rich Ni-Mn-Ga and Ni-Mn-Ga-X alloys alloys, *e.g.*, a = 3.614 Å [62]; (3) the confirmation from XRD patterns, where the second phase peaks fit with an f.c.c. structure with large lattice parameter, as listed in

Table 5.4. Moreover, it should be noted that Ni_3Ti second phase was reported in the literature for Ti addition [177]. Though Hf is located in the same column as Ti and Ni_3Hf came in our mind in the first place, this type of second phase (hexagonal structure) was finally ruled out based on our measurements and analysis.

The nearly double lattice parameter suggests building up the unit cell of the new phase from an array of 2x2x2 = 8 basic f.c.c. cells containing 32 atoms in total. As the new phase appears in alloys with Hf addition, the Hf atoms must be responsible of the double period. The Hf content measured by EDX (12 - 14 at.%) indicates that 4 Hf atoms are located in the unit cell, which corresponds to an ideal content of 12.5 at.% Hf, compatible with the EDX results. The four atomic sites for Hf that can double the period are: (1/2 1/4 1/4), (0 3/4 1/4), (0 1/4 3/4), (1/2 3/4 3/4), corresponding to face-center sites of the basic f.c.c cubes. For the rest of Ni, Mn and Ga atoms, two possibilities are considered: i) completely random occupation of the remaining sites (disordered structure) and ii) specific positions for the different elements, according to the measured EDX composition (ordered structure). The ordered and disordered unit cells proposed are depicted in Fig. 5.2.2.

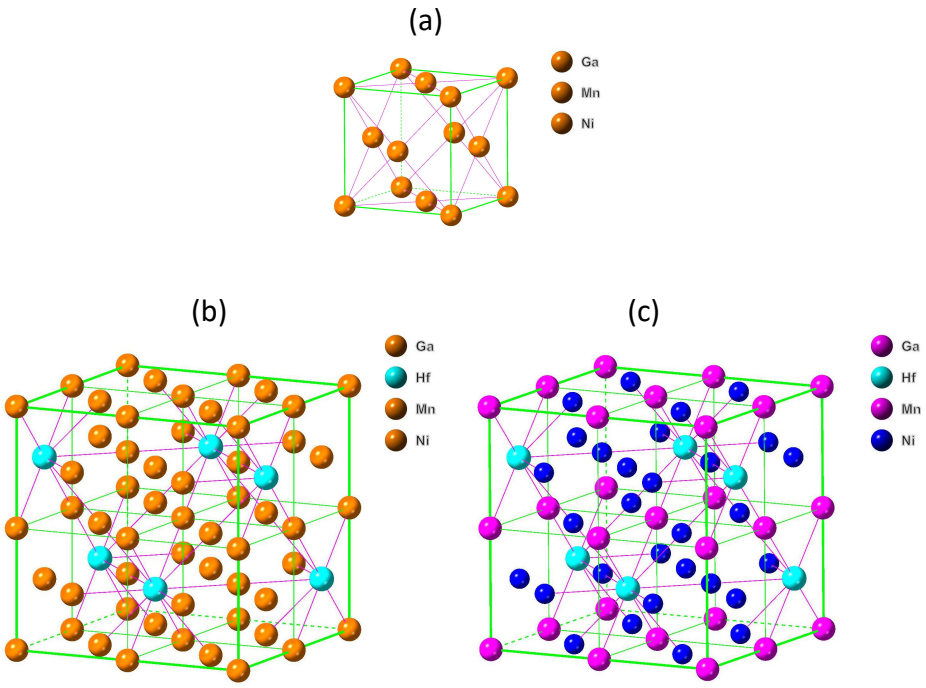

Fig. 5.2.2. The unit cell structure of the precipitates: (a) f.c.c. disordered γ phase with Ni:Mn:Ga atoms occupation = 2:1:1; (b) disordered structural model for the f.c.c. precipitates in Ni-Mn-Ga-Hf alloys; (c) Ni-ordered structural model for the f.c.c. precipitates in Ni-Mn-Ga-Hf alloys. The lattice sites in brown color means they could be randomly occupied by Ni, Mn or Ga; the cyan sites represent the Hf atoms; the pink sites are randomly occupied by Mn or Ga; the blue sites stand for Ni atoms. Additional bonds of Hf-(Ni, Mn, and Ga) are marked in (b) and (c).

The differences come from the distribution of the Ni, Mn and Ga atoms. In the disordered model (Fig. 5.2.2 (b)), Ni, Mn and Ga atoms are randomly located at vertices or face-center sites of the basic f.c.c. cubes (in brown color), with a probability of occupation following the composition obtained by EDX. The occupation ratio of each mixed site is Ni:Mn:Ga = 0.71:0.20:0.09. On the other hand, the second type of model possesses more order not only in Hf sites but also in Ni sites, which is similar to the ordered γ' phase observed in some alloys as Co-Ni-Ga [208, 209]. Based on the EDX measurements, it is not hard to find that there are some close content ratios among the elements: (Ni+Hf):(Mn+Ga) = 3:1, Ni:Hf = 5:1, Mn:Ga = 7:3, which results in 4 Hf atoms, 20 Ni atoms and 8 (Mn,Ga) atoms in one cell. The second model is shown in Fig. 5.2.2 (c), where Ni and Hf occupy the face-center sites (in blue and cyan color, respectively) and Mn, Ga randomly occupy the vertices sites (in pink color) with occupation ratio Mn:Ga = 0.7:0.3. The second model generates a nominal composition as $Ni_{62.5}Mn_{17.5}Ga_{7.5}Hf_{12.5}$, which is very close to the EDX measurements.

Both structural models, Ni-ordered and Ni-disordered, have been simulated by "CrystalMaker" software. The simulated electron diffraction patterns are presented in Fig. 5.2.3. The simulated XRD patterns are presented in Appendix B, together with additional crystallographic information. Concerning the electron diffraction, all the experimental zone axes observed (shown in section 5.1.3) have been simulated and present a good agreement with the simulations. Fig. 5.2.3 shows the simulated diffraction patterns for [110], [211] and [301] zone axes, the Ni-ordered model in the left column and the Ni-disordered model in the right column. As it is shown, basically identical patterns can be observed for both models in terms of the distance, angles and intensities of the diffracted spots, which are also verified from the internal calculation of "CrystalMaker" software.

Furthermore, the same structures have been simulated by another "Carine" software, where some differences can be found despite all the similarity. Actually, some planes, *e.g.*, (-113), (0-22), (-153), exhibit very weak intensity. The extremely weak intensity of superlattice spots could be attributed to the limitation of simulation software. The experimental intensities of diffraction spots are generated from the multiple times of electron scattering related to the thickness of sample, and additionally the manually converged beam can further enhance the intensities for better contrast. For both of the simulation software, they only consider the kinematic approximation, *i.e.*, missing out the dynamic effects of multiple electron scattering. However, the "CrystalMaker" software can adjust the saturation parameter to intensify the spots reflected on the simulated pattern, which is just like the situation to simulate more converged beam to obtain stronger intensities. Therefore, the "CrystalMaker" software can generate similar simulations to our experimental results.

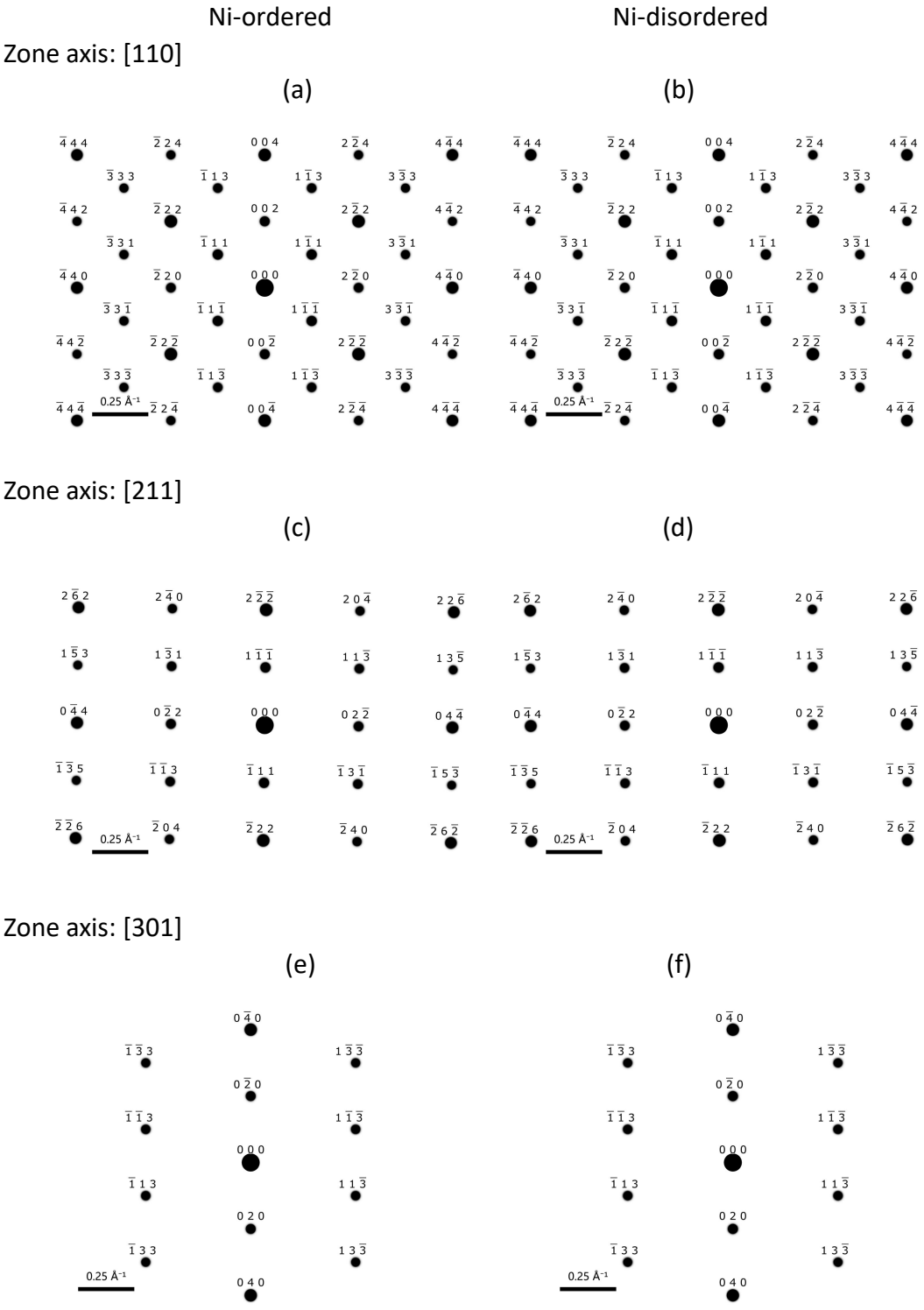

Fig. 5.2.3. Simulated diffraction patterns of two suggested structures of precipitates, the left column and right column are from Ni-ordered structure and Ni-disordered structure, respectively. The patterns (a) and (b), (c) and (d), (e) and (f) are under the zone axes [110], [211] and [301], respectively.

The proposed models based on a doubled face-centered cubic structure cannot be found in the space group corresponding to the cubic system. After checking the

multiplicity of the Hf atom positions, they are found to belong to the tetragonal system. This "tetragonal" structure is denoted as *A6 face-centered tetragonal* (*f.c.t.*) with space group I4/mmm (No. 139) and a lower unit cell volume. The relationship between the "cubic" and "tetragonal" axes is presented in the Fig. 5.2.4 (a) along with the new tetragonal unit cells (b) and (c), for the ordered and disordered structures, respectively. The Fig. 5.2.4 (a) presents four neighbor unit cells of the aforementioned Ni-disordered "cubic" model with small atom radius for convenience. The new A6 f.c.t. unit cell is marked with pink color links. It is obviously shown that the orientation relationships between the f.c.t. and cubic cells are: $a_{f.c.t.} = a_c / \sqrt{2}$, $c_{f.c.t.} = a_c$, $(100)_{f.c.t.}||(01\text{-}1)_c$, $(010)_{f.c.t.}||(011)_c$ and $(001)_{f.c.t.}||(100)_c$. The crystallographic description of the structures is shown in the Table 5.5 (Ni-disordered) and Table 5.6 (Ni-ordered), respectively. As shown in Fig. 5.2.4 (b), for the disordered model the Hf atoms take the 8 vertices and the body center positions, whereas Ni, Mn and Ga are located at the other sites in the occupation ratio seen in Table 5.5. Fig. 5.2.4 (c) shows that the Hf atoms locate at vertices and body center positions; Ni are occupying the half-edge positions of four long-faces, top and bottom face center positions, and 1/4 body diagonal positions; and Mn/Ga are randomly located at the four long-face center positions and half-edge positions of both top and bottom faces. The corresponding atom Wyckoff positions are listed in Table 5.6.

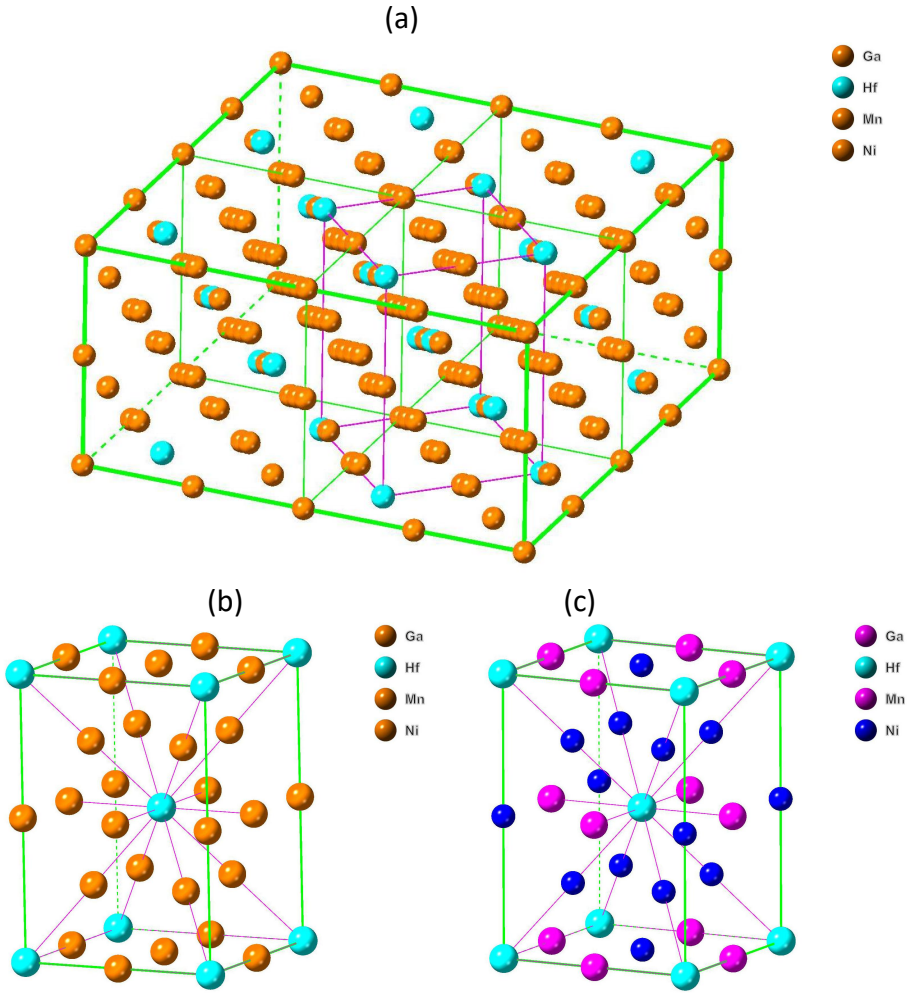

Fig. 5.2.4. Simulated cell structures of precipitates in Ni-Mn-Ga-Hf alloys: (a) relationship

between “cubic” axes and “tetragonal” axes; and A6 f.c.t. unit cell under “tetragoanl” axes (b) Ni-disordered, (c) Ni-ordered. The Ni and Hf atoms are presented in blue and cyan, respectively. Additionally, the brown color and pink color means the disorder of Ni, Mn, Ga and Mn, Ga, respectively. Additional bonds of Hf-(Ni, Mn, and Ga) are marked in (b) and (c).

Table 5.5. Atom position of Ni-disordered A6 f.c.t. precipitates in Ni-Mn-Ga-Hf alloys.

Atom	Element	Wyckoff letter	Multiplicity	x	y	z	Occupation
1	Hf	a	2	0	0	0	1
2	Ni	b	2	0	0	1/2	0.71
	Mn						0.20
	Ga						0.09
3	Ni	c	4	1/2	0	0	0.71
	Mn						0.20
	Ga						0.09
4	Ni	f	8	1/4	1/4	1/4	0.71
	Mn						0.20
	Ga						0.09

Table 5.6. Atom position of Ni-ordered A6 f.c.t. precipitates in Ni-Mn-Ga-Hf alloys.

Atom	Element	Wyckoff letter	Multiplicity	x	y	z	Occupation
1	Hf	a	2	0	0	0	1
2	Ni	b	2	0	0	1/2	1
3	Mn	c	4	1/2	0	0	0.70
	Ga						0.30
4	Ni	f	8	1/4	1/4	1/4	1

The indexation of XRD peaks and TEM diffraction patterns changes with the crystallographic axes chosen to buid-up the unit cell. However, for better comparison of similarities and differences with the known f.c.c. γ phase in other Ni-Mn-Ga-X alloys, the “cubic” axes and the corresponding indices have been used in this thesis instead of using “tetragonal” axes repeatedly. The correspondence can be easily deduced from the orientation relationships given above. The XRD and TEM diffraction patterns simulated and indexed according to the “tetragonal” axes will be presented in the Appendix B.

5.2.3 Thermomechanical and Mechanical Response

The details of mechanical and thermomechanical behavior of the Ni-Mn-Ga-Hf alloys have been shown in sections 5.1.4 and 5.1.5. Hence, only some important characteristics will be listed here as general discussion.

The thermomechanical plots show that the Hf addition strongly reduces the transformation strain (about 2/3 factor for Hf3) as a result of second phase formation, which does not participate in the martensitic transformation. Despite the decrease of transformation temperatures caused by Hf addition, the thermomechanical actuation still takes place around 500 K for Hf2, 460 K for Hf3 and 425 K for Hf4, which is valid for HTSMA candidates. It should be noted that the alloys with Hf exhibit very low hysteresis even under high applied stress levels, *e.g.*, Hf3 has 8 K hysteresis under 300 MPa, which is a remarkable result for high temperature actuation applications, but with limited strain. Moreover, it is generally considered that the slope of strain-temperature curve is related to the stored elastic strain energy, where a steep slope with small under cooling indicates low stored elastic strain energy [8]. The slopes of Hf0 to Hf4 alloys under 100 MPa are -0.1, -0.07, -0.06, -0.03, -0.03, and -0.03 K^{-1}, respectively. The decreasing slope indicates a stored elastic strain energy increasing with the Hf content. Therefore, according to this theory the stored elastic strain energy without significant dissipation can assist the reverse transformation, contributing to the low hysteresis.

Compared to Ni-Mn-Ga-Ti alloys that possess improved mechanical properties due to the strengthening effect of the Ni_3Ti second phase grown by proper ageing [177], the grid of precipitates observed in Ni-Mn-Ga-Hf with micrometric sizes cannot cannot share coherency with the matrix and are not expected to strengthen the material significatively. As mentioned above, the second phase particles are stable up to very high temperatures close to the melting point and they cannot be dissolved nor modified in their distribution and size by thermal treatments. Other production technologies such as rapid solidification or powder metallurgy techniques should be used to try to obtain small precipitates of the second phase.

The severe drop of the transformation strain with Hf addition cannot be quantitatively scaled with the increasing fraction of second phase. As mentioned in Section 5.1.4, the latter fraction has been estimated from the area occupied by the second phase in SEM images, being 8%, 16% and 21% for Hf2, Hf3 and Hf4 alloys, respectively. This gives transformable fractions of 92%, 84% and 79% of the material, respectively. The fraction of transformable material can also be estimated from the calorimetric data of Table 5.1, considering the ratio of the enthalpy change of these alloys related to the Hf0 with no second phase. Such ratios are 73%, 75%, and 65% for Hf2, Hf3, and Hf4, respectively. On its turn, the ratios of transformation strain under 300 MPa of Hf2, Hf3 and Hf4 alloys related to Hf0 are as low as 47%, 33% and 28%, respectively. Such low ratios are by far not comparable to the transformable fraction of material and indicate a significant decrease of the amount of oriented martensite variants favored by the external stress when increasing the Hf content. This fact was also pointed out in section 5.1.4 from the lack of saturation in the transformation strain values vs. the applied stress and the large Clausius-Clapeyron slopes observed in alloys with high Hf content (Figs. 5.1.15 (a) and (d)). In these alloys, the transformable material is in form of isolated zones surrounded by the

network of large second phase particles that produce a “shielding” effect of the applied external stress. In this way, the effective stress existing in the transformable zones is significantly lower than the applied stress and can only produce limited fractions of oriented martensite in the thermomechanical tests, which reduces the measured uniaxial transformation strain.

This also explains the lack, or very poor, superelastic effect observed in these alloys. Very high applied stresses are needed to activate the stress-induced transformation in the transformable regions, which also promotes the plastic deformation or even crack propagation (observed in Hf4), both effects being favored by the elevated test temperatures. The Hf2 specimen exhibits relatively some recoverable strain under applied stress up to 600 MPa compared to the other Ni-Mn-Ga-Hf alloys with more volume fraction of precipitates, which also show less irrecoverable strain about 0.3% similar to the ternary alloy and no fracture. Besides the plastic deformation, another source of irrecoverability maybe the mechanical stabilization of martensite activated by the high stress. The stress induced martensite cannot reverse into austenite upon unloading due to the detwinning of martensite and the obstruction of the lattice defects [215-217]. This possibility has been tested by heating experiments up to A_f + 100 K after the mechanical cycles, measuring the difference in sample length to detect some shape recovery. In most cases, the observed recovery is almost insignificant (less than 0.02%). The exceptions are Hf2 alloy mechanically tested at 500 K and Hf4 alloy at 460 K, which show about 0.09% and 0.17% additional recovery strain after heating up to 580 K and 530 K, respectively. This part of strain is marked in Figs. 5.1.15 (b) and (d) with a red arrow at the end of the unloading cycle. Therefore, only a small part of the stress-induced martensite shows low mechanical stabilization. The remaining part of the permanent irrecoverable strain is due to deeply stabilized martensite that cannot be removed by further heating or due to plastic deformation.

Finally, we can comment that the appearance of 14M modulated martensite in Hf4 alloy seems not have big influence on the mechanical properties. There is no sign of multiple stages of transformation under stress in Hf4 alloy (Fig. 5.1.14 (f)), at difference from Ni-Mn-Ga single crystals free of second phase, which show multiple stages related to the different martensitic phases [67]. Probably, the minor fraction of 14M martensite forms in Hf4 alloy to accommodate the internal stresses of the large networks of second phase particles and transforms/retransforms together with the non-modulated martensite in a single stage transformation event.

5.3 Summary of Ni-Mn-Ga-Hf Alloys

1. The martensitic transformation properties and the microstructure as a function of the Hf addition have been studied in Ni-Mn-Ga alloy system. The composition design is based on former studies ($Ni_{53.0}Mn_{31.1Z}Ga_{17.7Z}Hf_X$, Z = (47-X)/48.8, with X = 0, 0.5, 1, 2, 3, 4). A high Ni content is kept in order to improve the ductility of the alloy by

producing the dual phase structure with high transformation temperature.

2. The dual phase structure of studied alloys has been observed with Hf addition over 1 at.% under room temperature. The martensite phase is found to be the non-modulated body centered tetragonal structure in all the studied alloys, which has been verified by TEM and XRD experiments. It should be noted that a small fraction of 14M modulated martensite has been observed in Hf4 alloy, which demonstrates extra peaks in XRD and satellite spots along <0014> direction in SADP. Moreover, the decrease of enthalpy change can be ascribed to the loss of martensitic volume fraction due to the growth of non-transformed second phase particles.

3. It has been observed that the decrease of e/a and c/a are responsible for the continuously declining MTTs due to the matrix composition change by adding the fourth element Hf. The transformation hysteresis also decreases with Hf addition, reaching a value as low as 8 K for 3 at.% and 4 at.% Hf addition, despite the large reduction of martensite plate size caused by the networks of large second phase particles. A good compatibility of the austenite and martensite crystal lattices promoted by the larger atomic radius of Hf can be responsible of the low hysteresis. This point will be further discussed in the next chapter. Moreover, the stored elastic energy is increased with Hf addition that could also assist reverse transformation, contributing to the low hysteresis.

4. The Hf3 with dual phase structure specimens demonstrate high thermal stability under DSC cycling as the result of pining effect of precipitates. Moreover, after prolonged ageing treatment under 870 K, Hf2 and Hf3 show little change on size and morphology, but a slight composition variation related to atom diffusion resulting in 8 K temperature drop of the martensite peak temperature M_p.

5. A unique type of second phase particles, different from the typical γ or γ’ phases observed in Ni-Mn-Ga-X and other ferromagnetic shape memory alloys, has been observed in the studied alloys by adding the fourth element Hf into Ni-Mn-Ga alloy system. The new phase possesses the face centered cubic structure but double value of the lattice parameter, compared to the common f.c.c. γ phase. Two crystallographic models, with ordered or disordered positions of the Ni atoms, are suggested to explain the observations. Both models demonstrate XRD and TEM diffraction patterns coincident with the experimental results, though differences in intensity are still existing due to the limitation of simulation program. The double f.c.c. cell does not correspond to a space group of the cubic system. The correct crystallographic description of the new phase corresponds to the tetragonal system with space group I4/mmm (No. 139) and A6 face-centered tetragonal type of unit cell.

6. Ni-Mn-Ga-Hf alloys show typical thermomechanical behavior, which exhibit less recoverable strain compared to ternary alloy as the result of formation of

non-transformed precipitates, *e.g.*, Hf2 possesses about 1.2% total strain and 0.3% irrecoverable strain. The precipitates have small effect on plastic deformation resistance due to the large size and incoherent relation to the matrix, but could be the reason for low hysteresis as about 8 K of Hf3 and Hf4 under 300 MPa. However, the studied quarternary alloys show basically no or little superelasticity effect due to the restrained reorientation process by the precipitates grid. Hf2 alloy shows a small recoverable strain due to the relatively low volume fraction of precipitates, while Hf4 finally exhibit 1% recoverable strain at the expense of sample fracture.

Chapter Ⅵ Ni-Mn-Ga-Zr

As it has been thoroughly discussed before, Ti addition was reported to not only elevate the transformation temperature but also enhance the strength of matrix as the result of formation of Ni_3Ti precipitates [177, 178]. In the previous chapter, the effect of Hf addition has been presented and the behaviour is very different from Ti addition. Hence, Zr element, located at the same column of periodic table as Ti and Hf, has been chosen to add into Ni-Mn-Ga alloy system to study its influence to induce ductile precipitates and, eventually, improve the mechanical properties. To the author's knowledge, Zr was only investigated by substituting Cu in Ni-Mn-Ga-Cu alloy system with 4 at.% and 8 at.% [182-184]. However, the shape memory properties with low addition of Zr has not been clearly reported. Therefore, the impact of Zr addition in Ni-Mn-Ga alloy system on the MTTs, microstructure and thermomechanical properties was systematically investigated, in a similar way to the Hf addition presented in the previous chapter. In this chapter we present the effect of Zr addition into Ni-Mn-Ga HTSMAs. Like previous chapters and based on the Ni-Mn-Ga equilibrium phase diagram [71], the ternary nominal composition $Ni_{53.0}Mn_{30.0}Ga_{17.0}$ has been chosen as the reference alloy named as "Sn0" in Ni-Mn-Ga-Sn chapter and "Hf0" in Ni-Mn-Ga-Hf chapter. This alloy exhibits high martensitic transformation temperature and more tendency to form β + γ dual-phase microstructure. Ni-Mn-Ga-Zr polycrystalline alloys were prepared by induction and arc melting with nominal compositions ($Ni_{53.0}Mn_{31.1Z}Ga_{17.7Z}Zr_X$, Z = (47-X)/48.8, with X = 0, 0.5, 1, 2, 3, 4), and then they were cut into pieces and solution heat treated at 1270 K for 48 h for homogenization followed by water quench.

6.1 Results of Analysis and Observation

6.1.1 Calorimetric Analysis

Fig. 6.1.1 shows DSC measurements of Ni-Mn-Ga-Zr alloys with different Zr content. All the specimens have been tested with cooling and heating cycles under the same temperature range from 720 K to 270 K. It clearly shows that the peaks of martensitic transformation continuously shift to lower temperature as a function of Zr addition. For example, the M_p decreases from 590 K for Zr0 to 433 K for Zr4 (about 27% lower value), while A_p decreases from 628 K for Zr0 to 440 K for Zr4 (about 30% reduction), respectively. The enthalpy change is also decreasing with Zr addition, *e.g.*, 27% reduction of average enthalpy change with 4 at.% Zr addition, indicating the decrease of transformable volume fraction. It needs to be noted that two consecutive DSC cycles were tested for each alloy and are plotted in Fig. 6.1.1, to confirm the stability of the transformation. A broad transformation with multi-peaks appears in Zr0.5 and

Zr1 alloys and this is reproducible in the two thermal cycles. Therefore, the unchanged multiple peaks of Zr0.5 and Zr1 as well as the broad peaks of Zr2 alloy are considered to be a result of inhomogeneous composition / microstructure instead of transient effects related to quenched in defects [117].

Table 6.1 shows the nominal composition, the corresponding valence electron concentration of all the alloys and the characteristics of the martensitic transformation obtained from the DSC thermograms (Fig. 6.1.1). It should be noted that the ternary alloy samples denoted as *Zr0* throughout this chapter are the same specimens named as Hf0 in previous chapter, as mentioned before. The valence electron concentration has been calculated from the nominal composition and shows a decreasing tendency. Consequently, both the direct and the reverse transition peak temperatures (M_p and A_p) are continuously decreasing with the increase in Zr content. The ΔA_p is relatively larger than ΔM_p resulting in a reduction of hysteresis (A_p-M_p) from 38 K for Zr0 to 8 K for Zr4. Therefore, Zr addition causes a thermal response completely parallel to Hf addition, shown in the previous chapter.

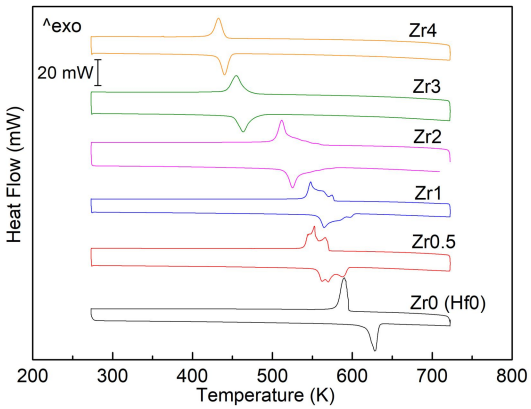

Fig. 6.1.1. DSC analysis of solution heat treated (SHT) 1270 K for 48 h Ni-Mn-Ga-Zr_X (X=0, 0.5, 1, 2, 3, 4) alloys.

Table 6.1. Nominal composition and values of the valence electron concentration (e/a), DSC peak temperatures for the direct and reverse transformation (M_p, A_p, respectively), hysteresis (calculated as A_p–M_p) and average enthalpy change (ΔH) for the investigated alloys after solution heat treatment at 1270 K.

Alloy	Nominal composition	e/a	M_p /K	A_p /K	Hysteresis /K	ΔH / J/g
Zr0/Hf0	$Ni_{53.0}Mn_{30.0}Ga_{17.0}$	7.91	590	628	38	14.3
Zr0.5	$Ni_{53.0}Mn_{29.6}Ga_{16.9}Zr_{0.5}$	7.90	553	570	17	14.2
Zr1	$Ni_{53.0}Mn_{29.3}Ga_{16.7}Zr_{1.0}$	7.89	548	565	17	13.4
Zr2	$Ni_{53.0}Mn_{28.7}Ga_{16.3}Zr_{2.0}$	7.88	512	525	13	11.9
Zr3	$Ni_{53.0}Mn_{28.0}Ga_{16.0}Zr_{3.0}$	7.86	455	463	9	10.7
Zr4	$Ni_{53.0}Mn_{27.4}Ga_{15.6}Zr_{4.0}$	7.85	433	440	8	10.4

The stability of the martensitic transformation upon ageing in austenite phase and thermal cycling through DSC has been also studied in Ni-Mn-Ga-Zr alloys. As seen in Fig. 6.1.1, the Zr3 alloy shows single peak transformation with narrow hysteresis, so it has been selected for this study due to its relatively homogeneous microstructure. Fresh neighbor specimens were cut from the initial ingot of Zr3 alloy to keep the similar initial state (composition, microstructure, transformation temperature, etc.), and they were encapsulated and aged at 870 K for different times. Fig. 6.1.2 (a) shows the DSC results for 24 and 72 h of ageing. As it is shown, the M_p, A_p values of the SHT state (182 K, 190 K) are slightly raised up to 187 K, 195 K and 184 K, 192 K by ageing for 24 h and 72 h, respectively. Meanwhile, the average enthalpy change remains basically stable, from 10.7 J/g for SHT to 10.7 J/g for 24 h and 9.7 J/g for 72 h respectively. Hence, the Zr3 alloy demonstrates very high thermal stability under prolonged ageing at high temperature, which is similar to the Hf3 alloy as shown in Fig. 5.1.2 (b) of the previous chapter. However, there are some differences that will be further discussed later in the discussion section.

The effect of thermal cycling through the martensitic transformation has also been studied up to 20 consecutive cycles by DSC, performed at a constant heating / cooling rate of 10 K/min. The DSC results of Zr3 alloy are presented in Fig. 6.1.2 (b). The peak temperatures of Zr3 are marked in the graphs, *e.g.*, 453 K and 462 K for direct and reverse transformation, respectively. The average transformation enthalpy change of Zr3 are 10.7 J/g and 10.3 J/g for direct and reverse transformation respectively. It is obvious that after 20 times cycling the Zr3 shows perfect thermal stability with unchanged peak temperature and enthalpy change, indicating no degradation or stabilized martensite. Therefore, Zr3 alloy shows a high stability like Hf3 alloy (Fig. 5.1.3) upon both prolonged ageing and cycling, indicating a common reason, *i.e.*, the presence of dual phase structure that will be further discussed in the next section.

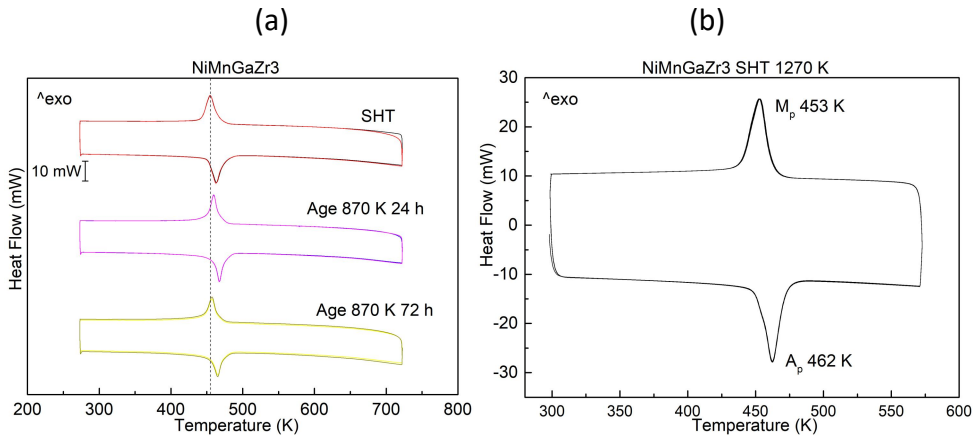

Fig. 6.1.2. DSC results of NiMnGaZr3 alloy: (a) SHT 1270 K for 48 h with additional ageing at 870 K, (b) SHT 1270 K for 48 h thermal cycling 20 times.

6.1.2 XRD Analysis

Different polycrystalline specimens have been investigated by XRD, and the patterns are plotted in the sequence of Zr content in Fig. 6.1.3. All the specimens have been subjected to solution heat treatment at 1270 K for 48 h and water quenching. Each alloy has been studied in two different orientations, parallel and perpendicular to the arc flame, and show different relative intensities of the diffracted peaks. As already mentioned in chapter 5 about Ni-Mn-Ga-Hf alloys, this is indicative of texture in the ingots produced by arc melting, together with the use of samples in form of bulk polycrystalline alloys instead of powder. Hence, tests on both orientations have been performed to obtain as much information as possible. In Fig. 6.1.3 (a), corresponding to Zr0.5 alloy, the major peaks are consistent with the body centered tetragonal martensite, *e.g.*, $202_{b.c.t.}$ and $220_{b.c.t.}$. These peaks have been used to calculate the primary lattice parameters followed by refinement with the rest of detected multiple peaks. Moreover, some low intensity peaks can be indexed as ZrC like the 111_{ZrC} and 200_{ZrC}, whereas the tiny extra peak located at about 2θ = 49° is consistent with the ZrO_2 phase, (220) planes. Similar to Hf-containing alloys, diffracted peaks of the f.c.c. precipitated phase are visible in the XRD spectra for Zr addition above 1 at.%, as shown in Figs. 6.1.3 (b) - (e), which are marked with letter “P”. Their intensity is relatively higher in the orientation perpendicular to the arc flame, except for Zr3 alloy that shows better definition of these peaks in the parallel direction (Fig. 6.1.3 (d)). In Fig. 6.1.3 (e), corresponding to Zr4 alloy, the $202_{b.c.t.}$ peak exhibits some weak double peak shape in the left side that can be traced back to be the 125_{14M}. This could indicate the presence of a small fraction of modulated 14M martensite in Zr4 alloy, coexisting with non-modulated b.c.t. martensite, in a similar way to the Hf4 alloy shown in the previous chapter. The lattice parameters of the b.c.t martensite and f.c.c. precipitates in both orientations have been calculated for all Zr-containing alloys and are shown in the Table 6.2.

Fig. 6.1.3 (f) shows the results of *in-situ* heating experiments performed on Zr4 alloy with the orientation perpendicular to arc flame, using the same sample of the previous test shown in Fig. 6.1.3 (e), but after another mechanical polishing process. At room temperature (RT), small peaks consistent with the modulated 14M martensite are better defined after the new polishing process, which confirms the presence of 14M phase in Zr4 alloy. Upon heating up to the A_s, A_p and A_f temperatures revealed by DSC (431 K, 440 K and 448 K, respectively), clear changes in the XRD spectrum can be observed. The 200_{14M} peak becomes lower in intensity and shifts to higher 2θ angle, almost coinciding with the $202_{b.c.t.}$ peak, while 127_{14M} and $12\text{-}9_{14M}$ peaks are shifting to lower 2θ angle. In addition, the 040_{14M} peak is only visible at room temperature and disappears at higher temperatures, indicating the 14M martensite to austenite transition. As for the other peaks corresponding to f.c.c. precipitates and/or b.c.t. martensite, they show a little change of location. Moreover, it is clearly shown that the relative intensity of $202_{b.c.t.}$ peak is gradually decreasing

upon heating up as the result of reverse transformation, but it does not disappear completely from the pattern even at A_f. Furthermore, the reverse transformation can be observed through the appearance of the 422_{L21} peak starting from the A_s temperature. However, the 220_{L21} peak does not changed too much in intensity, which could be attributed to the overlapped peak of precipitates, *i.e.*, 311_P, that do not transform during the heating process. The same happens with the 12-7_{14M} peak, which is also overlapped with 311_P of precipitates. The lattice parameters of 14M obtained from Fig. 6.1.3 (f) at RT are a = 4.287 Å, b = 5.452 Å, c = 29.664 Å and β = 94.3° adjusted with MAUD software. However, it should be noted that the lattice parameters of 14M are not totally accurate since some fundamental peaks are overlapping with other phases with stronger peak intensity. In conclusion, XRD results of Ni-Mn-Ga-Zr alloys are completely parallel to those of Ni-Mn-Ga-Hf, with the same type of phases detected in both quaternary additions.

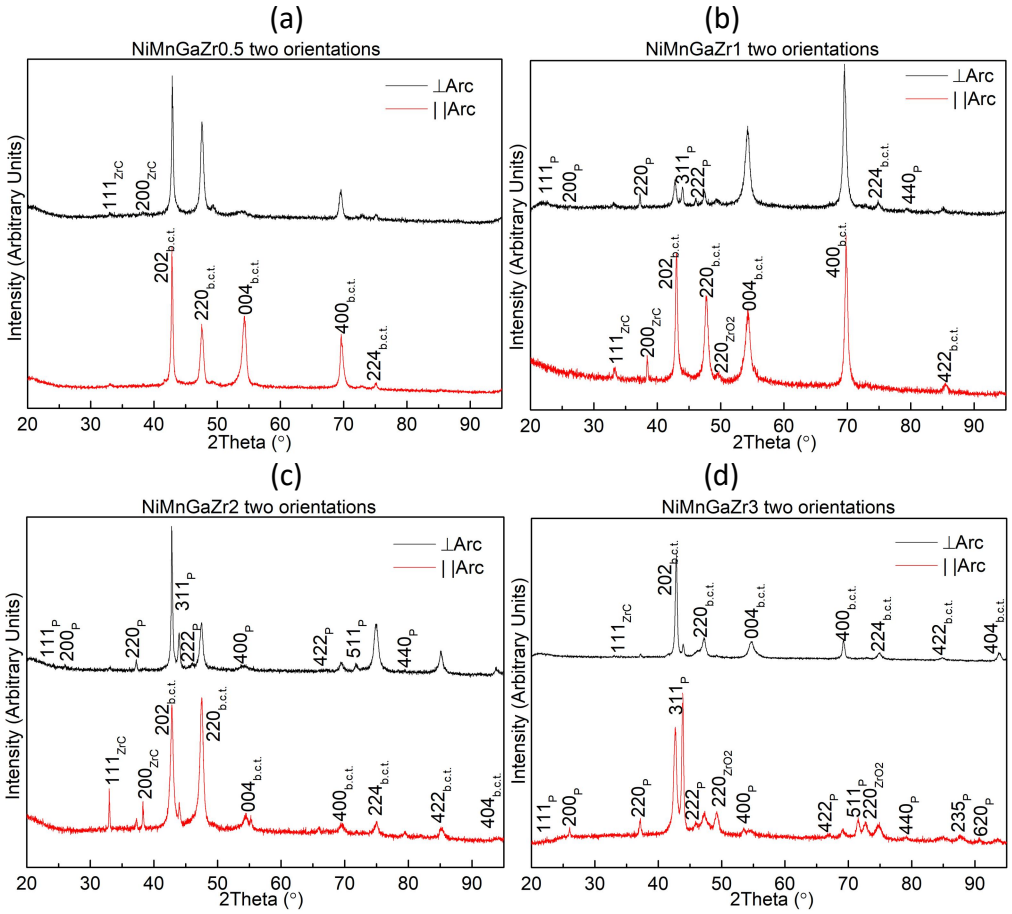

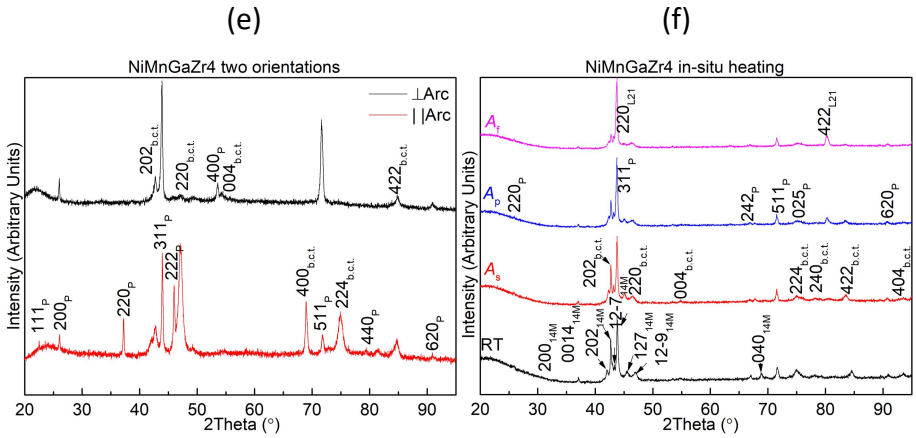

Fig. 6.1.3. XRD analysis of Ni-Mn-Ga-Zr SHT 1270 K for 48 h alloys: (a) Zr0.5, (b) Zr1, (c) Zr2, (d) Zr3, (e) Zr4 with two orientations (perpendicular and parallel to arc flame); (f) Zr4 *in-situ* XRD results under room temperature, A_s, A_p and A_f, respectively.

Table 6.2. lattice parameter of martensite (b.c.t.) and precipitates, number one is the orientation parallel to arc flame, and number two is the orientation perpendicular to arc flame.

Lattice parameter / Addition	a_1 Å	c_1 Å	a_2 Å	c_2 Å	a'_1 Å	a'_2 Å
Zr0.5	5.403	6.749	5.408	6.738		
Zr1	5.386	6.746	5.405	6.768		6.823
Zr2	5.419	6.739	5.416	6.718	6.812	6.807
Zr3	5.429	6.750	5.429	6.698	6.832	6.837
Zr4	5.457	6.741	5.433	6.726	6.830	6.843

6.1.3 Microstructure

Optical microscopy and SEM observations

The Ni-Mn-Ga-Zr alloys were observed under SEM at room temperature after homogenization at 1270 K for 48 hours. Some images are presented in Fig. 6.1.4 in the sequence of increasing Zr content. As we can see, the Zr0.5 alloy only contains small inclusions of Zr carbide or oxide in the martensitic matrix, while Zr1 to Zr4 alloys present larger f.c.c. second phase particles increasing with the Zr addition; consequently, the martensite volume fraction and plate size is continuously decreasing. The plate size reduction becomes evident by comparing Zr1 and Zr2 alloys, *i.e.*, in Fig. 6.1.4 (b) many martensite plates are longer than the imaged area, while in Fig. 6.1.4 (c) the martensite is confined in areas between the second phase network (below ~50 µm) with much shorter plate size. Moreover, Zr3 and Zr4 show higher density of precipitates and less distance among them that further limit the

space for martensite variants. The proportion of area occupied by the second phase has been measured through the PS software from the SEM images in Fig. 6.1.4 to be about 5%, 10%, 20% and 24% for Zr1, Zr2, Zr3 and Zr4, respectively. The f.c.c. second phase particles are very similar to those formed in Ni-Mn-Ga-Hf alloys and their shapes can also be considered as dendrites and ellipses. For Zr2 specimen (Fig. 6.1.4 (c)) the dendrites have lengths ~8 - 20 μm and widths ~2 - 7 μm, while the ellipses have the length ~2 - 8 μm and width about ~1 - 5 μm. The sizes are very similar to Hf2 alloy (see Table 5.2 in previous chapter).

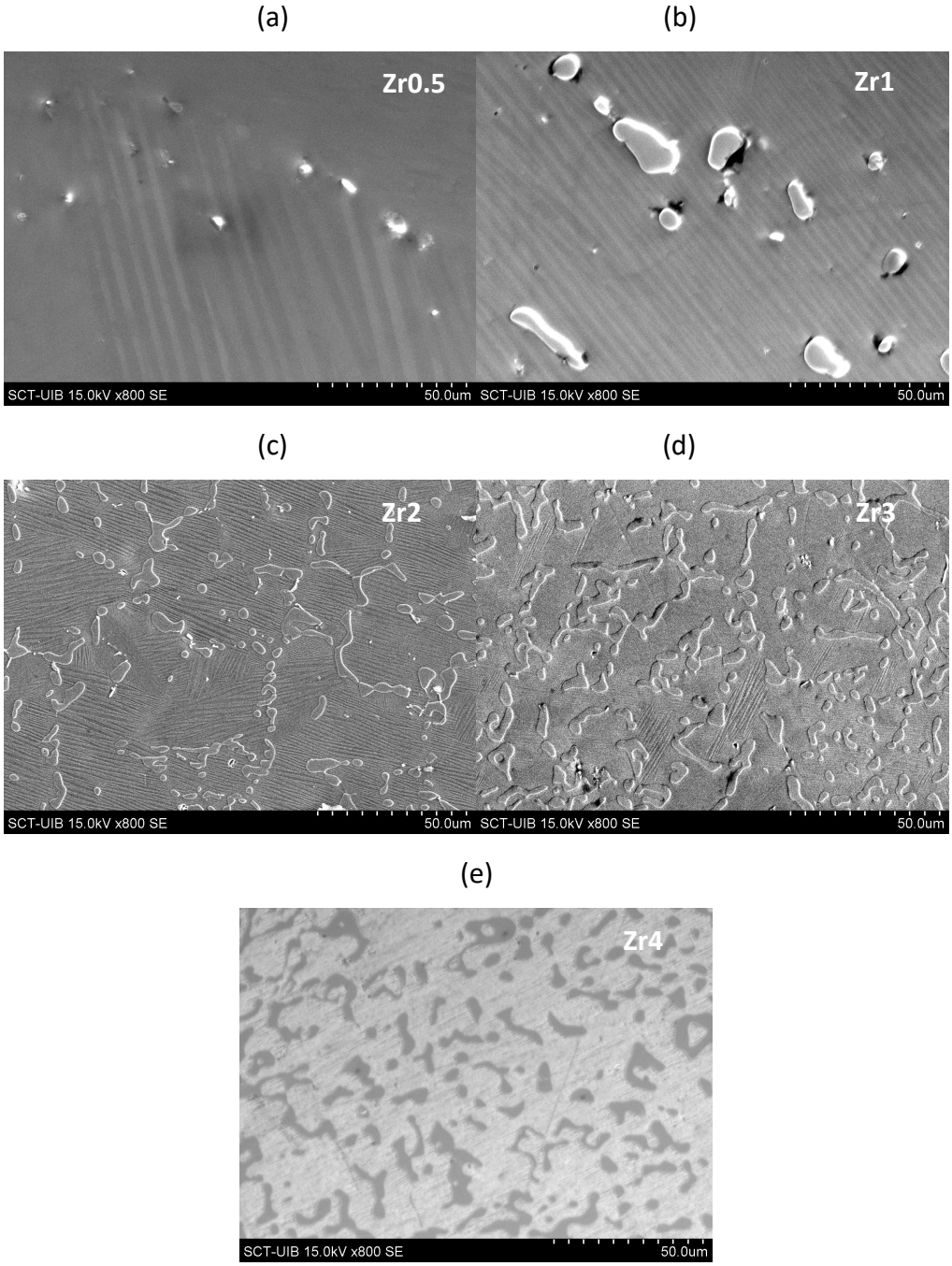

Fig. 6.1.4. SEM observations of Ni-Mn-Ga-Zr SHT 1270 K for 48 h alloys: (a) Zr0.5, (b) Zr1, (c) Zr2, (d) Zr3 and (e) Zr4.

Since the SEM captures the morphology of precipitates at small scale, the optical microscopy observations are presented in Fig. 6.1.5 to show the distribution of precipitates at larger scale. The samples have the orientation parallel to arc flame. Fig. 6.1.5 (a) shows the Zr1 alloy, and it can be clearly seen that the number of precipitates is rather low and they are mostly located at grain boundaries. Two different zones of Zr2 alloy (same sample) are shown in Figs. 6.1.5 (b) and (c), where different density and interspace of precipitates can be observed. Fig. 6.1.5 (b) exhibits relatively higher density of precipitates with interstice lower than ~50 µm, while (c) shows bigger interspace (martensite grains) about ~100 µm or above, due to heterogeneous distribution of precipitates. Zr3 alloy possesses even larger precipitates density than Zr2 alloy, and some degree of uneven distribution of precipitates can still be observed in Fig. 6.1.5 (d). Additionally, another zone of Zr3 SHT alloy can be found in Fig. 6.1.7 (a) with relatively homogeneous overall arrangement. Fig. 6.1.5 (e) represents the Zr4 alloy with the highest density of precipitates compared to the other compositions and also some inhomogeneous distribution; the right part of the image shows much smaller interspaces than the left part.

(a)

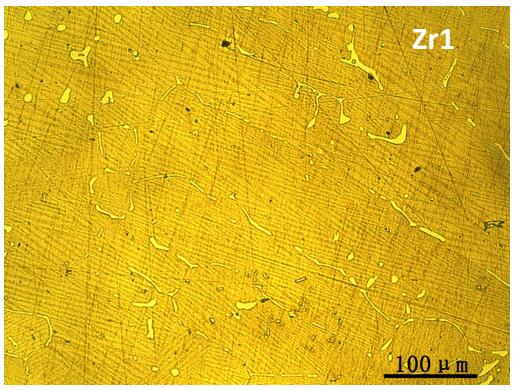

(b) (c)

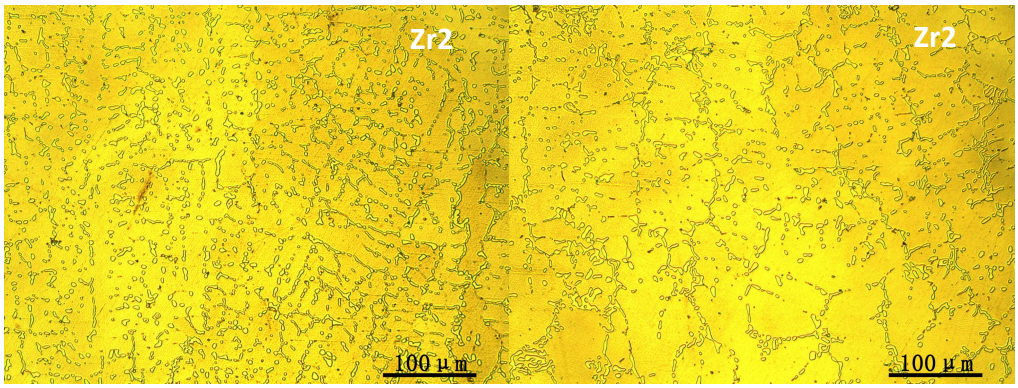

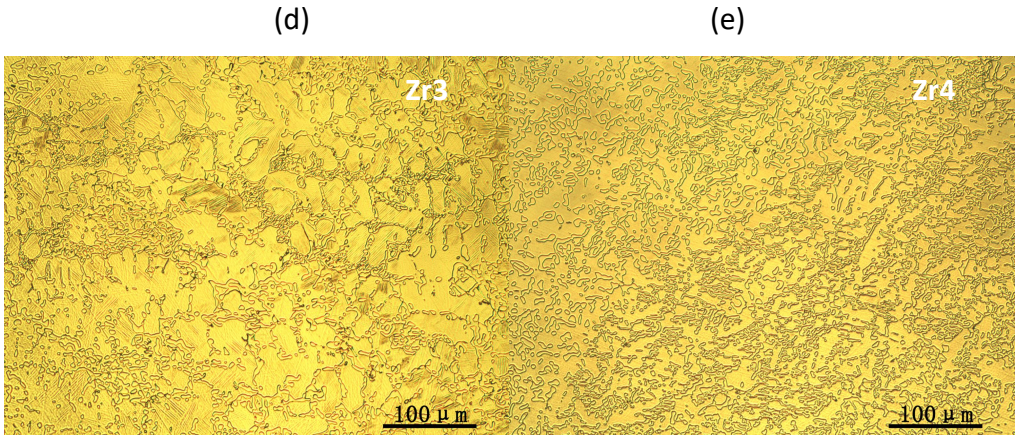

Fig. 6.1.5. Optical observations of Ni-Mn-Ga-Zr alloys SHT 1270 K for 48h in the orientation parallel to arc flame: (a) Zr1, (b) Zr2 zone one and (c) 2 zone two, (d) Zr3, (e) Zr4.

Similar to the situation observed in Ni-Mn-Ga-Hf alloys, we can expect some differences in the distribution and density of phases depending on the sample orientation, which is also reflected in XRD patterns (Fig. 6.1.3). This has been analyzed by OM observations in the orientation perpendicular to the arc flame, shown in Fig. 6.1.6. For example, the XRD spectrum of Zr1 alloy shows no obvious peaks of the f.c.c. precipitates in the orientation parallel to the arc flame, while they are visible in the other orientation (Fig. 6.1.3 (b)). This is in line with the optical microscopy observations, which only show a few precipitates for the orientation parallel to arc (Fig. 6.1.5 (a)), while the perpendicular orientation contains more precipitates (Fig. 6.1.6 (a)). Additionally, in the perpendicular orientation there is a slightly higher amount of second phase located at grain boundaries and dispersed round particles inside the matrix, as seen from Fig. 6.1.6 (a). For Zr2 alloy, the distribution of precipitates in the perpendicular orientation (Figs. 6.1.6 (b) and (c)) is more or less similar to the other orientation (Figs. 6.1.5 (b) and (c)). Both images show areas with relatively developed network structure of second phase and other areas with individual particles and bigger interstices. For these samples, the corresponding XRD patterns still show some differences in the peak intensity (Fig. 6.1.3 (c)), *e.g.*, $(311)_P$ is intense in the orientation perpendicular to arc while $(440)_P$ is intense in the other orientation. Such differences should be attributed to the orientational texture of the ingot. Fig. 6.1.6 (d) corresponds to the Zr3 alloy in the perpendicular orientation, and it looks like that the second phase is more evenly dispersed than in the orientation parallel to arc (Fig. 6.1.5 (d)). Finally, for the Zr4 alloy the extremely dense zones of precipitates appearing in the orientation parallel to arc (Fig. 6.1.5 (e)) become less dense in the orientation perpendicular to arc, with a bit larger particle size and interparticle distances (Fig. 6.1.6 (e)).

In conclusion, similar to Ni-Mn-Ga-Hf alloys, Ni-Mn-Ga-Zr alloys show a clear increase in density of precipitates as a function of Zr addition. For an equal Zr content, the distribution of the f.c.c. second phase may present some differences when observed in the orientations parallel or perpendicular to the arc flame. This fact, together with

the orientational texture developed in the ingot and the use of bulk sample (not powder) produce the large variations in the intensities of the XRD peaks in both orientations. The images from both orientations indicate that the precipitates form first at grain boundaries and then inside the grains. Upon increasing the Zr content, the inner precipitates grow and form networks that reduce the size of the domains of austenite/martensite phase, producing a grain refinement effect.

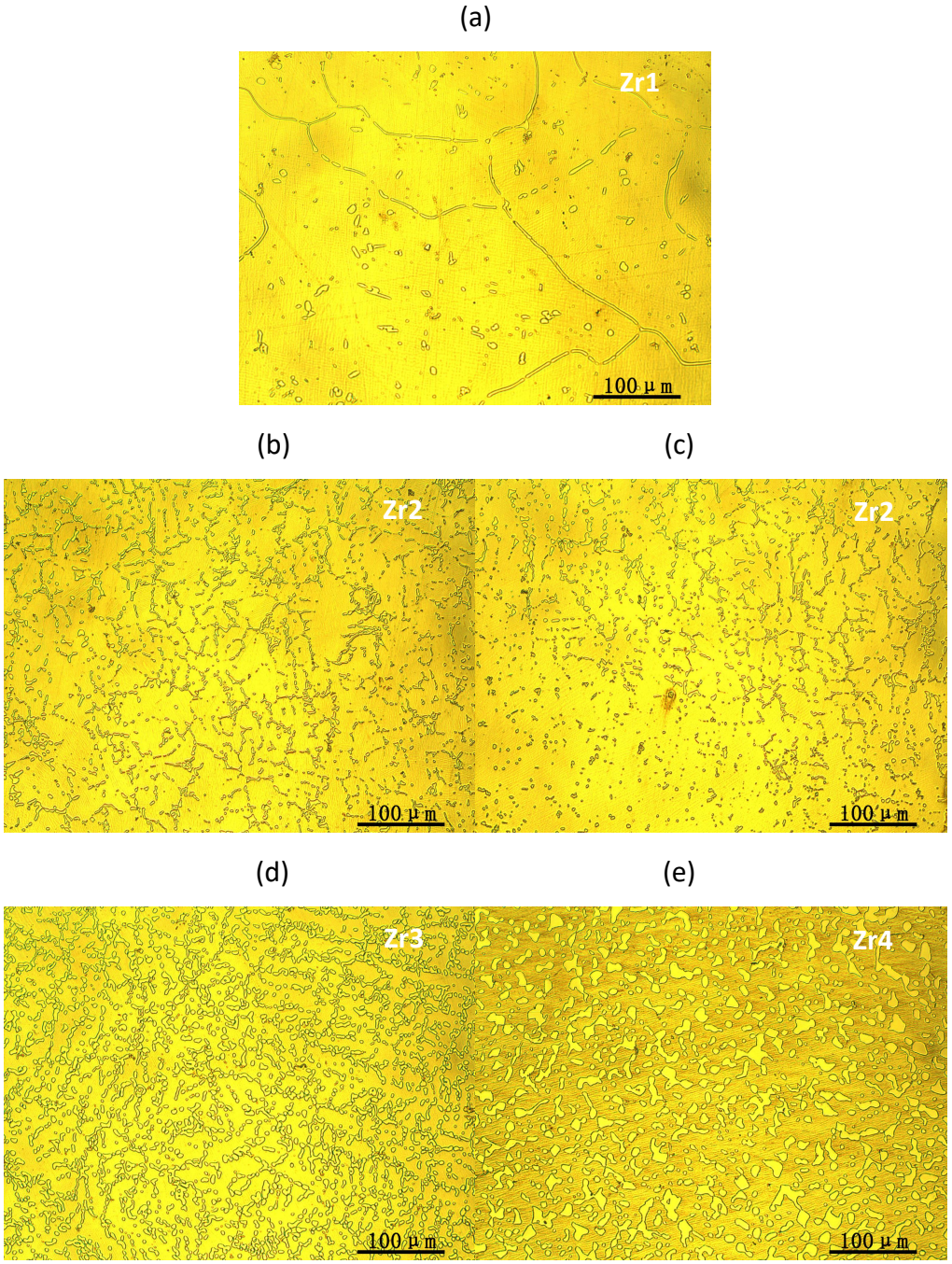

Fig. 6.1.6. Optical observations of Ni-Mn-Ga-Zr alloys SHT 1270 K for 48 h with the orientation perpendicular to arc flame: (a) Zr1, (b) Zr2 zone one and (c) Zr2 zone two, (d) Zr3, (e) Zr4.

The microstructural evolution of Zr3 alloy SHT at 1270 K for 48 h with additional ageing at 870 K for 24 h and 72 h is presented in Fig. 6.1.7. As it is shown, basically no change in the precipitates size nor volume fraction occurs after ageing up to 72 h. For the observed ageing stages, the second phase dendrites possess length ~9 - 25 µm and width ~1 - 6 µm; the ellipses have length about ~2 - 7 µm and width ~1 - 5 µm (Fig. 6.1.7 (d)). The change in the particle contrast visible in Fig. 6.1.7 (c) is due to slightly different focus and polarized light conditions in the optical microscope. The absence of remarkable microstructural evolution is in line with the good thermal stability upon ageing obtained by DSC (Fig. 6.1.2).

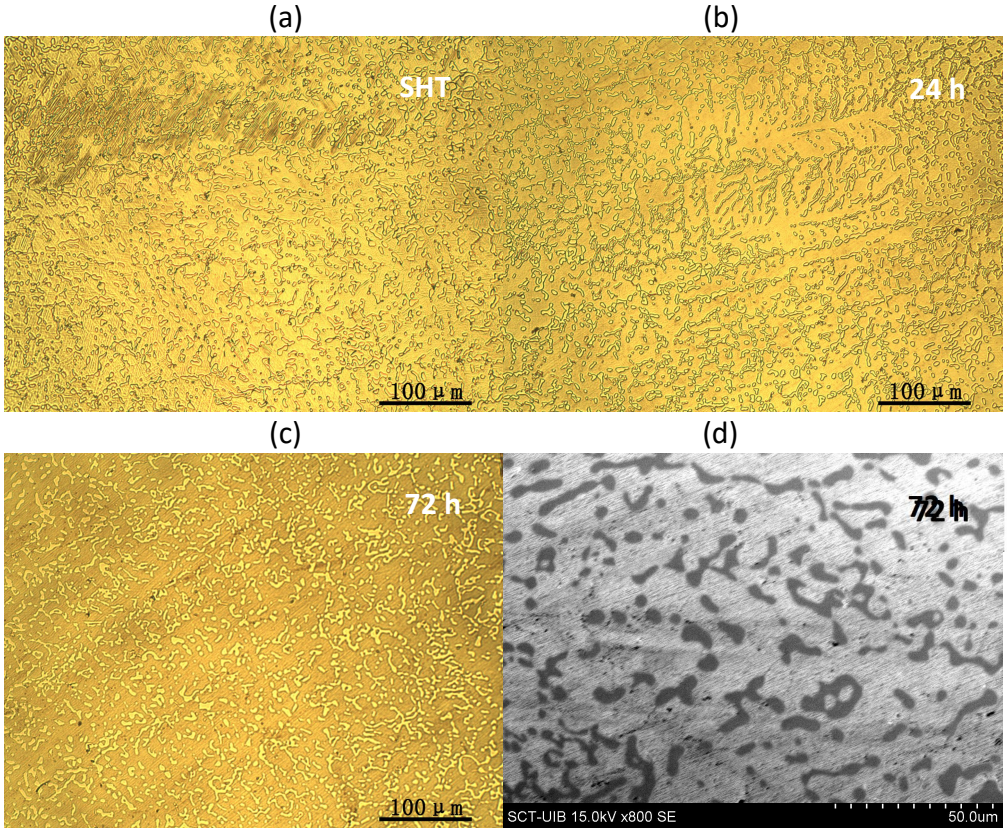

Fig. 6.1.7. Optical observations of NiMnGaZr3 specimen: (a) SHT 1270 K for 48 h, (b) additional ageing at 870 K for 24 h and (c) for 72 h; (d) SEM observation in larger scale corresponding to (c).

Compositional study by EDX

As observed in the previous SEM images (Fig. 6.1.4), there are two types of particles in the Ni-Mn-Ga-Zr alloys. One type are the small particles with the highest bright white contrast, that correspond to the Zr carbide or oxide particles inevitably introduced during the alloy preparation process. They have been tested many times by EDX point analysis, and the average composition is presented in the Table 6.3 for the Zr0.5 alloy using bold red font. The carbon and oxygen content corresponds to the difference to 100%. The particles are very rich in Zr; however, as already discussed in the previous chapter, the composition is not accurate due to the low

signal of the light C, O elements and to the relatively large volume of sample affected by the microanalysis in the SEM, which contains not only the small particles but also the surrounding martensite matrix. This type of particles appears in all the investigated alloys with Zr addition, and it is the only kind of particles present in Zr0.5. The other type of particles is the f.c.c. second phase formed with Zr content above 0.5 at.%. Their averaged composition for multiple times EDX point tests is shown in Table 6.3 with standard black font. This phase contains relatively higher amount of Ni and is much richer in Zr in comparison with the matrix. It is also worthy to note in Table 6.3 that the matrix in all the studied alloys always contain more or less the same small amount of Zr (below 0.8 at.%), indicating that Zr exhibits extremely low solubility in the Heusler structure. The solubility of Zr is relatively lower than Hf (around 1 at.%, as seen in Table 5.3). Moreover, we can notice that the Ni content in the matrix tends to slightly decrease from Zr0.5 to Zr4 alloys and it is always lower than the target (53 at.%). This agrees with the large increase in the fraction of second phase, which causes the Ni depletion of the matrix. A slight decrease of Ni content is also observed in the f.c.c precipitates upon increasing the Zr addition, which moderates the Ni depletion of the matrix for the Zr3 and Zr4 alloys, despite their large fraction of the f.c.c. phase.

Table 6.3. Composition of Ni-Mn-Ga-Hf alloys with thermal treatment SHT and additional ageing measured EDX consisted of matrix, precipitates and carbides.

Alloy	**Treatment**	**Martensite**				**Precipitates (or Carbides)**			
		Ni at.%	Mn at.%	Ga at.%	Zr at.%	Ni at.%	Mn at.%	Ga at.%	Zr at.%
Zr0.5	SHT 1270 K 48 h	51.3	30.0	18.1	0.6	**17.4**	**11.2**	**5.6**	**42.4**
Zr1	SHT 1270 K 48 h	50.3	30.5	18.7	0.5	59.3	17.8	9.2	13.7
Zr2	SHT 1270 K 48 h	50.8	30.5	18.1	0.6	58.6	19.0	9.4	13.0
Zr3	SHT 1270 K 48 h	49.5	31.2	18.6	0.7	57.2	19.3	10.0	13.6
	Aged 870 K 72 h	50.4	30.6	18.4	0.6	58.5	17.6	9.4	14.5
Zr4	SHT 1270 K 48 h	49.5	30.5	19.3	0.7	57.9	18.1	9.7	14.3

TEM observations

Fig. 6.1.8 presents some TEM images of the martensitic matrix for the SHT Zr2 and Zr4 alloys. The diffraction pattern in Fig. 6.1.8 (b) corresponds to the internally twinned martensite on the upper left side of Fig. 6.1.8 (a) and reveals the $(022)_M$ twinning plane of the non-modulated b.c.t. structure. As for the Zr4 specimen, the SADP (Fig. 6.1.8 (d)) corresponds to the $[111]_{b.c.t.}$ zone axis of the non-modulated b.c.t. martensite, and the bright field image of martensite is presented in Fig. 6.1.8 (c). The electropolished TEM discs of Zr4 alloy contained small observable thin areas and it was not possible to detect the modulated 14M martensite by electron diffraction in the TEM. Therefore, it can be concluded that all the studied

Ni-Mn-Ga-Zr alloys possess the non-modulated b.c.t. martensite, but the Zr4 alloy also contains a low fraction of the modulated 14M martensite, which could be detected in the XRD patterns, Fig. 6.1.3 (f).

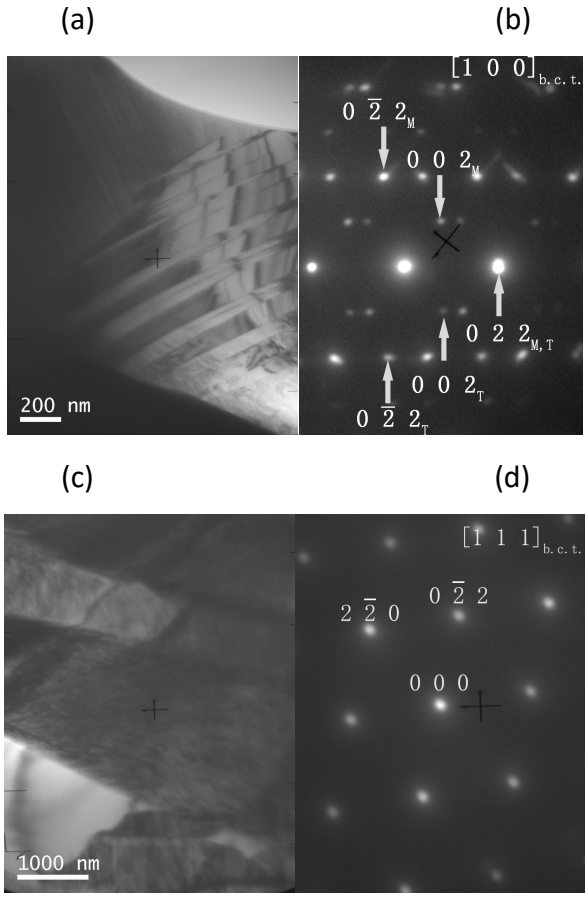

Fig. 6.1.8. TEM observations of the matrix for (a) Zr2 alloy, (b) corresponding SADP of (a); (c) Zr4 alloy SHT 1270 K for 48 h, (d) corresponding SADP of (c).

TEM observations of the second phase particles are shown in Fig. 6.1.9 for alloys with relatively high Zr addition (2 - 4 at.%), which contain a large amount of second phase embedded in the matrix and provide large possibility for observation. Fig. 6.1.9 (a) shows a big precipitate particle of Zr2 alloy in the center of the image. The SADP of this big particle is presented in Fig. 6.1.9 (b) and reveals the $[110]_P$ zone axis of the f.c.c. structure. Fig. 6.1.9 (c) is from Zr3 alloy and shows a big precipitate in the center, oriented along the zone axis $[211]_P$ (Fig. 6.1.9 (d)). The Zr4 alloy shows a big number of precipitates, as expected, and they exhibit a higher transparency than the matrix (Figs. 6.1.9 (e) and (f)), due to a preferential electropolishing of the second phase. Fig. 6.1.9 (g) shows the $[211]_P$ zone axis of precipitates corresponding to Fig. 6.1.9 (e). Moreover, all the diffraction patterns from the precipitates in the Ni-Mn-Ga-Zr alloys exhibit closer distance of the diffracted spots than the normal γ phase reported in other Ni-Mn-Ga-X systems. In fact, the diffraction patterns reveal an equivalent structure as that observed in Ni-Mn-Ga-Hf alloys, as will be discussed later.

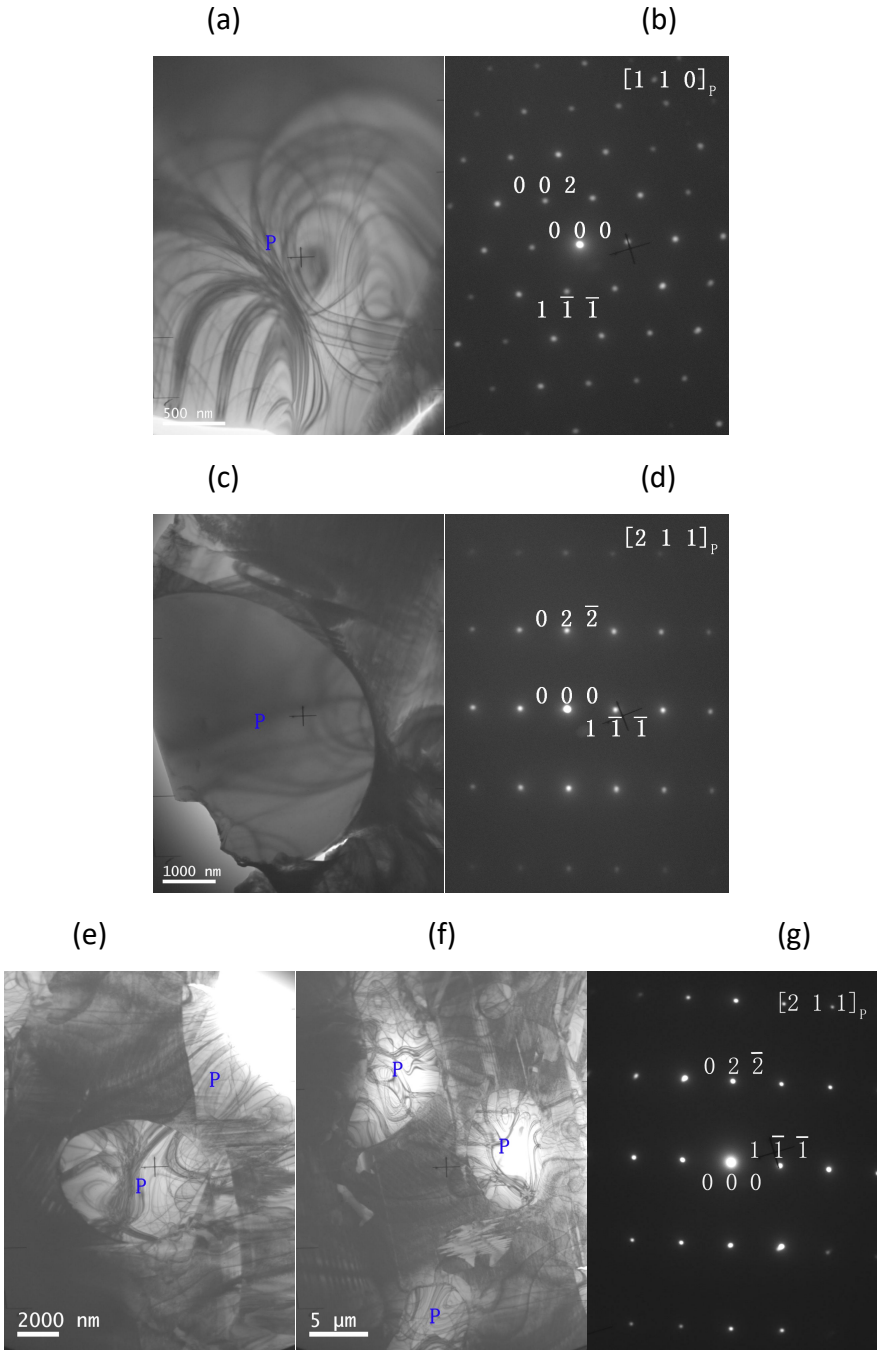

Fig. 6.1.9. TEM observations of the second phase for (a) Zr2 alloy, (b) corresponding SADP; (c) Zr3 alloy , (d) corresponding SADP; (e,f) Zr4 alloy, (g) SADP of image (e).

6.1.4 Thermomechanical Experiments

The results of thermomechanical tests (cooling/heating under different levels of compressive stress) performed on Ni-Mn-Ga-Zr alloys are presented in the Fig. 6.1.10 to characterize their shape memory effect. The same temperature (**X**-axis) and strain (**Y**-axis) scales are used for each alloy to facilitate the visualization of the evolution of the mechanical response with Zr addition. As it is shown, the transformation temperature is continuously decreasing as a function of Zr addition, as well as the

values of strain, which is consistent with the DSC results seen from Fig. 6.1.1. For example, under 100 MPa constant applied stress the M_s decreases from 606 K for Zr0 to 445 K for Zr4, and the total transformation strain drops from 1.63% to about 0.45%, respectively. It should be noted that the ternary alloy denoted as Zr0 here (Fig. 6.1.10 (a)) is the same sample denoted as Hf0 in the previous chapter. With low Zr addition 0.5 at.% (Fig. 6.1.10 (b)) and 1 at.% (Fig. 6.1.10 (c)), the transformation strain only reduces a little bit compared to Zr0, while the martensitic transformation temperature (M_s) decreases by about 50 K. Additionally, it has to be noted that the curves for Zr1 alloy under low compression stress (<100 MPa) present unusual large temperature extension of the transformation with irregular strain evolution, which could be related to a heterogeneous distribution of the precipitates in the matrix. The DSC results also present a multi-peak signal for this alloy (Fig. 6.1.1). As for the alloys with relatively large Zr content (Figs. 6.1.10 (d) - (g)), they show very low levels of irrecoverable strain, *e.g.*, Zr4 exhibits only 0.03% irrecoverable strain under 300 MPa. The specific data extracted from the Fig. 6.1.10 (transformation temperatures, thermal hysteresis, total and irrecoverable strains) are listed in the Appendix A.

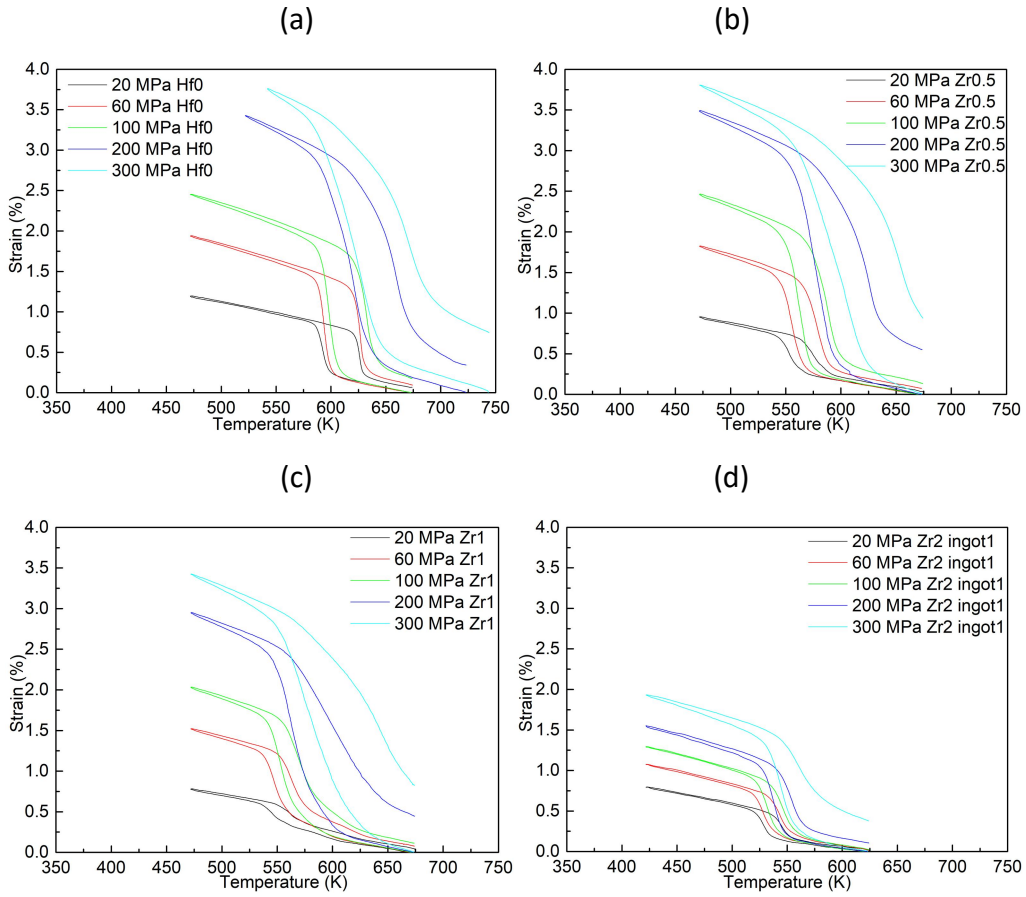

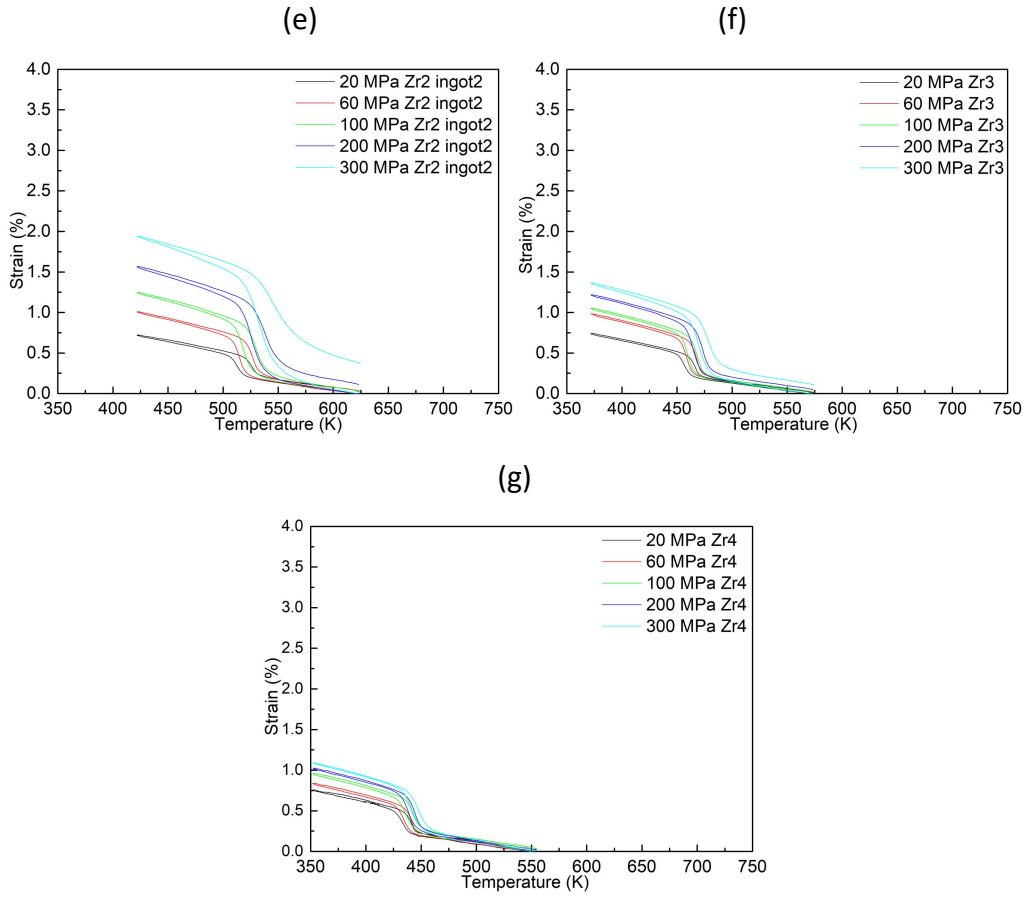

Fig. 6.1.10. Thermomechanical tests of Ni-Mn-Ga-Zr alloys with the thermal treatment SHT 1270 K for 48 h: (a) Zr0 (Hf0), (b) Zr0.5, (c) Zr1, (d) Zr2, (e) Zr2, (f) Zr3 and (g) Zr4.

Plots of the functional parameters extracted from the thermomechanical tests are presented in Fig. 6.1.11. The behaviour of the total strain, irrecoverable strain and its ratio as a function of the applied stress (Figs. 6.1.11 (a), (b) and (c)) is very similar to the Ni-Mn-Ga-Hf alloys (Fig. 5.1.15 in the previous chapter). The total and irrecoverable strains increase with the external applied stress, *e.g.*, for Zr2 specimen (pink color) the total strain grows from 0.28% (20 MPa) to 1.30% (300 MPa) while the irrecoverable strain increases from 0.03% (20 MPa) to 0.38% (300 MPa). The total strain tends to saturation for Zr0, Zr0.5 and Zr1 alloys, while for higher Zr content the total strain increases continuously up to 300 MPa, which means that the fraction of martensite oriented by the applied stress is not saturated and could be increased with further stress increment. In addition, a relatively large gap is visible between the curves for Zr1 and Zr2 alloys, in agreement with the big difference in the volume fraction of second phase precipitates. The ratio of Irr/Total strains (Fig. 6.1.11 (c)) initially decreases with stress until 100 MPa and, then, increases continuously for all alloys (though reaching lower values for increasing Zr content), except for the Zr4 specimen that is basically constant. This behaviour is completely parallel to the Ni-Mn-Ga-Hf alloys. As discussed in the previous chapter, it means that at the low stress levels, the increase in the fraction of oriented martensite variants predominates over the irreversible deformation, while at stress levels above 100 MPa

the irrecoverable strain grows faster. It also indicates that the precipitates have no or little strengthening effect to the matrix when Zr content is low. As for the Zr4 alloy with constant ratio, both strains evolve little with the applied stress as a result of the big volume fraction of the precipitates, which causes a nearly constant Irr/Total strain ratio, or even decreasing slightly with the applied stress.

Fig. 6.1.11 (d) presents the change of M_s temperature as a function of the applied stress, according to the Clausius-Clapeyron relationship. Again, the behaviour is very similar to the Ni-Mn-Ga-Hf alloys presented in previous chapter (Fig. 5.1.15 (d)) and the M_s temperature does not follow a unique linear dependence on stress especially for the low Zr content (below 2 at.%). At low stress level (≤100 MPa) the slopes are fitted as 9.6 MPa/K, 8.0 MPa/K, 9.3 MPa/K and 9.2 MPa/K for Zr0 to Zr2 alloys, respectively, while at higher stress level (≥ 100 MPa) the slopes are fitted as 4.7 MPa/K, 3.7 MPa/K, 4.6 MPa/K and 9.4 MPa/K, for the same alloys. The responses of the Zr3 and Zr4 alloys are linear in the whole stress range with slopes 16.8 MPa/K and 21.7 MPa/K, respectively. As discussed in the previous chapter, the different response at low and high stress values can be related to the role of the internal stress fields existing in the material, that compensate the external applied stress and reduce the change in the M_s temperature. The results of Figs. 6.1.11 (c) and (d) indicate that the internal stress levels existing in these alloys are of the order of 100 MPa. Fig. 6.1.11 (e) shows the work output of the Ni-Mn-Ga-Zr alloys as a function of applied stress, which is calculated with Eq. 3.1.3 from the recoverable strain and the applied stress values. The work output is increasing with the applied stress for each sample due to the rise in the total and recoverable transformation strains, *e.g.*, Zr1 presents 1.3 J/cm^3 under 100 MPa applied stress and 4.7 J/cm^3 under 300 MPa. However, the work output is sharply declined with increasing the Zr doping, *e.g.*, from 6.1 J/cm^3 of Zr0 to 1.6 J/cm^3 of Zr4 under 300 MPa, as the result of the big volume fraction of non-transformed precipitates and concomitant large drop of the transformation strain. Hence, the large gap observed between the curves for Zr0, 0.5 ,1 and Zr2, 3, 4 alloys is caused by the big differences in the volume fraction of precipitates. This is, again, a behaviour very similar to the Ni-Mn-Ga-Hf alloys presented in previous chapter (Fig. 5.1.15 (e)).

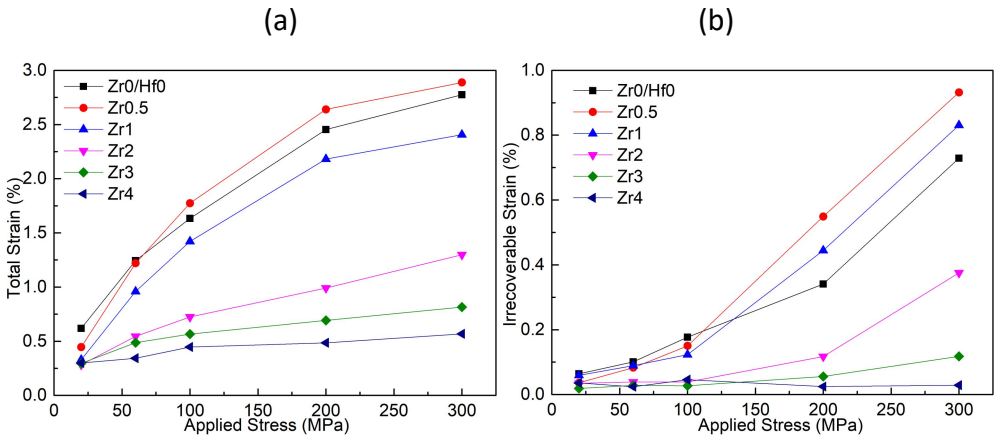

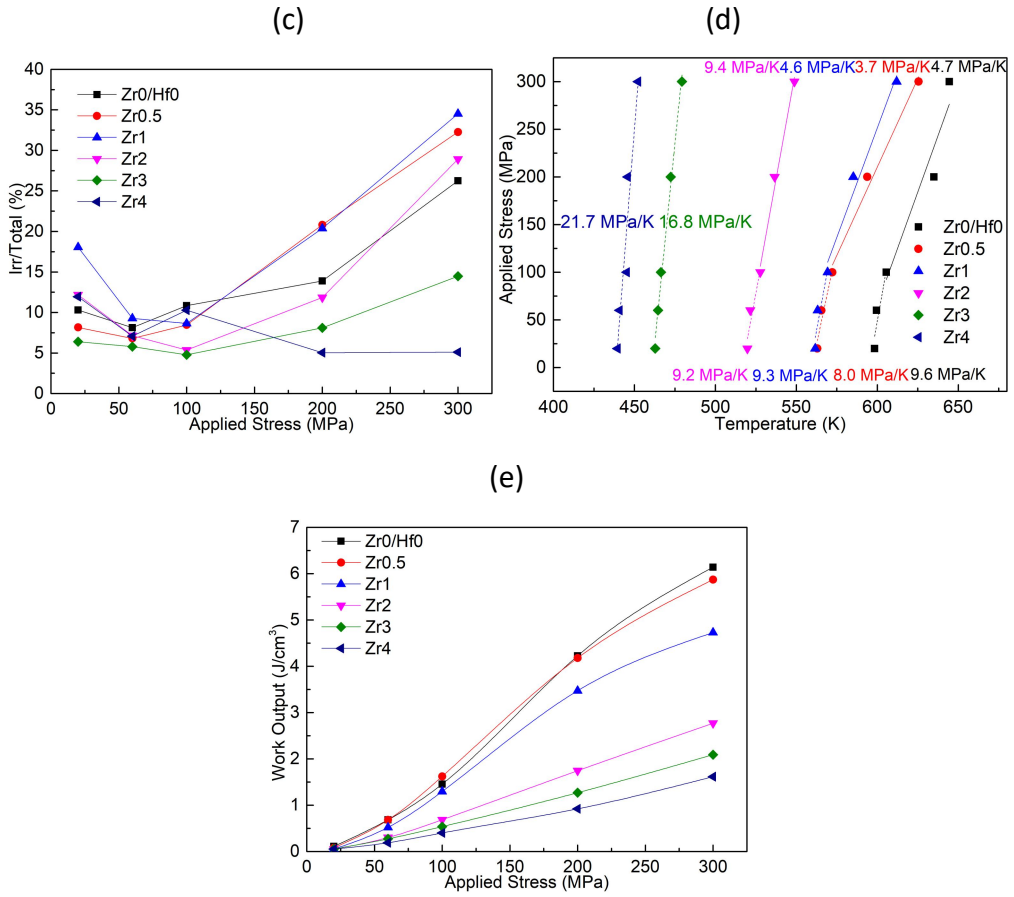

Fig. 6.1.11. Thermomechanical results of Ni-Mn-Ga-Zr alloys as the result of Zr addition: (a) total strain, (b) irrecoverable strain and (c) ratio of irr/total strain as a function of applied stress; (d) applied stress and M_s related to Clausius-Clapeyron equation; (e) work output as a function of applied stress.

6.1.5 Mechanical Experiments

Fig. 6.1.12 presents the mechanical tests (stress-strain curves) of Zr2, Zr3 and Zr4 alloys in compression, measured at temperatures above the A_f value of each alloy obtained from DSC analysis, *i.e.*, A_f + 10 K, + 30 K, + 50 K. It is clear that basically no or very little strain recovery is obtained in all samples, which indicates the absence of superelasticity effect. In addition, after every compression cycle the specimen was heated up to A_f + 100 K to eliminate some existing stabilized martensite. The small recovered strain obtained in the last cycles performed up to the maximum applied deformation is marked by red arrows in Fig. 6.1.12.

For Zr2 specimen (Fig. 6.1.12 (a)), there is some sign of strain recovery upon unloading with large hysteresis in the tests performed at 580 K and 620 K. However, only about 0.4% recoverable strain can be measured. Moreover, it should be noted that there is some accommodation of the specimen when touching the compression head at low stress level (below 50 MPa), due to the lack of perfect parallelism, which causes a smooth shape of the σ-$\mathcal{E}$ curve, which may affect the measurement of the

irrecoverable strain. After subsequent heating up to A_f + 100 K, the Zr2 specimen shows about 0.15% and 0.07% additional recoverable strain in the tests performed at 580 K and 620 K, respectively. At 620 K, the strain is too small to be marked with arrow. Zr3 specimen also shows little recoverable strain (0.4%) at 525 K, and the irrecoverable is the same as Zr2 (0.5%) after being compressed above 700 MPa. The Zr4 specimen is compressed up to almost 1000 MPa at 500 K, but only shows a little increase of recoverable strain (0.8%), with irrecoverable strain ~0.7%. Therefore, the induced strain is mainly derived from plastic deformation or highly stabilized martensite, and only a very small part is from reversible martensite. Again, the mechanical behaviour of Ni-Mn-Ga-Zr alloys is very similar to Ni-Mn-Ga-Hf. The reasons for the very poor strain recovery have been discussed in the previous chapter.

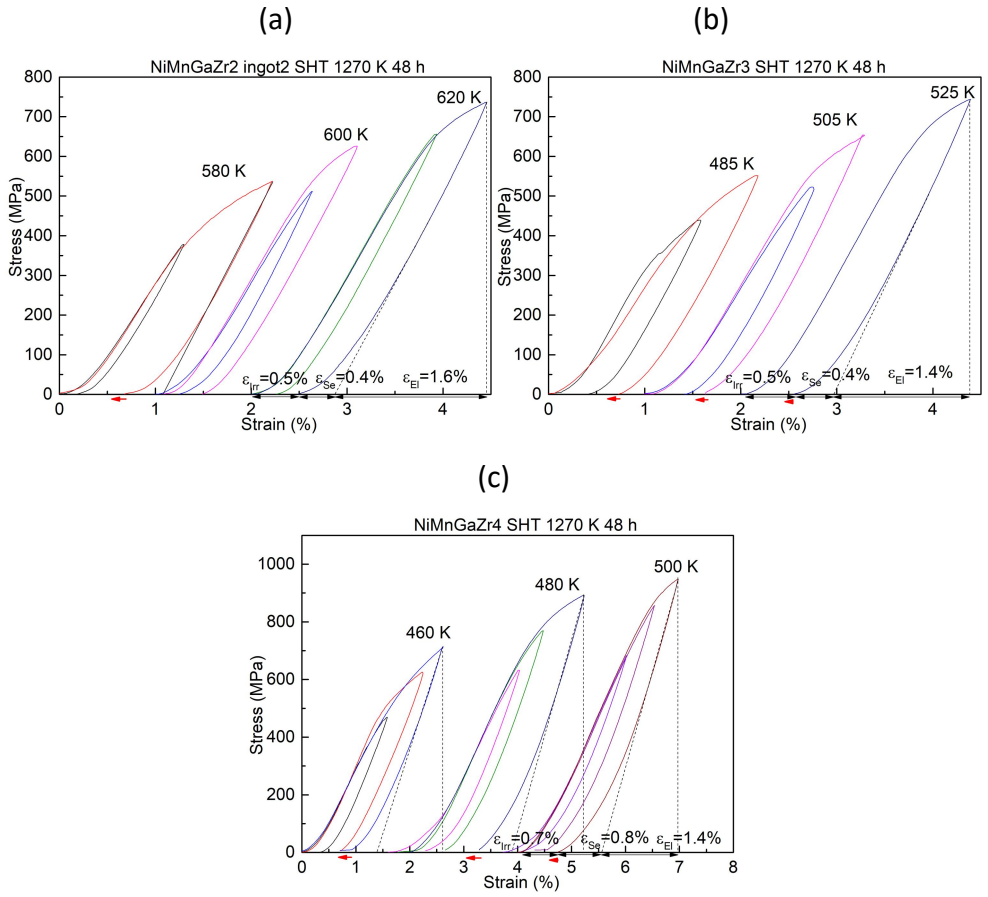

Fig. 6.1.12. Mechanical tests on Ni-Mn-Ga-Zr alloys with thermal treatment SHT 1270 K for 48 h, stress-strain curves of (a) Zr2, (b) Zr3 and (c) Zr4.

6.2 Discussion of the results and comparison with Ni-Mn-Ga-Hf Alloys

In this section, the characteristics of Ni-Mn-Ga-Zr alloys presented in the previous section will be further discussed and compared with Ni-Mn-Ga-Hf.

6.2.1 Transformation Temperatures and Other Thermal Characteristics

As we have stated before the martensitic transformation temperature can be changed due to the competition between the valence electron concentration per atom (*e*/*a*) and the effect of lattice parameter variation [61, 62, 173]. The overall trend of DSC peak temperature (M_p) in Ni-Mn-Ga-Zr alloys appears to be continuously decreasing from 590 K of Zr0 to 433 K of Zr4, which follows the decay tendency of *e*/*a* ratio given in Fig. 6.2.1 (a) and of *c*/*a* tetragonality seen from Fig. 6.2.1 (b). The *e*/*a* and *c*/*a* values were calculated from the experimental EDX microanalysis and XRD (orientation perpendicular to arc flame) data. In these graphs, the results of Ni-Mn-Ga-Hf alloys are plotted together with Ni-Mn-Ga-Zr alloys for comparison. Though a significant dispersion of data can be observed for both quaternary additions (due to small deviations from the nominal composition occurring in the alloy production, together with the experimental error of the EDX technique), an overall correlation of transformation temperatures with *e*/*a* and *c*/*a* ratios can be observed in both plots, as the alloys with low quaternary content are located at right top part of the plots while high quaternary content are at left bottom part. Moreover, it is worth noting that there are some inhomogeneities in the transformation DSC peaks of Hf/Zr 0.5 and Hf/Zr 1 alloys (Figs. 5.1.1 and 6.1.1) due to the heterogeneous precipitation process, which could further influence the collection data by EDX. In addition, for the *c*/*a* data of high Hf/Zr content alloys (Figs. 5.2.1 (b) and 6.2.1 (b)), the internal stress fields induced by the large amount of second phase particles could also influence the lattice parameters of the martensite phase.

In comparison, both quaternary alloys possess similar range of *e*/*a* and *c*/*a* values of the martensite matrix. The transformation temperatures of the alloys with low quaternary content (0.5 and 1 at.%) are rather similar for both Hf and Zr additions. However, for contents above 1 at.%, the Ni-Mn-Ga-Zr alloys systematically exhibit higher transformation temperatures than the corresponding Ni-Mn-Ga-Hf alloys with the same nominal quaternary addition, which could be related to the lower solubility of the Zr element in the matrix (~0.7 at.%) compared to Hf (~1 at.%), according to the EDX measurements.

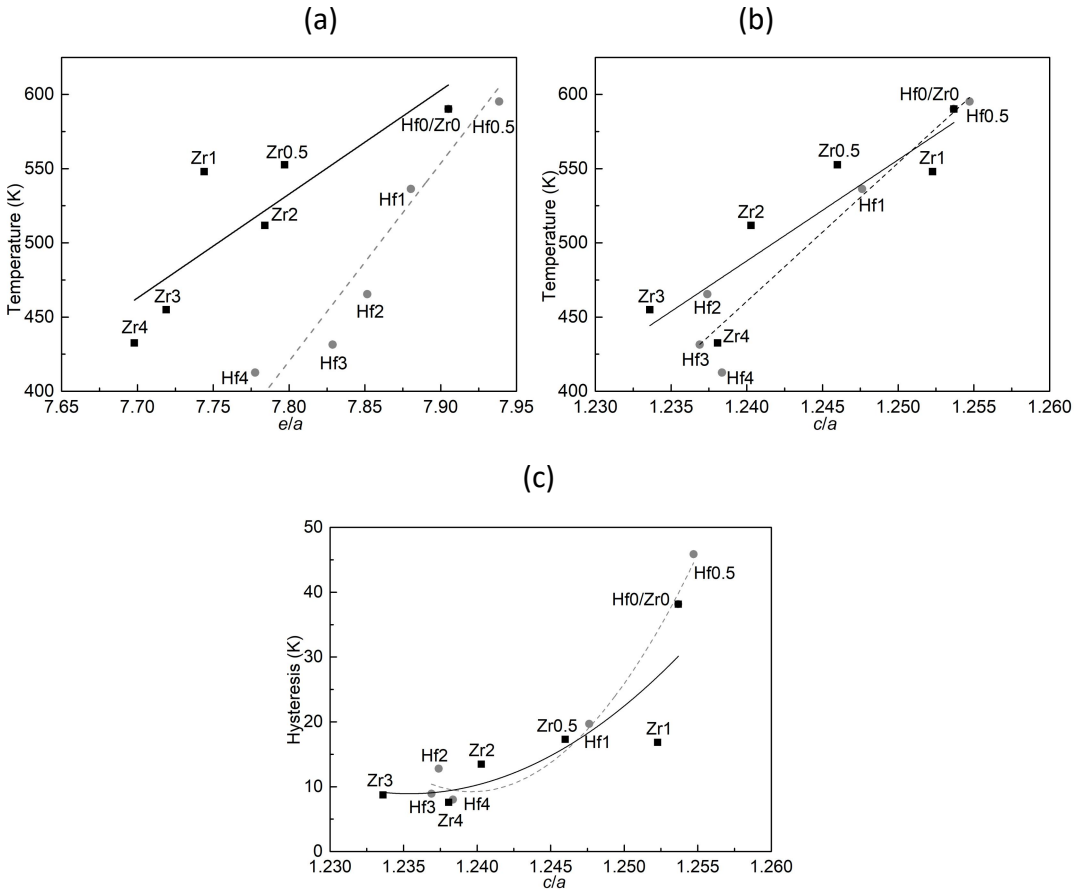

Fig. 6.2.1. Ni-Mn-Ga-Zr and Ni-Mn-Ga-Hf alloys transformation peak temperature (M_p) as a function of (a) valence electron concentration per atom (e/a) and (b) as a function of tetragonality (c/a) of matrix. (c) Hysteresis variation as a function of c/a.

Fig. 6.2.1 (c) shows a good correlation between the thermal hysteresis of transformation and the tetragonality (c/a) of the martensite phase for both quaternary additions. A parallel tendency of Ni-Mn-Ga-Hf and Ni-Mn-Ga-Zr alloys is shown. The tetragonality and hysteresis decrease fast with low Hf/Zr addition (below 2 at.%), and then remain essentially constant with further addition (>2 at.%). Further discussion of this correlation will be presented in the next section.

Fig. 6.2.2 shows the transformation hysteresis measured from the thermomechanical tests as a function of the applied stress. The data for zero stress corresponds to the hysteresis measured by DSC. For low Hf/Zr addition (below 2 at.%) the hysteresis shows little evolution until 100 MPa and then a significant increase with the applied stress. For example, the hysteresis of Zr1 alloy increases from 16 K to 59 K under 20 MPa and 300 MPa, respectively. Instead, for higher Hf/Zr content the transformation hysteresis becomes almost constant, independent of the applied stress, except for Hf2 alloy that shows a notable increase of hysteresis between 200 and 300 MPa. In particular, Zr4 and Hf4 alloys exhibit the lowest hysteresis among all the studied alloys, being almost constant around 6 to 8 K for all the applied stresses. The evolution of hysteresis with the applied stress follows the same trends as the

irrecoverable strain, shown in Figs. 5.1.15 (b) and 6.1.11 (b), which evidences the close correlation between both variables.

The results indicate that the heterogeneous oxide/carbide inclusions and f.c.c. precipitates in the low Zr/Hf doped alloys that can provide limited pining effect to the dislocations and once the applied stress is big enough (above 100 MPa), the accumulated dislocations can easily move between the particles, leading to plastic deformation. On the contrary, the alloys with higher Zr/Hf content (3 - 4 at.%) exhibit stable and low values of hysteresis and irrecoverable strain up to 300 MPa due to the stronger pining effect of the precipitate networks. Comparing the results of Hf2 and Zr2 alloys, both with similar distributions of second phase precipitates, it seems that addition of Hf has a better effect on reducing the hysteresis than Zr, since Hf2 shows less inclined growing tendency and lower values of hysteresis than Zr2 (Fig. 6.2.2).

The enthalpy change measured from DSC, shown in Table 6.1, allows to figure out the fraction of transformable material present in the alloys with Zr addition. The value is decreased from 14.3 J/g for Zr0 to 10.4 J/g for Zr4, so about 27% loss of martensitic transformation can be estimated, due to the formation of non-transforming precipitates. In comparison, the enthalpy change of Hf4 reduces to 9.3 J/g, as shown in Table 5.1, which represent a 35% loss. Hence, roughly speaking, Ni-Mn-Ga-Zr/Hf alloys with 4 at.% fourth element addition contain a mixture of about 65 - 70% austenite/martensite and 30 - 35% precipitates, though the estimations based on the SEM images reduce the fraction to 21 - 24%.

In turn, as discussed in the previous chapter for Hf addition, the decrease of recoverable strain measured in the thermomechanical tests of alloys with Zr addition is much larger than the reduction in transformable volume fraction. The recoverable strain decreases from 2.0% for Zr0 (Hf0) to 0.5% for Zr4 and 0.6% for Hf4, under 300 MPa applied stress, indicating a loss of ~75% and ~70%, respectively. The loss of recoverable strain is more than two times larger than the reduction in transformable volume fraction caused by the precipitates, which demonstrates the limited ability of the applied stress to favour the oriented martensite variants (those producing uniaxial compression) in these samples. As discussed in section 5.2.3 of the previous chapter, the connected network of precipitates produces a “shielding” effect of the external stress, which limits the selection of the compressive martensite variants. This explains the lack of saturation of the transformation strain observed in Figs. 6.1.11 (a) and 5.1.15 (a) for high Hf/Zr content, in spite of the rather high applied stress level (300 MPa) reached in the present study.

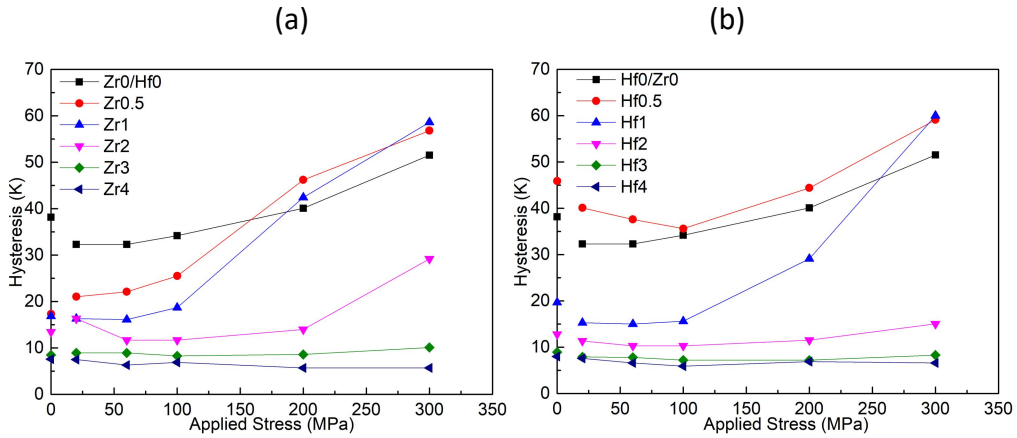

Fig. 6.2.2. Hysteresis measurement from DSC and thermomechanical cycling of (a) Ni-Mn-Ga-Zr alloys and (b) Ni-Mn-Ga-Hf alloys.

The Hf3 and Zr3 alloys both have demonstrated excellent thermal stability upon both thermal cycling and prolonged ageing at 870 K (Figs. 6.1.2 and 5.1.2, 5.1.3). The thermal cycling stability can be correlated with the low hysteresis, which implies a good lattice correspondence between austenite and martensite structures (as will be discussed in the next section) and, then, absence of dislocation generation upon repeated transformation. Although these alloys present enough stability upon prolonged ageing at 870 K, there are still minor temperature variation and reduction of enthalpy change detected by DSC. The shift of transformation temperatures after 72h ageing at 870 K go in opposite directions for Hf3 and Zr3 alloys, being -8 K and +2 K, respectively. The microscopy observations (Fig. 6.1.7 and Fig. 5.1.9) exhibit no obvious change of microstructure. However, EDX measurements provide evidence of atomic diffusion effects existing at 870 K producing slight compositional changes, as can be seen in Table 6.4. In spite that EDX results are not very accurate, the overall tendency still presents a small increase of e/a in NiMnGaZr3 and a basically constant e/a in NiMnGaHf3 after 72 h ageing at 870 K, calculated from the data in Table 6.4. These changes are more or less consistent with the opposite shifts of transformation temperatures observed by DSC considering the EDX inaccuracy. This situation could be linked to the differences of solubility of Zr/Hf atoms, where Zr possesses more solubility in the precipitates instead of martensite and Hf has more tendency to diffuse into martensite in order to reach the equilibrium state at 870 K.

Table 6.4. Composition measurement of martensite for NiMnGaZr3/Hf3 by EDX.

Element / **Thermal treatment**	**NiMnGaZr3**				**NiMnGaHf3**			
	Ni at.%	Mn at.%	Ga at.%	Zr at.%	Ni at.%	Mn at.%	Ga at.%	Hf at.%
SHT	49.5	31.2	18.6	0.7	51.2	30.9	16.9	1.0
Aged at 870 K for 72 h	50.4	30.6	18.4	0.6	51.1	31.1	16.9	0.9

6.2.2 Microstructure

The XRD (Fig. 6.1.3) and TEM (Fig. 6.1.8) results have illustrated that the non-modulated body centered tetragonal (b.c.t.) martensite variants exist in all the Ni-Mn-Ga-Zr alloys, in the same way as Ni-Mn-Ga-Hf and the ternary alloy. Moreover, the Zr4 and Hf4 alloys not only possess b.c.t. non-modulated martensite but also show a low fraction of modulated 14M martensite, seen in Figs. 6.1.3 (f) and 5.1.4, 5.1.12. It should be noted that the two types of martensite seem to be randomly distributed in the material, as no clear preferential location of the 14 M martensite could be detected in these samples. Additionally, the size of martensite variants are gradually reduced to less than ~50 μm as a function of Zr or Hf addition due to formation of a connected network of f.c.c. second phase particles that produce a grain refining effect.

The lattice compatibility between austenite and b.c.t. martensite has been studied in the Zr4 alloy by *in-situ* heating XRD analysis, as shown in Fig. 6.2.3 (a) (reproduced from Fig. 6.1.3 (f)) as well as in Hf4 alloy, as shown in Fig. 6.2.3 (b). These experiments not only present the evolution of the phases during the reverse transformation, discussed in the previous section, but also reveal the lattice parameters of austenite and martensite at high temperature. The patterns recorded at A_f temperature are used to calculate the lattice parameters of b.c.t. martensite and $L2_1$ austenite since both phases are co-existing at this temperature. The results are shown in the Table 6.5 in bold red color font, together with the lattice parameters of the b.c.t martensite recorded at room temperature in all the alloys, shown in black font. The latter parameters correspond to the orientation perpendicular to arc flame and are extracted from Tables 5.4 and 6.2.

According to the theory that has been discussed in the section 5.2.1 of the previous chapter, the compatibility between the parent phase and martensite phase can be associated with the hysteresis and reversibility of transformation [212]. The theory was developed for the cubic to orthorhombic B2-B19 transformation in Ni-Ti based alloys. Typically, for orthorhombic martensite the lattice parameter *b* (projected along the crystallographic axes of the cubic austenite) is close to the lattice parameter of austenite, a_0, while the other parameters *a* and *c* are shorter and larger than a_0, respectively. In this case, the low hysteresis of transformation occurs when the second eigenvalue λ_2 is very close to 1 [212-214].

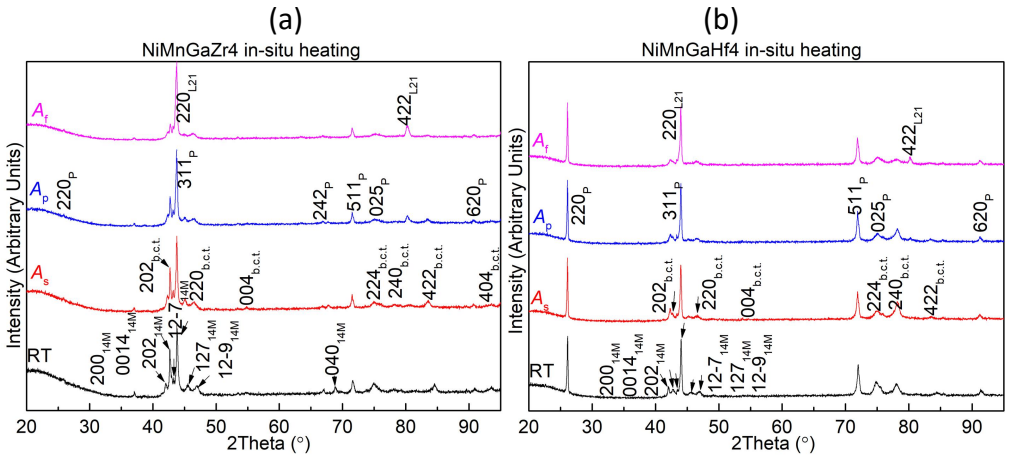

Fig. 6.2.3. *In-situ* XRD patterns of (a) NiMnGaZr4 and (b) NiMnGaHf4 SHT 1270 K for 48 h specimens recorded at room temperature, A_s, A_p and A_f, respectively.

Table 6.5. Lattice parameters of martensite and austenite in Ni-Mn-Ga-Hf and Ni-Mn-Ga-Zr alloys.

Alloys	**Martensite b.c.t.**						**Austenite b.c.c.**		**M/A**
	a Å	c Å	λ_1,λ_2 a/a_0	λ_3 c/a_0	det$\boldsymbol{U}$ $\lambda_1\cdot\lambda_2\cdot\lambda_3$	diagonal $\sqrt{a^2+c^2}$ Å	a_0 Å	diagonal $\sqrt{2}a_0$ Å	dM/dA $\frac{\sqrt{a^2+c^2}}{\sqrt{2}a_0}$
Hf0/Zr0	5.388	6.754	0.920	1.153	0.976	8.640			1.043
Hf0.5	5.385	6.757	0.919	1.153	0.974	8.640			1.043
Hf1	5.407	6.746	0.923	1.152	0.981	8.645			1.044
Hf2	5.430	6.719	0.927	1.147	0.986	8.639			1.043
Hf3	5.429	6.715	0.927	1.146	0.985	8.635			1.042
Hf4	5.435	6.731	0.928	1.149	0.990	8.651			1.044
Hf4	**5.509**	**6.590**	**0.940**	**1.125**	**0.994**	**8.589**	**5.858**	**8.284**	**1.037**
Zr0.5	5.408	6.738	0.923	1.150	0.980	8.640			1.043
Zr1	5.405	6.768	0.923	1.156	0.985	8.661			1.046
Zr2	5.416	6.718	0.925	1.147	0.981	8.629			1.042
Zr3	5.429	6.698	0.927	1.144	0.983	8.622			1.041
Zr4	5.433	6.726	0.928	1.148	0.989	8.646			1.044
Zr4	**5.491**	**6.618**	**0.938**	**1.130**	**0.994**	**8.599**	**5.857**	**8.283**	**1.038**

For the present case, the tetragonal unit cell of the b.c.t. martensite is built on crystallographic axes parallel to those of austenite and, therefore, the stretch matrix is:

$$U = \begin{bmatrix} a/a_0 & 0 & 0 \\ 0 & a/a_0 & 0 \\ 0 & 0 & c/a_0 \end{bmatrix}$$

The eigenvalues are: $\lambda_1 = \lambda_2 = a/a_0$, $\lambda_3 = c/a_0$. Typically, the lattice parameters a and b ($a = b$) are shorter than a_0 and c is larger, in such a way that the second eigenvalue λ_2

is more deviated from 1 in comparison with the orthorhombic martensite, as can be observed in the Table 6.5. It should be noted that the austenite lattice parameters have been measured only for Hf4 and Zr4 alloys at the A_f temperature, since the other alloys have too high reverse transformation temperatures for the *in-situ* cooling/heating chamber of the XRD equipment. Hence, the lattice parameters of austenite in Hf4 and Zr4 alloys are used for all the other Ni-Mn-Ga-Hf and Ni-Mn-Ga-Zr alloys, respectively. As the compositional difference of the studied alloys is rather low, we can expect a very little variation of the a_0 parameter within the different alloys, which still gives validity to the present analysis. An overall tendency can be observed in Table 6.5 that the lattice parameters of martensite are gradually getting close to the lattice parameter of parent phase (and λ_2 gradually increases towards the value of 1) with the increase of the fourth element addition, which is concomitant with the reduction of tetragonality (c/a) and hysteresis of transformation. In the same way, det$\boldsymbol{U}$ = $\lambda_1 \cdot \lambda_2 \cdot \lambda_3$, which corresponds to the relative volume change between the martensite and austenite unit cells, also increases gradually to the value of 1 with the quaternary addition. For example, the parameters a, c evolve form 5.388, 6.754 Å for Hf0/Zr0 alloy to 5.435, 6.731 Å for Hf4 and 5.433, 6.726 Å for Zr4 alloys, while det$\boldsymbol{U}$ increases from 0.976 for Hf0/Zr0 alloy to 0.990 for Hf4 and 0.989 for Zr4, respectively. Additionally, thermal expansion should also be considered, since significant differences can be observed in the martensite lattice parameters of Hf4 and Zr4 alloys between room temperature and A_f. At the transformation temperature, the values of det$\boldsymbol{U}$ and λ_2 approach still further to 1. Therefore, the decrease of hysteresis with the increase of the quaternary element, observed experimentally, can be linked with an improvement of the lattice compatibility between the b.c.t. martensite and $L2_1$ austenite.

Furthermore, we can take into account that the real space group of the non-modulated martensite corresponds to a tetragonal $L1_0$ unit cell and for this cell the **a** and **b** axes are along the <011> directions of the b.c.t. cell, as shown in Fig. 1.1.11. Additionally, the modulated martensite (14M, 10M) can be formed by shuffling on (110) basal plane along the [1-10] direction. Therefore, it is worth to analyze the lattice compatibility between austenite and martensite in the <011> direction. For this purpose, the “diagonal lengths” of the martensite and austenite unit cells, calculated as $\sqrt{a^2+c^2}$ and $\sqrt{2}a_0$, have been also included in Table 6.5. The last column shows the ratio of the diagonal lengths, and we can observe that the values also approach to 1, being even closer to 1 than the second eigenvalue λ_2. Again, the effect of thermal expansion is visible on the diagonal directions, as the ratio obtained at the A_f temperature for Hf4 and Zr4 alloys approaches further to 1, compared to the values measured at room temperature.

The observation of the modulated 14M martensite in Hf4 and Zr4 alloys will be briefly discussed now. It was suggested by Khachaturyan *et al*. [218] that the modulated martensite observed in Ni-Al alloys can be considered as an “adaptive” phase of the basic tetragonal $L1_0$ martensite. In fact, the {110} planes are the twinning planes for cubic to tetragonal transition and the (5-2) stacking sequence of

the {110} planes in the modulated structure is considered as a microtwining mode of the basic tetragonal structure. In addition, it is also suggested that the adaptive phase is easier to form with small twin surface energy, big crystal-lattice mismatch and it is sensitive to applied stress. As was demonstrated in ref. [218], when the thickness of the twin lamellae is reduced to a few atomic planes, the symmetry of the basic martensitic unit cell must change from tetragonal to orthorhombic, to accomplish with the condition of undistorted habit plane with austenite. Good agreement between the theoretical lattice parameters of the adaptive phase and the experimental parameters of the modulated martensite of Ni-Al alloys was reported in ref. [218]. J. Pons *et al*. [64] verified the the agreement of the lattice parameters of 14M martensite in Ni-Mn-Ga alloys with the theoretical adaptive phase. Jiang Chengbao *et al*. [219] reported that the non-modulated martensite is more stable than 7-layered martensite due to lower free energy under the same composition $Ni_{50}Mn_{30}Ga_{20}$ with similar saturation magnetizations. Furthermore, the non-modulated martensite also shows higher thermal hysteresis and enthalpy change than 14M. In fact, Kaufmann *et al*. [220] considered that the 14M structure is not a thermodynamically stable phase, but an ultrafinely twinned metastable structure, though this is subject of controversy. In the case of the studied Ni-Mn-Ga-Hf/Zr alloys, the 14M phase has been observed in Hf4 and Zr4 alloys, which contain the network of connected second phase precipitates that restrict the growth of martensite in small domains. In this way, the “adaptive” nature of the 14M phase may favor the accommodation of martensite within the restricted domains, in coexistence with the basic non-modulated martensite. Additionally, the low hysteresis gives equal chance for both the non-modulated martensite and 14M martensite to exist.

The microstructure of Ni-Mn-Ga-Zr alloys, presented by SEM, optical microscopy and TEM in Figs. 6.1.4 to 6.1.9, includes two types of second phases, the f.c.c. precipitates and Zr carbides/oxides, based on XRD analysis (Fig. 6.1.3). The f.c.c. precipitates start to appear with Zr content over 1 at.% and become the major second phase for higher Zr addition. The precipitates in Ni-Mn-Ga-Zr alloys present the same diffraction patterns as those of Ni-Mn-Ga-Hf with very similar intensities and spacing of the diffracted spots, from which we can assume that they have the same crystal structure, discussed in the previous chapter. To avoid repeatability, only the “Ni-ordered” unit cell is presented here in Fig. 6.2.4 (a), where the mixture of Mn, Ga are occupying the pink atoms in a specific ratio while Ni and Zr atoms are represented in dark blue and gray, respectively. Based on this structure, it has been confirmed that the simulated electron diffraction patterns are in accordance with the experimental patterns under $[110]_P$ and $[211]_P$ zone axes given in Fig. 6.1.9, and so are the XRD patterns shown in Fig. 6.1.3. The simulated patterns are presented in the Apendix B. Considering the nominal composition of the Ni-ordered model, $Ni_{62.5}Mn_{17.5}Ga_{7.5}Hf/Zr_{12.5}$, it should be noted that the experimental composition measured by EDX (Table 6.3) shows a little deviation with a slightly lower content of Ni compensated by slightly higher contents of the other elements, which could arise

from both EDX uncertainties and/or real compositional change during precipitation process. The second structural possibility with totally disordered Ni, Mn and Ga atomic positions but fixed Zr atoms (like the one in Fig. 5.2.2 (b)), exhibits similar XRD and electron diffraction patterns, as shown in the Appendix B.

Fig. 6.2.4 (b) presents the same Ni-ordered model of the precipitates in Ni-Mn-Ga-Zr alloys, but under the "tetragonal" axes consistent with the I4/mmm space group with A6 face-centered tetragonal cell (No. 139). This structure has been fully introduced in chapter 5, together with the relationship between the "cubic" and "tetragonal" axes, as shown in Fig. 5.2.4. The atom positions can be found in Table 5.5 and 5.6. For the Ni-Mn-Ga-Zr alloys, the Hf (0 0 0) Wyckoff positions are just needed to be replaced by Zr atoms. It is also needed to be noted again that all the XRD peaks and electron diffraction patterns of the precipitates in this thesis have been indexed according to the "cubic" axes for easier comparison with the normal γ phase. The simulated XRD and electron diffraction patterns of Ni-ordered cells indexed under "cubic" and "tetragonal" axes can be found in the Appendix. They show basically identical patterns but just with different indices.

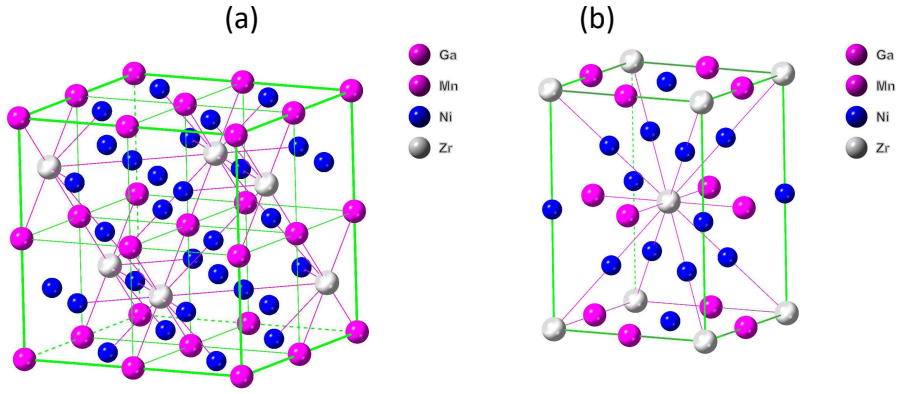

Fig. 6.2.4. Crystal structure of the precipitates in Ni-Mn-Ga-Zr alloys: (a) Ni-ordered cell under "cubic" axes, and (b) Ni-ordered cell under "tetragonal" axes. The pink atoms are randomly occupied by Mn and Ga in a certain occupation ratio based on EDX measurement, while dark blue and gray atoms are occupied by Ni and Zr atoms, respectively. Additional bonds of Zr-(Ni, Mn, and Ga) are marked in (a) and (b).

6.2.3 Thermomechanical and Mechanical Response

As commented above, the thermomechanical behaviour of Ni-Mn-Ga-Zr and Ni-Mn-Ga-Hf alloys are very similar to each other, and the discussion presented in section 5.2.3 of the previous chapter is valid for both quaternary additions. In this section, the role of the stored elastic strain energy will be discussed, which can be estimated from the slope of the hysteresis loop, where low elastic energy is coincident with a steep slope and vice versa [8]. For example, Some slope values of studied ternary and Ni-Mn-Ga-Hf/Zr alloys are presented in the Table 6.6 extracted from thermomechanical cycles under 100 MPa. Moreover, in some cases, the slope

of the reverse transformation can be steeper than the direct transformation, indicating the dissipation of the stored elastic strain energy, which cannot assist the reverse transformation [197]. For our studied alloys, it is clearly presented in Fig. 6.1.10 (Ni-Mn-Ga-Zr) and Fig. 5.1.14 (Ni-Mn-Ga-Hf) that the slopes of both direct and reverse transformations are almost parallel for applied stresses below a critical level, for which basically no dissipation of stored elastic strain energy occurs. The critical applied stress level is lower than 100 MPa for low quaternary content and increases with addition of Zr/Hf, *e.g.*, Zr3/Hf3 and Zr4/Hf4 still show the same slopes of direct and reverse transformations under the highest applied stress of 300 MPa. Moreover, for ternary alloys and quaternary alloys with little amount of Zr/Hf, the reverse transformation becomes more diffuse and exhibit an extended A_f temperature when the applied stress level is increased. This is due to the larger work output developed by these alloys during the reverse transformation, which demands an extra heating to overcome the applied external stress, resulting in the extended reverse transformation slope with wider hysteresis. In fact, if the applied over heating is not enough, the retained martensite may become a component of the observed irrecoverable strain.

Table 6.6. The hysteresis loop slopes of studied alloys extracted from thermomechanical cycles under 100 MPa.

Content / **Element**	0 at.%	0.5 at.%	1 at.%	2 at.%	3 at.%	4 at.%
Hf	-0.1	-0.07	-0.06	-0.03	-0.03	-0.03
Zr		-0.08	-0.05	-0.04	-0.04	-0.03

For the mechanical tests, neither Ni-Mn-Ga-Zr nor Ni-Mn-Ga-Hf alloys demonstrate obvious superelasticity effect with a clear reverse transformation plateau due to the limited stress applied on the matrix to induce the martensitic transformation, which is partially “shield” by the network of connected precipitates, seen in Fig. 6.1.12 and Fig. 5.1.15. As commented in previous chapter, only some weak sign of recoverable strain induced by transformation can be roughly seen but under high stress level accompanied with larger hysteresis. The Hf4 alloy is cracked under the maximum stress of 800 MPa while Zr4 survives up to almost 1000 MPa stress level. In comparison, Ni-Mn-Ga-Zr alloys demonstrate relatively wider hysteresis and bigger irrecoverable strain, which mainly comes from plastic deformation instead of stabilized martensite. Considering the relatively higher solubility of Hf atoms in the matrix, compared to Zr, it seems that the soluble quarternary atoms can enhance the strength of the matrix, leading to less generation of dislocations during transformation.

6.3 Summary of Ni-Mn-Ga-Zr Alloys

1. The martensitic transformation properties and the microstructure have been

studied in the high temperature Ni-Mn-Ga shape memory alloy system with increasing Zr addition up to 4 at.%. The quaternary addition causes the reduction of the martensitic transformation temperature as the result of declining *e*/*a* and *c*/*a* ratios. All the Ni-Mn-Ga-Zr (0 - 4 at.%) alloys studied present the MT above 430 K, which makes them still valid as HTSMAs.

2. The hysteresis of transformation shows a clear correlation with the tetragonality ratio (*c*/*a*) of the b.c.t. martensite and reaches very low values for elevated Zr content, *i.e.*, Zr4 presents 8 K from DSC measurement and 6 K from thermomechanical test under 300 MPa. The *in-situ* XRD analysis on Zr4 and Hf4 alloys shows that the determinant of the transformation stretch matrix ***U*** and its middle eigenvalue λ_2 approach both to 1 with the increase of Zr or Hf content, indicating the improvement of the crystallographic compatibility between $L2_1$ austenite and b.c.t. martensite, concomitant with the decrease of hysteresis.

3. All the alloys contain dispersions of Zr carbide and oxide inclusions. In addition, f.c.c. precipitates start to form for 1 at.% Zr addition and its volume fraction increases continuously with the increase of Zr addition. For 3 at.% and 4 at.% Zr content, networks of second phase big particles are formed that leave micrometric sized domains of transformable matrix, producing a significant grain refinement effect. The non-modulated b.c.t. martensite forms in all quaternary alloys and a small fraction of modulated 14M martensite has been also found in the Zr4 alloy. The diffraction patterns of the second phase precipitates indicate a f.c.c. structure with lattice parameter double than the normal γ phase observed in Ni-Mn-Ga alloys. Based on the compositional analysis by EDX, some structural models have been proposed for the second phase, using a double f.c.c. unit cell or a smaller A6 face-centered tetragonal unit cell corresponding to the I4/mmm space group.

4. The Zr3 alloy presents high thermal stability by DSC thermal cycling up to 20 cycles and prolonged ageing at 870 K. However, there is a little drop of enthalpy change (1 J/g) and increase of transformation temperature of about 2 K after ageing at 870 K due to a slight atomic diffusion of Zr towards the second phase particles. In comparison, for the Hf3 alloy the slight atomic diffusion of Hf goes in the opposite direction (from particles to the matrix). The different diffusive processes, after ageing, alter the composition and *e*/*a* ratio of the matrix to reach the equilibrium state and cause the variation of transformation temperatures. The different behavior is explained in terms of the relatively lower solubility of Zr in the transformable matrix (~0.7 at.%) with larger atomic radius, compared to Hf (~1 at.%) with relatively smaller atomic radius.

5. Ni-Mn-Ga-Zr alloys show a significant reduction of MTT, recoverable and irrecoverable strains and thermal hysteresis obtained from thermomechanical tests as a function of Zr addition under the same applied stress levels that is attributed to the formation of precipitates. During the mechanical tests, the growth of oriented

martensite plates is extremely restrained by the networks of precipitates, that shield the external applied stress. As a result, no obvious superelasticity behavior can be observed. Compared with Ni-Mn-Ga-Hf alloys, the Zr addition seems to produce a slightly lower resistance to plastic deformation due to the lower solubility inside the matrix.

6. Finally, a summary of the major shape memory properties of the NiMnGaZr4 and NiMnGaHf4 alloys in comparison with the ternary alloy is presented in the Table 6.7, in order to disclose the minor differences and similarities of both quaternary additions to Ni-Mn-Ga HTSMAs.

Table 6.7. Comparison of ternary alloy, NiMnGaZr4 and NiMnGaHf4.

SM properties \ **Alloys**		**Hf0/Zr0**	**NiMnGaZr4**		**NiMnGaHf4**	
		Abs.	Abs.	Δ	Abs.	Δ
Thermal parameters	M_p (K)	590	433	157	412	178
	A_p (K)	628	440	188	420	208
	Hysteresis (K)	38	8	30	8	30
	Enthalpy change (J/g)	14.3	10.4	3.9	9.3	5.0
4^{th} element content in martensite	X at.% (X = Hf, Zr)	/	0.7		1.0	
Tetragonality	c/a	1.254	1.238	0.016	1.238	0.016
f.c.c. precipitates	a' (Å)	/	6.84		6.81	
Mechanical parameters (300 MPa)	ε_{Total} (%)	2.77	0.57	2.20	0.63	2.14
	ε_{Irr} (%)	0.73	0.03	0.70	0.06	0.67

Chapter Ⅶ MAIN CONCLUSIONS AND FUTURE DIRECTIONS

The present work has systematically investigated the shape memory properties of Ni-rich Ni-Ti-Zr and Ni-Mn-Ga-X (X = Cu, Sn, Hf, Zr) HTSMA and the effect of thermal treatments when they were applied for specific purposes, *e.g.*, homogenization, induction of precipitates, study of the transformation stability, *etc*. Hereafter, some summary of the most important contributions of this Ph.D. thesis is presented, following the sequence of chapters in the manuscript.

Ni-rich Ni-Ti-Zr

1. Ageing at 770 K or 870 K for 3 h produces the best thermomechanical response in $Ni_{50.3}Ti_{29.7}Zr_{20}$ or $Ni_{50.3}Ti_{29.7}Hf_{20}$ alloys at around 400 K, as it is well-known from literature. The behaviour of $Ni_{50.3}Ti_{24.7}Zr_{25}$ polycrystalline alloy has been investigated here and, among other treatments explored, the former thermal treatments also show the best results, with an increase of the transformation temperatures by about 50 K. The thermomechanical behavior in compression shows ~0.8% and ~0.2% of recoverable and irrecoverable strains, respectively, under applied stresses in the range 400 - 600 MPa, with a significant hysteresis about 75 - 90 K. In addition, the $Ni_{50.3}Ti_{24.7}Zr_{25}$ alloy demonstrates an unclear superelasticity effect at temperatures over 550 K up to applied stress about 1600 MPa. This is a worse behavior compared to $Ni_{50.3}Ti_{29.7}Zr_{20}$ or $Ni_{50.3}Ti_{29.7}Hf_{20}$ alloys, the latter showing 3 times larger recoverable strain in compression and 1/3 of the hysteresis as compared to the $Ni_{50.3}Ti_{24.7}Zr_{25}$ alloy. Such a worsening of the functional properties has been ascribed to an excessive number of H-phase precipitates in the alloy with 25 at.% Zr induced by the increment in Zr.

2. The suppression of martensitic transformation has been found in $Ni_{50.9}Ti_{24.1}Zr_{25}$ SHT alloy and in $Ni_{50.3}Ti_{24.7}Zr_{25}$ and $Ni_{50.3}Ti_{29.7}Zr_{20}$ alloys after low temperature (520 K) prolonged ageing treatments. These alloys also demonstrate overall austenite structure (B2) observed by TEM/XRD along with diffuse scattering streaks in SADP at low temperature without further development into long range ordered martensite variants, as well as frequency dependent *IF* peak and *E* modulus minimum fitting the Vogel-Fulcher relationship observed by DMA. These results are indicative of the strain glass state containing B19'-like nanodomains. The strain glass is more easily induced in compositions with more Ni and Zr content. This supports the idea of the precursor H-phase (locally reordered Ti and Zr atoms concentrated to form the precursor nuclei of H phase) as origin of the SG state observed in these alloys.

3. The $Ni_{50.3}Ti_{29.7}Zr_{20}$ SHT alloy shows the typical superelasticity effect, with a normal evolution of the σ_{SIM} as a function of temperature. However, the same alloy in the strain glass state still presents 4% recoverable strain with much lower hysteresis, high strength above 1 GPa and nearly temperature independent quasilinear σ - ε curves. This is a remarkable behavior for use in applications that require a stable mechanical response at different temperatures.

4. The DMA and resonant ultrasonic techniques present a basically unchanged elastic modulus in a wide temperature range upon cooling, *i.e.*, "elinvar" effect, in the $Ni_{50.9}Ti_{24.1}Zr_{25}$ SHT alloy with SG transition, whereas the $Ni_{50.3}Ti_{24.7}Zr_{25}$ with not well-developed SG transition, and the $Ni_{50.3}Ti_{29.7}Zr_{20}$ SHT alloy with normal MT, show stronger temperature dependence of *E* modulus (softening) and absence of elinvar effect. The almost temperature independence of the *E* modulus in the alloys with SG has been attributed to the formation of martensitic-like nanodomains in a wide temperature range, which creates a limited and gradual softening of the *E* modulus that compensates the normal modulus hardening due to anharmonic atomic vibrations, resulting in a wide temperature range of stable *E* modulus.

Ni-Mn-Ga-Cu/Sn

1. $Ni_{50.3}Mn_{31.0}Ga_{17.7}Cu_{1.0}$ and $Ni_{50.5}Mn_{30.5}Ga_{18.0}Cu_{1.0}$ polycrystalline alloys (H3 and H4) slightly Ni rich and with low Cu content demonstrated high thermal stability upon ageing at 670 K and furnace cooling thermal treatments, and a complete absence of precipitation. The good compatibility between austenite and martensite unit cells demonstrated in this Ph.D. could be related to the low thermal hysteresis of these alloys. These results together with previous reports on compositions with higher Cu content seem to prove the impossibility to induce nanometric precipitates in the Ni-Mn-Ga-Cu system, which were expected to improve the mechanical properties of these alloys.

2. Thermomechanical tests in compression were applied to the as-treated Ni-Mn-Ga-Cu H3 and H4 alloys. The relatively large irrecoverable strains generated in both alloys above 100 MPa suggest this stress as the best compromise between work output and irrecoverable strain for potential application as thermal actuators.

3. Doping Ni-Mn-Ga with Sn strongly reduces the transformation temperatures (from 590 K to 314 K with 4 at.% addition of Sn) and increases brittleness. The high brittleness of the material and the sharp decrease in the transformation temperatures are strong reasons to rule out the Ni-Mn-Ga-Sn system as HTSMA.

Ni-Mn-Ga-Hf/Zr

1. The martensitic transformation properties and the microstructure as a function of the composition were studied in $Ni_{53}Mn_{31.1Z}Ga_{17.7Z}Hf_X/Zr_X$ alloys, with Z = (47-X)/48.8, and X = 0, 0.5, 1, 2, 3, 4. These alloys were designed to obtain high transformation temperatures and better ductility than the ternary alloy by producing a dual phase structure.

2. Transformation temperatures drop with the increase of Hf/Zr content as the result of decreasing *e*/*a* and *c*/*a* ratios. However, all the alloys present the MT above 410 K and can still be categorized as HTSMAs. The transformation hysteresis also decreases and exhibits a clear correlation with the *c*/*a* of the b.c.t. martensite. *In-situ* XRD analysis on Zr4 and Hf4 alloys shows that both the determinant of the transformation stretch matrix ***U*** and its middle eigenvalue λ_2 approach to 1 with the increase in Zr/Hf content, indicating the improvement of the crystallographic compatibility between $L2_1$ austenite and b.c.t. martensite, concomitant with the decrease in hysteresis.

3. The dual phase microstructure is observed in alloys with Hf/Zr over 1 at.%, and the volume fraction of precipitates continuously increases with the content of the fourth element. The martensite phase shows the non-modulated body centered tetragonal structure in all the studied alloys, although a small fraction of 14M modulated martensite is also identified in the alloys with 4 at.% Hf/Zr.

4. The second phase precipitates exhibit a f.c.c. structure with lattice parameter double than the normal γ or γ’ phases observed in most of the Ni-Mn-Ga-X and other ferromagnetic shape memory alloys. Two structural models, with ordered or disordered positions of the Ni atoms, were proposed for the second phase, using a double f.c.c. unit cell with 32 atoms. However, the double f.c.c. cell does not correspond to a space group of the cubic system and the correct crystallographic description of the new phase has been found to belong to the tetragonal system, space group I4/mmm (No. 139), and A6 face-centered tetragonal type of unit cell.

5. Ni-Mn-Ga-Hf/Zr alloys show a reduction of transformation temperatures, thermal hysteresis and recoverable and irrecoverable strains from thermomechanical tests as a function of Hf/Zr addition due to the formation of non-transforming precipitates. For 3 and 4 at.% addition, there is a very low hysteresis (7 - 8 K) and practically no irrecoverable strain under 200 - 300 MPa applied stress, but the recoverable strain is reduced to less than 1% due to the large amount of precipitated phase. Furthermore, the studied quaternary alloys show basically no or little superelasticity effect, which are associated to the restrained growth of oriented martensite plates during the mechanical tests as a consequence of the networks of precipitates.

6. Comparing Ni-Mn-Ga-Hf and Ni-Mn-Ga-Zr alloys with the same amount of the fourth element, some similarities and differences can be underlined. Zr containing alloys show more or less similar hysteresis and lattice parameters, but relatively higher transformation temperatures as compared to Hf containing alloys. Moreover,

Ni-Mn-Ga-Zr alloys exhibit lower recoverable and irrecoverable strains. These differences are mainly correlated to the differences in solubility of the fourth element in the matrix.

Future work

Al least two topics directly linked with the results shown in this Ph.D. have an obvious line to be further studied. From the one hand, the strong reduction of transformation hysteresis caused by the Hf/Zr addition to Ni-Mn-Ga HTSMAs, related to the better compatibility between austenite and martensite lattices, is a very good result. However, the dual phase structure induced in these alloys contains too big and incoherent particles of the second phase that strongly reduce the transformation strain and do not enhance the mechanical properties of the matrix. Therefore, alternative methods to produce the material, for instance fast solidification methods as melt-spinning or splat quenching, are worth to investigate. The objective is to obtain lower fraction of second phase and much smaller precipitates with positive influence on the strengthening of the matrix. On the other hand, the existence of the SG state in HTSMA was firstly demonstrated in this work together with the confirmation of other unique properties, as the elinvar effect and temperature independent mechanical response with high recoverable strain. However, after prolonged ageing, the $Ni_{50.3}Ti_{24.7}Zr_{25}$ alloy still shows an intermediate state with suppressed martensitic transformation in the DSC, but not yet well established strain glass state. Thus, the boundary between these two stages is not clearly revealed yet and constitutes an interesting fundamental subject to be further studied in the future, as well as deeper microstructural characterization with the High Resolution TEM recently installed in the UIB that could shed some light into this interesting topic.

REFERENCES

[1] Kurdjumov GV, Izv. Akad. Nauk SSSR Otd. Him. Nauk 1936;2:271.

[2] Roitburd AL, Kurdjumov GV. The nature of martensitic transformations. Mater Sci Eng 1979;39:141.

[3] Wechsler MS. On the theory of the formation of martensite. Trans Aime 1953;197:1503.

[4] Lieberman DS, Wechsler MS, Read TA. Cubic to orthorhombic diffusionless phase change-experimental and theoretical studies of AuCd. J Appl Phys 1955;26:473.

[5] Bowles JS, Mackenzie JK. The crystallography of martensite transformations I. Acta Metall 1954;2:129.

[6] Bowles JS, Mackenzie JK. The crystallography of martensite transformations III. Face-centred cubic to body-centred tetragonal transformations. Acta Metall 1954;2:224.

[7] Otsuka K, Wayman CM. Shape memory materials. Cambridge university press 1999.

[8] Hamilton RF, Sehitoglu H, Chumlyakov YI, Maier HJ. Stress dependence of the hysteresis in single crystal NiTi alloys. Acta Mater 2004;52:3383.

[9] Mula DS. Athermal and isothermal characteristics in difusionless martensitic transformations. Ph.D. Thesis Universitat de les Illes Balears 2014.

[10] Massalski TB. Comments concerning some features of phase diagrams and phase transformations. Mater Trans 2010;51:583.

[11] Lagoudas DC (editor). Shape memory alloys: modeling and engineering applications. Springer 2008.

[12] Liu Y, Liu Y, Van Humbeeck J. Two-way shape memory effect developed by martensite deformation in NiTi. Acta Mater 1998;47:199.

[13] Ma J, Karaman I, Noebe RD. High temperature shape memory alloys. Int Mater Rev 2010;55:257.

[14] Jani JM, Leary M, Subic A, Gibson MA. A review of shape memory alloy research, applications and opportunities. Mater Design 2014;56:1078.

[15] DesRoches R, McCormick J, Delemont M. Cyclic properties of superelastic shape memory alloy wires and bars. J Struct Eng 2004;130:38.

[16] Sarkar S, Ren X, Otsuka K. Evidence for strain glass in the ferroelastic-martensitic system $Ti_{50-x}Ni_{50+x}$. Phys Rev Lett 2005;95:205702.

[17] Wang Y, Ren X, Otsuka K, Saxena A. Temperature-stress phase diagram of strain glass $Ti_{48.5}Ni_{51.5}$. Acta Mater 2008;56:2885.

[18] Zhang Z, Wang Y, Wang D, Zhou Y, Otsuka K, Ren X. Phase diagram of $Ti_{50-x}Ni_{50+x}$: Crossover from martensite to strain glass. Phys Rev B 2010;81:224102.

[19] Wang D, Wang Y, Zhang Z, Ren X. Modeling abnormal strain states in ferroelastic systems: the role of point defects. Phys Rev Lett 2010;105:205702.

[20] Zhou Y, Xue D, Ding X, Wang Y, Zhang J, Zhang Z, Wang D, Otsuka K, Sun J, Ren X. Strain glass in doped $Ti_{50}(Ni_{50-x}D_x)$(D= Co, Cr, Mn) alloys: Implication for the generality of strain glass in defect-containing ferroelastic systems. Acta Mater 2010;58:5433.

[21] Wang D, Zhang Z, Zhang J, Zhou Y, Wang Y, Ding X, Wang Y, Ren X. Strain glass in Fe-doped Ti-Ni. Acta Mater 2010;58:6206.

[22] Ramachandran B, Chang P, Kuo Y, Chien C, Wu SK. Characteristics of martensitic and strain-glass transitions of the Fe-substituted TiNi shape memory alloys probed by transport and thermal measurements. Sci Rep 2017;7:1.

[23] Zhou Y, Xue D, Ding X, Otsuka K, Sun J, Ren X. High temperature strain glass in $Ti_{50}(Pd_{50-x}Cr_x)$ alloy and the associated shape memory effect and superelasticity. Appl Phys Lett 2009;95:151906.

[24] Ren S, Xue D, Ji Y, Liu X, Yang S, Ren X. Low-field-triggered large magnetostriction in iron-palladium strain glass alloys. Phys Rev Lett 2017;119:125701.

[25] Ma H, Yang J, Lu F, Qin F, Xiao W, Zhao X. A FeNiMnC alloy with strain glass transition. Prog Nat Sci-Mater 2018;28:74.

[26] Wang Y, Huang C, Gao J, Yang S, Ding X, Song X, Ren X. Evidence for ferromagnetic strain glass in Ni-Co-Mn-Ga Heusler alloy system. Appl Phys Lett 2012;101:101913.

[27] Wang DP, Chen X, Nie ZH, Li N, Wang ZL, Ren Y, Wang YD. Transition in superelasticity for $Ni_{55-x}Co_xFe_{18}Ga_{27}$ alloys due to strain glass transition. EPL 2012;98:46004.

[28] Wang Y, Huang C, Wu H, Gao J, Yang S, Wang D, Ding X, Song X, Ren X. Spontaneous strain glass to martensite transition in ferromagnetic Ni-Co-Mn-Ga strain glass. Appl Phys Lett 2013;102:141909.

[29] Wu Z. Strain glass behaviour of Ni-Co-Mn-Sn ferromagnetic shape memory alloys. Phys Status Solidi (RRL) 2015;9:317.

[30] Nii Y, Arima T, Kim HY, Miyazaki S. Effect of randomness on ferroelastic transitions: Disorder-induced hysteresis loop rounding in Ti-Nb-O martensitic alloy. Phys Rev B 2010;82:214104.

[31] Wang Y, Gao J, Wu H, Yang S, Ding X, Wang D, Ren X, Wang Y, Song X, Gao J. Strain glass transition in a multifunctional β-type Ti alloy. Sci Rep 2014;4:1.

[32] Zhang J, Xue D, Cai X, Ding X, Ren X, Sun J. Dislocation induced strain glass in $Ti_{50}Ni_{45}Fe_5$ alloy. Acta Mater 2016;120:130.

[33] Liang Q, Wang D, Zhang J, Ji Y, Ding X, Wang Y, Ren X, Wang Y. Novel B19’ strain glass with large recoverable strain. Phys Rev Mater 2017;1:33608.

[34] Ji Y, Ding X, Lookman T, Otsuka K, Ren X. Heterogeneities and strain glass behavior: role of nanoscale precipitates in low-temperature-aged $Ti_{48.7}Ni_{51.3}$ alloys. Phys Rev B 2013;87:104110.

[35] Zhou Z, Cui J, Ren X. Strain glass state as the boundary of two phase transitions. Sci Rep 2015;5:1.

[36] Chien C, Tsao CS, Wu SK, Chang CY, Chang PC, Kuo YK. Characteristics of the strain glass transition in as-quenched and 250 °C early-aged $Ti_{48.7}Ni_{51.3}$ shape memory alloy. Acta Mater 2016;120:159.

[37] Monroe JA, Raymond JE, Xu X, Nagasako M, Kainuma R, Chumlyakov YI, Arroyave R, Karaman I. Multiple ferroic glasses via ordering. Acta Mater 2015;101:107.

[38] Kustov S, Salas D, Cesari E, Santamarta R, Mari D, Van Humbeeck J. Structural anelasticity, elasticity and broken ergodicity in Ni-Ti shape memory alloys. Acta Mater 2014;73:275.

[39] Zhang J, Wang Y, Ding X, Zhang Z, Zhou Y, Ren X, Wang D, Ji Y, Song M, Otsuka K, Sun J. Spontaneous strain glass to martensite transition in a $Ti_{50}Ni_{44.5}Fe_{5.5}$ strain glass. Phys Rev B 2011;84:214201.

[40] Hou S, Wang Y, Zhang J, Wang D, Ren S, Ren X. Evidence for crossover martensite in $Ti_{50}Ni_{45}Fe_5$: An intermediate state between normal martensite and strain glass. EPL 2012;100:58001.

[41] Lu J, Martinez GT, Aert SV, Schryvers D. Lattice deformations in quasi-dynamic strain glass visualised and quantified by aberration corrected electron microscopy. Phys Status Solidi B 2014;251:2034.

[42] Wang Y, Ren X, Otsuka K, Saxena A. Evidence for broken ergodicity in strain glass. Phys Rev B 2007;76:132201.

[43] Ren X, Wang Y, Zhou Y, Zhang Z, Wang D, Fan G, Otsuka K, Suzuki T, Ji Y, Zhang J, Tian Y, Hou S, Ding X. Strain glass in ferroelastic systems: Premartensitic tweed versus strain glass. Philos Mag 2010;90:141.

[44] Wang Y, Ren X, Otsuka K. Shape memory effect and superelasticity in a strain glass alloy. Phys Rev Lett 2006;97:225703.

[45] Wang Y, Song X, Ding X, Yang S, Zhang J, Ren X, Otsuka K. Stress changed damping and associated transforming behavior in a $Ti_{48.5}Ni_{51.5}$ strain glass. Appl Phys Lett 2011;99:051905.

[46] Tang Z, Wang Y, Liao X, Wang D, Yang S, Song X. Stress dependent transforming behaviors and associated functional properties of a nano-precipitates induced strain glass alloy. J Alloy Compd 2015;622:622.

[47] Hane KF, Shield TW. Microstructure in the cubic to monoclinic transition in titanium–nickel shape memory alloys. Acta Mater 1999;47:2603.

[48] Kudoh Y, Tokonami M, Miyazaki S, Otsuka K. Crystal structure of the martensite in Ti-49.2 at.% Ni alloy analyzed by the single crystal X-ray diffraction method. Acta Metall 1985;33:2049.

[49] Evirgen A, Karaman I, Santamarta R, Pons J, Hayrettin C, Noebe RD. Relationship between crystallographic compatibility and thermal hysteresis in Ni-rich NiTiHf and NiTiZr high temperature shape memory alloys. Acta Mater 2016;121:374.

[50] Saburi T, Watanabe Y, Nenno S. Morphological characteristics of the orthorhombic martensite in a shape memory Ti–Ni–Cu alloy. ISIJ Int 1989;29:405.

[51] Ren X, Otsuka K. The role of softening in elastic constant c {sub 44} in martensitic transformation. Script Mater 1998;38:1669.

[52] Miyazaki S, Otsuka K. Deformation and transition behavior associated with the R-phase in Ti-Ni alloys. Metall Trans A 1986;17:53.

[53] Otsuka K, Ren X. Physical metallurgy of Ti–Ni-based shape memory alloys. Prog Mater Sci 2005;50:511.

[54] Tadaki T, Nakata Y, Shimizu K, Otsuka K. Crystal structure, composition and morphology of a precipitate in an aged Ti-51 at.% Ni shape memory alloy. Trans Japan Inst Met 1986;27:731.

[55] Han XD, Wang R, Zhang Z, Yang DZ. A new precipitate phase in a TiNiHf high temperature shape memory alloy. Acta Mater 1998;46:273.

[56] Yang F, Coughlin DR, Phillips PJ, Yang L, Devaraj A, Kovarik L, Noebe RD, Mills MJ. Structure analysis of a precipitate phase in an Ni-rich high-temperature NiTiHf shape memory alloy. Acta Mater 2013;61:3335.

[57] Santamarta R, Arróyave R, Pons J, Evirgen A, Karaman I, Karaca HE, Noebe RD. TEM study of structural and microstructural characteristics of a precipitate phase in Ni-rich Ni-Ti-Hf and Ni-Ti-Zr shape memory alloys. Acta Mater 2013,61:6191.

[58] Santamarta R, Muntasell J, Font J, Cesari E. Thermal stability and microstructure of Ni-Mn-Ga-Cu high temperature shape memory alloys. J Alloy Compd 2015;648:903.

[59] Sarkar SK, Sarita, Babu PD, Biswas A, Siruguri V, Krishnan M. Giant magnetocaloric effect from reverse martensitic transformation in Ni-Mn-Ga-Cu ferromagnetic shape memory alloys. J Alloy Compd 2016;670:281.

[60] Singh S, Roy RK, Ghosh M, Manik NB, Mitra A, Panda AK. Modification in martensite morphology and magneto-strain through rapid solidification and heat treatment of NiMnGaAl alloy. J Magn Magn Mater 2013;343:169.

[61] Xin Y, Zhou Y. Martensitic transformation and mechanical properties of NiMnGaV high-temperature shape memory alloys. Intermetallics 2016;73:50.

[62] Ma YQ, Lai SL, Yang SY, Luo Y, Wang CP, Liu XJ. $Ni_{56}Mn_{25-x}Cr_xGa_{19}$ (x= 0, 2, 4, 6) high temperature shape memory alloys. Trans Nonferrous Met Soc China 2011;21:96.

[63] Chen XQ, Lu X, Qin ZX. Martensitic transformation and microstructure of polycrystalline Ni-Mn-Ga and C-doped Ni-Mn-Ga Heusler alloys. Mater Sci Tech 2009;25:829.

[64] Pons J, Chernenko VA, Santamarta R, Cesari E. Crystal structure of martensitic phases in Ni-Mn-Ga shape memory alloys. Acta Mater 2000;48:3027.

[65] Tadaki T, Tokoro M, Shimizu K. Thermoelastic nature and crystal structure of the Cu-Zn martensite related to the shape memory. Trans Japan Inst Met 1975;16:285.

[66] Morito S, Otsuka K. Electron microscopy of new martensites with long period stacking order structures in $Ni_{50}Al_xMn_{50-x}$ alloys Ⅰ. Structures and morphologies. Mater Sci Eng A 1996;208:47.

[67] Martynov VV, Kokorin VV. The crystal structure of thermally-and stress-induced martensites in Ni2MnGa single crystals. J Phys Ⅲ 1992;2:739.

[68] Pons J, Santamarta R, Chernenko VA, Cesari E. Long-period martensitic structures of Ni-Mn-Ga alloys studied by high-resolution transmission electron microscopy. J Appl Phys 2005;97:083516.

[69] Xin Y, Li Y. Microstructure, mechanical and shape memory properties of polycrystalline Ni-Mn-Ga high temperature shape memory alloys. Mater Sci Eng A 2016;649:254.

[70] Cesari E, Font J, Muntasell J, Ochin P, Pons J, Santamarta R. Thermal stability of high-temperature Ni-Mn-Ga alloys. Scripta Mater 2008;58:259.

[71] Santamarta R, Cesari E, Muntasell J, Font J, Pons J, Ochin P. Thermal and microstructural evolution under ageing of several high-temperature Ni-Mn-Ga alloys. Intermetallics 2010;18:977.

[72] Ma Y, Xu L, Li Y, Jiang C, Xu H, Lee YK. Martensitic transformation, ductility, and shape-memory effect of polycrystalline $Ni_{56}Mn_{25-x}Fe_xGa_{19}$ alloys. Z Metallkd 2005;96:843.

[73] Hartl DJ, Lagoudas DC. Aerospace applications of shape memory alloys. J Aerospace Eng 2007;221:535.

[74] Epps JJ, Chopra I. In-flight tracking of helicopter rotor blades using shape memory alloy actuators. Smart Mater Struct 2001;10:104.

[75] Rey T, Le Cam JB, Chagnon G, Favier D, Rebouah M, Razan F, Robin E, Didier P, Heller L, Faure S, Janouchova K. An original architectured NiTi silicone rubber structure for biomedical applications. Mater Sci Eng C;2014,45:184.

[76] Oehler SD, Hartl DJ, Lopez R, Malak RJ, Lagoudas DC. Design optimization and uncertainty analysis of SMA morphing structures. Smart Mater Struct 2012;21:094016.

[77] Benafan O, Noebe RD, Halsmer TJ. Static rock splitters based on high temperature shape memory alloys for planetary explorations. Acta Astronaut 2016;118:137.

[78] Kirsch SM, Welsch F, Ehl L, Michaelis N, Motzki P, Schütze A, Seelecke S. Continuous Operating Elastocaloric Heating and Cooling Device: Air Flow Investigation and Experimental Parameter Study. Smart Mater 2019;59131:V001T04A018.

[79] Chatterjee S, Giri S, De SK, Majumdar S. Giant magneto-caloric effect near room temperature in Ni-Mn-Sn-Ga alloys. J Alloy Compd 2010;503:273.

[80] Karhu M, Lindroos T. Long-term behaviour of binary Ti-49.7 Ni (at.%) SMA actuators-the fatigue lives and evolution of strains on thermal cycling. Smart Mater Struct 2010;19:115019.

[81] Patoor E, Lagoudas DC, Entchev PB, Brinson LC, Gao X. Shape memory alloys, Part Ⅰ: General properties and modeling of single crystals. Mech Mater 2006;38:391.

[82] Otsuka K, Ren X. Mechanism of martensite aging effects and new aspects. Mater Sci Eng A 2001;312:207.

[83] Chu CL, Wu SK, Yen YC. Oxidation behavior of equiatomic TiNi alloy in high temperature air environment. Mater Sci Eng A 1996;216:193.

[84] Wu Z, Mahmud A, Zhang J, Liu Y, Yang H. Surface oxidation of NiTi during thermal exposure in flowing argon environment. Mater Design 2018;140:123.

[85] Bhattacharya K, Kohn RV. Symmetry, texture and the recoverable strain of shape-memory polycrystals. Acta Mater 1996;44:529.

[86] Shimizu S, Xu Y, Okunishi E, Tanaka S, Otsuka K, Mitose K. Improvement of shape memory characteristics by precipitation-hardening of Ti-Pd-Ni alloys. Mater Lett 1998;34:23.

[87] Kockar B, Atli KC, Ma J, Haouaoui M, Karaman I, Nagasako M, Kainuma R. Role of severe plastic deformation on the cyclic reversibility of a $Ti_{50.3}Ni_{33.7}Pd_{16}$ high temperature shape memory alloy. Acta Mater 2010;58:6411.

[88] Atli KC, Karaman I, Noebe RD. Work output of the two-way shape memory effect in $Ti_{50.5}Ni_{24.5}Pd_{25}$ high-temperature shape memory alloy. Scripta Mater 2011;65:903.

[89] Ramaiah KV, Saikrishna CN, Bhaumik SK. $Ni_{24.7}Ti_{50.3}Pd_{25.0}$ high temperature shape memory alloy with narrow thermal hysteresis and high thermal stability. Mater Design 2014;56:78.

[90] Sasaki TT, Hornbuckle BC, Noebe RD, Bigelow GS, Weaver ML, Thompson GB. Effect of aging on microstructure and shape memory properties of a Ni-48Ti-25Pd (At. Pct) alloy. Metall Mater Trans A 2013;44:1388.

[91] Benafan O, Garg A, Noebe RD, Bigelow GS, Padula II SA, Gaydosh DJ, Vaidyanathan R, Clausen B, Vogel SC. Thermomechanical behavior and microstructural evolution of a Ni(Pd)-rich $Ni_{24.3}Ti_{49.7}Pd_{26}$ high temperature shape memory alloy. J Alloy Compd 2015;643:275.

[92] Atli KC, Karaman I, Noebe RD. Influence of tantalum additions on the microstructure and shape memory response of $Ti_{50.5}Ni_{24.5}Pd_{25}$ high-temperature shape memory alloy. Mater Sci Eng A 2014;613:250.

[93] Ramaiah KV, Saikrishna CN, Bhagyaraj J, Gouthama, Bhaumik SK. Influence of Sc addition on microstructure and transformation behaviour of $Ni_{24.7}Ti_{50.3}Pd_{25.0}$ high temperature shape memory alloy. Intermetallics 2013;40:10.

[94] Ramaiah KV, Saikrishna CN, Bhaumik SK. Microstructure and transformation behavior of $Ni_{24.7}Ti_{50.3}Pd_{25}$ high temperature shape-memory alloy with Sc micro-addition. Mater Charact 2015;106:36.

[95] Kumar PK, Desai U, Monroe JA, Lagoudas DC, Karaman I, Bigelow G, Noebe RD. Experimental investigation of simultaneous creep, plasticity and transformation of $Ti_{50.5}Pd_{30}Ni_{19.5}$ high temperature shape memory alloy during cyclic actuation. Mater

Sci Eng A 2011;530:117.

[96] Rios O, Noebe R, Biles T, Garg A, Palczer A, Scheiman D, Seifert HJ, Kaufman M. Characterization of ternary NiTiPt high-temperature shape memory alloys. Smart Mater Struct 2005;5761:376.

[97] Lin B, Gall K, Maier HJ, Waldron R. Structure and thermomechanical behavior of NiTiPt shape memory alloy wires. Acta Biomater 2009;5:257.

[98] Yang F, Noebe RD, Mills MJ. Precipitates in a near-equiatomic (Ni+Pt)-rich TiNiPt alloy. Scripta Mater 2013;69:713.

[99] Noebe R, Draper S, Gaydosh D, Garg A, Lerch B, Penney N, Bigelow G, Padula S, Brown J. Effect of thermomechanical processing on the microstructure, properties, and work behavior of a $Ti_{50.5}Ni_{29.5}Pt_{20}$ high-temperature shape memory alloy. Proc. Int. Conf. on Shape Memory and Superelastic Technologies SMST-2006, ASM International 2008, p. 409.

[100] O'Donoghue L, Gandhi AA, Butler J, Redington W, Tiernan P, McGloughlin T, Carlson JC, Lavelle S, Tofail SAM. X-ray and microstructural investigation of NiTiPt alloys homogenised at intermediate to high temperatures. Nucl Instrum Methods Phys Res Sect B 2010;268:287.

[101] Casalena L, Bigelow GS, Gao Y, Benafan O, Noebe RD, Wang Y, Mills MJ. Mechanical behavior and microstructural analysis of NiTi-40Au shape memory alloys exhibiting work output above 400 °C. Intermetallics 2017;86:33.

[102] Firstov GS, Van Humbeeck J, Koval YN. High-temperature shape memory alloys: some recent developments. Mater Sci Eng A 2004;378:2.

[103] Wua SK, Hsieh SF. Martensitic transformation of a Ti-rich $Ti_{40.5}Ni_{49.5}Zr_{10}$ shape memory alloy. J Alloy Compd 2000;297:294.

[104] Meng XL, Zheng YF, Wang Z, Zhao LC. Effect of aging on the phase transformation and mechanical behavior of $Ti_{36}Ni_{49}Hf_{15}$ high temperature shape memory alloy. Scripta Mater 2000;42:341.

[105] Kim HY, Mizutani M, Miyazaki S. Crystallization process and shape memory properties of Ti-Ni-Zr thin films. Acta Mater 2009;57:1920.

[106] Yi X, Sun K, Gao W, Meng X, Cai W, Zhao L. Microstructure design of the

excellent shape recovery properties in (Ti, Hf)$_2$Ni/Ti-Ni-Hf high temperature shape memory alloy composite. J Alloy Compd 2017;729:758.

[107] Suresh KS, Kim D, Bhaumik SK, Suwas S. Evolution of microstructure and texture in $Ni_{49.4}Ti_{38.6}Hf_{12}$ shape memory alloy during hot rolling. Intermetallics 2013;42:1.

[108] Yi X, Wen G, Sun K, Gao W, Wang H, Sun B, Meng X, Cai W, Zhao L. Fabrication, characterization and potential application of larger bulk Ti-Ni-Hf high temperature shape memory alloy composite reinforced by hybrid particles. J Alloy Compd 2018;764:347.

[109] Canadinc D, Trehern W, Ma J, Karaman I, Sun F, Chaudhry Z. Ultra-high temperature multi-component shape memory alloys. Scripta Mater 2019;158:83.

[110] Prasad RVS, Park CH, Kim SW, Hong JK, Yeom JT. Microstructure and phase transformation behavior of a new high temperature NiTiHf-Ta shape memory alloy with excellent formability. J Alloy Compd 2017;697:55.

[111] Yi X, Gao W, Meng X, Gao Z, Cai W, Zhao L. Martensitic transformation behaviors and mechanical properties of $(Ti_{36}Ni_{49}Hf_{15})_{100-x}Y_x$ high temperature shape memory alloys. J Alloy Compd 2017;705:98.

[112] Karaca HE, Acar E, Ded GS, Saghaian SM, Basaran B, Tobe H, Kok M, Maier HJ, Noebe RD, Chumlyakov YI. Microstructure and transformation related behaviors of a $Ni_{45.3}Ti_{29.7}Hf_{20}Cu_5$ high temperature shape memory alloy. Mater Sci Eng A 2015;627:82.

[113] Sandu AM, Tsuchiya K, Yamamoto S, Todaka Y, Umemoto M. Influence of isothermal ageing on mechanical behaviour in Ni-rich Ti-Zr-Ni shape memory alloy. Scripta Mater 2006;55:1079.

[114] Sandu AM, Tsuchiya K, Tabuchi M, Yamamoto S, Todaka Y, Umemoto M. Microstructural evolution during isothermal aging in Ni-rich Ti-Zr-Ni shape memory alloys. Mater Trans 2007;48:432.

[115] Meng XL, Cai W, Chen F, Zhao LC. Effect of aging on martensitic transformation and microstructure in Ni-rich TiNiHf shape memory alloy. Scripta Mater 2006;54:1599.

[116] Meng XL, Cai W, Fu YD, Li QF, Zhang JX, Zhao LC. Shape-memory behaviors in an

aged Ni-rich TiNiHf high temperature shape-memory alloy. Intermetallics 2008;16:698.

[117] Moshref-Javadi M, Seyedein SH, Salehi MT, Aboutalebi MR. Age-induced multi-stage transformation in a Ni-rich NiTiHf alloy. Acta Mater 2013;61:2583.

[118] Bigelow GS, Garg A, Padula II SA, Gaydosh DJ, Noebe RD. Load-biased shape-memory and superelastic properties of a precipitation strengthened high-temperature $Ni_{50.3}Ti_{29.7}Hf_{20}$ alloy. Scripta Mater 2011;64:725.

[119] Coughlin DR, Phillips PJ, Bigelow GS, Garg A, Noebe RD, Mills MJ. Characterization of the microstructure and mechanical properties of a 50.3Ni-29.7Ti-20Hf shape memory alloy. Scripta Mater 2012;67:112.

[120] Benafan O, Noebe RD, Padula II SA, Vaidyanathan R. Microstructural response during isothermal and isobaric loading of a precipitation-strengthened Ni-29.7Ti-20Hf high-temperature shape memory alloy. Metall Mater Trans A 2012;43:4539.

[121] Evirgen A, Karaman I, Noebe RD, Santamarta R, Pons J. Effect of precipitation on the microstructure and the shape memory response of the $Ni_{50.3}Ti_{29.7}Zr_{20}$ high temperature shape memory alloy. Scripta Mater 2013;69:354.

[122] Evirgen A, Basner F, Karaman I, Noebe RD, Pons J, Santamarta R. Effect of aging on the martensitic transformation characteristics of a Ni-rich NiTiHf high temperature shape memory alloy. Funct Mater Lett 2012;5:1250038.

[123] Evirgen A, Karaman I, Santamarta R, Pons J, Noebe RD. Microstructural characterization and shape memory characteristics of the $Ni_{50.3}Ti_{34.7}Hf_{15}$ shape memory alloy. Acta Mater 2015;83:48.

[124] Karaca HE, Saghaian SM, Ded G, Tobe H, Basaran B, Maier HJ, Noebe RD, Chumlyakov YI. Effects of nanoprecipitation on the shape memory and material properties of an Ni-rich NiTiHf high temperature shape memory alloy. Acta Mater 2013;61:7422.

[125] Benafan O, Garg A, Noebe RD, Bigelow GS, Padula II SA, Gaydosh DJ, Schell N, Mabe JH, Vaidyanathan R. Mechanical and functional behavior of a Ni-rich $Ni_{50.3}Ti_{29.7}Hf_{20}$ high temperature shape memory alloy. Intermetallics 2014;50:94.

[126] Prasher M, Sen D. Influence of aging on phase transformation and microstructure of $Ni_{50.3}Ti_{29.7}Hf_{20}$ high temperature shape memory alloy. J Alloy Compd 2014;615:469.

[127] Hayrettin C, Karakoc O, Karaman I, Mabe JH, Santamarta R, Pons J. Two way shape memory effect in NiTiHf high temperature shape memory alloy tubes. Acta Mater 2019;163:1.

[128] Saghaian SM, Karaca HE, Tobe H, Souri M, Noebe R, Chumlyakov YI. Effects of aging on the shape memory behavior of Ni-rich $Ni_{50.3}Ti_{29.7}Hf_{20}$ single crystals. Acta Mater 2015;87:128.

[129] Karakoc O, Hayrettin C, Bass M, Wang SJ, Canadinc D, Mabe JH, Lagoudas DC, Karaman I. Effects of upper cycle temperature on the actuation fatigue response of NiTiHf high temperature shape memory alloys. Acta Mater 2017;138:185.

[130] Karakoc O, Hayrettin C, Evirgen A, Santamarta R, Canadinc D, Wheeler RW, Wang SJ, Lagoudas DC, Karaman I. Role of microstructure on the actuation fatigue performance of Ni-Rich NiTiHf high temperature shape memory alloys. Acta Mater 2019;175:107.

[131] Prasher M, Sen D, Bahadur J, Tewari R, Krishnan M. Correlative SANS and TEM investigation on precipitation kinetics of H-phase in $Ni_{50.3}Ti_{29.7}Hf_{20}$ high temperature shape memory alloy. J Alloy Compd 2019;779:630.

[132] Dai Hsu DH, Hornbuckle BC, Valderrama B, Barrie F, Henderson HB, Thompson GB, Manuel MV. The effect of aluminum additions on the thermal, microstructural, and mechanical behavior of NiTiHf shape memory alloys. J Alloy Compd 2015;638:67.

[133] Patriarca L, Sehitoglu H. High-temperature superelasticity of $Ni_{50.6}Ti_{24.4}Hf_{25.0}$ shape memory alloy. Scripta Mater 2015;101:12.

[134] Sehitoglu H, Wu Y, Patriarca L. Shape memory functionality under multi-cycles in NiTiHf. Scripta Mater 2017;129:11.

[135] Umale T, Salas D, Tomes B, Arroyave R, Karaman I. The effects of wide range of compositional changes on the martensitic transformation characteristics of NiTiHf shape memory alloys. Scripta Mater 2019;161:78.

[136] Saghaian SM, Karaca HE, Tobe H, Pons J, Santamarta R, Chumlyakov YI, Noebe

RD. Effects of Ni content on the shape memory properties and microstructure of Ni-rich NiTi-20Hf alloys. Smart Mater Struct 2016;25:095029.

[137] Coughlin DR, Casalena L, Yang F, Noebe RD, Mills MJ. Microstructure-property relationships in a high-strength 51Ni-29Ti-20Hf shape memory alloy. J Mater Sci 2016;51:766.

[138] Saghaian SM, Karaca HE, Tobe H, Turabi AS, Saedi S, Saghaian SE, Chumlyakov YI, Noebe RD. High strength NiTiHf shape memory alloys with tailorable properties. Acta Mater 2017;134:211.

[139] Benafan O, Bigelow GS, Scheiman DA. Transformation behavior in NiTi-20Hf shape memory alloys-Transformation temperatures and hardness. Scripta Mater 2018;146:251.

[140] Evirgen A, Karaman I, Santamarta R, Pons J, Noebe RD. Microstructural characterization and superelastic response of a $Ni_{50.3}Ti_{29.7}Zr_{20}$ high-temperature shape memory alloy. Scripta Mater 2014;81:12.

[141] Evirgen A, Karaman I, Pons J, Santamarta R, Noebe RD. Role of nano-precipitation on the microstructure and shape memory characteristics of a new $Ni_{50.3}Ti_{34.7}Zr_{15}$ shape memory alloy. Mater Sci Eng A 2016;655:193.

[142] Wu GH, Yu CH, Meng LQ, Chen JL, Yang FM, Qi SR, Zhan WS, Wang Z, Zheng YF, Zhao LC. Giant magnetic-field-induced strains in Heusler alloy NiMnGa with modified composition. Appl Phys Lett 1999;75:2990.

[143] Tickle R, James RD, Shield T, Wuttig M, Kokorin VV. Ferromagnetic shape memory in the NiMnGa system. IEEE Trans Magn 1999;35:4301.

[144] Murray SJ, Marioni M, Allen SM, O'handley RC, Lograsso TA. 6% magnetic-field-induced strain by twin-boundary motion in ferromagnetic Ni-Mn-Ga. Appl Phys Lett 2000;77:886.

[145] Sozinov A, Likhachev AA, Lanska N, Ullakko K. Giant magnetic-field-induced strain in NiMnGa seven-layered martensitic phase. Appl Phys Lett 2002;80:1746.

[146] Chernenko VA, Cesari E, Kokorin VV, Vitenko IN. The development of new ferromagnetic shape memory alloys in Ni-Mn-Ga system. Scripta Metal Mater 1995;33:1239.

[147] Chernenko VA, L'ov V, Pons J, Cesari E. Superelasticity in high-temperature Ni-Mn-Ga alloys. J Appl Phys 2003;93:2394.

[148] Xu H, Ma Y, Jiang C. A high-temperature shape-memory alloy $Ni_{54}Mn_{25}Ga_{21}$. Appl Phys Lett 2003;82:3206.

[149] Jiang C, Liang T, Xu H, Zhang M, Wu G. Superhigh strains by variant reorientation in the nonmodulated ferromagnetic NiMnGa alloys. Appl Phys Lett 2002;81:2818.

[150] Ma Y, Jiang C, Li Y, Xu H, Wang C, Liu X. Study of $Ni_{50+x}Mn_{25}Ga_{25-x}$ (x= 2-11) as high-temperature shape-memory alloys. Acta Mater 2007;55:1533.

[151] Xin Y, Li Y, Liu Z. Thermal stability of dual-phase $Ni_{58}Mn_{25}Ga_{17}$ high-temperature shape memory alloy. Scripta Mater 2010;63:35.

[152] Cai W, Gao L, Liu AL, Sui JH, Gao ZY. Martensitic transformation and mechanical properties of Ni-Mn-Ga-Y ferromagnetic shape memory alloys. Scripta Mater 2007;57:659.

[153] Gao L, Cai W, Liu AL, Zhao LC. Martensitic transformation and mechanical properties of polycrystalline $Ni_{50}Mn_{29}Ga_{21-x}Gd_x$ ferromagnetic shape memory alloys. J Alloy Compd 2006;425:314.

[154] Zhang X, Sui J, Zheng X, Yang Z, Tian X, Cai W. Effect of Ni substitution for Ga on the polycrystalline Ni-Mn-Ga-Gd high-temperature shape memory alloys. J Alloy Compd 2013;557:60.

[155] Zhang X, Sui J, Cai W, Liu Q, Liu A. Deformation mechanism of $Ni_{54}Mn_{25}Ga_{20.9}Gd_{0.1}$ high-temperature shape memory alloy. Intermetallics 2015;67:52.

[156] Yao J, Cui B, Zheng X, Wu Y, Sui J, Cai W. Thermal stability and high-temperature shape memory effect of $Ni_{55.2}Mn_{24.7}Ga_{19.9}Gd_{0.2}$ thin film. Vacuum 2018;147:78.

[157] Tsuchiya K, Tsutsumi A, Ohtsuka H, Umemoto M. Modification of Ni-Mn-Ga ferromagnetic shape memory alloy by addition of rare earth elements. Mater Sci Eng A 2004;378:370.

[158] Wu Y, Wang J, Jiang C, Xu H. Effect of coherent nanoprecipitates on martensitic transformation in Tb-doped NiMnGa melt-spun ribbons. Intermetallics 2018;97:42.

[159] Tian B, Ji R, Tong YX, Li L, Zheng YF. Microstructure, phase transformation and mechanical property of Nb-doped Ni-Mn-Ga alloys. Intermetallics 2015;64:37.

[160] Xu HB, Li Y, Jiang CB. Ni-Mn-Ga high-temperature shape memory alloys. Mater Sci Eng A 2006;438:1065.

[161] Villa E, Villa E, D'Eril MM, Nespoli A, Passaretti F. The role of γ-phase on the thermo-mechanical properties of NiMnGaFe alloys polycrystalline samples. J Alloy Compd 2018;763:883.

[162] Yang SY, Liu Y, Wang CP, Shi Z, Liu XJ. The mechanism clarification of Ni-Mn-Fe-Ga alloys with excellent and stable functional properties. J Alloy Compd 2013;560:84.

[163] Yang S, Su Y, Wang C, Hu Y, Liu X. Microstructure and martensitic transformation behavior of Ni-Mn-Fe-Ga-B high-temperature shape memory melt-spun ribbons. Mater Lett 2013;92:169.

[164] Yang S, Ma Y, Jiang H, Liu X. Microstructure and shape-memory characteristics of $Ni_{56}Mn_{25-x}Co_xGa_{19}$ (x= 4, 8) high-temperature shape-memory alloys. Intermetallics 2011;19:225.

[165] Nespoli A, Biffi CA, Villa E, Tuissi A. Effect of heating/cooling rate on martensitic transformation of NiMnGa-Co high temperature ferromagnetic shape memory alloys. J Alloy Compd 2017;690:478.

[166] Yang S, Wang C, Liu X. Simultaneous improvement of ductility and shape memory effect of two-phase $Ni_{53}Mn_{22}Co_6Ga_{19}$ high-temperature shape memory alloy with the addition of Ta. Mater Lett 2012;75:4.

[167] Singh S, D'Souza SW, Mukherjee K, Kushwaha P, Barman SR, Agarwal S, Mukhopadhyay PK, Chakrabarti A, Sampathkumaran EV. Magnetic properties and magnetocaloric effect in Pt doped Ni-Mn-Ga. Appl Phys Lett 2014;104:231909.

[168] Glavatskyy I, Glavatska N, Dobrinsky A, Hoffmann JU, Söderberg O, Hannula SP. Crystal structure and high-temperature magnetoplasticity in the new Ni-Mn-Ga-Cu magnetic shape memory alloys. Scripta Mater 2007;56:565.

[169] Wang J, Bai H, Jiang C, Li Y, Xu H. A highly plastic $Ni_{50}Mn_{25}Cu_{18}Ga_7$ high-temperature shape memory alloy. Mater Sci Eng A 2010;527:1975.

[170] Ni Z, Guo X, Li Q, Liang Z, Luo H, Meng F. Effect of Zn-doping on the phase transition and magnetic properties of Heusler alloys $Ni_2MnGa_{1-x}Zn_x$ (x = 0, 0.25, 0.5, 0.75 and 1). J Magn Magn Mater 2018;464:65.

[171] Zhang X, Liu Q, Zeng X, Sui J, Cai W, Wang H, Feng Y. Microstructure, mechanical properties and shape memory effect of Ni-Mn-Ga-B high-temperature shape memory alloy. Intermetallics 2016;68:113.

[172] Abhyankar AC, Yu YT, Kuo YK, Huang GW, Lue CS. Thermal and transport properties of $Ni_2MnGa_{1-x}Al_x$ alloys. Intermetallics 2010;18:2090.

[173] Singh S, Roy RK, Ghosh M, Mitra A, Panda AK. Martensitic transformation and magneto-strain in melt spun NiMnGaAl ferromagnetic shape memory alloys. Intermetallics 2013;43:147.

[174] Glavatskyy I, Glavatska N, Söderberg O, Hannula SP, Hoffmann JU. Transformation temperatures and magnetoplasticity of Ni-Mn-Ga alloyed with Si, In, Co or Fe. Scripta Mater 2006;54:1891.

[175] Chatterjee S, Giri S, Majumdar S, De SK, Koledov VV. Effect of Sn doping on the martensitic and premartensitic transitions in Ni_2MnGa. J Magn Magn Mater 2012;324:1891.

[176] Tian F, Cao K, Zhang Y, Zeng Y, Zhang R, Chang T, Zhou C, Xu M, Song X, Yang S. Giant spontaneous exchange bias triggered by crossover of superspin glass in Sb-doped $Ni_{50}Mn_{38}Ga_{12}$ Heusler alloys. Sci Rep 2016;6:1.

[177] Gao ZY, Dong GF, Cai W, Sui JH, Feng Y, Li XH. Martensitic transformation and mechanical properties in an aged Ni-Mn-Ga-Ti ferromagnetic shape memory alloy. J Alloy Compd 2009;481:44.

[178] Dong GF, Gao ZY, Tan CL, Sui JH, Cai W. Phase transformation and magnetic properties of Ni-Mn-Ga-Ti ferromagnetic shape memory alloys. J Alloy Compd 2010;508:47.

[179] Gao Z, Chen B, Meng X, Cai W. Site preference and phase stability of Ti doping Ni-Mn-Ga shape memory alloys from first-principles calculations. J Alloy Compd 2013;575:297.

[180] Dong GF, Cai W, Gao ZY, Sui JH. Effect of isothermal ageing on microstructure,

martensitic transformation and mechanical properties of $Ni_{53}Mn_{23.5}Ga_{18.5}Ti_5$ ferromagnetic shape memory alloy. Scripta Mater 2008;58:647.

[181] Dong GF, Tan CL, Gao ZY, Feng Y, Sui JH, Cai W. The effect of ageing on the microstructure and mechanical properties of $Ni_{53}Mn_{23.5}Ga_{18.5}Ti_5$ ferromagnetic shape memory alloy. Scripta Mater 2008;59:268.

[182] Tian B, Chen F, Tong YX, Li L, Zheng YF, Li QZ. Microstructure and phase transformation of $Ni_{46}Mn_{33}Ga_{17}Cu_{4-x}Zr_x$ alloys. Mater Lett 2014;116:307.

[183] Tian B, Jiang YL, Chen F, Tong YX, Li L, Zheng YF. Effect of Zr addition on the microstructure, phase transformation and mechanical property of $Ni_{50}Mn_{25}Ga_{17}Cu_8$ alloy. Mater Sci Eng A 2014;617:46.

[184] Tian B, Tong YX, Chen F, Li L, Zheng YF. Effect of aging and ball milling on the phase transformation of $Ni_{50}Mn_{25}Ga_{17}Cu_{8-x}Zr_x$ alloys. Intermetallics 2015;58:56.

[185] Cesari E, Chernenko VA, Kokorin VV, Pons J, Segui C. Internal friction associated with the structural phase transformations in Ni-Mn-Ga alloys. Acta Mater 1997;45:999.

[186] Liu Y. The work production of shape memory alloy. Smart Mater Struct 2004;13:552.

[187] Pérez-Sierra AM, Pons J, Santamarta R, Karaman I, Noebe RD. Stability of a Ni-rich Ni-Ti-Zr high temperature shape memory alloy upon low temperature aging and thermal cycling. Scripta Mater 2016;124:47.

[188] San Juan J, Nó ML. Damping behavior during martensitic transformation in shape memory alloys. J Alloy Compd 2003;355:65.

[189] Panchenko E, Tokhmetova A, Surikov N, Eftifeeva A, Tagiltsev A, Timofeeva E, Chumlyakov YI, Gerstein G, Maier HJ. Temperature dependence of martensite variant reorientation in stress-induced martensite aged $Ni_{49}Fe_{18}Ga_{27}Co_6$ single crystals. Scripta Mater 2021;194:113618.

[190] Kustov S, Golyandin S, Ichino A, Gremaud G. A new design of automated piezoelectric composite oscillator technique. Mater Sci Eng A 2006;442:532.

[191] Fan G, Zhou Y, Otsuka K, Ren X, Nakamura K, Ohba T, Suzuki T, Yoshida I, Yin F. Effects of frequency, composition, hydrogen and twin boundary density on the

internal friction of $Ti_{50}Ni_{50-x}Cu_x$ shape memory alloys. Acta Mater 2006;54:5221.

[192] Sapozhnikov K, Torrens-Serra J, Cesari E, Van Humbeeck J, Kustov S. Effect of Hydrogen on the Elastic and Anelastic Properties of the R Phase in $Ti_{50}Ni_{46.1}Fe_{3.9}$ Alloy. Metals 2017;7:493.

[193] Mazzolai G. Recent progresses in the understanding of the elastic and anelastic properties of H-free, H-doped and H-contaminated NiTi based alloys. Aip Adv 2011;1:040701.

[194] Sapozhnikov K, Torrens-Serra J, Cesari E, Van Humbeeck J, Kustov S. On the effect of hydrogen on the low-temperature elastic and anelastic properties of Ni-Ti-based alloys. Materials 2017;10:1174.

[195] Zhang L, Wang D, Ren X, Wang Y. A new mechanism for low and temperature-independent elastic modulus. Sci Rep 2015;5:1.

[196] Wang J, Jiang C. A single-phase wide-hysteresis shape memory alloy $Ni_{50}Mn_{25}Ga_{17}Cu_8$. Scripta Mater 2010;62:298.

[197] Isola LM, Malvasio BF, Giordana MF, Malarria J. Effect of the precipitates on the thermodynamics of the martensitic transformations in Ti-rich Ni-Ti-Co thin films. J Alloy Compd 2020;818:152904.

[198] Kustov S, Pons J, Cesari E, Van Humbeeck J. Pinning-induced stabilization of martensite Part Ⅰ. Stabilization due to static pinning of interfaces. Acta Mater 2004;52:3075.

[199] Kustov S, Pons J, Cesari E, Van Humbeeck J. Pinning-induced stabilization of martensite: Part Ⅱ. Kinetic stabilization in Cu-Zn-Al alloy due to pinning of moving interfaces. Acta Mater 2004;52:3083.

[200] Kustov S, Pons J, Cesari E, Van Humbeeck J. Chemical and mechanical stabilization of martensite. Acta Mater 2004;52:4547.

[201] Picornell C, Pons J, Cesari E, Dutkiewicz J. Thermal characteristics of Ni-Fe-Ga-Mn and Ni-Fe-Ga-Co ferromagnetic shape memory alloys. Intermetallics 2008;16:751.

[202] Kustov S, Pons J, Cesari E, Van Humbeeck J, Morin M. Stabilization and hyperstabilization of Cu-Al-Be β_1' martensite by thermal treatment and plastic

deformation. Mater Sci Eng A 2004;378:283.

[203] Morgan NB, Friend CM. A review of shape memory stability in NiTi alloys. J Phys IV 2001;11:Pr8.

[204] Font J, Muntasell J, Pons J, Cesari E. Thermal cycling effects in high temperature Cu-Al-Ni-Mn-B shape memory alloys. J Mater Res 1997;12:2288.

[205] Auguet C, Cesari E, Rapacioli R, Mañosa L. Effect of γ precipitates on the martensitic transformation of β Cu-Zn-Al studied by calorimetry. Scripta Metall 1989;23:579.

[206] Cesari E, Pons J, Chandrasekaran M. The influence of γ precipitates on the martensitic transformation and related effects in Cu-based shape memory alloys. Trans Mater Res Soc Japan 1994;18B:903.

[207] Dutkiewicz J, Pons J, Cesari E. Effect of γ precipitates on the martensitic transformation in Cu-Al-Mn alloys. Mater Sci Eng A 1992;158:119.

[208] Kireeva IV, Pons J, Picornell C, Chumlyakov YI, Cesari E, Kretinina IV. Influence of γ′ nanometric particles on martensitic transformation and twinning structure of $L1_0$ martensite in Co-Ni-Ga ferromagnetic shape memory single crystals. Intermetallics 2013;35:60.

[209] Kireeva IV, Picornell C, Pons J, Kretinina IV, Chumlyakov YI, Cesari E. Effect of oriented γ′ precipitates on shape memory effect and superelasticity in Co-Ni-Ga single crystals. Acta Mater 2014;68:127.

[210] Panchenko EY, Chumlyakov YI, Kireeva IV, Ovsyannikov AV, Sehitoglu H, Karaman I, Maier YHJ. Effect of disperse Ti_3Ni_4 particles on the martensitic transformations in titanium nickelide single crystals. Phys Met Metall 2008;106:577.

[211] La Roca P, Isola L, Vermaut P, Malarría J. Relationship between grain size and thermal hysteresis of martensitic transformations in Cu-based shape memory alloys. Scripta Mater 2017;135:5.

[212] Cui J, Chu YS, Famodu OO, Furuya Y, Hattrick-Simpers J, James RD, Ludwig A, Thienhaus S, Wuttig M, Zhang Z, Takeuchi I. Combinatorial search of thermoelastic shape-memory alloys with extremely small hysteresis width. Nat Mater 2006;5:286.

[213] Zhang Z, James RD, Müller S. Energy barriers and hysteresis in martensitic

phase transformations. Acta Mater 2009;57:4332.

[214] Zarnetta R, Takahashi R, Young ML, Savan A, Furuya Y, Thienhaus S, Maaß B, Rahim M, Frenzel J, Brunken H, Chu YS, Srivastava V, James RD, Takeuchi I, Eggeler G, Ludwig A. Identification of quaternary shape memory alloys with near-zero thermal hysteresis and unprecedented functional stability. Adv Funct Mater 2010;20:1917.

[215] Picornell C, Pons J, Cesari E. Stabilisation of martensite by applying compressive stress in Cu-Al-Ni single crystals. Acta Mater 2001;49:4221.

[216] Picornell C, Pons J, Cesari E. Mechanical stabilisation and anomalous behaviour of the stress-strain loops in Cu-Al-Ni single crystals. Scripta Mater 2006;54:459.

[217] Picornell C, Pons J, Paulsen A, Frenzel J, Kaminskii V, Sapozhnikov K, Van Humbeeck J, Kustov S. Burst-like reverse martensitic transformation during heating, cooling and under isothermal conditions in stabilized Ni-Ti-Nb. Scripta Mater 2020;180:23.

[218] Khachaturyan AG, Shapiro SM, Semenovskaya S. Adaptive phase formation in martensitic transformation. Phys Rev B 1991;43:10832.

[219] Jiang C, Muhammad Y, Deng L, Wu W, Xu H. Composition dependence on the martensitic structures of the Mn-rich NiMnGa alloys. Acta Mater 2004;52:2779.

[220] Kaufmann S, Rößler UK, Heczko O, Wuttig M, Buschbeck J, Schultz L, Fähler S. Adaptive modulations of martensites. Phys Rev Lett 2010;104:145702.

APPENDIX

Appendix A

Table A1. NiMnGaHf0 transformation characteristics obtained from thermomechanical experiments.

Stress	M_s	M_f	A_s	A_f	**Hysteresis**	**Total Strain**	**Irrecoverable Strain**	**Irr/Total**
MPa	K	K	K	K	K	%	%	
20	598	587	620	631	32	0.62	0.06	0.10
60	600	588	621	631	32	1.24	0.10	0.08
100	606	590	625	639	34	1.63	0.18	0.11
200	635	597	640	673	40	2.45	0.34	0.14
300	644	592	650	687	52	2.77	0.73	0.26

Table A2. NiMnGaHf0.5 transformation characteristics obtained from thermomechanical experiments.

Stress	M_s	M_f	A_s	A_f	**Hysteresis**	**Total Strain**	**Irrecoverable Strain**	**Irr/Total**
MPa	K	K	K	K	K	%	%	
20	605	591	636	649	40	0.21	0.04	0.19
60	612	590	630	651	38	0.93	0.01	0.01
100	611	593	630	646	36	1.28	0.10	0.08
200	622	601	648	664	44	2.01	0.45	0.22
300	649	597	663	695	59	2.26	0.79	0.35

Table A3. NiMnGaHf1 transformation characteristics obtained from thermomechanical experiments.

Stress	M_s	M_f	A_s	A_f	**Hysteresis**	**Total Strain**	**Irrecoverable Strain**	**Irr/Total**
MPa	K	K	K	K	K	%	%	
20	545	532	547	559	15	0.32	0.04	0.13
60	548	532	547	563	15	0.79	0.07	0.08
100	555	535	551	569	16	1.15	0.07	0.06
200	570	540	572	596	29	1.90	0.31	0.16
300	600	541	608	646	60	2.39	0.77	0.32

Table A4. NiMnGaHf2 transformation characteristics obtained from thermomechanical experiments.

Stress	M_s	M_f	A_s	A_f	**Hysteresis**	**Total Strain**	**Irrecoverable Strain**	**Irr/Total**
MPa	K	K	K	K	K	%	%	
20	488	469	481	499	11	0.37	0.03	0.08
60	489	469	480	499	10	0.53	0.03	0.06
100	493	471	483	503	10	0.71	0.04	0.06
200	504	477	490	513	12	0.93	0.12	0.13
300	515	478	494	523	15	1.21	0.26	0.21

Table A5. NiMnGaHf3 transformation characteristics obtained from thermomechanical experiments.

Stress	M_s	M_f	A_s	A_f	**Hysteresis**	**Total Strain**	**Irrecoverable Strain**	**Irr/Total**
MPa	K	K	K	K	K	%	%	
20	442	426	434	448	8	0.34	0.03	0.08
60	446	427	435	453	8	0.50	0.04	0.08
100	446	429	436	453	7	0.55	0.02	0.04
200	454	432	439	460	7	0.72	0.08	0.11
300	462	435	444	466	8	0.83	0.16	0.19

Table A6. NiMnGaHf4 transformation characteristics obtained from thermomechanical experiments.

Stress	M_s	M_f	A_s	A_f	**Hysteresis**	**Total Strain**	**Irrecoverable Strain**	**Irr/Total**
MPa	K	K	K	K	K	%	%	
20	417	405	412	423	8	0.26	0.03	0.11
60	420	404	411	425	7	0.43	0.05	0.11
100	420	406	412	425	6	0.47	0.03	0.05
200	430	408	414	434	7	0.56	0.07	0.13
300	431	412	419	436	7	0.63	0.06	0.10

Table A7. NiMnGaZr0.5 transformation characteristics obtained from thermomechanical experiments.

Stress	M_s	M_f	A_s	A_f	**Hysteresis**	**Total Strain**	**Irrecoverable Strain**	**Irr/Total**
MPa	K	K	K	K	K	%	%	
20	563	544	567	584	21	0.45	0.04	0.08
60	566	545	568	587	22	1.22	0.08	0.07
100	572	550	576	596	26	1.77	0.15	0.08
200	594	558	607	635	46	2.64	0.55	0.21
300	626	558	622	668	57	2.89	0.93	0.32

Table A8. NiMnGaZr1 transformation characteristics obtained from thermomechanical experiments.

Stress	M_s	M_f	A_s	A_f	**Hysteresis**	**Total Strain**	**Irrecoverable Strain**	**Irr/Total**
MPa	K	K	K	K	K	%	%	
20	602	536	553	622	16	0.33	0.06	0.18
60	605	537	554	631	16	0.96	0.09	0.09
100	569	540	560	587	19	1.42	0.12	0.09
200	585	546	591	622	42	2.18	0.44	0.20
300	612	550	616	656	59	2.41	0.83	0.35

Table A9. NiMnGaZr2 transformation characteristics obtained from thermomechanical experiments.

Stress	M_s	M_f	A_s	A_f	**Hysteresis**	**Total Strain**	**Irrecoverable Strain**	**Irr/Total**
MPa	K	K	K	K	K	%	%	
20	520	505	519	533	16	0.28	0.03	0.12
60	522	507	520	533	12	0.55	0.04	0.07
100	528	508	520	538	12	0.72	0.04	0.05
200	537	515	529	549	14	0.99	0.12	0.12
300	549	516	547	5705	29	1.30	0.38	0.29

Table A10. NiMnGaZr3 transformation characteristics obtained from thermomechanical experiments.

Stress	M_s	M_f	A_s	A_f	**Hysteresis**	**Total Strain**	**Irrecoverable Strain**	**Irr/Total**
MPa	K	K	K	K	K	%	%	
20	463	451	460	472	9	0.30	0.02	0.06
60	465	452	461	473	9	0.49	0.03	0.06
100	466	452	461	475	8	0.57	0.03	0.05
200	472	456	465	480	9	0.69	0.06	0.08
300	479	459	470	487	10	0.81	0.12	0.14

Table A11. NiMnGaZr4 transformation characteristics obtained from thermomechanical experiments.

Stress	M_s	M_f	A_s	A_f	**Hysteresis**	**Total Strain**	**Irrecoverable Strain**	**Irr/Total**
MPa	K	K	K	K	K	%	%	
20	440	426	434	446	8	0.30	0.04	0.12
60	441	428	434	447	6	0.34	0.02	0.07
100	445	428	434	451	7	0.45	0.05	0.10
200	446	431	436	451	6	0.49	0.02	0.05
300	452	432	439	457	6	0.57	0.03	0.05

Appendix B

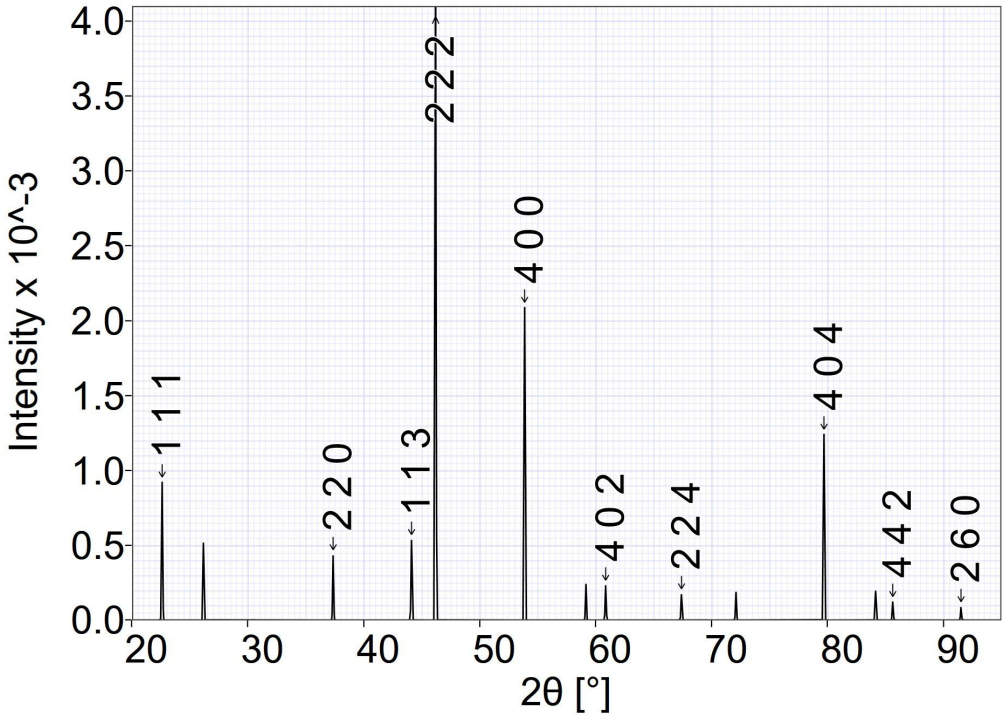

Fig. A1. Simulated XRD pattern of Ni-ordered f.c.c. precipitates under “cubic” axes in Ni-Mn-Ga-Hf alloys.

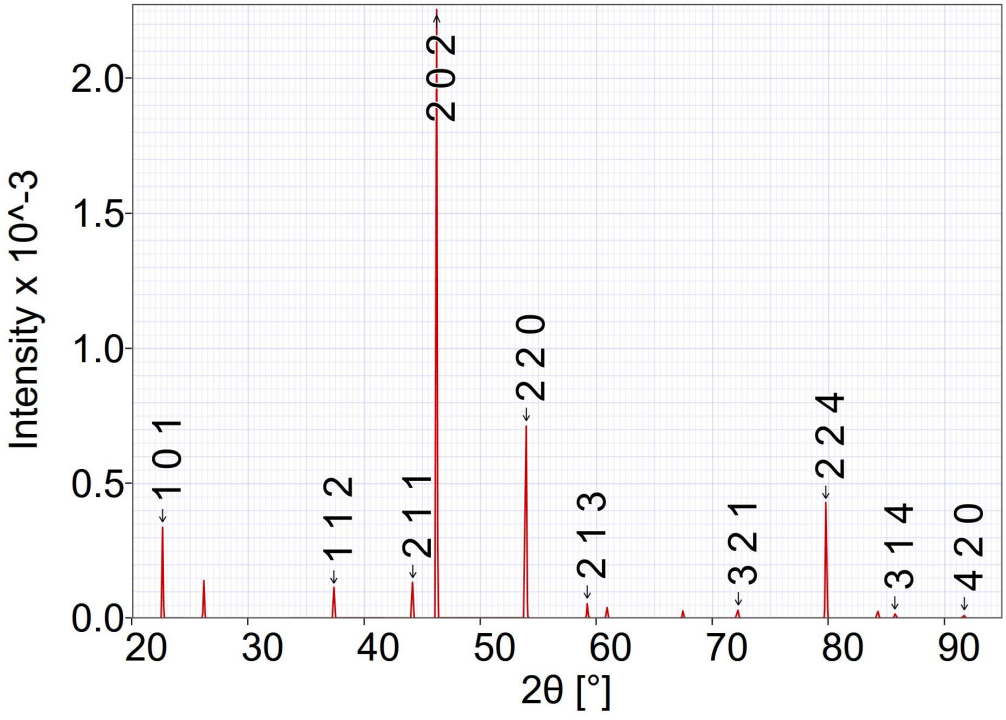

Fig. A2. Simulated XRD pattern of Ni-ordered f.c.t. precipitates under “tetragonal” axes in Ni-Mn-Ga-Hf alloys.

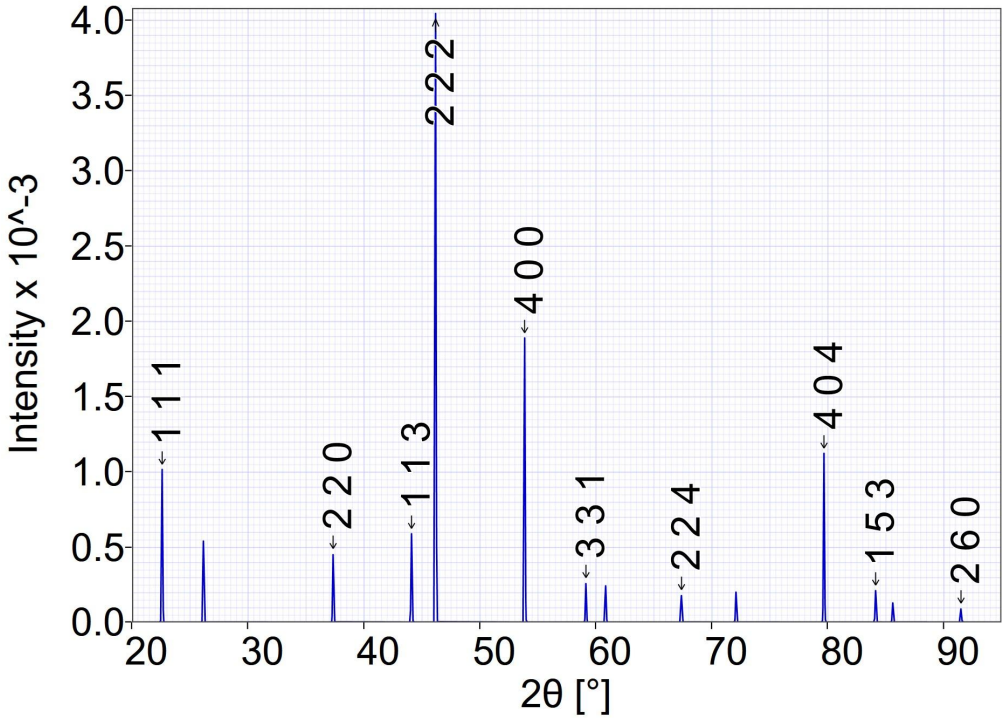

Fig. A3. Simulated XRD pattern of Ni-disordered f.c.c. precipitates under “cubic” axes in Ni-Mn-Ga-Hf alloys.

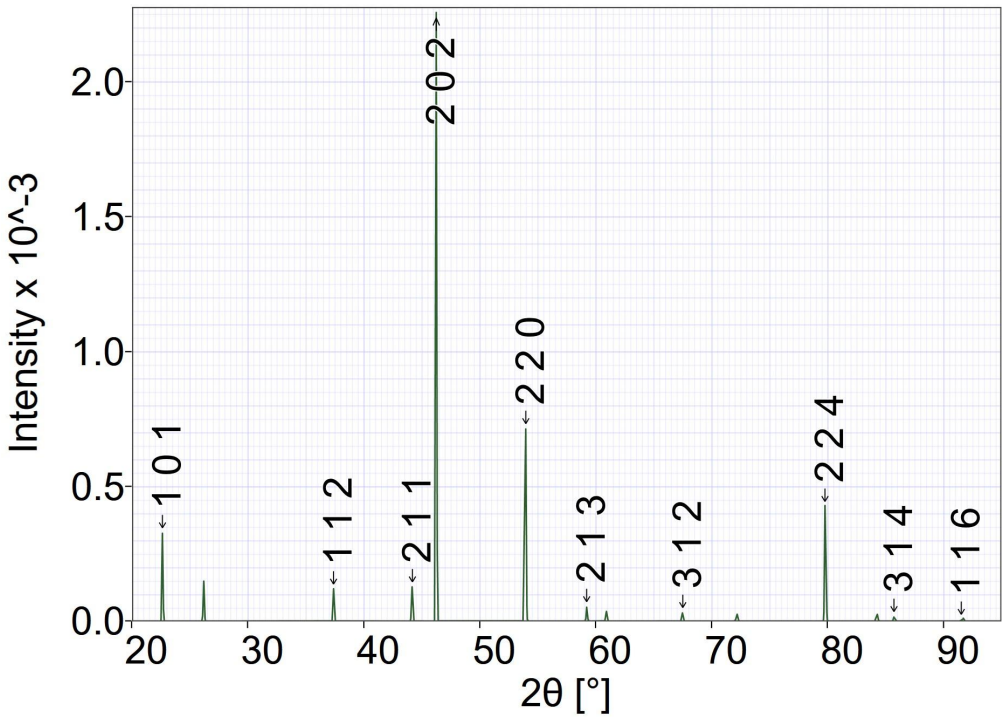

Fig. A4. Simulated XRD pattern of Ni-disordered f.c.t. precipitates under “tetragonal” axes in Ni-Mn-Ga-Hf alloys.

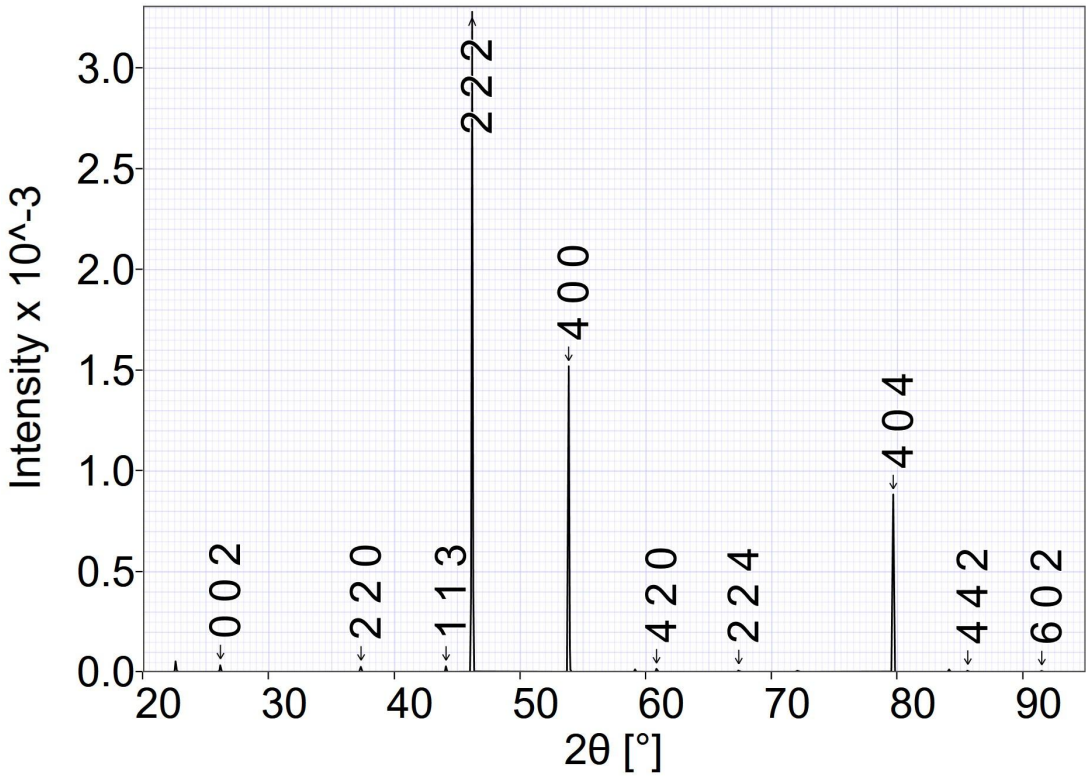

Fig. A5. Simulated XRD pattern of Ni-ordered f.c.c. precipitates under “cubic” axes in Ni-Mn-Ga-Zr alloys.

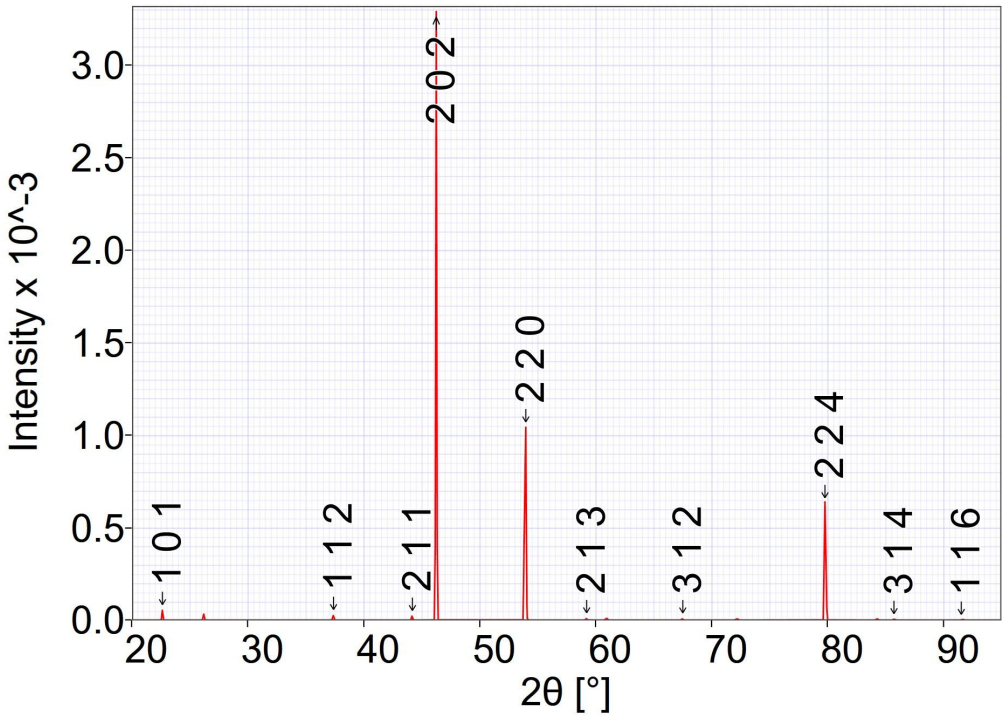

Fig. A6. Simulated XRD pattern of Ni-ordered f.c.t. precipitates under “tetragonal” axes in Ni-Mn-Ga-Zr alloys.

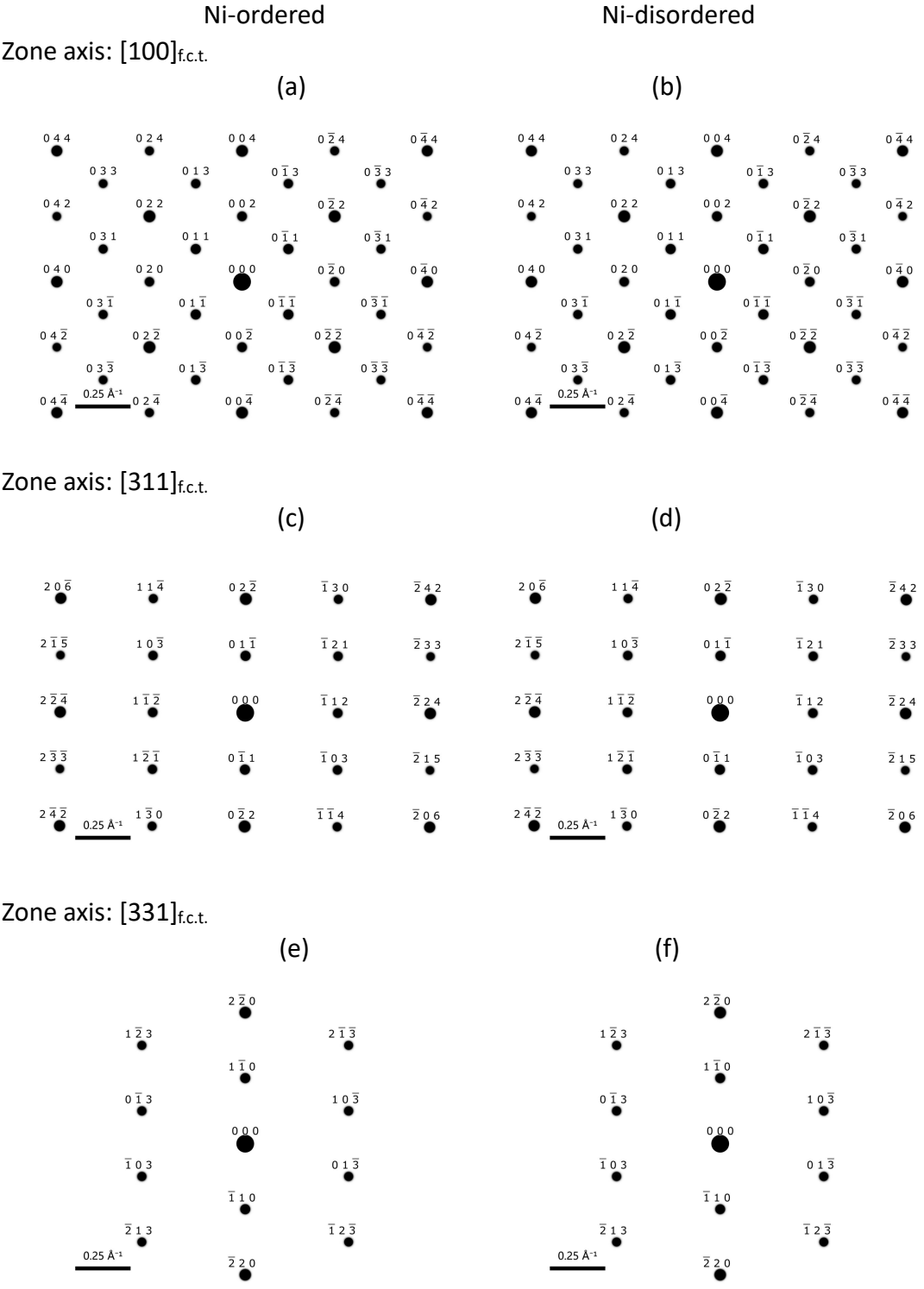

Fig. A7. Simulated diffraction patterns of precipitates under “tetragonal” axes in Ni-Mn-Ga-Hf alloys, the left column and right column are from Ni-ordered f.c.t. structure and Ni-disordered f.c.t. structure, respectively. The patterns (a) and (b), (c) and (d), (e) and (f) are under the zone axes $[100]_{f.c.t.}$, $[311]_{f.c.t.}$ and $[331]_{f.c.t.}$, respectively.

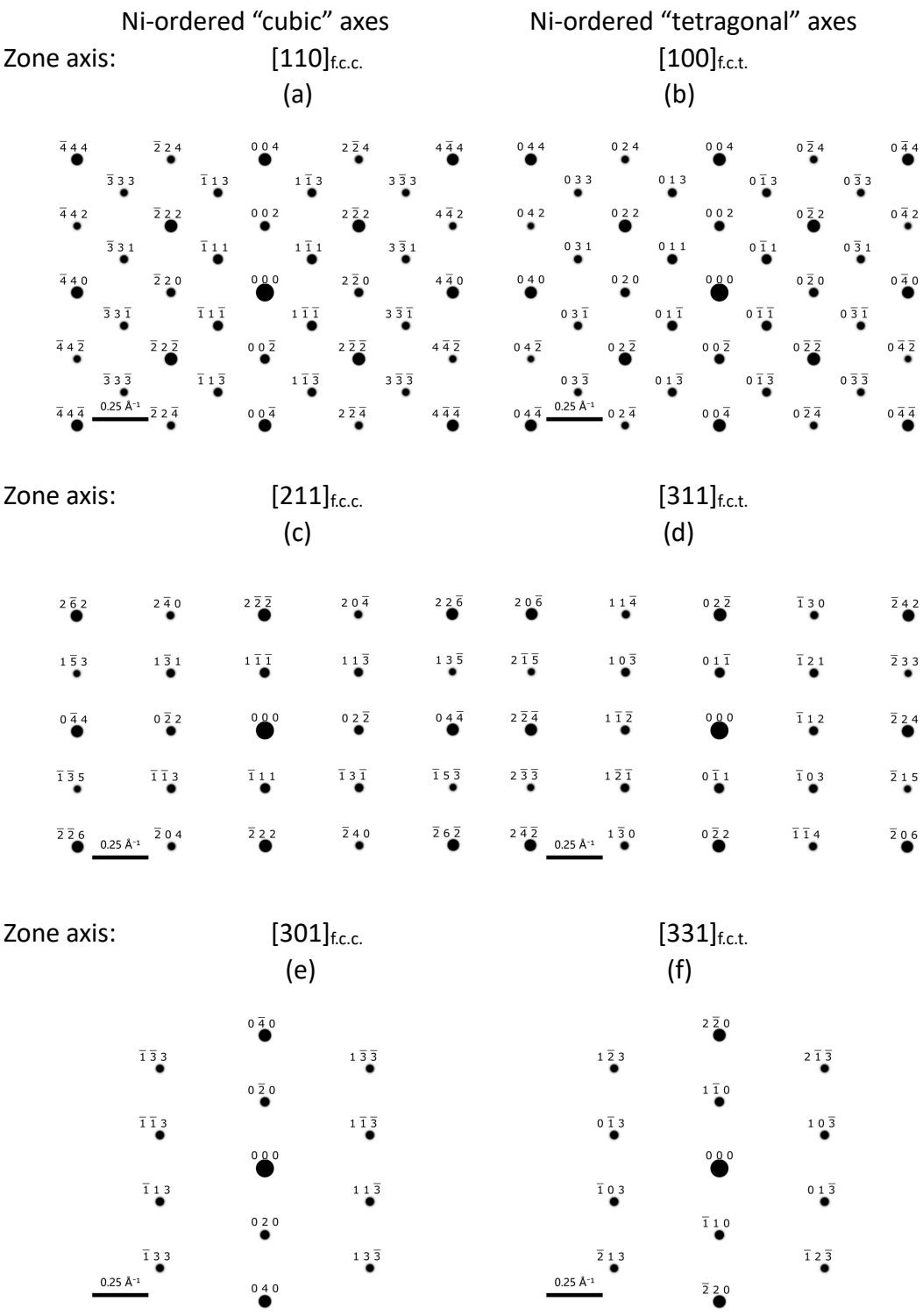

Fig. A8. Simulated diffraction patterns of precipitates under “cubic” and “tetragoanl” axes in Ni-Mn-Ga-Zr alloys, the left column and right column are from Ni-ordered f.c.c. structure and Ni-ordered f.c.t. structure, respectively. The patterns (a) and (b), (c) and (d), (e) and (f) are under the zone axes $[110]_{f.c.c.}$ and $[100]_{f.c.t.}$, $[211]_{f.c.c.}$ and $[311]_{f.c.t.}$, $[301]_{f.c.c.}$ and $[331]_{f.c.t.}$, respectively.